IMAGING X-RAY ASTRONOMY:

THE CYGNUS LOOP SNR

by

MICHAEL ANTHONY KAYAT, B.Sc. M.Sc.

A Thesis submitted to the

UNIVERSITY OF LEICESTER

for the degree of

DOCTOR OF PHILOSOPHY IN PHYSICS

X-Ray Astronomy group
Department of Physics
University of Leicester

To my Mother and Father

Masters, I am to discuss wonders : but
ask me not what; for if I tell you,
I am no true Athenian. I will tell you
everything, right as it fell out.

Bottom, the Weaver

in

A Midsummer - Nights Dream, Act IV, Scene II

W. Shakespeare, ca. 1594

CONTENTS

ABSTRACT

Supernovae and supernova remnants (SNR) are probably important energy sources in the interstellar medium (ISM) and an understanding of the intermediate and advanced stages of SNR evolution are particularly essential.

This thesis describes, first a brief review of the current understanding of the ISM and later stages of SNR evolution, then a detailed review of observations of the Cygnus Loop SNR, a relatively old SNR. Details are given of the design and instrumentation of a rocket - borne experiment, which subsequently was utilized to obtain the first X-ray image of a SNR, the Cygnus Loop. The results of X-ray image and spectral analysis are presented, and discussed with respect to previous optical, radio and X-ray observations, and to current SNR blast wave and ISM models.

ACKNOWLEDGMENTS

The following pages may convey some insight into how an experiment in space research is carried out, as well as reporting on the astrophysical result obtained. Many very able people contributed throughout, from design and build, to integration aboard a rocket, to launching, to preliminary and detailed data analysis.

Firstly and foremost, I wish to express my thanks and deep appreciation to Professor K.A. Pounds, Director of the X-ray Astronomy Group at Leicester, for enabling me to undertake the research related in this thesis, and for encouragement and help of all kinds. I am also deeply grateful to my supervisor Dr. K. Evans, who provided much encouragement and help at all stages. Dr. G. Smith, my colleague during all stages of the research and development of the hardware, provided the skills and experience to overcome some vary difficult problems, and without whom, the experiment could not have been possible. Mr. A. Wells, Space Projects Manager, efficiently managed the experiment and gave encouragement and help at all stages.

Mr. D. Watson, Mr. J. Dowson, Mr. R. Cooper and Mr. D. Johnson provided first class support of research design and testing and subsequent preparation of hardware, for flight.

All members of the physics workshop gave excellent and invaluable hardware support.

I am very grateful for all the support and encouragement and software help I received from all members of the X-ray Astronomy Group. In particular, Dr. R. Willingale and Mr. D. Rolf provided great help and encouragement during the data analysis stages, and many enjoyable discussions on all aspects of research. I am also very grateful to support and encouragement from Mr. G. Fraser, Mrs. M. Lewis, Mr. R. Hall and Mr. M. Sims.

The experiment was in collaboration with the Massachussetts Institute of Technology (MIT). I am very grateful to Professor S. Rappaport for encouragement, help and for imparting much knowledge of X-ray astronomy and techniques. Dr. A. Levine and Mr. R. Petre gave much support and hospitality. Mr. E. Boughan and Mr. F. Miller did an excellent job of design and build of the Astrobee payload and imparted much experience on experimental rocket research.

At Goddard Space Flight Centre, many people gave excellent support to the payload, in particular Mr. F. Lau and Mr. J. Cameron. The Navy members of the White Sands launch crew conducted a perfect launch. To everyone concerned at GSFC and WSMR, I am very grateful.

My Mother and Father have provided constant support and help during this time and others, and to them I extend my most deep gratitude.

MEMORANDUM

I hereby declare that no part of this thesis has been previously submitted to this or any other University as part of the requirements for a higher degree. The research described in this thesis was conducted and performed by the undersigned, except for the contribution from colleagues, listed in the Acknowlegment or as referrenced in the text.

M. A. Kayat

M. A. Kayat

Chapter 1. CONTEMPORY UNDERSTANDING OF ADVANCED SUPERNOVA REMNANT EVOLUTION IN THE INTERSTELLAR MEDIUM

Chapter 1. CONTEMPORY UNDERSTANDING OF ADVANCED SUPERNOVA REMNANT EVOLUTION IN THE INTERSTELLAR MEDIUM.

1. Introduction

Until recently, the interstellar medium (ISM) was mainly considered to consist of cool ($\sim$ 100 K) clouds embedded in a substrate of warm ($\sim 10^4$ K) intercloud medium of partially ionised HI and HII and that the main source of heating was ionisation by low energy cosmic rays, soft X-rays and extreme UV. However, recent $\overline{OVI}$ (Jenkins and Meloy (1974), York (1974)) and soft X-ray observations (Burstein et al. 1977) indicate the presence of hot (10^6 K) coronal - type gas, possibly occupying most of the interstellar volume, and in which the intercloud medium and cool clouds are embedded. Relatively high shocks $\gtrsim$ 20 km/s occur in the ISM, from optical, radio and UV observations, and may originate from winds from early OB type stars or from supernovae and supernova remnants (SNR) evolution, with overlapping SNR possibly giving rise to ISM shock structure, apparent in large regions of the (local) ISM. The interiors of SNR consist of coronal gas, and as interiors overlap, interconnecting tunnel systems of coronal gas may be produced. The energy from shock waves in SNR is most likely responsible for the production and maintaining of coronal interstellar gas. The dominant cooling mechanism of the hot gas may be thermal conduction at the surfaces with the cooler regions, and possibly causing cloud evaporation effects.

The high velocity shocks characterising SNR evolution at intermediate (120 - 500 km/s) and advanced (20 - 100 km/s) stages have also recently been investigated observationally and theoretically, to account for the optical, X-ray and radio emission, and incorporating interactions with ISM clouds, to account for the structure observed.

A brief review of the present description of the ISM is given below and then a somewhat more detailed review of the intermediate stage of SNR evolution in such an ISM, to enable some understanding of the soft X-ray image of the Cygnus Loop SNR, presented in Chapter 6.

1.2 Contempory description of the interstellar medium.

1.2.1 The discrete cloud model.

Due to the extreme inhomogeneity in the distribution of interstellar matter in the Galaxy, discernable on all scales ranging from globules $\sim O(10^3$ AU) to complexes of clouds $\sim O(10^3$ pc), a number of models have been adapted in discussing the ISM.

The discrete cloud model (Abartsumian and Gondeladse (1938), Abartsumian (1940), Agekyan (1955)) invoked spherical clouds, randomly dispersed in space, moving with a Gaussian velocity distribution. Supportive evidence came from primarily HI studies (Miller (1957), Westerhout (1957)) and multiple absorption lines of Na I, Ca II in the spectra of bright stars (Adams (1949), Blaauw (1952), Munch (1957)). Spitzer (1968) summarised the parameters of the 'standard' cloud, Table 1.1.

TABLE 1.1

Parameters for the standard cloud.

Radius	7 pc
Number density	5×10^4 Kpc^{-3}
Number in line of sight	8
Cloud filling factor	0.07
Photographic extinction/cloud	0.2^m
Mass	400 $M_\odot$
HI density	10 cm^{-3}
Cloud dispersion (1 - d)	8 km/s
Maxwellian temperature	80 K

A correlation of decrease in cloud size and density with increased distance from the galactic plane was found by Agekyan (reported in Kaplan and Pikelner (1970)), Table 1.2.

TABLE 1.2

b^o	Mean cloud θ (pc)	Absorption/cloud (^{m})
15	110 $\pm$ 16	0.6 $\pm$ 0.07
32.5	17 $\pm$ 7	0.23 $\pm$ 0.08
52.5	4.5 $\pm$ 3.1	0.12 $\pm$ 0.08

1.2.2 Contempory observations and models.

Recent reviews of the ISM observations have been reported by Myers (1978) and McCray and Snow (1979). Myers compiled over 200 observations, in seven spectral line surveys, of interstellar gas properties : coronal and intercloud gas, diffuse clouds, dark clouds, Bok globules, molecular clouds associated with HII regions, and HII regions. Each survey enabled a determination of interstellar gas temperature and particle, density for each gas type (Myers (1978) and references therein), in the ranges $1 \lesssim \log_{10} T \lesssim 6$, $-3 \lesssim \log_{10} n \lesssim 5$, Fig. 1.1 and Table 1.3. summarises Fig. 1.1.

In particular, Myers points out that for the coronal gas, intercloud gas and diffuse cloud gas, the decrease of temperature with particle density is very uncertain, since the filling factors and cloud sizes are not well known. In Table 1.3, it was assumed the cloud filling factor $f_c \sim 0.1$, the intercloud factor $f_i \sim 1$ and scale length $L \sim 5\ pc$. However, by assuming instead that the low pressure equilibrium, constraints were derived on f_c, f_i, L and diffuse cloud

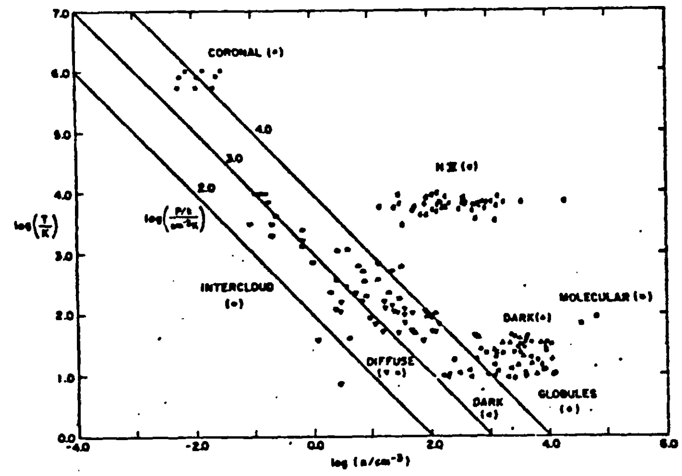

Interstellar gas temperature, density, and pressure, based on seven galactic spectral line surveys. *Circles*, representative points for coronal gas observed in 1032 Å O VI line, based on filling factor f_c = 0.1, 0.2, and 0.4, and on $n(T)$ power-law exponent η = 0.0, 0.5, and 1.0; *semicircles pointing down*, intercloud gas observed in 21 cm H I line; *semicircles pointing up* and *triangles pointing down*, diffuse clouds observed in 21 cm H I line; *triangles pointing up*, dark clouds observed in 21 cm H I line; *triangles pointing left*, dark clouds observed in 2.6 mm CO lines; *diamonds*, Bok globules observed in 2.6 mm CO lines; *squares*, molecular clouds associated with nebulosity, observed in 2.6 mm CO lines; *semicircles pointing left*, H II regions observed in 6 cm H109α line and 6 cm continuum.

Fig. 1.1 (Myers (1978))

TABLE 1.3 (Myers (1978))

INTERSTELLAR GAS PROPERTIES

Gas Type	Ref.	Points	L (pc) m	L (pc) σ	n (cm⁻³) m	n (cm⁻³) σ	T (K) m	T (K) σ	P/k (cm⁻³ K) m	P/k (cm⁻³ K) σ	$M/M_\odot$ m	$M/M_\odot$ σ	Note
Coronal (O VI)....	*a–c*	48	...	...	1.5 (−2)	8.3 (−3)	4.4 (5)	3.5 (5)	1.1 (4)	8.4 (3)	...	...	1
Intercloud (H I)...	*d*	12	...	...	3.6 (−1)	3.0 (−1)	4.5 (3)	3.8 (3)	1.0 (3)	4.4 (2)	...	...	
Diffuse cloud (H I)	*e*	28	5.0	0.0	3.5 (1)	3.7 (1)	1.3 (2)	1.2 (2)	3.1 (3)	2.9 (3)	7.1 (1)	7.7 (1)	2
Diffuse cloud (H I)	*d*	17	5.0	0.0	2.1 (1)	3.1 (1)	4.1 (2)	3.4 (2)	5.2 (3)	5.2 (3)	4.3 (1)	6.3 (1)	2
Dark cloud (H I)..	*f*	14	2.9	4.8	3.3 (3)	2.5 (3)	3.2 (1)	1.4 (1)	8.9 (4)	7.4 (4)	1.1 (3)	2.8 (3)	3
Dark cloud (^{12}CO, ^{13}CO)...	*g*	14	4.2	3.6	2.7 (3)	7.0 (3)	1.0 (1)	1.8 (0)	3.0 (4)	7.7 (4)	1.8 (3)	2.7 (3)	4
Molecular cloud (^{12}CO, ^{13}CO)...	*h–s*	21	5.4	3.3	7.8 (3)	1.4 (4)	3.2 (1)	1.8 (1)	4.8 (5)	1.3 (6)	4.0 (4)	8.2 (4)	5
Bok globule (^{12}CO, ^{13}CO)...	*t*	11	0.87	0.95	6.8 (3)	3.5 (3)	1.3 (1)	4.7 (0)	8.8 (4)	4.8 (4)	4.2 (2)	1.2 (3)	5
H II region (H109α)	*u*	47	7.2	8.8	8.8 (2)	2.7 (3)	6.4 (3)	1.6 (3)	5.9 (6)	2.0 (7)	1.4 (3)	3.4 (3)	6

NOTES.—(1) Means and standard deviations are based on the nine points resulting from combinations of η = 0, 0.5, 1.0 and f_c = 0.1, 0.2, 0.4. (2) L = 5.0 pc (Baker and Burton 1975). (3) H I temperature corrected for foreground emission; L = 1.5L(dust). (4) L = 1.5L(dust). (5) L based on ^{12}CO or ^{13}CO map. (6) L based on Gaussian diameter of continuum map.

REFERENCES.—(*a*) Jenkins and Meloy 1974. (*b*) Jenkins 1978*a*. (*c*) Jenkins 1978*b*. (*d*) Davies and Cummings 1975. (*e*) Lazareff 1975. (*f*) Knapp 1974*a*. (*g*) Dickman 1975. (*h*) Blair *et al*. 1978. (*i*) Elmegreen and Elmegreen 1978*b*. (*j*) Elmegreen and Elmegreen 1978*a*. (*k*) Elmegreen and Lada 1978. (*l*) Elmegreen, Dickinson, and Lada 1978. (*m*) Evans, Blair, and Beckwith 1977. (*n*) Lada 1976. (*o*) Lada and Reid 1978. (*p*) Liszt *et al*. 1974. (*q*) Loren 1976. (*r*) Loren 1977*a*. (*s*) Loren 1977*b*. (*t*) Martin and Barrett 1978. (*u*) Reifenstein *et al*. 1970.

density. The value for the gas pressure $\simeq$ 3700 cm^{-3} K for the coronal. intercloud gas and diffuse clouds was adapted (Jenkins (1978)). Table 1.4 summarises the results of Myers (1978), for the three gas types.

TABLE 1.4

Low pressure gas parameters.

Gas type	Pressure (cm^{-3} K)	Filling factor	Scale length (pc)	Density (cm^{-3})
Coronal	3700	0.55 ± 0.25		
Intercloud	3700	0.3 ± 0.1		
Diffuse	3700	0.2	5.7 ± 5.5	34 ± 27

In order to account for the observed ISM characteristics, summarised above particularly for the coronal intercloud gas and diffuse cloud properties, recent models of the ISM have been presented where the dynamics are dominated by SNR (and SNR evolution modified). Cox and Smith (1974) noted that galactic SN may occur at a rate to produce an interconnecting tunnel system of coronal gas. They considered a cavity formed at $\sim 10^6$ K and 3×10^{-3} cm^{-3}, approximately 4×10^6 years after the original SN event, with initial burst energy 4×10^{50} erg, evolving in an ISM of density $\sim$ 1 cm^{-3}. Since the cavity persists for so long (due to inefficient radiation loss) the possibility exists for nearby (young) SNR to encounter the cavity, increasing the volume, and by repeated encounters, build up a chain of connected tunnels, surrounded by walls of cool, dense HI at $< 10^3$ K and > 10 cm^{-3}. Essentially, the Cox and Smith ISM model invokes a three phase medium : coronal gas at 10^6 K, 3×10^{-3} cm^{-3} with filling factor $\sim$ 0.5; cool, dense tunnel phase $\sim$ 20 pc diameter; a surrounding, warm envelope 10^4 K, 1 cm^{-3}. However, the model assumes initial SNR formation in an ISM of uniform density, $\sim$ 1 cm^{-3}, higher than observed values.

McKee and Ostriker (1977) further suggested that the volume fraction of hot gasmay be so great that the ISM consists of disconnected regions of HI and HII embedded in a substrate of low density coronal gas. McKee and Ostriker combined the SNR adiabatic blast wave formalism (1.3) and theory of conductive surfaces (Cowie and McKee (1977)) within the framework of the Cox and Smith model, and proposed a model of which there are four phases (in pressure equilibrium), Table 1.5, regulated by SNR evolution (1.3).

TABLE 1.5

Properties of McKee and Ostriker ISM model.

Gas type	Filling factor	Density. cm^{-3}	Temperature. K.
Cool, neutral	0.03	40	80
Warm, neutral	0.2	0.25	8000
Warm, ionised	0.1	0.4	8000
Hot, ionised	0.7	3×10^{-3}	5×10^5

A SMALL CLOUD

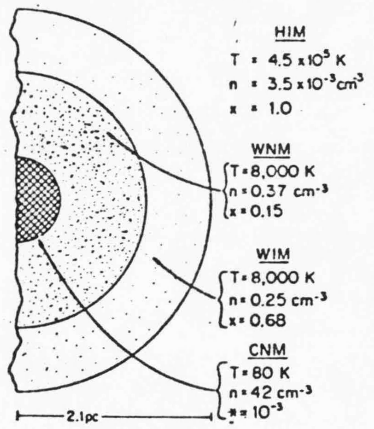

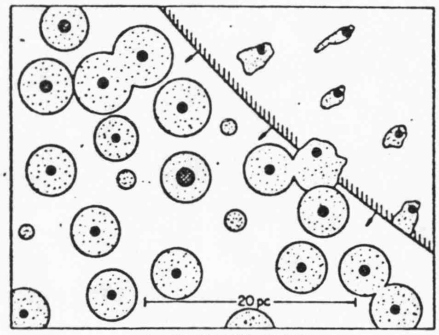

A CLOSE UP VIEW

Cross section of a characteristic small cloud. The crosshatched region shows the cold core, which gives the usual optical absorption lines. Next is the warm neutral medium (WNM) with ionization produced by soft X-ray background. The outer layer (WIM) is gas largely ionized by stellar UV background. Typical values of hydrogen density n, temperature T, and ionization $x = n_e/n$ are shown for each component, except that a higher than average value of the soft X-ray flux has been assumed in order to produce a significant amount of WNM at this pressure.

Small-scale structure of the interstellar medium. A cross section of a representative region 30 pc × 40 pc in extent is shown, with the area of the features being approximately proportional to their filling factors. A supernova blast wave is expanding into the region from the upper right. The radius of the neutral cores of the clouds (represented by crosshatching) ranges from about 0.4 to 1 pc in this small region; all the clouds with cores have warm envelopes (*dotted regions*) of radius $a_w \sim 2.1$ pc. A few clouds are too small to have cores. The envelopes of clouds inside the SNR are compressed and distorted.

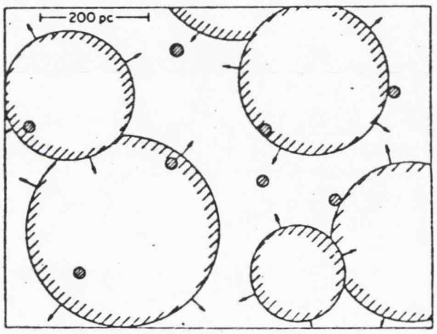

A LARGE SCALE VIEW

Large-scale structure of the interstellar medium. The scale here is 20 times greater than in Fig.   the region is 600 × 800 pc. Only SNRs with $R < R_c = 180$ pc and clouds with $a_0 > 7$ pc are shown. Altogether about 9000 clouds, most with $a_w \sim 2.1$ pc, would occur in a region this size.

Fig. 1.2 (McKee (1977))

TABLE 1.6 (McKee (1977))

INTERSTELLAR CLOUD PROPERTIES FOR TYPICAL CONDITIONS

Average Cloud Properties	Cold Cores	Warm Ionized Component
Hydrogen density, n (cm^{-3}).........	42	0.25
Fractional ionization, x............	...	0.68
Assumed temperature, T (K)........	80	8,000
Filling factor, f....................	0.024	0.23
Intercloud distance, λ (pc)..........	88	12
Cloud radii (pc):		
Largest........................	10.0	10.8
Mean*.........................	1.6	2.1
Smallest.......................	0.38	2.1
Column densities (10^{18} cm^{-2}):		
Largest........................	173	.22
Mean*.........................	27	.22
Smallest.......................	0.5	.22

* Weighted by cloud area.

The model consists of cool clouds, embedded in a coronal envelope, occupying a large volume of the ISM. The clouds are composed of cold (80 K) cores surrounded successively by a layer of warm (8000 K) HI partially ionised and heated by soft X-rays and cosmic rays, and then by a layer of warm HII. By assuming a reasonable spectrum of cloud sizes, a mean interstellar density, a mean SN rate and blast energy, McKee and Ostriker can account for many ISM observations : cloud pressure and motions, galactic soft X-ray background, O VI absorption line observations, ionization and heating of most of the ISM.

Derived properties of clouds are summarised in Table 1.6 and Fig. 1.2. However, the inclusion of the morphology of clouds (maybe more like sheets) and the statistical distribution of SN, may have some perturbing quantitative effects.

These ISM models have incorporated SNR evolution. A review is given below, of SNR evolutionary models in a homogenous and an inhomogenous ISM, to account for the observed structure and emission from particularly the intermediate stages. Briefly, SNR evolutionary models define several phases. Initially the supernova outburst occurs with most of the energy transformed to kinetic energy of the ejected mass. The first phase of SNR evolution is one of free expansion, with the dynamics being determined by the initial conditions. When the ejecta begins to interact strongly with the surrounding medium,a shell, preceeded by a shock will be formed. The energy is transferred to the ISM, resulting in an adiabatic blast wave. Initially, the shell is hot and pressure forces important, in this second phase, but later, radiative cooling becomes effective, with the resulting formation of a cool, dense shell, defining the third phase. Ultimately, the shell velocity becomes comparable to that of the random interstellar motion, and the shell dissipates. Recently, the phases, and phase transitions have been investigated in more detail, and are discussed below. Detailed radio, optical or X-ray observations of individual SNR are not reviewed here. Reviews by Mills (1974), Clark and Caswell (1976), Goss (1978),Milne (1979) on the radio properties and parameters; by Van den Burgh et al. (1971), Van den Burgh (1978)on the optical properties and parameters; Gorenstein et al. (1974), Clark and Culhane (1976), Culhane (1977), on the X-ray properties and parameters, have been compiled.

1.3 Supernova remnant evolution in the interstellar medium.

1.3.1 Evolution in a homogenous medium.

In the ideal instance of an initially homogenous gaseous medium, the expansion of a single supernova can be successfully treated in spherically symmetry. During intermediate phases, the expansion is approximately described by the shock wave similarity solution for a point explosion (Sedov (1959)).

Several phases of SNR evolution were originally defined by Shklovsky (1968), Woltjer (1970) :-

(1) Phase I : After an instantaneous explosion, energy is imparted to mass m_0 in a relatively cold ISM of density n_0 , with total energy $\mathcal{E}_0$. If the shock radius is R then $m_0 \gg (4\pi/3) n_0 R^3$, the dynamics depend on m_0 .

(2) Phase II : $m_0 << (4\pi/3) n_0 R^3$, $\int (d\mathcal{E}/dt)_{rad.} \ll \mathcal{E}_0$, the SNR is now dominated by the swept up matter, radiative losses are negligable and energy is conserved.

In this phase, neglecting the effects of relativistic particles and magnetic fields, thermal conduction and ISM inhomogenieties, the Sedov (1959) solution for self - similar blast waves has been applied to describe SNR evolution. In these solutions, an amount of energy (zero mass) is instantaneously injected into a uniform, infinite medium, and a spherical shock propagates into the undisturbed medium, and the flow behind the shock is described. In these self - similar solutions, there are no external time or length scales; the flow quantities depend only on a single, dimentionless parameter involving R, t and the dimensionless constants of the problem, instead of R, t independantly. Quantitatively, these similarity solutions yield good approximations, provided that a sufficiently large time has elapsed from the outburst, so that the details of the initial conditions are no longer important and that they contain an adequate physical description, i.e. that energy loss and transport remain unimportant, that a one - fluid hydrodynamical flow is applicable, and that the shock is strong. (Strong, but, initially non - similar explosions appear to evolve eventually into a self - similar state, Chevalier (1974), Falla (1975)).

Using the Sedov formalism, the adiabatic shock wave radius

$$R_s = 12.9 \left(\mathcal{E}_{51}/n_0 \right)^{1/5} t_4^{\;2/5} \qquad pc$$

where $\mathcal{E}_{51} = \mathcal{E}_0/10^{51}$ erg , $t_4 = t/10^4$ yr . The shock temperature T_s and velocity v_s

$$T_s = 11 \cdot 3 \; v_s^2 \qquad K$$

$$v_s \cong \frac{2}{5} \cdot \frac{R_s}{t_4} \times 10^2 \qquad km/s$$

The density and velocity of the post - shocked material is $n = 4n_0$, $v = 3/4 \, v_s$ respectively, for $\gamma = 5/3$. Then, for constant density within the expanding shell (of swept - up matter), the shell luminosity

$$L = 4\pi R_s^2 \cdot \Delta R_s \, . \, n^2 P(T)$$

where $P(T)$ is the volume emissitivity for unit density of plasma in a given energy interval, and $\Delta R_s / R_s = 1/12$ from mass conservation.

As the shell slows down, radiative losses become important, and for a hot gas of solar abundances, bremsstrahlung radiation by H and He dominates for $T > 5 \times 10^6 K$, while at lower temperatures line emission from heavier elements is more important.

(3) Phase III : If t_{rad} is the time when $\int (d\mathcal{E}/dt)_{rad} \sim O(\mathcal{E}_0)$, for $t > t_{rad}$, the radiative cooling time is short. Pressure forces are weak and the resulting dense shell enters the momentum conserving phase, with velocities $\sim O$ (100 km/s).

(4) Phase IV : The shell expansion velocity becomes comparable to that of the random motions of the ISM, $\sim$ 10 km/s, and the shell dissipates.

Table 1.7 summarises SNR evolution based on the simplfied shock model. To give some feeling as to the SNR parameter values for each phase transition, it has been assumed that a (Type II) SN outburst occured, imparting a velocity of $v_0 = 10^4$ km/s to mass $m_0 = 1 M_\odot$ with energy $\mathcal{E}_0 = 10^{51}$ erg in an ISM of density $n_i = 0.5\ \mathrm{cm}^{-3}$.

TABLE 1.7

Simple shock model SNR parameters.

Phase	Time t (yr)	Shock temperature T_s (K)	Radius R_s (pc)	Shock velocity v_s (km/s)	Swept up mass $M_\odot$
I - II*	250	10^9	2.5	1.3×10^4	1.4
II - III**	3×10^4	5×10^5	20	200	200
III - IV	1.6×10^5	10^3	40	10	4000

(e.g. Woltjer (1972), Gorenstein (1974)).

*
$$v_s \cong 4/3\, v_0 \quad \text{km/s}$$
$$T_s = 11.3\, v_s^2 \quad K$$
$$R_s \cong 2\,(m_0/n_i)^{1/3} \quad pc$$
$$t \simeq 4 \times 10^5\, R_s/v_s \quad yr.$$

**
$$R_s \simeq 5.2 \times 10^2 \left\{ \frac{\mathcal{E}_0}{10^{51}} \cdot \frac{1}{n_i} \right\}^{1/5} t^{2/5} \quad pc$$
$$t_{rad} \simeq 3.5 \times 10^{-8}\ \frac{\mathcal{E}_0^{4/17}}{n_i^{9/17}} \quad yr.$$

Recent numerical and analytical work on SNR evolution (in a uniform ISM) for the early, intermediate and late phases has been presented, incorporating mass ejecta - post shock gas interactions; magnetic field and relativistic particles; thermal conduction effects; instabilities; and calculations of shock spectra.

Gull (1973, 1975) discussed the early phases of SNR evolution, when the SNR expands adiabatically, and considered the sudden creation of a sphere of hot gas in a colder, initially uniform ISM and followed the subsequent behavior numerically (including instabilities), to find that the flow relaxed to the Sedov solution. Both Gull and McKee (1974), who invoked a reverse shock process to account for soft X-ray flux from young SNR, assumed a smooth shell of ejecta, while Chavalier (1975b) considered evolution of fast moving knots of stellar material in a uniform ISM, together with thermal conduction effects. After energy transfer to the ISM initiating the Sedov shock, the knots remain near the SNR centre. Rosenberg and Scheuer (1973) considered the ejection of a thin, massive spherical piston into a uniform ISM, eventually leading to the Sedov solution. Depending on the explosion energy and ambient density, radiative cooling may become important before flow has relaxed to a blast wave. Chevalier (1974) and Falle (1975) discussed the intermediate - late SNR phases, with spherical symmetry models and a uniform ISM, using the Sedov formalism, and including magnetic fields and a range of initial conditions. Chevalier (1974) also included discussions on ionization and recombination of hydrogen and shock spectra. A (UV optically thick) dense, neutral shell was predicted to form and ultimately cool to IR temperatures, and that magnetic field did not affect the SNR dynamics. Mansfield and Salpeter (1974) in considering the evolution of a spherically symmetric ejecta in a uniform ISM obtained similar results. Chevalier (1975b) considered the effects of heat conduction during the Sedov phase, which may serve to smooth the large temperature gradients interior to SNR, and which may define a new SNR evolutionary phase. Late phases of SNR evolution have been discussed by Straka (1974) and Cox (1972 a,b,c), when radiative losses become important, and a thin dense shell forms. (Chevalier (1974)). Cox investigated in detail the transition stage to the radiative cooling shell, and discussed a model for the optical spectrum and filaments of the Cygnus Loop.

For the early phase (I), emission from most observed, young SNR may be due to interactions of the SNR with the ISM. As the SN ejecta sweep up the ISM, shock waves may be driven both into the surrounding medium and back into the ejecta (McKee (1974), Gull (1975)) where the reverse shock may be radiative (Chevalier and Klein (1978)). Optical emission may originate from the reverse shock moving into the ejecta, which may be, inhomogenous through instabilities occurring early in the SNR expansion. (The fast moving knots of Cas A may be derived from this process). X-ray observations of Cas A and Tycho SNR (Davidson et al. (1976)) may be interpretated on the reverse shock model - the softer X-ray flux being associated with the lower velocity reverse shock. Radio observations (non - thermal synchrotron radiation from relativistic electrons) of young SNR such as Cas A, exhibit large energies indicating recent particle acceleration, and apparent annular structure of the SNR suggests that acceleration arises in the outer parts. Gull (1973a, 1975) suggested that there is a turbulant acceleration mechanism associated with the interaction of the SN ejecta with the ISM. The reverse shock decelerating the SN ejecta may cause Rayleigh - Taylor instabilities at the interface between the dense shell and ISM. The instabilities may generate the turbulant motion.

(Young SNR such as the Crab and 3C58 SNR ~~and~~ are most likely dominated by a central pulsar that supplies energy for the nebulae, with the ISM interaction having only a small effect, although the ISM may confine the relativistic gas produced by the pulsar).

For the intermediate phase (II), thermal conduction effects have been investigated. Chevalier (1975a) showed that an electron conduction front (thermal wave) can move out from the hot gas generated by an SNR more rapidly than a shock wave. Solinger et al. (1975) pointed out that the large temperature gradients predicted by the adiabatic model may be inconsistent with the assumed neglect of heat flux, and investigated isothermal blast wave solutions (infinite conductivity) for SNR in a phase where thermal waves were important and before radiative cooling sets in. However, Solinger et al. showed that the basic SNR parameters (derived from X-ray and optical observations) are approximately the same for both adiabatic and isothermal models. Cowie (1977) assumed ion - electron equipartition at the shock front and no conductive flux through the shock. Thermal conduction kept the electron gas behind the shock isothermal while the ion temperature increased, as in the Sedov model, towards the centre. Through expansion, the gas cools and is then described by the isothermal models. Chevalier (1975b) found that the high interior temperature in the adiabatic models may give significant deviations from a single temperature bremsstrahlung spectrum on the assumption that the electrons and ions are in temperature equilibrium. Two (hydrodynamic) fluid models to derive optical shock spectra, were investigated by Raymond (1976). He considered the ionization balance of the pre - shock gas rather than assuming ionization equilibrium at the post shock temperature, and considered the behavior of neutral and ionized particles in the SNR evolution, to account for differences in spectra taken in different parts of the Cygnus Loop. Partial ionization of the ISM through which a SNR may evolve, may arise through the initial SN outburst UV and X-ray radiation.

The interaction of ambient cosmic rays with the SNR shock wave, may play a role in the radio synchrotron emission observed in old SNR (e.g. Cygnus Loop, IC443). In SNR with cooling shock waves, the density can rise considerably behind the initial shock wave. Van der Laan (1962 discussed how the adiabatic compression of ambient magnetic fields and relativistic particles can lead to the observed emission strengths.

The observed soft X-ray emission of old SNR (e.g. Cygnus Loop, IC443, Vela X, Puppis A, W44, Lupus Loop) have been interpreted on the basis of the Sedov adiabatic model (Gorenstein et al. (1974)) to yield SNR X-ray parameters comparable with radio and optical values.

Optical emission of old SNR was considered to be derived from the later phases of the adiabatic expansion, where radiative cooling was important. The optical emission from the Cygnus Loop was discussed by Cox (1972 a,b,c) and the irregular structure (characteristic of old SNR), by McCray et al. (1975), for a uniform ISM.

For the late phase III, shock spectra and the formation of the dense shell, with radiative transfer and magnetic field effects have been investigated by Cox (1972 a,b,c). The evolution to the dense shell for an old SNR was quantitatively examined by Cox. The times when (1) the temperature distribution begins to deviate from an adiabatic model, (2) the dynamics begin to be affected by cooling, and (3) rapid cooling and shell formation are complete were presented. The equivalent shock radius were given by Cox for each of the three phases, and for complete cooling

$$R_s^{(c)} = 24.3 \left(\mathcal{E}_{51}/n_0\right)^{5/17} n_0^{-2/7} \quad \text{pc}$$

For the example of the hypothetical SN case above, $R_s^{(c)} \sim 30\ \text{pc}$. Cox proposed that the Cygnus Loop, was in the cooling phase, that the shock velocity was equal to the optical filament expansion (2.2.3) $\sim$ O(100 km/s), implying that the optical emission originated in the cooling regions behind the shock, with pre - shock density $\sim$ 6 cm^{-3} ISM ambient density. Cox thus allowed for density inhomogenieties but did not include the corresponding variations in shock velocity. Subsequent observations have confirmed Cox's analysis of the optical emission spectrum (Miller (1974)) but have tended to rule out his model for X-ray emission. Tucker (1971) had originally proposed that from X-ray observations and spectral analysis of the Loop (Gorenstein et al. (1971)) the X-ray shock velocity was $\sim$ O(400 km/s) and that the X-rays originated from an ambient density of $\sim$ 0.2 cm^{-3}. Tucker suggested that for some unspecified reason, the filaments were moving slower than the actual shock wave. Also, X-ray maps (Rappaport et al. (1974)) showed a high correlation of X-rays with the optical filaments, indicating, along with spectral temperatures of $\sim$ O(10^6 K), that the Cygnus Loop was still in the adiabatic phase.

Particularly for SNR in the intermediate phase, the basic SNR parameters such as age, initial energy release and ambient ISM density, as computed for the Sedov shock model for X-ray emission, are in good agreement with independent determinations of these quantities. The shock wave model explains gross features of the X-ray emission of SNR older than $\sim 0(10^3$ yr) and provides an overall evolutionary scenario. However, the inhomogenous nature of the ISM and its profound effect on SNR evolution, has been the subject of most recent studies, reviewed briefly below.

1.3.2 Supernova evolution in an inhomogenous medium.

The models of SNR briefly reviewed in (1.3.1) generally emphasised those properties of SNR that can be understood with the assumption of a homogenous medium. However, some features of the SNR e.g. the irregular structure of the optical filaments, provide direct evidence for significant ISM inhomogeneities, which must be considered if the SNR features are to be understood. In the case of Cas A, Van den Burg (1971) proposed that the low velocity optical nebulosity was composed of circumstellar clouds, while Cox (1972a) developed a late stage evolutionary model for the Cygnus Loop, in which the optical emission originates in the cooling gas behind a shock wave, with a pre - shock density of ~ 6 cm^{-3}, more characteristic of an interstellar cloud than the intercloud medium.

Recent models (Sgro (1975), McKee and Cowie (1975), McKee and Ostriker (1977), McKee et al. (1978)) of SNR blast wave - cloud interactions have been presented, to account for optical and X-ray features observed in SNR (e.g. Cas A, Cygnus Loop).

Sgro (1975) discussed a model of a shock wave - interstellar (circumstellar) cloud collision where a shock enveloped a cloud, a shock was transmitted through the cloud, and a shock was reflected from the cloud. Depending on a critical cloud density, the post - transmitted shock either cooled rapidly to emit optical line emission or the cloud remained hot for several thousand years and becomes a source of X - radiation, at temperatures less than the intercloud gas. After the transmitted shock passes, the cloud pressure is greater than the surrounding gas pressure, causing the cloud to expand and the emission to decrease from its value just after the collision. Sgro could account for the optical and X-ray observations of Cas A in the following way : prior to the outburst, the presupernova was surrounded by a gas of density n in which clouds of various densities n_c were embedded. The shock from the outburst collided with these clouds, causing the denser ones to become cold clouds (creating quasi - stationary flocculi) and the less dense ones to become hot clouds (sources of soft X-ray radiation). Sgro gave expressions for the cloud post - transmitted shock temperature, assuming a plane parallel shock, having velocity v km/s, colliding with a cloud of thickness d pc

$$T_t = 14(n/n_c)\beta v^2$$

where the ratio of the post - transmitted shock pressure to the post - incident shock pressure is β . The critical density n_c' was given by

$$n_c'/n = 5.8\times 10^{-4}\beta^{5/7} v^{10/7} (n\, d)^{-2/7} \quad \text{pc}$$

and $n_c > n_c'$ for a cold cloud $n_c < n_c'$ for a hot cloud. For a hot cloud, the cooling time was

$$\tau_H = 7\times 10^4 .\ T_6^2/n \quad \text{yr} \quad (T_6 = T\times 10^6\,\text{K})$$

McKee and Cowie (1975) also presented a model for a shock wave - cloud interaction. They derived the cloud shock as a function of cloud density and discussed the effects of thermal conduction between the blast wave and the shocked cloud. They argued that the optically observed filament of old SNR represent shocked interstellar clouds, with a significantly lower velocity than the shock wave propagated in the intercloud medium. The X-ray emission then would arise from the intercloud medium and the intercloud shock would accelerate clouds to a fraction of its velocity. The optical emission would arise in the cooling regions behind the cloud shock (Cox (1972a)). However, McKee and Cowie point out that the intercloud medium itself may be non - uniform in density, due to either pre - existing density inhomogeneities, prior to the passage of the shock wave, or to cloud evaporation behind the shock wave. The Cygnus Loop X-ray map of Rappaport et al. (1974) did reveal a rather closer correlation between optical and X-ray emission.

In the model of McKee and Ostriker (1977) (1.2.2), SNR propagate in a very low density medium ($\sim 10^{-3}$ cm^{-3}) in which there are large numbers of small clouds (average radii $\sim$ 0.2 pc). Once the clouds have been immersed in the hot gas of the SNR, they are evaporated by thermal conduction. The clouds have a small filling factor so that the blast wave propagation is determined by the density of the hot medium. The evaporation of clouds increases the density inside SNR compared to the ambient ISM. However, the rate of evaporation increases rapidly with temperature so that the mean density in the SNR drops with time. Table 1.8 compares the characteristics of the standard (Sedov) model, and the evaporative model.

TABLE 1.8

	Sedov	Evaporative
Ambient density	0.2 - 0.3 cm^{-3}	0.003 cm^{-3}
Shock radius	$\begin{cases} R_s \propto t^{2/5} & (R<R_c) \\ R_s \propto t^{1/3} & (R>R_c) \end{cases}$	$R_s \propto t^{3/5}$
Cooling radius	$R_c \sim 30-40$ pc	$R_c \sim 180$ pc
SNR density	$\begin{cases} \rho_{SNR} \propto R_s^0 & (R<R_c) \\ \rho_{SNR} \propto R_s^{-3} & (R>R_c) \end{cases}$	$\rho_{SNR} \propto R_s^{-4/3}$

Because SNR expand in such a low density medium in the model of McKee and Cowie, they do not enter the cooling phase of evolution until they have reached a radius of $\sim$ 180 pc, close to the radius at which SNR may overlap.

McKee and Ostriker claim that the density of hot gas in SNR derived from X-ray observations (Gorenstein and Tucker (1976)) tends to decrease as predicted on the evaporative model, with SNR radius. However, mean values of $\sim$ 0.2 - 0.3 cm^{-3} are actually found, but most of the X-ray luminous SNR have radii $\lesssim$ 50 pc, where the evaporative evolution may not apply , because the conduction is saturated for SNR with radii $<$ 50 pc. (Mckee and Ostriker (1977)).

The two models, standard and evaporative, predict very different radii at which radiative cooling becomes important. Several SNR (e.g. S147) may be in the radiative phase with radii   30 - 40 pc, with optical emission over all the perimeters. Other SNR show filamentary structure over only part of their area (e.g. Cygnus Loop) and are probably interacting with clouds, with the clouds large, comparable in size to the SNR radii, indicating no evidence for many small cloud interactions.

The acceleration of the clouds by shock waves was investigated by McKee et al. (1978), who defined two phases : the propagation of the shock wave through the cloud, followed by a phase of smooth acceleration by the ram pressure of the low density medium. McKee et al. applied their model to the Cygnus Loop to account for the high velocity gas observed (2.2.3) and predicted that fast clouds of HI should be observable, but recent HI observations (2.3.3) were negative.

At the present time, the observations relevant to SNR evolution appear to be more consistent with the standard model rather than the evaporative model, together with the recent work on shock wave - cloud models (Sgro (1975), McKee and Cowie (1975)).

1.4 Summary.

An overview of contempory observations and models of the ISM, and SNR evolution, has been presented. The standard cloud model for the ISM, together with the standard adiabatic blast wave model of SNR evolution, which both describe gross properties, have recently been adapted to account for detailed SNR evolution and its effects on the ISM. The intermediate stages of SNR evolution have been described in more detail, together with shock wave - cloud interactions, to yield a description of the features of old SNR, to facilitate interpretation of an X-ray image of the Cygnus Loop, presented in Chapter 6.

References.

Abartsumian, V. and Gordeladse, S., 1938. Bull. Ab., 2, 37.

Abartsumian, V., 1940. Bull. Ab., 4, 17.

Adams, W., 1949. Ap. J., 109, 354.

Agekyan, J., 1955. Astron. Zh., 32, 416.

Blaauw, A., 1952. BAN, 11, 459.

Burstein, P., Borken, R., Kraushaar, W. and Sanders, W., 1976. Ap. J., 213, 405.

Chevalier, R., 1974. Ap. J., 188, 501.

Chevalier, R., 1975a. Ap. J., 198, 355.

Chevalier, R., 1975b. Ap. J., 200, 698.

Chevalier, R. and Klein, R., 1978. Ap. J., 219, 994.

Cowie, L. and McKee, C., 1977. Ap. J., 211, 135.

Cowie, L., 1977. Ap. J., 215, 226.

Cox, D., 1972a. Ap. J., 178, 143.

Cox, D., 1972b. Ap. J., 178, 158.

Cox, D., 1972c. Ap. J., 178, 169.

Cox, D. and Smith, B., 1974. Ap. J., 189, L105.

Clark, D. and Caswell, J., 1976. MNRAS, 174, 267.

Clark, D. and Culhane, L., 1976. MNRAS, 175, 573.

Culhane, L., 1977. Supernovae, ed. D. Schramm, Dordrecht, Reidel.

Davidson, P., Culhane, L. and Mitchell, R., 1976. Ap. J., 206, L37.

Falle, S., 1975. MNRAS, 172, 55.

Gorenstein, P., Harris, B., Gursky, H., Giacconi, R., Novick, R. and Van den Bout, P., 1971. Science, 172, 369.

Gorenstein, P., Harnden, F. and Tucker, W., 1974. Ap. J., 192, 661.

Gorenstein, P. and Tucker, W., 1976. Ann. Rev. Astron. Ap., 14, 373.

Goss, M., 1978. Mem. Soc. Astr. it., 49, 567.

Gull, S., 1973a. MNRAS, 161, 47.

Gull, S., 1973b. MNRAS, 162, 135.

Gull, S., 1975. MNRAS, 171, 263.

Jenkins, E. and Meloy, D., 1974. Ap. J., 193, L121.

Jenkins, E., 1978. Ap. J., 219, 845.

Kaplan, S. and Piklener, S., 1970. The Interstellar Medium, HUP, Cambridge, Mass.

Mansfield, V. and Salpeter, E., 1974. Ap. J., 191, 305.

McCray, R., Stein, R. and Kafatos, M., 1975. Ap. J., 196, 565.

McCray, R. and Snow, T., 1979. Ann. Rev. Astron. Ap., 17, 213.

McKee, C., 1974. Ap. J., 188, 335.

McKee, C. and Cowie, L., 1975. Ap. J., 195, 715.

McKee, C. and Ostriker, J., 1977. Ap. J., 218, 148.

McKee, C., Cowie, L. and Ostriker, J., 1978. Ap. J., 219, L28.

Miller, J., 1974. Ap. J., 189, 239.

Milne, D., 1979, Aust. J. Phys., 32, 83.

Mills, B., 1974. IAU Symp. 60, ed. F. Kerr and S. Simonson, Dordrecht, Reidel.

Muller, C., 1957. Ap. J., 125, 830.

Munch, G., 1957. Ap. J., 125, 42.

Myers, P., 1978. Ap. J., 225, 380.

Rappaport, S., Doxsey, R., Solinger, A. and Borken, R., 1974. Ap. J., 194, 329.

Raymond, J., 1976. Thesis, University of Wisconsin.

Rosenberg, I. and Scheuer, P., 1973. MNRAS, 161, 27.

Sedov, L., 1959. Similarity and Dimensional Methods in Mechanics, Academic, NY.

Shklovsky, I., 1968. Supernovae, London, Wiley.

Sgro, A., 1975. Ap. J., 197, 621.

Solinger, A., Rappaport, S. and Buff, J., 1975. Ap. J., 201, 381.

Spitzer, L., 1968. Nebulae and Interstellar matter, ed. B. Middlehurst and L. Aller, UC, Chicago.

Straka, W., 1974. Ap. J., 190, 59.

Tucker, W., 1971. Science, 172, 372.

Van den Berg, S., 1971. Ap. J., 165, 457.

Van den Berg, S., Marscher, A. and Terzian, Y., 1973. Ap. J., Suppl., 26, 19.

Van den Berg, S., 1978. Mem. Soc. Astro. it., 49, 471.

Van der Laan, H., 1962. MNRAS, 124, 125.

Westerhout, G., 1957. BAN, 13, 201.

Woltjer, L., 1970. Interstellar Gas Dynamics, IAU Symp. 39, 208.

Woltjer, L., 1972. Ann. Rev. Astron. Ap. 10, 129.

York, D., 1974. Ap. J., 193, L127.

Chapter 2. A REVIEW OF SIGNIFICANT ASTROPHYSICAL OBSERVATIONS OF THE CYGNUS LOOP SNR.

Chapter 2. A REVIEW OF SIGNIFICANT ASTROPHYSICAL OBSERVATIONS OF THE CYGNUS LOOP SNR.

2.1 Introduction.

The expanding, optically visible ($m_v \sim 17$) nebulae, composed of intense, sharp filaments and diffuse wisps found in the constellation Cygnus and called variously, the Cygnus Loop or the Veil Nebula, is a Type II supernova remnant (SNR). The Cygnus Loop exhibits a non-thermal, shell-like radio source with mean spectral index $\bar{\alpha} \sim 0.5$. It has a collisionally excited optical spectrum with intense forbidden lines. The expanding filamentary shell comprising high electron densities, is not associated with a central ionizing star. Most recently, the Loop has been found to be an extended soft X-ray source. From the kinematics of the optical expanding shell and estimates of the local interstellar particle density, together with the fact that the remnant lies near the galactic plane, indicates that the Cygnus Loop is most probably the remnant of a Type II supernova, occurring some 20,000 - 50,000 years ago.

The Cygnus Loop SNR, one of the brightest Type II radio sources, has been studied in some detail at optical, radio and X-ray wavelengths. These observations, which are important for developing an understanding of how SNR evolve in the interstellar medium, are reviewed here.

2.2 Optical Astronomy.

2.2.1 Position.

Fig. 2.1 gives the region of the sky containing the Cygnus Loop. From direct observations, Minkowski (1958) estimated the centre to be located at α(1950), δ(1950) = $20^h\ 49^m\ 30^s$, + $30^\circ\ 48'.5$; l^{II}, b^{II} = $72^\circ.6$, - $8^\circ.2$ while van den Burgh (1973) gave a centroid position of $20^h\ 49^m\ 30^s$, + $30^\circ\ 45$; l^{II} , b^{II} = 74°, - 8°.

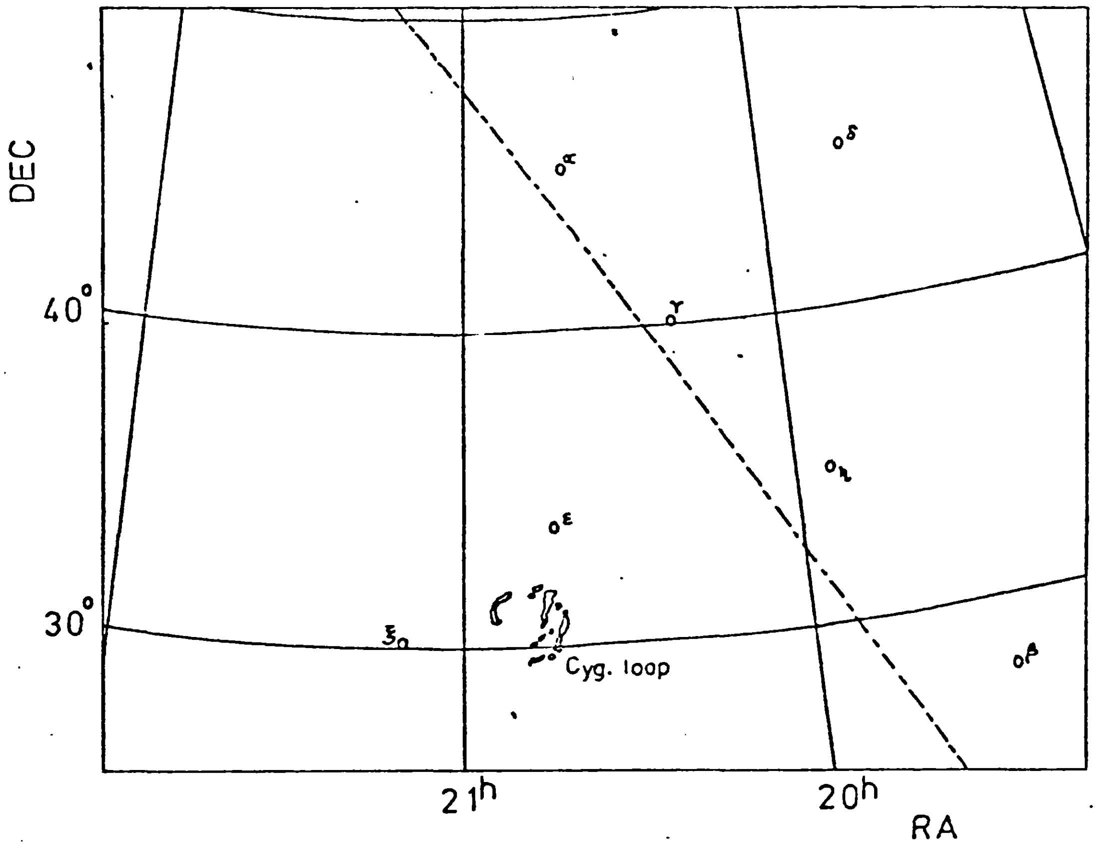

Fig. 2.1 The Cygnus Loop $\sim$ 40 pc in diameter (for $\sim$ 770 pc distance) is at a position z = 100 pc below the galactic plane (- - -). Assuming a plane stratified ISM density described by a barometric equation, the value of z is equivalent to one scale height. The actual environment local to the SNR has been found, from HI and optical studies, to contain a number of diffuse clouds and dark nebulae, particularly to the West, North and North - West regions.

Other X-ray, radio and optical sources are not shown.

2.2.2 Structure.

Plates 2.1 - 2.5 are red Palomar Sky Survey points of the Cygnus Loop (minimum detectable brightness $\sim 4 \times 10^{-6}$ erg/cm^2.s. (Peimbert et al.(1975)). Most of the observed filaments, each of thickness $\leqslant 1 - 2''$ and length $\sim (10')$, appear to form an incomplete shell with radius $\sim 80'$, centred at 20 49 .5, + 30°.7. In the southern part of the Loop, filaments extend $\sim 130'$. There is no hot, ionizing star associated with the Loop. The shell structure has been observed to be expanding (2.2.3). The brighter parts of the shell most probably indicate the sites of interaction with the local interstellar inhomogenieties. A decrease in star density to the west of NGC 6960 (Plate 2.4) was observed by Wolf (1923), indicating the presence of a dark cloud with total absorption of $\sim 1^m.0$ at a distance of $\sim$ 600 pc.

2.2.3 Distance.

The kinematics of the Cygnus Loop were first investigated by Hubble (1937) and Minkowski (1958) and then Doroshenko (1970). The expansion of the dense filament edges of NGC 6960 and 6992 indicated a proper motion of 0.03"/yr (Hubble 1937). This would give an upper limit in SNR age of 150,000 years, for uniform expansion. Minkowski (1958) obtained slit spectra for H_α, [NII], covering both the diffuse features and edges (NGC 6960/6992) of the Loop, enabling a distribution of radial velocities to be determined. From a plot of radial velocities against radial distance from the Loop centre, it was found that nearly all the velocities were in the range + 65 $\rightarrow$ - 65 km/s, between $40'$ and $80'$, in the local standard of rest, with one value near the centre of $\sim$ 85 km/s. From the difference between the centre and edge velocities, Minkowski concluded that the Loop was expanding at $\sim$ 116 km/s, away from the centre, with

Plate 2.1

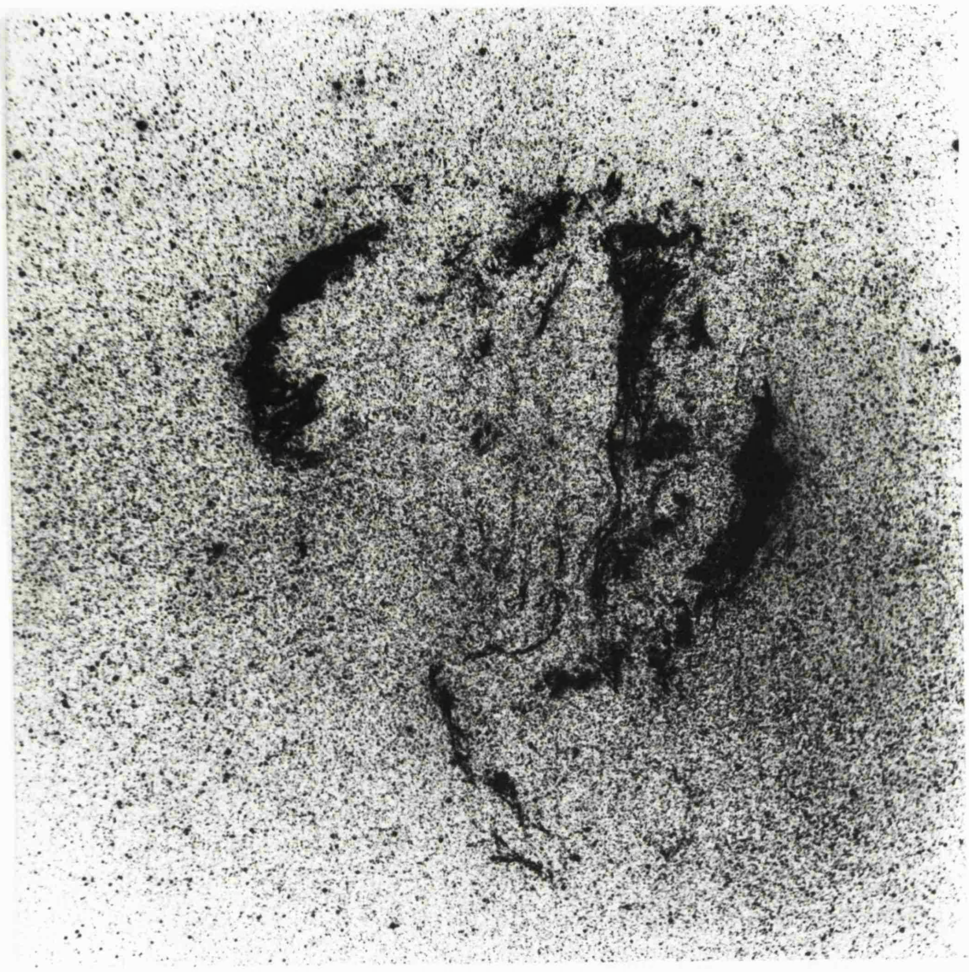

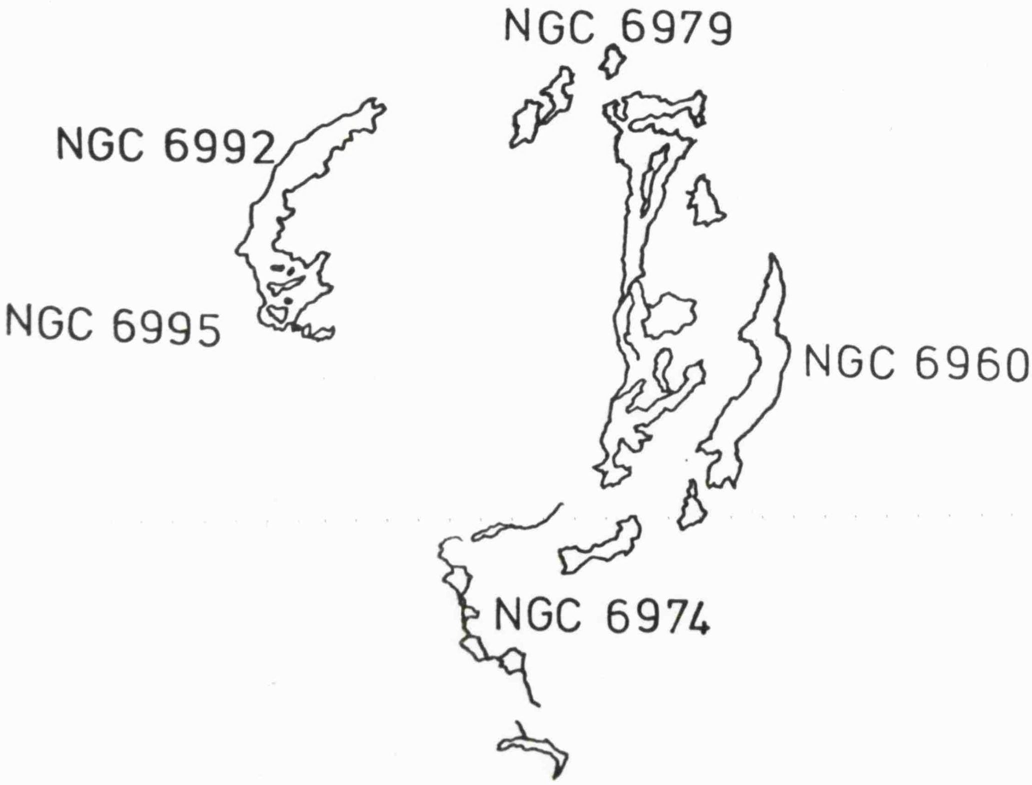
NGC 6979
NGC 6992
NGC 6995
NGC 6960
NGC 6974

Plate 2.2

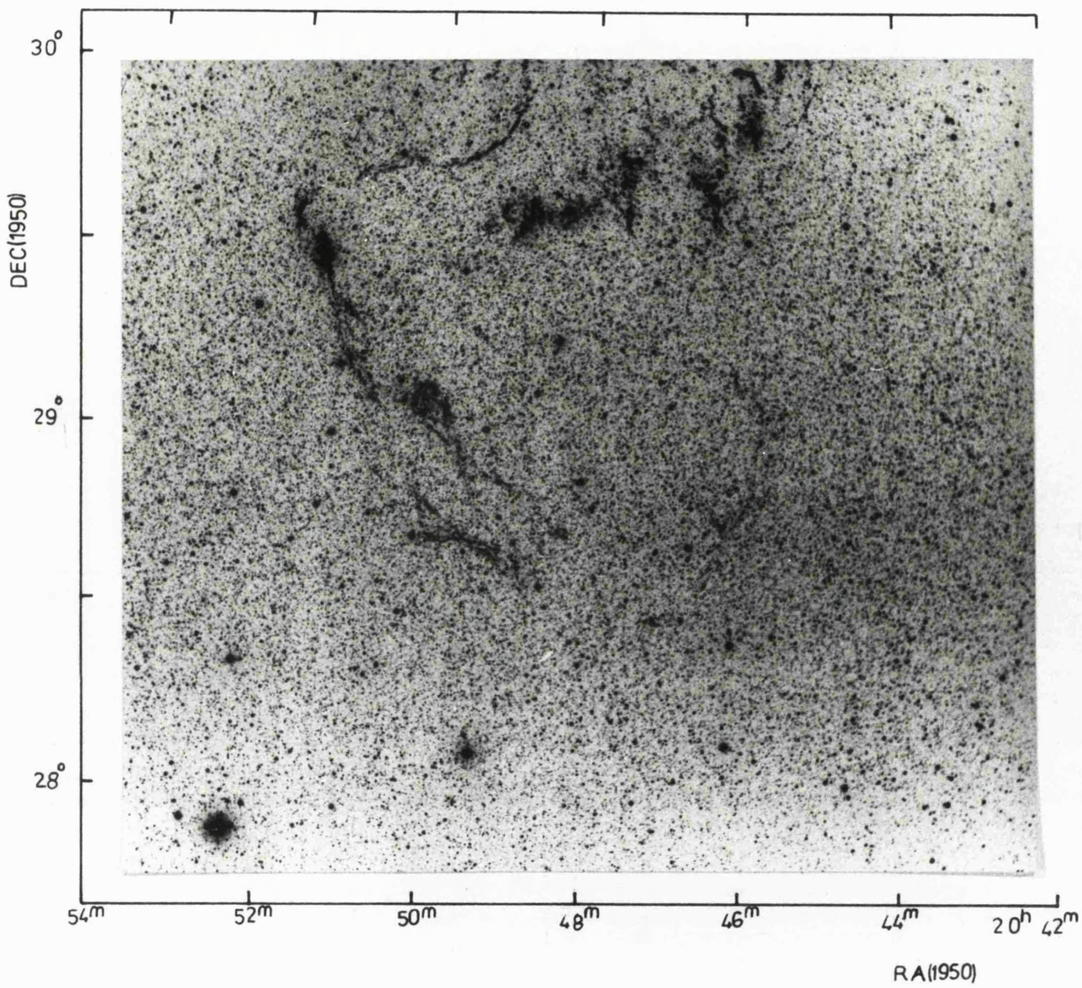
30°
29°
28°
DEC(1950)
54m
52m
50m
48m
46m
44m
20h 42m
RA(1950)

Plate 2.3

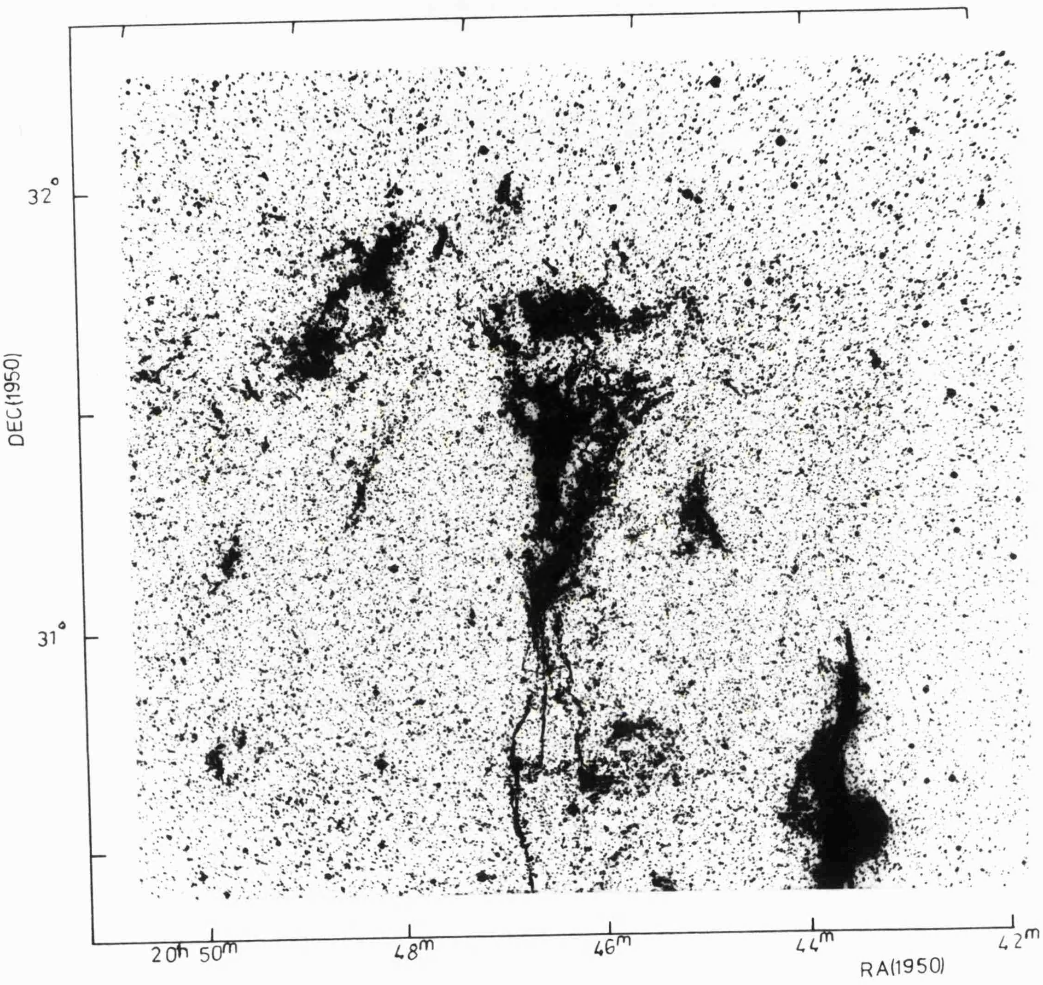
32°
31°
DEC(1950)
20h 50m
48m
46m
44m
42m
RA(1950)

Plate 2.4

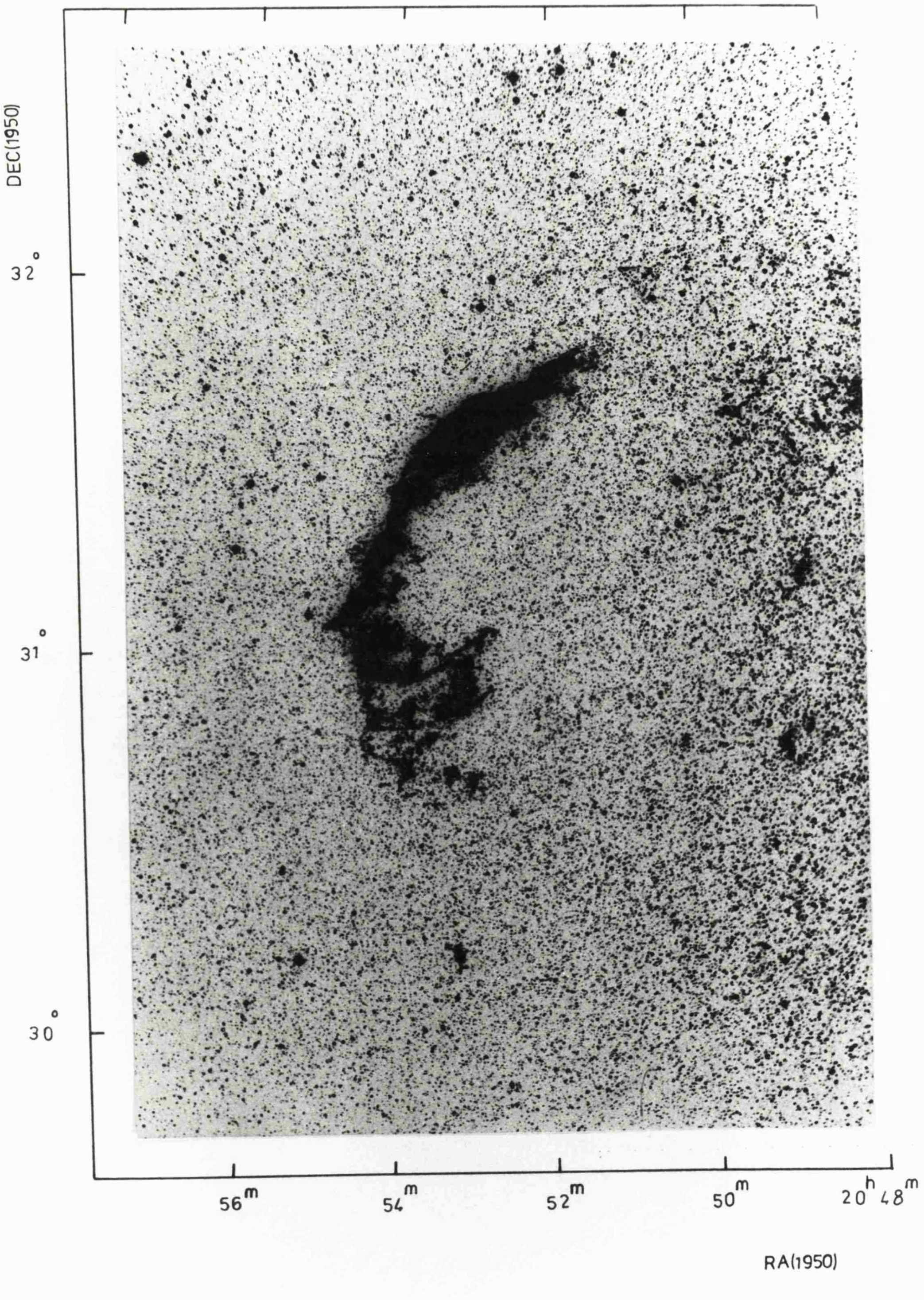
DEC(1950)
32°
31°
30°
56m
54m
52m
50m
20h 48m
RA(1950)

Plate 2.5

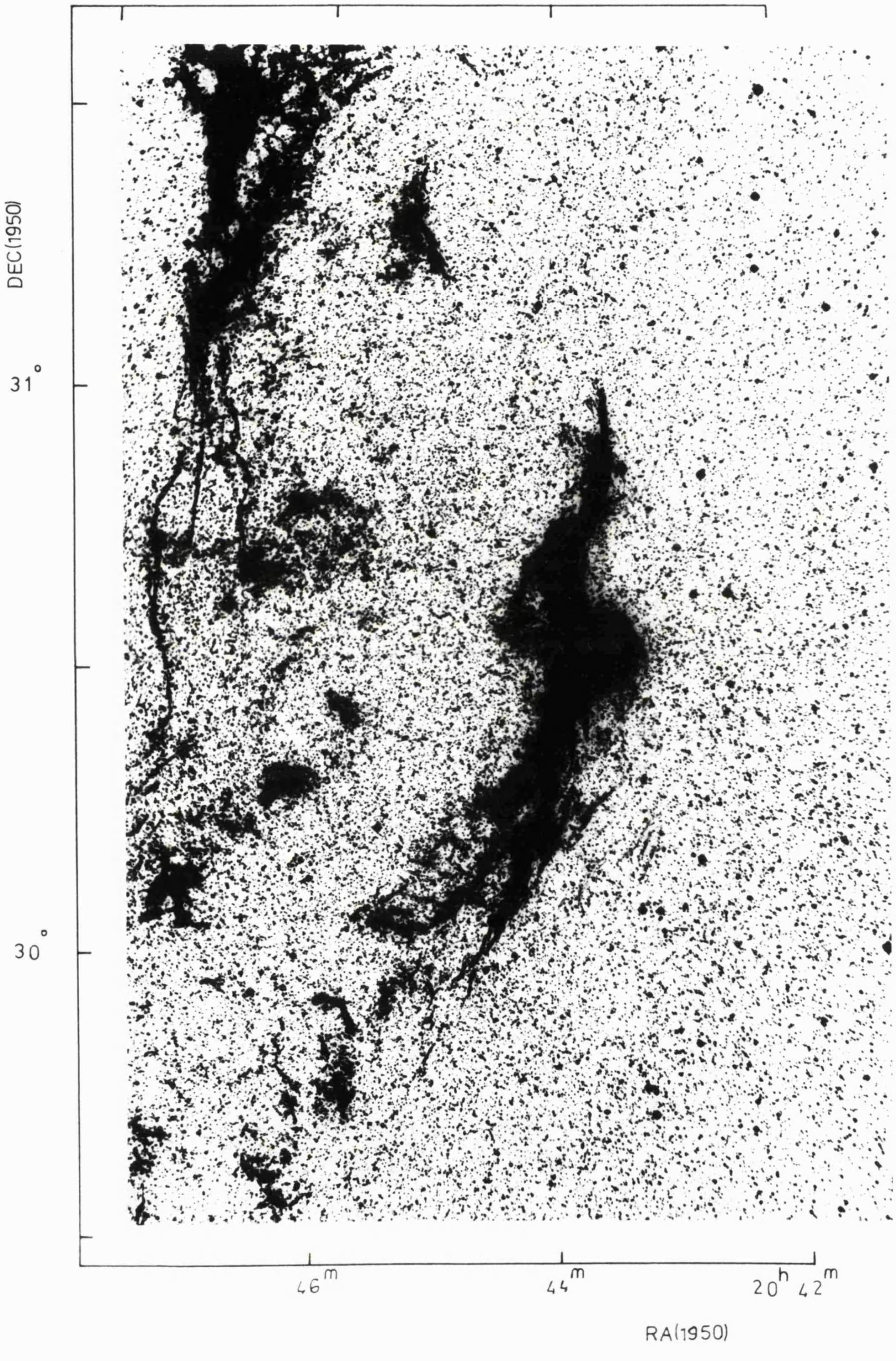

DEC(1950)
31°
30°
46m
44m
20h 42m
RA(1950)

the centre moving 33 km/s relative to the local standard of rest. Doroshenko (1970) used an imaging Fabry - Perot interferometer to measure the $H\alpha$ radial velocity and line width at the edges of the Loop. Velocities in the range + 135 $\longrightarrow$ - 15 km/s were observed, indicating confirmation of Minkowski's result. Hence, the expansion velocity of 116 km/s for NGC 6960/6992 was combined with the proper motion of 0.03$''$/yr to give a distance determination of 770 pc , and radius of 19 pc . More recent radial velocity measurements have been reported by Kirshner and Taylor (1976), revealing high velocity, low surface brightness regions. Using a Fabry - Perot monochromator providing accurate radial velocities of low surface brightness $H\alpha$ emission (the diffuse features), values in the range + 200 $\longrightarrow$ - 300 km/s were observed. The radial velocities were found to increase towards the Loop centre with maximum value $\sim$ 300 km/s relative to the local standard rest frame velocity $\sim$ + 35 km/s.

Thus, the Cygnus Loop distance estimate of 770 pc may be in error by a factor 3. The interpretation of the correlation of the higher radial velocities with the low surface brightness filaments, and the lower radial velocities with the high surface brightness filaments is discussed in Chapters 1 and 6.

2.2.4 Optical spectrum.

The optical spectrum from the Cygnus Loop has been studied in detail, particularly the spectra of the brightest filaments NGC 6960, 6992-5 (Chamberlain (1953), Pikelner (1954), Minkowski (1958), Osterbrock (1958), Harris (1962), Parker (1964a, b, 1967) and Miller (1972, 1974)). Primarily, the forbidden lines [S II], [N II], [O I], [O II] and Balmer lines were studied, to reveal large variations in electron temperatures and densities throughout the filaments, and even for each observed filament. Photo-electric measurements of line and continuum intensities in three bright regions, with 3 $''$ slits, were made by

Miller (1974) and temperatures were derived from [O III] line intensities in the range 3.9 - 4.9 x 10 K, while [O II], [N II], [S II] line intensities indicated 0.84 - 1.7 x 10^4 K. Electron densities derived from [O II] fluxes were 100 - 275 cm^{-3} and from [S II], 520 - 1500 cm^{-3}. Both Parker (1964a) and Miller found that there were no large differences in the general features of the spectra of different regions. From considerations of the shapes of the optical filaments, small observed thicknesses with high surface brightnesses with relatively high associated electron densities, prompted Poveda (1965) and Parker (1967) to suggest that the filaments were planar shock fronts seen edge-on. Unless the interstellar gas outside the filamentary shell had a temperature above 10^5 K, or was moving with the expanding filaments, the observed radial velocities were supersonic (cf. $\sim$ O(10 km/s) for cool interstellar gas steady state motion). Parker (1964a) and Miller (1974) estimated the depth of radiating material in a filament to be several times its width., a factor of $\lesssim$ 10 or more, 0.01 - 0.1 pc. A summary of the optical properties of the Cygnus Loop is shown in Table 2.1. Information on element abundances was deduced as follows. The strong O,N,S forbidden lines required a higher abundance of these elements relative to C, Si compared to the Allen (1973) cosmic abundances. The strong [Ne II] line indicated that the abundances of Ne relative to O was twice the cosmic abundance. Also, the S lines implied an over abundance of S by a factor 2, while the cosmic N to O abundance ratio was as expected. Raymond (1976) has argued that the above may be explained by a partial condensation of heavy elements onto grains.

Models for the optical filament formation (McKee and Cowie (1975)) and optical spectrum (Cox (1972a,b,c), Chevalier (1974a), Falle (1975), Raymond (1976)) are discussed in Chapter 1.

Finally, the optical coronal lines, the green [Fe XIV] λ5303 and red [Fe X] λ6374 have been detected to verify the presence of hot $\sim$ O(10^6 K), optically thin X-ray emitting

TABLE 2.1

Optical properties of the Cygnus Loop SNR.

Approximate centre (1950)	$20^h49^m.5$, $30^\circ 48'.5$ ($74^\circ.3$, $-8^\circ.49$)	
Angular diameter	$\sim 3^\circ$	
Filament proper motion	$\leq 0''.03$/yr	?
Filament radial velocity	$\sim$ 100 km/s (bright filaments) $\sim$ 300 km/s (faint filaments)	
Distance	$\sim$ 800 pc (300 - 3000 pc)	?
z	$\sim$ 100 pc	
Radius	$\sim$ 20 pc (8 - 80 pc)	?
Filament electron density	$\sim$ 80 - 400 cm^{-3} ([O II])	
Filament electron temperature	4×10^4 K ([O III])	
Volume	10^{60} cm^3	
HI density at $z \sim 100$ pc	0.1 - 1 cm^{-3}	
Swept up mass	$10^2 - 10^3$ $M_\odot$	
Average filament mass	2×10^{-4} $M_\odot$	
Total mass of all visible filaments	0.1 $M_\odot$	

plasma in the Cygnus Loop, (Shcheglov (1968), Woodgate et al. (1974, 1975)). in the regions coincident with intense X-ray emission and optical filaments. These data are discussed below (2.4.3).

2.3 Radio Astronomy.

2.3.1 Radio survey observations.

The Cygnus Loop has been observed at radio frequencies with total flux density measurements made between 38 - 4940 MHz (Costain (1960), Baldwin (1950), Costain and Lish (1960), Eaton and Krans (1959), Kenderline (1963), Westerhout (1958), Kundu and Becker (1972)) with a non - thermal spectral index of $\alpha = 0.4$ (38 - 960 MHz), $\alpha = 0.62$ (960 - 4940 MHz) and total flux density of 280 $\pm$ 50 Jy (200 MHz) (Kundu and Velusamy (1967)). Essentially, the Cygnus Loop exhibits a simple power law spectrum at high frequencies although there are some indications of a high frequency steepening at ~ 1 GHz observed by Kundu and Becker (1972), who explained this in terms of a break in the cosmic ray background spectrum. Since the break in the galactic radio spectrum occurs at ~ 0.2 GHz (Bridle 1967), then the change in frequency to the 1 GHz turnover was taken as a measure of the local magnetic field amplification caused by the passage of the shock wave through the interstellar medium (Van der Laan (1962)) and a typical value of $H \sim 10^{-5}$ gauss deduced in the Cygnus Loop radio shell.

From Clark and Caswell (1976), using $\Sigma_{408} = 3.6 \times 10^{-5} D_{pc}^{-10}$, the distance to the Cygnus Loop was determined as 0.8 Kpc and also from Milne (1979), with the additional Z - dependant

$$\Sigma = 2.88 \times 10^{-14} D_{pc}^{-4} \exp\{-|z|/54\}, \quad d_{Kpc} = 0.8 \text{ Kpc}$$

$$D_{pc} = 41.3 \text{ pc}, \; z = -117 \text{ pc}.$$

2.3.2 High resolution radio maps.

The Cygnus Loop has been mapped at 408 MHz through 10 GHz with increasing angular resolution :-

Frequency (MHz)	Resolution, HPBW (arc min.)	
430 195 41	17 35 136	Kundu and Velusamy (1967)
750 1400	18.5 11	Hogg (1969)
2700	11	Kundu (1969)
1420	3.3 x 4.7	Moffat (1971)
408	3 x 10	Colla et al. (1971)
5000	6	Kundu and Becker (1972)
2700 10700	4.8 1.25	Keen et al. (1973)
610	10	DeNoyer (1974)
1420	10	DeNoyer (1975)
1420	1.4 x 2.8	Geiss (1978)
1420	5.6	Giovanelli and Haynes (1979)

The radio surface brightness and polarisation maps of the Loop, relative to the optical remnant will be discussed here. The 1420 MHz observations are discussed in (2.3.3), with respect to the HI shell, interior to the optical filament, for SNR in the radiative phase (Cox (1972 b), Masefield and Salpeter (1973), Falle (1975), Straka (1974), Chevalier (1974) and the search for the predicted, accelerated HI clouds within the Loop (McKee and Cowie (1975), McKee, Cowie and Ostriker (1978)).

(i) Structure.

The radio surface brightness of the Cygnus Loop has been shown to bear a similar, but not exact resemblance to the optical image, and to be a typical non - thermal radio shell source. The correlation of the optical and radio features of SNR was first noted by Rishbeth (1956) for IC443 and was explained by the optical and radio emission resulting from interaction with the interstellar medium - collisional heating leading to optical emission and compression of matter and magnetic fields, leading to strong non - thermal emission (Minkowski (1958)). The radio spectrum of the Loop, discussed below, has been determined to be essentially non - thermal without flattening out at high frequencies, expected if a large part of the radiation were thermal. The early Loop radio maps revealed structure of more than six discrete sources, most of them associated with the optical nebulosities, shells and filaments. Bright, narrow radio ridges were found to coincide with the optical filaments NGC 6992 - 5 and NGC 6960, with a third bridge running along the entire SW and SE boundary, where there is a faint optical emission. In Fig. 2.2 the high resolution map of Keen et al. (1973), is shown, together with data on associated, unresolved source (Colla et al. (1970), Colla et al. (1972), Moffat (1971)). Besides increased detail observed in Fig. 2.2 over earlier maps, direct observation of regions corresponding to strong optical filaments, having radio contours steepening towards the outside of the source was made. A secondary ring of radio emission, deviating from the overall circular symmetry was seen in the south. In the regions NGC 6992, $\sim 1'$ correlation between radio and optical features was found.

Two small, intense point sources were observed, CL4 and CL2 (Fig. 2.2). CL2 was found to be possibly extra - galactic. CL4, $\sim 20'$ from the Loop centre, was found to undergo flux variations with the Loop, suggested by an observation of 2.7 GHz emission connecting CL4 with the main northern filamentary structure. Webster and Ryle (1976) measured the position and flux density of CL4 at 5 GHz, 1.4 GHz and 408 MHz. A position of $20^h\ 48^m\ 47^s.38$, $31^\circ\ 16'\ 10''.95$ was found and a 17^m stellar object on POSS found to be $\sim 2''$ RA of CL4. Argue et al. (1978) carefully measured the position of the 17^m object to have a $2''.4$ from the 5 GHz position, large compared with the mean error $\sim 0''.1$ and suggested that the offset was a physically meaningful parameter. Observations at 15 GHz placed an upper limit on the angular diameter of $< 1''.5$

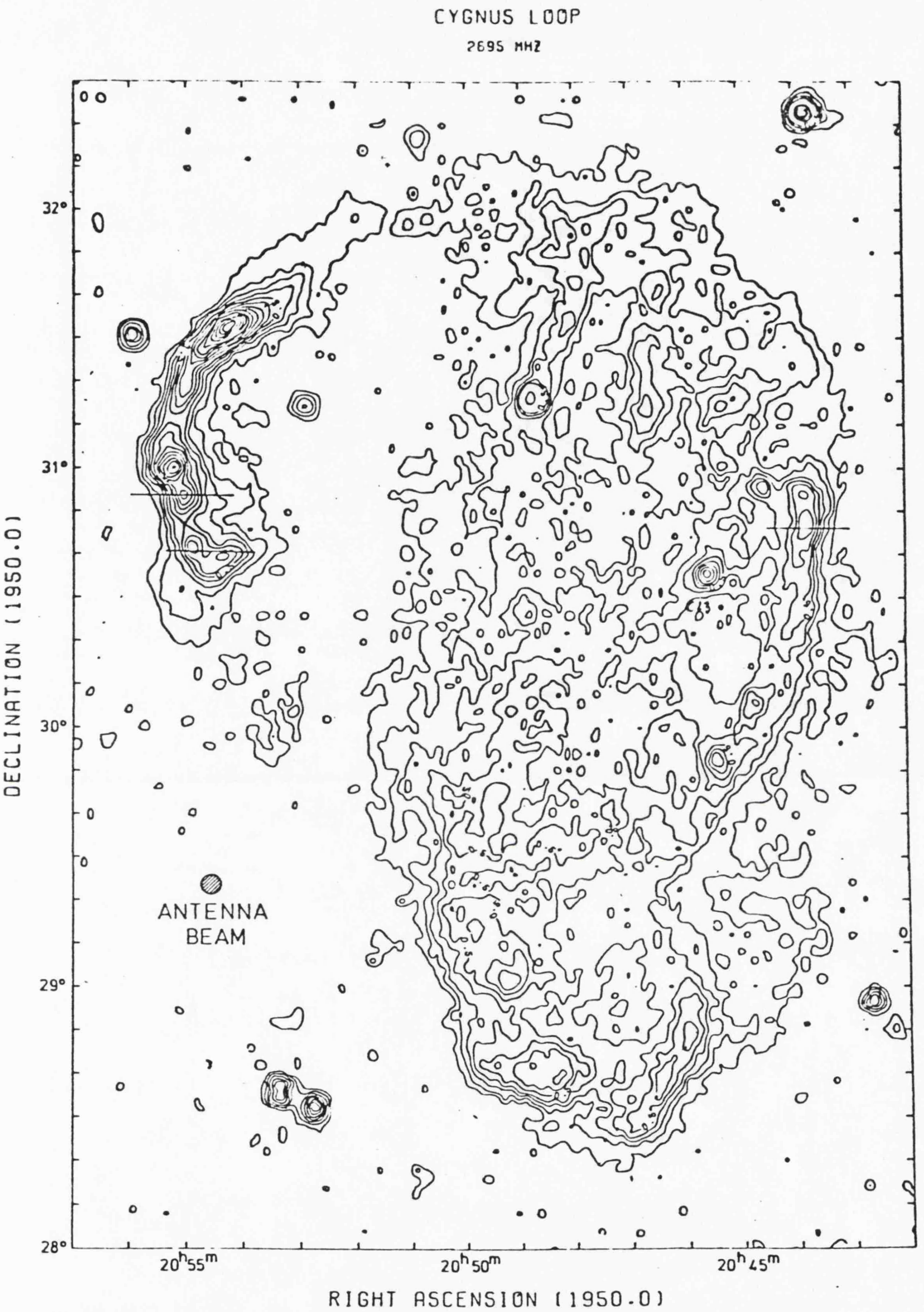

Total intensity map of the Cygnus Loop at 2.7 GHz. The contour interval is 0.1 K in T_b. The horizontal lines indicate locations of sampl scans at 10.7 GHz

Fig. 2.2.

(Keen et al. 1973)

Table Unresolved sources in the Cygnus Loop, with flux > 0.2 f.u. at 2.7 GHz

Source	Position (1950.0)		Flux Density			Spectral
	R.A.	Dec.	S_{408}	S_{1400}	S_{2695}	index α
			($\times 10^{-26}$ W m^{-2} Hz^{-1})			($S \propto f^{\alpha}$)
CL 1	20h42m40.6s	28°57'.0	0.98		0.27	−0.68
CL 2a)	20 43 47.3	32 22.7	1.66		0.74	−0.48
CL 3	20 45 34.9	30 35.7	1.04		0.48	−0.41
CL 4a)	20 48 47.3	31 16.5	0.6		0.58	−0.02
CL 5	20 52 44.9	28 32.4	1.72		0.35	−0.84
CL 6	20 52 54.3	31 14.3	—	0.27	0.19	−0.55
CL 7	20 55 56.6	31 30.6	1.21	0.63	0.35	−0.52b); −0.91c)

a) 5 GHz positions from Westerbork (van der Laan and Duin, private communication)

CL 4 {20h48m47.35s, 31°16' 10.3"}   CL 2 {20h43m47.53s, 32°22' 50".6}

b) Between 408 MHz and 1.4 GHz

c) Between 1.4 GHz and 2.7 GHz

From the low HI absorption measurements, CL4 was deduced to be galactic. Attempted measurements of the proper motion and parallax by Webster and Ryle gave a lower distance limit of > 80 pc. Geldzahler (1978) carried out VLBI observations at 810 GHz and 1071 GHz with $< 0''.001$ angular resolution of CL4. A size $< 0''.001$ was found, equivalent to 1 AU for a 770 pc distance.

The current data on CL4 and other similar sources (Caswell (1977)) has led Ryle et al. (1978) to postulate a new class of radio sources, possibly associated with stellar remnants of SNR.

(ii) <u>Polarization.</u>

Polarization studies have been carried out in detail by Kundu (1969), Moffat (1971) and Kundu and Becker (1972). An irregular distribution of linear polarization over the Loop was observed, with the polarization strongest at higher frequencies. Kundu (1969) reported 15 - 25% in the southern region of the Loop, with a magnetic field distribution tangential to the southern boundary of the source. No significant polarization was observed in the northern regions $\delta > 30^{\circ}$ at 11 cm. Moffat (1972) found $\lesssim$ 35% polarization in the southern region (including NGC 6974) with average values of 25%, indicating a well - ordered magnetic field. For $\delta < 29^{\circ} 25'$, the transverse component of the magnetic field was found to align roughly parallel to the ridges of radio emission, and hence to the general alignment of the optical filaments, particularly in the SW, and implying that the field derived from local compression of the interstellar magnetic field. In the northern regions, and NGC 6992 - 5, Moffat (1972) again found a non - thermal spectrum, but with $<$ 4% polarization. Moffat explained this fact by inciting a higher local interstellar electron density giving rise to a higher compressed field and hence a higher Faraday de - polarization. Indeed, Moffat deduced that local interstellar medium density variations, up to $\sim 5\ cm^{-3}$, gave rise to many of the intensity and polarization features observed.

Kundu and Becker (1972) confirmed Moffat's results at 6 cm., with significant polarization around NGC 6992 - 5. Both Moffat and Kundu and Becker, on applying the shell compression model of Van der Laan (1962), a compression of $\sim$ 9 for the magnetic field was found. Taking the average of the observed radio parameters of the Cygnus Loop, - the shell radius, shell thickness, spectral index and angle between the magnetic field and expansion velocity ($\sim 90^{o}$), the expected total non - thermal flux from a Van der Laan shell was approximately that observed.

(iii) Spectrum.

Kundu and Velusamy (1967) first investigated the variation of relative spectral index at different regions of the Loop, to find a significant softening towards the NE, SE directions, away from the galactic plane. In the region NGC 6992 - 95, Kundu and Becker (1972) found for frequencies between 178 - 960 MHz, $\alpha \sim 0.25$ and $\alpha \sim 0.53$ for higher frequencies. However, both Moffat (1971) and Keen et al. (1973) found no significant differences in spectral index in NGC 6992 - 5, from the rest of the Loop, with no flattening of the spectrum at higher frequencies.

The overall radio emission can be described as originating from a shell with $\alpha \sim 0.4$ (38 MHz - 1 GHz) and mainly from the synchrotron process.

2.2.3 HI investigations.

Detailed HI studies near the Cygnus Loop have been performed by DeNoyer (1975), Geiss (1978) and Giovanelli and Haynes (1979). Both DeNoyer and Geiss were searching for the cool, massive, thin HI shell, interior to the optical filaments of the SNR, predicted by SNR evolutionary models (Cox (1972b), Straka (1974), Mansfield and Salpeter (1974), Chevalier (1974)), which equate the present shock velocity with the low optical expansion velocity $\sim$ 0 (100 km/s) with respect to the LSR, for SNR in the radiative phase (Woltjer (1972).

DeNoyer (1975) found no evidence for the presence of an HI shell associated with any region of the Cygnus Loop, with an upper limit density about 20 times higher than that predicted for a 10 K shell. However, a correlation between the low velocity HI clouds 0 - 10 km/s and optical filaments was found and even with an absorption lane west of NGC 6960, which DeNoyer suggested may be an H_2 clound being ionised by X or UV radiation from the shock wave, expanding into the cloud. The HI density was estimated $\sim$ 5 - 10 cm^{-3}. Scoville et al. (1977) have observed CO features exterior to NGC 6960 coinciding with the region of optical extinction, and with an LSR velocity of 12 km/s, comparable with the mean 10 km/s of the local HI.

DeNoyer also observed a complex of negative velocity HI clouds possibly associated with the Cygnus Loop, with a filamentary structure resembling the optical, and showing emission features possibly indicating sites of SNR shock wave - cloud interactions (Sgro (1972)) near NGC 6990/6979. Geiss, with higher angular resolution, observed NGC 6960/6974, and also found no evidence for the SNR HI shell, and also suggested that the negative velocity hydrogen observed, had no real spatial connection with the Loop, but was a projection effect with a more likely association with the Orion arm. After further HI surveys of HB21 and CTB1 SNR, Geiss suggested that none of the SNR with optical filaments, and diameters between 30 - 100 pc have reached the radiative phase, but that their filaments represent the distribution of dense interstellar matter, local to the SNR, and undergoing interactions with the SNR shock wave.

Finally, Giovanelli and Haynes have recently searched for the presence of high velocity HI ($\rho \sim 10^{19}$ cm^{-2}) interior to the Cygnus Loop, predicted by McKee et al. (1978), who discussed the mechanism of acceleration of interstellar clouds encountered by a SNR shock wave. Evidence for the presence of high velocity gas within the Loop was possibly presented by earlier $H\alpha$ observations by Kirshner and Taylor (1976). However, when Giovanelli and Haynes observed areas of the SNR including those of Kirshner and Taylor, they found no evidence for low column density, high velocity clouds embedded in the SNR.

Table 2.2 summarises relevant radio parameters for the Cygnus Loop.

2.4 X-ray Astronomy.

2.4.1 X-ray survey observations.

The Cygnus Loop SNR was first definitely detected as an extended source of X-rays (0.2 - 1 keV) by Grader et al. (1970), using a rocket - borne proportional counter, and had previounsly predicted to be so, by Schklovsky (1968). Due to a high charged particle background, X-ray spectral information was degraded. Further, Bleach et al. (1972), gave an upper limit for the X-ray intensity from the Loop above 2 keV. The X-ray spectrum of the entire Loop has been observed mainly with rocket - borne, collimated, soft X-ray gas proportional counters, with $\Delta\varepsilon/\varepsilon \sim 80\%$ $(C\text{-}K_\alpha)$.

Energy range (keV)	Fitted spectral type *	Best fit electron temperature (10^6K)	
0.2 - 1.00	T + L	4.3	Gorenstein (1971)
0.16 - 6.70	T + G	2.3 - 2.9	Bleeker (1972)
0.15 - 1.00	T	4.1 ± 1.7	Borken (1972)
0.20 - 1.50	T + L	2.8 ± 0.2	Stevens (1973)
0.15 - 1.80	T + G + L	2.9 ± 1.5	Rappaport (1974)
0.15 - 1.50	T + G	2.1 ± 0.6	Charles (1976)
0.16 - 0.284	T	2.1 ± 0.8	Gronenschild (1976)

* See text below.

All the observations above were analysed using model fits, to pulse height data, of the simplified expression for thermal bremsstrahlung radiation from a hot, optically thin plasma (T) :

$$N(\varepsilon)\,d\varepsilon = C\,\frac{e^{-\frac{\varepsilon}{kT}}}{\varepsilon}\cdot\eta(\varepsilon, N_H)\,d\varepsilon \qquad cm^{-2}s^{-1}keV^{-1}$$

where C is the normalising constant in ph/cm^2/s, T the apparant plasma electron temperature in K, ε the X-ray energy in keV and $\eta(\varepsilon, N_H)$ the energy dependant interstellar medium soft X-ray transmission

TABLE 2.2

Radio properties of the Cygnus Loop SNR.

Angular diameter	$180'$
Flux density at 1 GHz	200 Jy
Spectral index at 1 GHz	-0.45
Surface brightness at 1 GHz	0.93×10^{-21} W/m^2/Hz/sr
Distance	0.8 kpc
Diameter	41.3 pc
Galactic height	-117 pc
HI column density between Sun and Loop	$7 - 15 \times 10^{20}$ cm^{-2}
Magnetic field in shell source	10^{-5} gauss
Polarization	15 - 25 %
HI cloud density local to Loop	5 - 10 cm^{-3}

$$\eta(\epsilon, N_H) = e^{-N_H \sigma(\epsilon)}$$

where N_H is the columnar density of neutral hydrogen in atom/cm^2 and $\sigma(\epsilon)$ is the photo - electric absorption cross - section per hydrogen atom in cm^2. (Brown and Gould (1970)). The parameters T, N_H are the undetermined fitting parameters. Approximations, for low Z plasmas, to the energy dependant Gaunt factor (Gorenstein et al. (1968)) were used (G). Also, calculations for the intensities of soft X-ray line emission from coronal - type plasmas with solar/cosmic abundances, were used (Tucker and Koren (1971)) (L).

Gorenstein et al. (1971) and Stevens et al. (1973) reported evidence for X-ray line emission from $O\,\overline{\underline{VII}} - O\,\overline{\underline{VIII}}$ ions (implying $T \sim 2 \times 10^6$ K) for 10 - 20% of the total X-ray flux, while Charles et al. (1975) and Gronenschild (1976), found no strong evidence, from long satillite observations (albeit of smaller field of view and of selected pointings, compared with the earlier rocket - borne large area counters).

Thus, from the broad band survey observations above, the effective (best fit) thermal plasma electron temperature $T \sim 2 - 4 \times 10^6$K and column density $N_H \sim 5 \times 10^{20}$ cm^{-2}, and for a distance of 770 pc, an X-ray luminosity Lx $\sim 10^{36}$ erg/s (0.2 - 1.5 keV). Even though the Tucker and Koren emission spectrum could be equally as well be fitted, the existence of X-ray lines could not be directly confirmed.

Gorenstein et al. (1971) first produced a one - dimensional X-ray emission survey scan (0.2 - 1.0 keV) of the Loop, with angular extent approximately that of the outermost optical filaments, and suggestive of a shell - like structure with X-ray emission falling sharply (within the 0.5^o resolution) at the optical filament boundaries. Borken et al. (1972) also produced a one - dimensional X-ray scan in a direction so as to resolve more clearly, the optical filaments, and which indeed showed strong correlation with the optical filaments.

2.4.2 X-ray emission morphological studies.

Stevens et al. (1973), Rappaport et al. (1973, 1974) first produced two - dimensional X-ray maps of the Cygnus Loop, using mechanically collimated detectors (Stevens) and one - dimensional reflectors (Rappaport), both $\sim 30'$ angular resolution. The technique involved multiple scans with rocket - borne, large area detectors, across the SNR, with the smaller field of view parallel to the scan path direction. Then to deduce two - dimensional X-ray surface brightness maps, the instrument point response function was de - convolved from the data, using an algebraic reconstruction technique (Stevens and Garmire (1973), Moore (1975)).

These X-ray maps were examined by Copernicus (Charles et al. (1975), Snyder et al. (1975)) and ANS (Gronenschild et al. (1976)). Gronenschild et al. also produced a two - dimensional X-ray map.

Energy band(keV)	FWHM f.o.v (degree)	
0.2 - 1.5	0.5 x 0.5	Stevens (1973)
0.15 - 1.8	0.5 x 9	Rappaport (1973)
0.5 - 1.5	0.2 x 0.2	Charles (1975)
0.16 - 0.284	0.6 x 0.6	Gronenschild (1976)

The maps produced by Stevens and Garmire (1973) showed strong limb brightening, implying a shell - like structure, with several regions of enhanced emission (Fig. 2.3), including an area near the Loop centre. The overall X-ray brightness correlated well with the optical filaments (N, NW regions) but not as well as the radio/optical correlation.

Rappaport et. al. (1974) produced a two - dimensional map of higher statistical precision and uniformity of exposure, Fig. 2.4, enhancing even more the deviations from circular symmetry in the X-ray emission, with emission much greater to the north than the south. Earlier, Ràppaport et al. (1974) had reported the existence of a centrally located ($20^h 49^m$, $30^\circ 43'$) point source of X-ray emission (0.4 - 0.85 keV) with frequency component 62 ms. Later observations by Weisskopf et al. (1974), and with Copernicus (Snyder et al. (1975)) yielded only upper limits to the flux above background, with no observable periodicity, and with the conclusions that either the source was strongly time - dependant or was at another location within the Loop. In Chapter 6, it is explained that the source was more likely the artifact of the ART algorithm used. Also, there appears to be no known radio pulsar associated with the Loop. (The anomalous behavior of the radio source CL4 was discussed in 2.3.2).

Stevens (1973) showed that the X-ray source distribution was quantitatively consistant with that expected from an expanding shock wave interacting with the interstellar medium, with the strength of such an interaction non - uniformly distributed around the expanding surface, to explain the observed intensity variations. For thermal radiation from a fully ionised plasma (65% H, 35% He) with electron temperature $T \sim 2.8 \times 10^6$ K, for the SNR in the adiabatic phase, the corresponding shock velocity $v_s = 0.3 \times T_s^{1/2} = 0.3\ (0.8\,T)^{1/2}$ km/s $\simeq$ 450 km/s. Thus, the velocity, behind the shock front, of material, $u = 2v_s/\gamma+1 \simeq 340$ km/s for $\gamma = 5/3$. To explain the discrepancy between the observed optical filament velocities of $\sim$ 120 km/s (2.2.3) and the X-ray shock velocity, Stevens invoked an inhomogenous model of the interstellar medium, having a local density inhomogeneity of the form $(r/r_0)^n$, $r_0 > r_s$. To model the correlation of X-ray/radio emission in the N, NW regions, and to achieve shock velocities of $\sim O$ (500 km/s), $n = 10$. Although such an unlikely local density gradient would not exist, Stevens (1973) had applied and adapted the Sedov adiabatic shock wave model to try to explain how the high X-ray surface brightness regions of the Cygnus Loop originate in regions of high local densities and lower shock velocities.

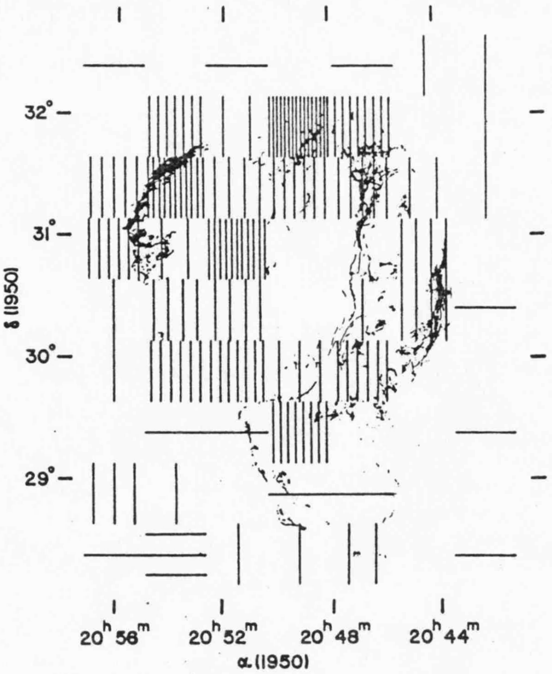

Stevens (1973)

Fig. 2.3. The X-ray intensity of the Cygnus Loop superposed on a sketch of the Hα emission. Each bar represents approximately 10^{-10} ergs (cm^2 s 0.25 deg^2)$^{-1}$, and two bars equal 1 σ above the mean background. NGC 6992–5 is the lower part of the bright arch on the eastern boundary. NGC 6960 is on the western edge and NGC 6995 is just above NGC 6992.

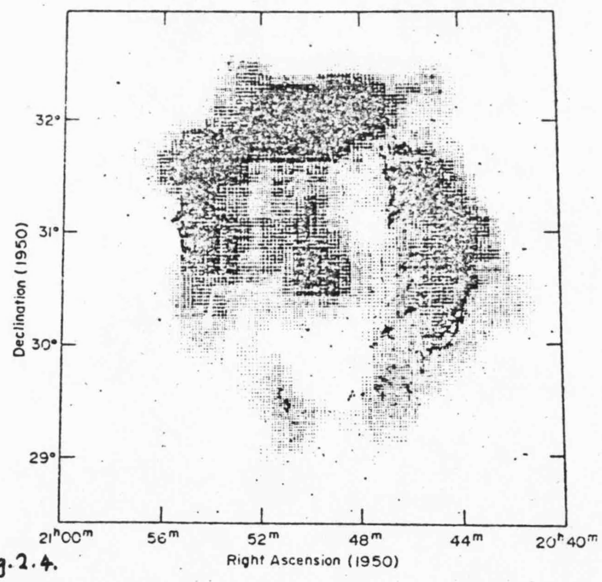

Fig. 2.4.

An ART map of the Cygnus Loop at energies below 1 keV. (Rappaport et al (1974)).

Rappaport et al. (1974) applied the Sedov equations for a homogenous medium, to derive values for SNR age, initial blast energy and ambient density, for an observed value of electron temperature averaged over the X-ray map. It was shown that the values were consistent with the Loop being in the adiabatic phase and that the age, as determined by the X-ray shock velocity, was $\sim 2 \times 10^4$ yr $< 5 \times 10^4$ yr as determined by the optical filament proper motions, and hence capable of harbouring an active stellar remnant (Rappaport et al. (1973)) similar to the situation for Vela X. No discussion was included concerning the optical/ X-ray velocity problem.

From the X-ray maps of Stevens and Garmire and Rappaport et al., spectral variations would be expected to be observable, due to the large intensity variations existing around the surface of the Loop. Charles et al. (1975) examined small regions of the Loop to estimate the accuracy of the earlier maps, and to investigate more closely the X-ray/radio correlation, and to perform broad band spectral observations. The regions included the bright radio/X-ray regions NGC 6992 - 5, NGC 6979 and CL4. Temperature estimates for the NGC regions were found to be the same to within errors, but lower than the previous overall Loop temperature estimates. However, the Copernicus results confirmed the existence of the bright X-ray emitting regions in the N, NE regions and that the minima in X-ray emission in NGC 6992 - 5 was highly correlated with the radio structure weaker in the N region. Again, no significant flux was detected in X-rays, from CL4.

Gronenschild (1976) reported ANS ($27' \times 34'$) results of 150 pointings uniformly distributed over the whole of the optical region of the Loop, and presented a two - dimensional map together with spectral fits (exponential spectra) from areas, including the N and E filaments and central regions. Keeping the value of N_H , found by analysing the data integrated over the entire Loop, constant, it was demonstrated that there were significant temperature variations ($\Delta\mathcal{E} = 0.16$ - 0.284 keV energy range) of 2 - 4×10^6 K, with higher temperatures occurring in the SE region. Comparison with

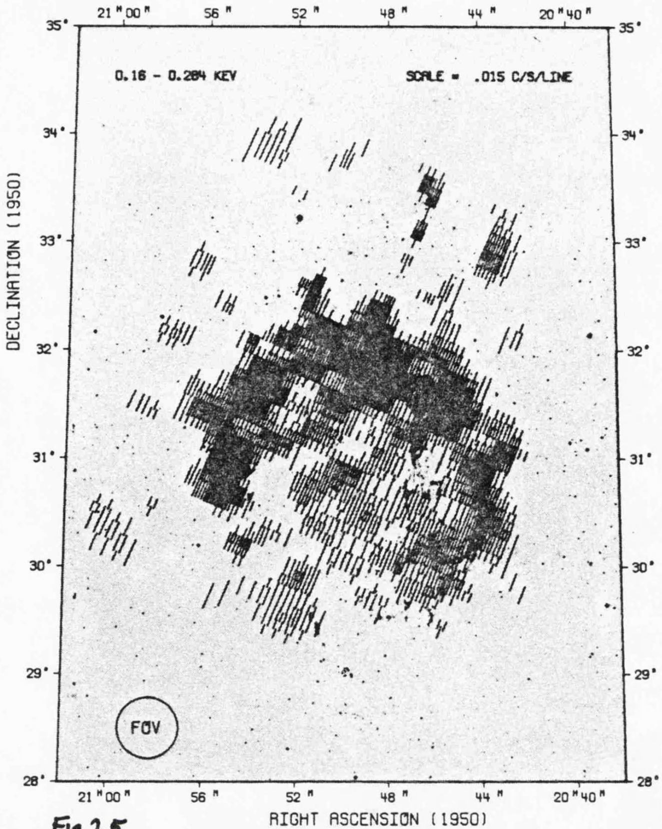

Fig. 2.5.

Soft X-ray brightness map of the Cygnus Loop. The cell size is $5' \times 6'.7$ and the density of lines in each cell is linearly proportional to the counting rate, i.e., every line corresponds to $0.015\ c\ s^{-1}$. The field of view (FOV) of the detector is shown in the lower left-hand corner. Superposed on the map is the red Palomar Sky Survey print (© National Geographic Society). From Monte Carlo studies it is derived that the brightest regions are significant to a level of about 15 sigma. The actual resolution of the X-ray map is better than about $10' \times 12'$ or about 2×2 cells. The isolated "sources" along the north and east (left-hand) edge may be not real but artifacts due to the Algebraic Reconstruction Technique (ART) used to obtain the map

Gronenschild (1979)

Stevens and Garmire (1973) and Rappaport et al. (1974) revealed higher values of X-ray intensity were obtained from the N and E filaments, $\simeq$ 55% the total X-ray flux from the Loop. The result of 4% total Cygnus Loop flux from the central regions, was in good agreement with Rappaport et al. (1974).

Using ART to deconvolve the ANS instrument response, Gronenschild (1978, 1979) has presented detailed X-ray surface brightness maps in the energy ranges 0.16 - 0.284 keV, 0.32 - 0.46 keV and 1 - 2.5 keV, binned in cells of $5' \times 6'.7$. From the reconstruction of a point source, the soft X-ray band was found to have a resolution $\sim$ $10' \times 12'$, with the other energy bands having resolutions of $25' \times 50'$ and $35' \times 75'$ respectively. The 0.16 - 0.284 keV map (Fig.2.5) shows good correlation with optical and radio maps, particularly for the outer radio contours of NGC 6992-5, 6990, with coinciding X-ray/radio maxima and minima between the brighter optical filaments. There is again no X-ray/radio correlation in the South, NGC 6974 (Keen et al. (1973)), containing the faint nebulosity. Comparing with the radio maps of Keen et al. and DeNoyer (1974), the X-ray emission extends $\sim$ 10 - 15$'$ outside the radio boundaries near NGC 6992-5, 6990. X-ray flux was possibly detected from CL6, CL7 (Keen et al.) which may be associated with the SNR.

The X-ray maps in the higher energy maps, were limited by low resolutions, but X-ray emission was observed to dominate in the Northern region, NGC 6992-5. No enhanced X-ray emission was observed near the centre of the Loop.

Gronenschild (1979) binned the ART maps in $30' \times 40'$ cells and presented results of spectral fits to the pulse height data from each cell (0.16 - 0.284 keV), using exponential (thermal continuum approximation) and line emission calculations (Mewe (1972), (1975), Gronenschild and Mewe (1979)), although to within the errors, the results were the same. Apparent electron temperatures were found to vary between $1.5 - 5 \times 10^6$K and the value of columnar density $0.5 - 100 \times 10^{20}$ cm^{-2}. It must be noted that the goodness of fits was specified only with a χ^2 with zero degrees of freedom, for the relatively narrow energy range 0.16 - 0.284 keV, which must have been dominated by the energy cut - off, due to absorption, and represented by N_H. The estimated distribution of temperatures and columnar densities presented by Gronenschild (1979) will be discussed in more detail in Chapter 6, together with results from pulse height analysis of the X-ray image (0.15 - 1.12 keV, $10'$ resolution) of the Cygnus Loop. Also, detailed comparison between the ANS X-ray map (0.16 - 0.284 keV) and the soft X-ray image, will be discussed, together with detailed correlation between the optical and radio maps.

2.4.3 High spectral resolution observations.

Direct measurements establishing the thermal nature of the X-ray emission process had first been reported by Shcheglov (1968), who detected the [Fe X] λ 6374 in the region NGC 6960, indicating 1 - 2 x 10^6 K (Kurtz et al. (1972), Mason (1975)). Shklovsky (1967) had first suggested that those SNR which emit thermal X-rays from (optically thin) hot plasmas at $\sim O(10^6$ K) will also emit optical coronal lines. Woodgate et al. (1974) first detected [Fe XIV] λ 5303 from regions exhibiting high X-ray flux in the X-ray map of Borken et al. (1972). Using an interference filter photometer (1° FOV) with 6 Å pass band (to allow for line broadening through mass motions caused by the shock waves), fields encompassing NGC 6992 - 5, 6979 and the central regions of the Loop, were observed. Estimating the ratio of [Fe XIV] coronal line flux to X-ray flux (Stevens and Garmire (1973)) in a field, yielded a value for the effective electron temperature (Kurtz et al. (1972)), assuming a thermal origin for the X-ray flux, and normal iron abundance (or which may be variable). From all regions observed, from the [Fe XIV] /X-ray flux ratio, temperatures of 2 - 3 x 10^6 K were derived, in agreement with the broad band X-ray observations.

Further, the 5303 Å line broadening was $<$ 8 Å , expected if a shock velocity 450 km/s were fully converted into mass motions, hence again indicating that the X-ray emission be produced immediately behind the present shock, and not fossil radiation. Thus, Minkowski's (1958) measurement of filament radial velocity was not a measurement of shock velocity and so comparison with proper motion becomes confused. (2.2.3).

Measurements of the one - dimensional radial distribution of [Fe XIV] emission across NGC 6992-5 were reported by Woodgate et al. (1977), with the observed emission extending $\sim 5'$ outside the optical filaments and being coincident with the filaments. Fitting the Sedov model to the calculated [Fe XIV] surface brightness, yielded a (poor fit) shock velocity of $\simeq$ 250 - 300 km/s, although the assumption of a homogenous sphere gave the poor fit. Derived SNR parameters were in agreement with X-ray spectral values. Woodgate et al. revealed the close correlation between [Fe XIV] and soft X-ray emission. Chapter 6 contains further discussion with respect to the X-ray image. No small fields of view (high spatial resolution) [Fe XIV] measurements have yet been reported on the Loop, to discover whether the evaporative cloud model (McKee and Ostriker (1977)) explains the [Fe XIV] /soft X-ray association, as has been suggested for regions of Puppis A SNR (Clark et al. (1979)).

Following the reports of the detection of O VII - O VIII X-ray lines at $\sim$ 19 Å, composing $\simeq$ 10 - 30% total X-ray flux from the Loop (0.2 - 1.5 keV) as reported by Gorenstein et al. (1971) and Stevens and Garmire (1973), Stark and Culhane (1978) carried out a narrow band (21.6, 21.8, 22.1 Å) search, using a rocket - borne, large area Bragg crystal spectrometer ($5^{\circ}.5$ FWHM). No significant flux was observed and a 3σ upper limit to the line flux of 6% total Loop X-ray flux (0.17 - 1.5 keV) from the X-ray map of Rappaport et al. (1974). Using the adiabatic and isothermal blast wave models (Sedov (1959), Solinger et al. (1975)), a range of temperatures of the post - shocked regions were assumed and the state of ionization equilibrium of oxygen ions investigated. From the isothermal model and the observed upper limit O VII flux, the effective electron (shock) temperature was constrained such that $T <$ 0.9 x 10^6 K and $T >$ 4.2 x 10^6 K with the SNR in non - equilibrium ionization. Alternatively, from the adiabatic model (homogenous medium) the shock temperature was constrained such that $T_s <$ 3 x 10^5 K and $T_s >$ 3.7 x 10^6 K (electron temperature 9 x $10^5 < T$, $T >$ 5.2 x 10^6 K, using the conversion of $T_s \rightarrow T$ from Stark and Culhane). Since the lower temperature implied ages of the Cygnus Loop indicative of the radiative phase (Cox (1972)), Stark and Culhane concluded that the effective electron temperatures of the Loop must be higher than previous values. Alternatively Stark and Culhane suggested that the oxygen abundance was low - factor 4 (isothermal), factor 10 (adiabatic, homogenous case). However, Raymond (1979) does not support any low O abundance from observations of filament optical spectra.

The high (and multiple) temperature scenario has recently been given some support. Recent rocket experiments (0.1 - 8 keV) employing the gas scintillation proportional counter (with more than twice the inherent proportional counter energy resolution, but retaining the same overall sensitivity) have been reported by Inoye et al. (1979), who observed (10° x 20°FOV) the entire Loop. Inoye et al. were unable to fit the pulse height data with a single temperature, but instead required initially two, 1.3 x 10^6 K and 4 x 10^6 K. A better fit was obtained, assuming the emission measure had a power law form of temperature, and using the Kato (1977) coronal spectrum, over the temperature range 0.4 - 10 x 10^6 K in 2 x 10^6 K temperature increments (15 components). Also, Inoye et al. found that the emission measure increased with higher temperature more rapidly than the Sedov adiabatic emission measure function would give, and they invoked the HI dense cloud evaporation and heating mechanism (McKee and Ostriker (1977)) as dominating the X-ray emission process from the Cygnus Loop.

Finally, Table 2.3 summarises parameters derived from recent soft X-ray observations of the Cygnus Loop SNR.

TABLE 2.3

X-ray properties of the Cygnus Loop SNR.	
X-ray radius	$\sim$ 19 d_* pc
X-ray temperature	1 - 10 x 10^6 K
X-ray luminosity (0.15 - 1.5 keV)	$\sim$ 2 x 10^{36} d_*^2 erg/s
Columnar density	$\sim$ 5 x 10^{-20} cm^{-2}
X-ray shell thickness	$\sim$ 2 - 5 pc
Ambient interstellar density	$\sim$ 0.2 - 0.5 cm^{-3}
Mass of X-ray shell	$\sim$ 4 $M_\odot$

$d_* = d/770$ pc

TABLE 2.4

Blast wave parameters of the Cygnus Loop.	
X-ray radius	$\sim$ 19 d* pc
X-ray temperature	$\sim 2.5 \times 10^6$ K
Shock temperature	$\sim 2 \times 10^6$ K
Shock velocity	$\sim$ 350 km/s
Explosion energy	$\sim 1.1 \times 10^{51}$ $d_*^{5/2}$ erg
Age	$\sim$ 20,000 yr

$d_* = d/770$ pc

2.5 Summary.

Observations of the Cygnus Loop SNR at optical, radio and X-ray wavelengths have revealed details of how a (Type II) SNR may be evolving in the interstellar medium local to the SNR, and how the large and small scale properties of the interstellar medium may effect such an evolution.

The optical, radio and X-ray maps are very similar in parts, and suggest a situation where the gross properties of the SNR evolution may be described by the Sedov adiabatic blast wave equations, but also, there are clear correlations of SNR emission intensity with interstellar medium inhomogeneities (clouds).

The Cygnus Loop is a non - thermal radio source, being described as a whole by the shell compression model. There is no evidence for the presence of a massive HI shell, associated with SNR in the radiative phase. The origin of the thermal soft X-rays is described in general by the Sedov blast wave model. The close correlation that most likely exists between the [Fe XIV] emission and soft X-rays may be explained by the cloud - shock wave interaction and cloud evaporation models.

X-ray imaging, with the advantage of uniform exposure and low background, with moderate angular resolution may further investigate :

(1) more detailed optical filament and [Fe XIV] /soft X-ray emission correlations.

(2) more detailed radio (knots)/soft X-ray emission correlations

(3) X-ray spectral variations over an energy band with dynamic range 10:1.

(4) the presence of any associated active stellar remnant (cf. sensitivities of an imaging telescope, Table 3.5).

References.

Allen, C., 1973. Astrophysical Qunatities. UL, Athlone Press.

Argue, A., Clements, E., Harvey, G., and Elsmore, B., 1978. Obs. 98, 160.

Baldwin, J., 1950. MNRAS, 115, 690.

Bleach, R., Boldt, E., Holt, S., Schwartz, D. and Serlemitsos, P., 1972. Ap. J., 171, 51.

Bleeker, J., Deerenberg, A., Yamashita, K., Hayakawa, S. and Tanaka, Y., 1972. Ap. J., 178, 377.

Borken, R., Doxsey, R. and Rappaport, S., 1972. Ap. J., 178, L115.

Bridle, A., 1967. MNRAS, 136, 319.

Burginyon, G., Hill, R. and Seward, F., 1975. Ap. J., 200, 163.

Burginyon, G., Hill, R., Palmieri, T., Scudder, J., Seward, F., Stoering, J. and Toor A., 1973. Ap. J., 179, 615.

Caswell, J., MNRAS, 181, 789.

Chamberlain, J., 1953. Ap. J., 117, 399.

Charles, P., Culhane, J. and Zarnecki, J., 1975. Ap. J., 196. L19.

Clarke, D. and Caswell, J., 1976. MNRAS, 174, 267.

Clarke, D., Murdin, P., Zarnecki, J. and Culhane, J., 1979. MNRAS, 188, 11P.

Chevalier, R., 1974. Ap. J., 188, 501.

Colla, G., Fanti, C., Fanti, R., Ficarra, A., Farmiggini, L., Gandolfi, E., Lari, C., Marano, B., Padrielli, L., Salter, C., Setti, G., and Tomasi, P., 1971. Astron. J., 76, 956.

Costain, P. and Lish, P., 1960. MNRAS, 120, 72.

Cox, D., 1972 a. Ap. J., 178, 143.

Cox, D., 1972 b. Ap. J., 178, 159.

Cox, D., 1972 c. Ap. J., 178, 169.

DeNoyer, L., 1974, Astron. J., 79, 1253.

DeNoyer, L., 1975, Ap. J., 196, 479.

Doroshenko, V., 1970, Sov. Astr. - AJ, 14, 237.

Eaton, J. and Krans, J., 1959. Ap. J., 129, 282.

Falle, S., 1975, MNRAS, 172, 55.

Geiss, S., 1978, Thesis, Cambridge.

Geldzahler, B., 1978, Memorie Soc. Astr. ital., 49, 577.

Giovanelli, R. and Haynes, M., 1979, Ap. J., 230, 404.

Brown, R. and Gould, R., 1970. Phys. Rev., D2, 2252

Grader, R., Hill, R. and Stoering, J., 1970, Ap. J., 161, L45.
Groneschild, E., Mewe, R., Heise, J., Brinkman, J., Boggende, A. and Shrijver, H., 1976, Astron. Ap., 49, 153.
Gronenschild, E., 1978. Memorie Soc. astr. ital., 49, 553.
Gronenschild, E., 1979, Utrecht preprint.
Gronenschild, E., and Mewe, R., 1978, Astr. Ap., Suppl. 32, 283.
Gorenstein, P., Harris, B., Gursky, H., Giacconi, R., Novick, R. and Van den Bout, P., 1971, Science, 172, 369.
Harris, D., 1962. Ap. J., 135, 661.
Hogg, D., 1968, Nebulae and Interstellar Matter ad. B. Middlehurst and L. Aller, U. Chicago Press.
Hubble, E., 1937, Carnegie Yb., 36, 189.
Inoye, H., Koyama, K., Matsuoka, M., Ohashi, T., Tanaka, Y. and Tsunemi, H., 1979. ISAS preprint.
Kato, T., 1976, Ap. J., Suppl. 30, 397.
Keen, N., Wilson, W., Haslam, C., Graham, D. and Thomasson, P., 1973. Astron. Ap., 28, 197.
Kenderline, S., 1973, MNRAS, 126, 55.
Kirshner, R. and Taylor, K., 1976, Ap. J., 208, L83.
Kundu, M., 1970, Ap. J., 162, 17.
Kundu, M. and Velusamy, J., 1967, Ann. d'Ap., 230, 723.
Kundu, M. and Becker, R., 1972, Astron. J., 77, 459.
Kurtz, D., Van den Bout, P. and Angel, J., 1972, Ap. J., 178, 701.
McKee, C. and Cowie, L., 1975, Ap. J., 195, 715.
McKee, C., Cowie, L. and Ostriker, J., 1978, Ap. J., 219, L23.
McKee, C. and Ostriker, J., 1977, Ap. J., 218, 148.
Mason, H., 1975, MNRAS, 170, 651.
Mansfield, V. and Salpeter, E., 1974, Ap. J., 190, 305.
Matheuson, D., Large, M. and Haslam, C., 1960, MNRAS.
Mewe, R., 1972, Sol. Phys. 22, 459.
Mewe, R., 1975, Sol. Phys. 44, 383.
Miller, J. and Mathews, W., 1972, Ap. J., 172, 593.
Miller, J., 1974, Ap. J., 189, 239.
Milne, D., 1979, Austr. J. Phys. 32, 83.
Minkowski, R., 1958, Rev. Mod. Phys. 30, 1048.
Minkowski, R., 1959, Paris Symp. Radio Astr., ed. R. Bracewell, Stanford, U.P.
Moffat, P., 1971, MNRAS, 153, 401.

Moore, W., 1975, Thesis, C.I.T.
Oort, J., 1946, MNRAS, 106, 159.
Osterbrock, D., PASP, 70, 180.
Parker, R., 1964a. Ap. j., 139, 493.
Parker, R., 1964b. Ap. J., 139, 208.
Parker, R., 1967, Ap. J., 149, 363.
Piembert, M., Rayo, J. and Torres - Piembert, S., 1975, Rev. Mex. Astr. Astroph. 1, 289.
Pikelner, S., 1954, Izvest. Crimean Ap. Obs. 12, 93.
Rappaport, S., Cash, W., Doxsey, R., Moore, G. and Borken, R., 1973, Ap. J. 186, L115.
Rappaport, S., Doxsey, R., Solinger, A. and Borken, R., 1974, Ap. J., 194, 329.
Raymond, J., 1976, Thesis, University of Wisconsin.
Raymond, J., 1979, Ap. J., Suppl., 39, 1.
Rishbeth, H., 1956, Aust. J. Phys. 9, 494.
Scoville, N., Irvine, W., Wannier, P. and Predmore, C., 1977, Ap. J. 216, 320.
Sedov, L., 1959, Similarity and Dimensional Methods in Mechanics, Academic P. (NY)
Shklovsky, I., 1967, Sov. Astr. - AJ, 10, 594.
Shklovsky, I., 1968, Supernovae, Wiley, London.
Shcheglov, P., 1968, Sov. Astr. - AJ, 11, 567.
Snyder, W., Henry, R., Charles, P., Culhane, J., Sanford, P., Bleach, R. and Drake, J., 1975, Ap. J., 186, L115.
Solinger, A., Rappaport, S. and Buff, J., 1975, Ap. J., 201, 381.
Stevens, J. and Garmire, G., 1973, Ap. J., 180, L19.
Stevens, J., Riegler, G. and Garmire, G., 1973, Ap. J., 183, 61.
Stevens, J., 1973, Thesis, C.I.T.
Straka, W., 1974, Ap. J., 190, 59.
Van der Laan, H., 1962, MNRAS, 124, 125.
Webster, A. and Ryle, M., 1976, MNRAS, 175, 95.
Weisskopf, M., Helava, H. and Wolff, R., 1974, Ap. J. 194, L71.
Westerhout, G., 1958, BAN, 14, 215.
Wolf, M., 1923, A.N., 223, 109.
Woltjer, L., 1972, Ann. Rev. Astron. Ap., 10, 129.
Woodgate, B., Stockman, H., Angel, J. and Kirshner, R., 1974, Ap. J., 188, L79.
Woodgate, B., Kirshner, R. and Balon, R., 1977, Ap. J., 218, L129.
Ryle, M., Caswell, J., Hine, R. and Shakeshaft, J., 1978. Nature, 276, 571
Tucker, W. and Koren, M., 1971. Ap. J., 168, 283

Chapter 3. DESCRIPTION OF A ROCKET-BORNE SOFT X-RAY TELESCOPE.

Chapter 3. DESCRIPTION OF A ROCKET-BORNE SOFT X-RAY TELESCOPE.

3.1 Introduction.

The design and operation of an X-ray telescope, to be integrated aboard a sounding rocket, is discussed. This work evolved from a proposal put forward to NASA by the MIT and Leicester X-ray astronomy groups (Rappaport et. al., 1974) for an all sky soft X-ray (0.15 - 1.5 keV) survey to be carried out with an X-ray telescope facility of large area ($\sim$ 350 cm^2 effective area at 0.25 keV) and modest angular resolution (2' - 10') over a large field of view ($\sim$ $2^o \times 2^o$). The experimental payload would comprise four sets of nested paraboloid/hyperboloid imaging X-ray mirrors with thin window imaging proportional counters at the confocal plane. In the spring of 1975 development of a prototype, low-cost telescope began at MIT and Leicester, to be integrated into a sounding rocket payload to perform astronomical X-ray imaging observations in the pre - HEAO-B era, and to demonstrate the feasibility of low cost imaging systems.

Imaging X-ray astronomy of extra-solar objects has just recently begun, as a result of the work of the SAO group (Harnden et al., 1977, Gorenstein et al., 1977, Gorenstein et al., 1978) who were primarily concerned with studying extra-galactic objects (Virgo and Perseus clusters of galaxies). The dedicated beginning of galactic imaging X-ray astronomy became the prime concern of the MIT - UL collaboration.

3.2 Principles of cosmic X-ray image formation and recording in space

Fig. 3.1 outlines the general principles for soft X-ray (0.1 - 2 keV) imaging astronomical objects. Clearly, there are several processes involved, but there exist three important stages of development :

(1) The astronomical object, whether extended or point-like (or a composition of the two) may exhibit both spatial and temporal variation in X-ray surface brightness. The

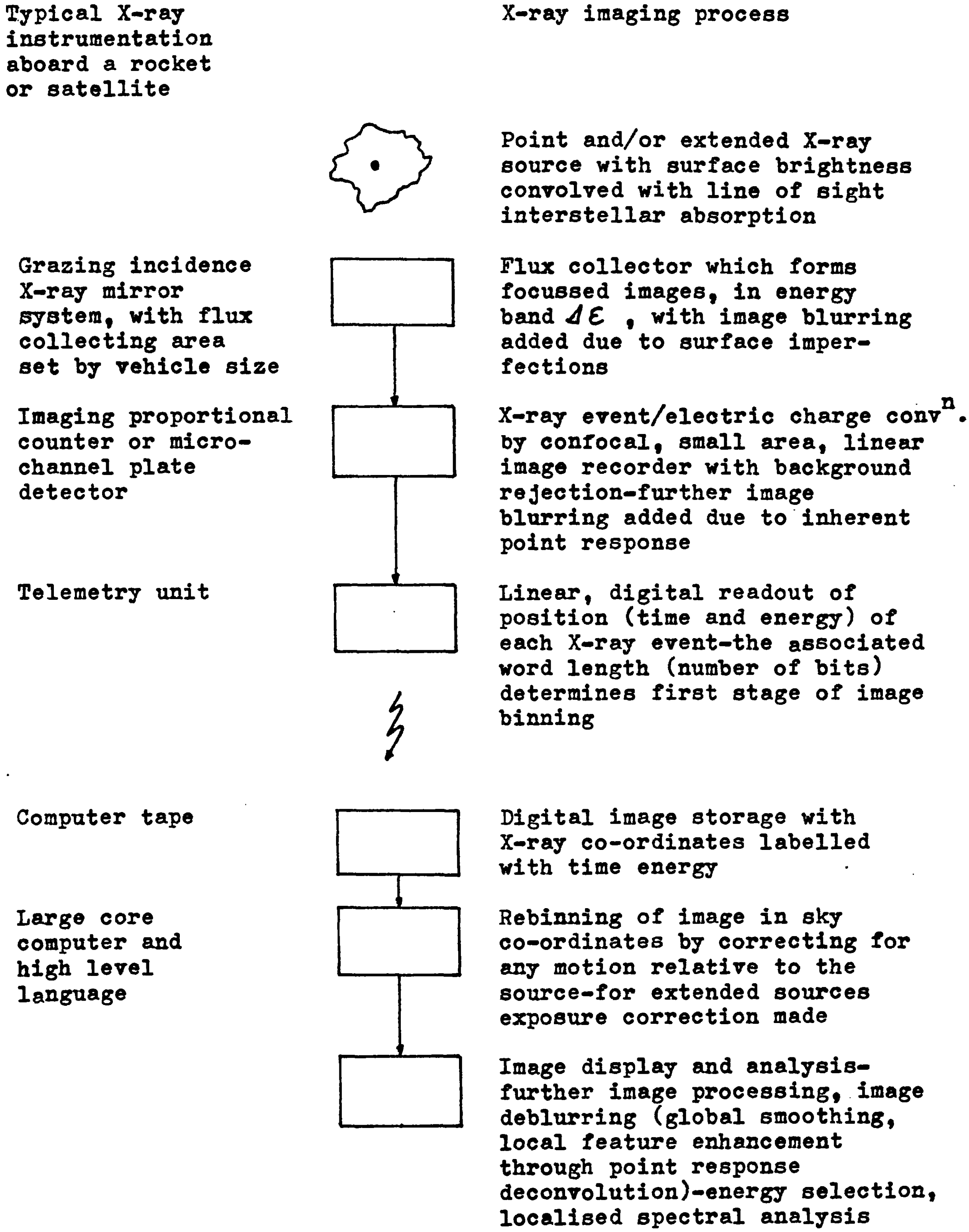

Fig. 3.1. Principles of imaging X-ray astronomy. For a high quantum efficiency, imaging detector a diffraction grating or crystal may be added after the mirror to perform narrow band imaging.

source characteristics may be modified by the material constitution of the interstellar medium, between the Sun and the source, depending on source galactic longitude and lattitude co-ordinates. All in all, what is imaged is a convolution of the soft X-ray emission from the source, and the line of sight absorption of the interstellar medium. The subsequent final presentation of the source X-ray image and comparison with emission and absorption data at other wavelengths, only then provides some astrophysical insight.

(2) The space-borne X-ray telescope intercepts the parallel X-ray flux from the astronomical object. Focussing and imaging occur followed by image readout. Practical systems utilise the principle of externally reflecting (2^n) times, grazing incident X-rays ($\lesssim$ 2 keV) at highly polished, metallic surfaces, which, shaped as conical sections of revolution, focus the X-ray image. In the confocal plane, a position sensitive radiation transducer, the practical forms of which utilise the photo - electric effect in a gas or solid, records the focussed X-ray image. Practical image readout techniques consist of encoding each analogue electronic signal from each X-ray event with subsequent digital decoding and transmission.

(3) Image processing where the image is presented in sky co-ordinates and may be subjected to noise suppression (for a photon count limited case) and possible feature enhancement through deconvolution of the (non - linear) telescope response from the initial image.

The above demarcation of X-ray image formation will be discussed in more detail, enabling a clearer understanding of the design feature of the MIT -UL X-ray telescope and of the subsequent results obtained. In particular, the stage (2) is presently discussed, with discussion of stages (1) and (3) being reserved for Chapters 5 and 6 together.

3.3 A rocket-borne X-ray telescope.

3.3.1 Design and characteristics of the focussing, imaging X-ray mirror system.

X-rays in vacuo or air undergo total specular reflection from polished surfaces of materials such as metal or glass, for glancing incidence angles (Compton 1923, Compton and Allison 1963). This reflection takes place because the real part of the complex refractive index, for X-rays, is less than 1 for all materials. The physics of X-ray reflection is summarised in Fig. 3.2. The actual functional form of the reflecting curve as a function of grazing angle can be evaluated from the Fresnel equations (Fig. 3.2). The essential elements of X-ray reflectivity are :

(1) Up to some critical angle, the reflectivity is very high.

(2) The critical angle is smaller with increasing X-ray energy.

(3) High Z (i.e high electron density) material should be used as the reflecting surface.

(4) The reflectivity, because of the existence of X-ray absorption edges in the surface material, is a complicated function of X-ray energy.

The fact that X-rays will undergo specular reflection with high efficiency allows for the construction of focussing X-ray mirrors. The basic line element producing focussing of parallel radiation, is a parabola.

Giacconi and Rossi (1960) first realised the potential usefulness of X-ray reflection for X-ray astronomy and proposed various focussing systems. Giacconi et al., (1969), Gursky and Schwartz (1974) and Underwood (1975) have reviewed several features of X-ray image forming, focussing mirrors, particularly those of the two surface, confocal, conic sections of revolution types, first studied by Wolter (1952a, 1952b). In general, grazing incidence imaging systems must have a number of reflecting surfaces in multiples of two, to overcome comatic aberration.

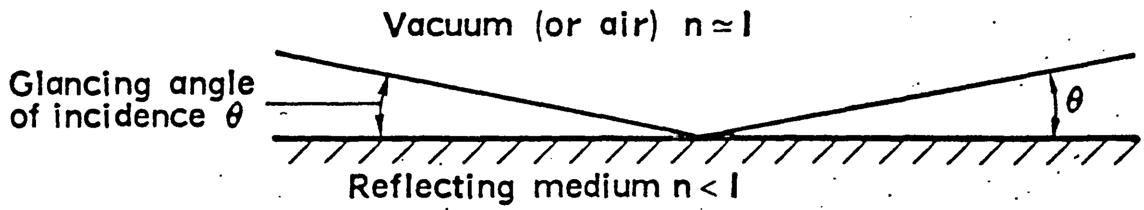

Complex index of refraction: $n = 1 - \delta - i\beta$ ($\delta \sim 10^{-5}$ to 10^{-6})

$\beta = \mu\lambda/4\pi$ (μ = linear absorption coefficient)

Critical glancing angle: $\theta_c = \sqrt{2\delta}$

Variation of reflectivity with θ (Fresnel's equation):

$$\frac{I}{I_0} = \frac{\left[\sqrt{2}\,X - \sqrt{\sqrt{(X^2-1)^2 + Y^2} + (X^2-1)}\right]^2 + \sqrt{(X^2-1)^2 + Y^2} - (X^2-1)}{\left[\sqrt{2}\,X + \sqrt{\sqrt{(X^2-1)^2 + Y^2} + (X^2-1)}\right]^2 + \sqrt{(X^2-1)^2 + Y^2} - (X^2-1)}$$

where $X = \theta / \theta_c$, $Y = \beta/\delta$

Penetration depth:

$$Z_{1/e} = \frac{\lambda}{4\pi\sqrt{\delta}\left\{\left[(X^2-1)^2 + Y^2\right]^{1/2} - (X^2-1)\right\}^{1/2}}$$

Physics of total reflection of X-rays

Fig. 3.2.(After Underwood 1975)

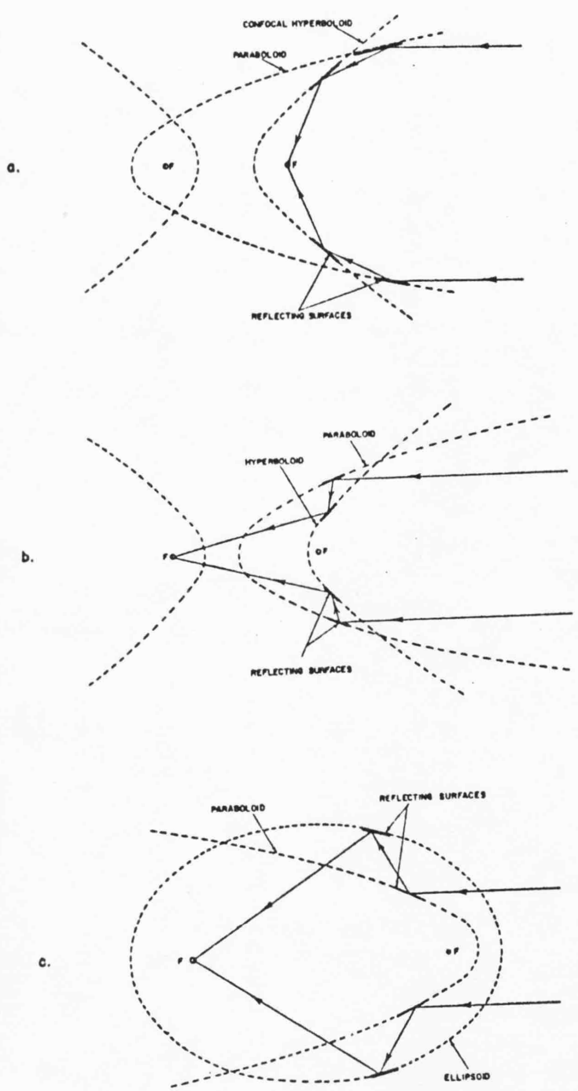

Three possible configurations for image-forming X-ray telescopes suggested by WOLTER (1952a, b).

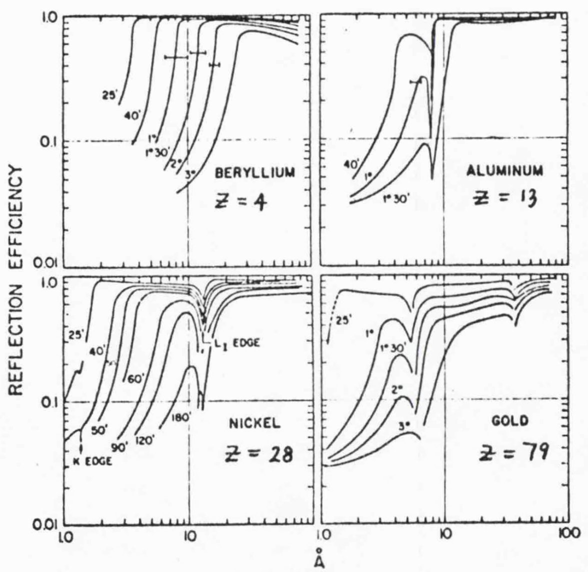

Theoretical reflection efficiency vs. wavelength for various grazing angles and reflection materials.

Fig. 3.3 (After Giacconi et al. 1969)

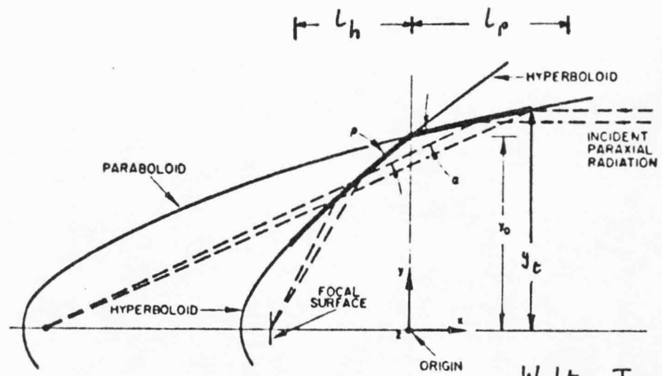

Wolter Type I

This design minimizes the difficulty of maintaining alignment between the two elements and maximizes the reflection efficiency for a system of a given focal length and diameter. Typically, the reflecting surfaces are pitched at angles of 40 to 80 arc min to rays which are incident parallel to the axis. The general equations for such a system can be written

$$\left.\begin{array}{ll} \text{Paraboloid} & y^2 + z^2 = 4p(x + p + c + k) \\ \text{Hyperboloid} & \dfrac{(x+k)^2}{h^2} - \dfrac{y^2 + z^2}{c^2 - h^2} = 1 \end{array}\right\} \qquad (5)$$

In order to maximize the two surface reflection efficiency, we impose the condition $\alpha = \varrho$, so that a paraxial ray will strike the first and second reflecting surfaces at about the same angle. With this condition, the four constants in Equation (5) may be expressed in terms of two initial design parameters: the focal length F, which is the distance from the intersection plane $x = 0$ of the paraboloid and hyperboloid to the nearer focus of the hyperboloid; and the radius y_0 of the telescope surface in the plane $x = 0$. These expressions are:

$$p = y_0^2/8F$$
$$c = F/2$$
$$k = (3/4)F$$
$$2h^2 = c^2 + k^2 + 4p(p + c + k) - [(c^2 + k^2 + 4p(p + c + k))^2 - 4c^2k^2]^{1/2}.$$

If L is the length of the paraboloidal reflecting surface along the optical axis, the geometric collecting area A is:

$$A \approx \pi y_0^2 L/2F.$$

A suitably positioned pair of aperture stops is used to prevent the undesired rays which do not strike the reflecting surfaces or strike only one of the surfaces from reaching the image area.

Kirkpatrick and Baez (1948) have also shown that real images can also be formed by successive reflection from perpendicular parabolic mirrors.

The X-ray imaging optics of Wolter (1952) and the properties of typical reflecting materials utilised are summarised in Fig. 3.3. The Wolter I system has been most thoroughly investigated, with regard to its use in solar imaging X-ray astronomy (Underwood et al., 1977). Both reflections take place on the internal surfaces thus maximising the reflection efficiency for a system of given focal length. There are also structural advantages in that the two surfaces may be joined. The mirrors may also be nested easily to increase the total collecting area.

The design of the MIT Wolter I mirror system, of two nested mirrors was based on work by Halpern (1976), who extended the work of Magnus and Underwood (1969) and Van Speybroeck and Chase (1962), by computing the properties of wide field of view ($2^{\circ} \times 2^{\circ}$), short focal length Wolter I systems. The principal design features were :

(1) The paraboloid and hyperboloid grazing angles were equal ($\alpha_p = \alpha_h = \alpha$, $\xi = 1$) (Fig. 3.3) to maximise the collecting area for a given total mirror length and because of the well - defined high energy cutoff for reflection at grazing angles, maximise the short wavelength range of the telescope. With a choice of α, the values for y_0 and L_p determined the effective area and angular resolution of the system. L_h was constrained such that a parallel ray striking the front edge of the paraboloid also strike the rear edge of the hyperboloid.

(2) For a given value of α and projected frontal area A to maximise the angular resolution, the outer diameter of the front paraboloid, y_t, was made as large as possible. The actual size was constrained by the 17" diameter Astrobee rocket payload configuration. The overall effective area was increased by nesting a smaller paraboloidal - hyperboloidal system, inside the

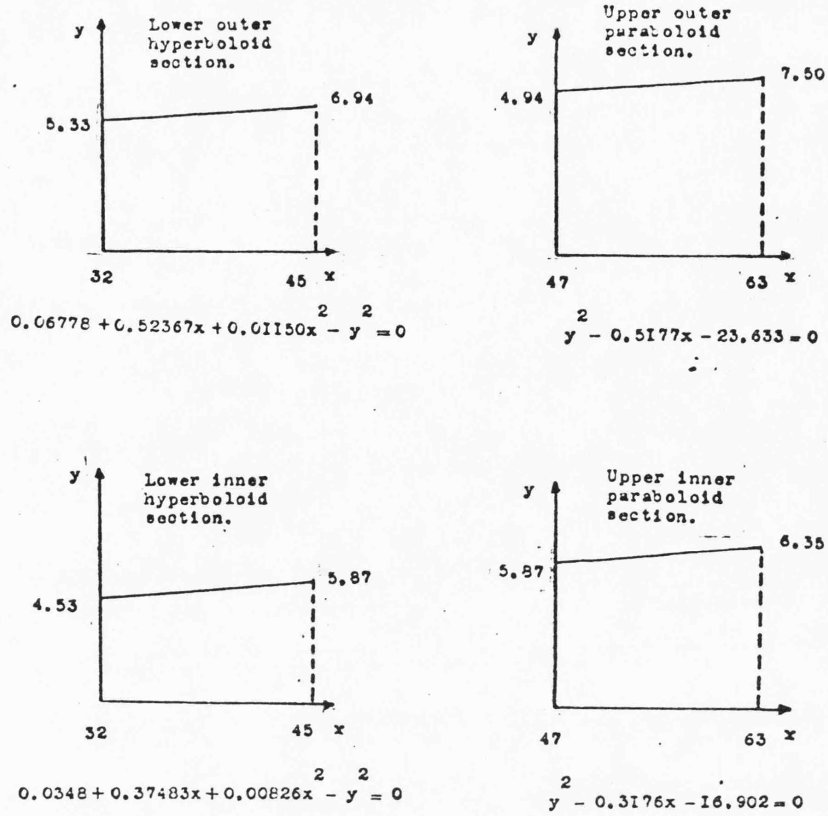

Fig. 3.4. The component sections of the MIT mirror (Woltjer I system). The conic equations give the design parameters in inches. The surfaces were machined from forged aluminium by a numerically controlled lathe. The internal surfaces are coated with Ni.

The entire mirror assembly is 32" long and 15½" in diameter. The 45" focal length corresponds to a focal plane plate scale 3'/mm.

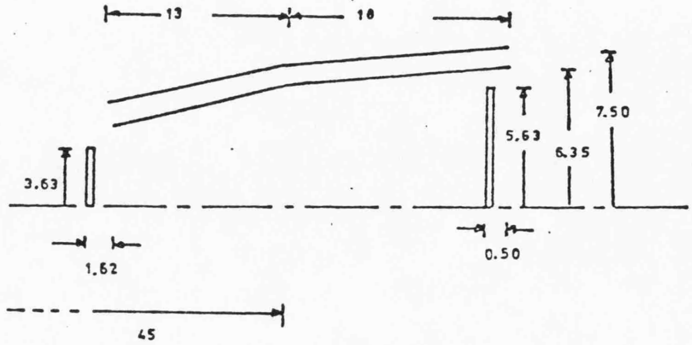

Fig. 3.5. Position of the baffles to prevent straight-through X-rays which undergo no external reflection at the two mirror surfaces, and to reduce single reflection X-rays from being scattered to the IPC.

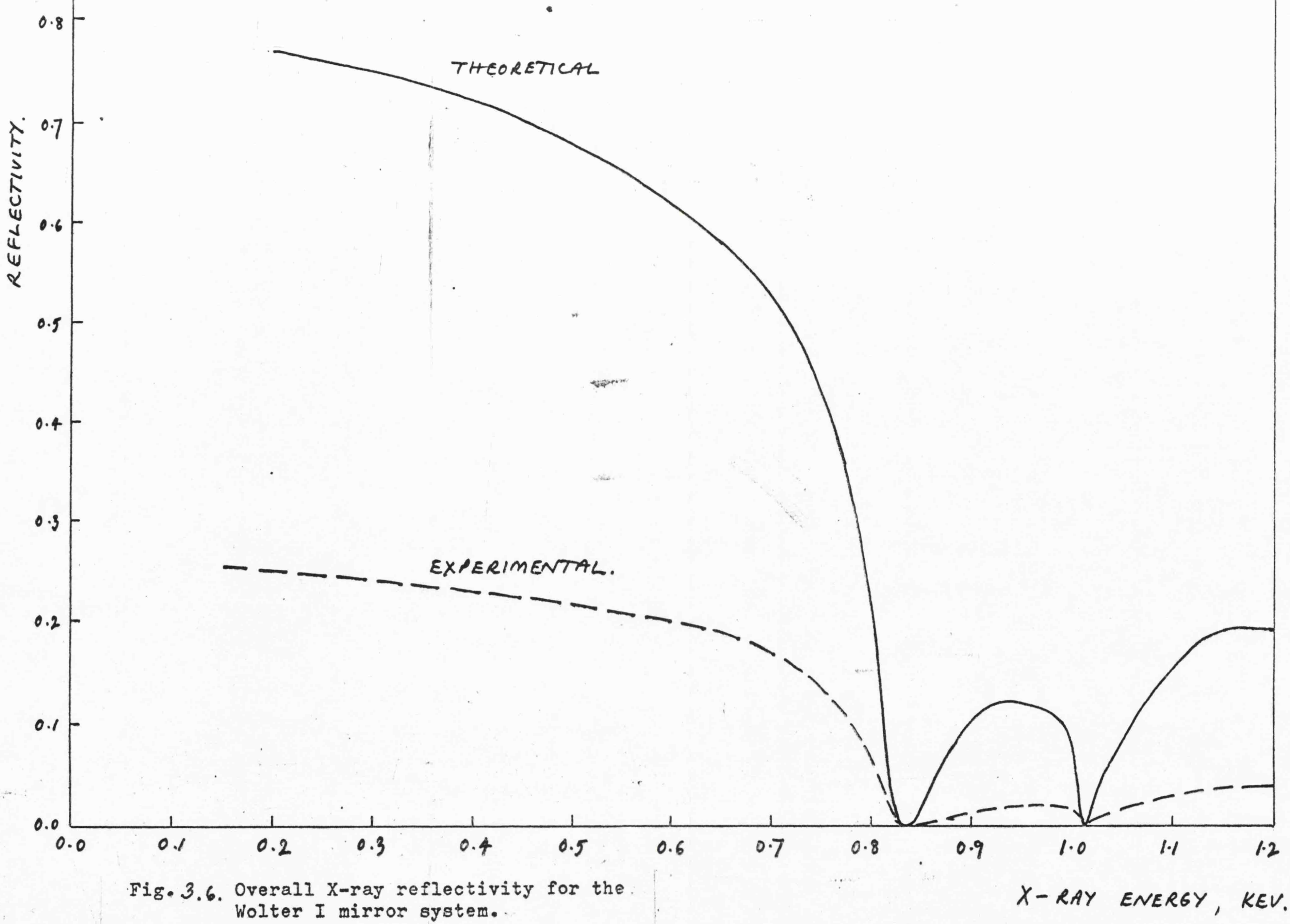

Fig. 3.6. Overall X-ray reflectivity for the Wolter I mirror system.

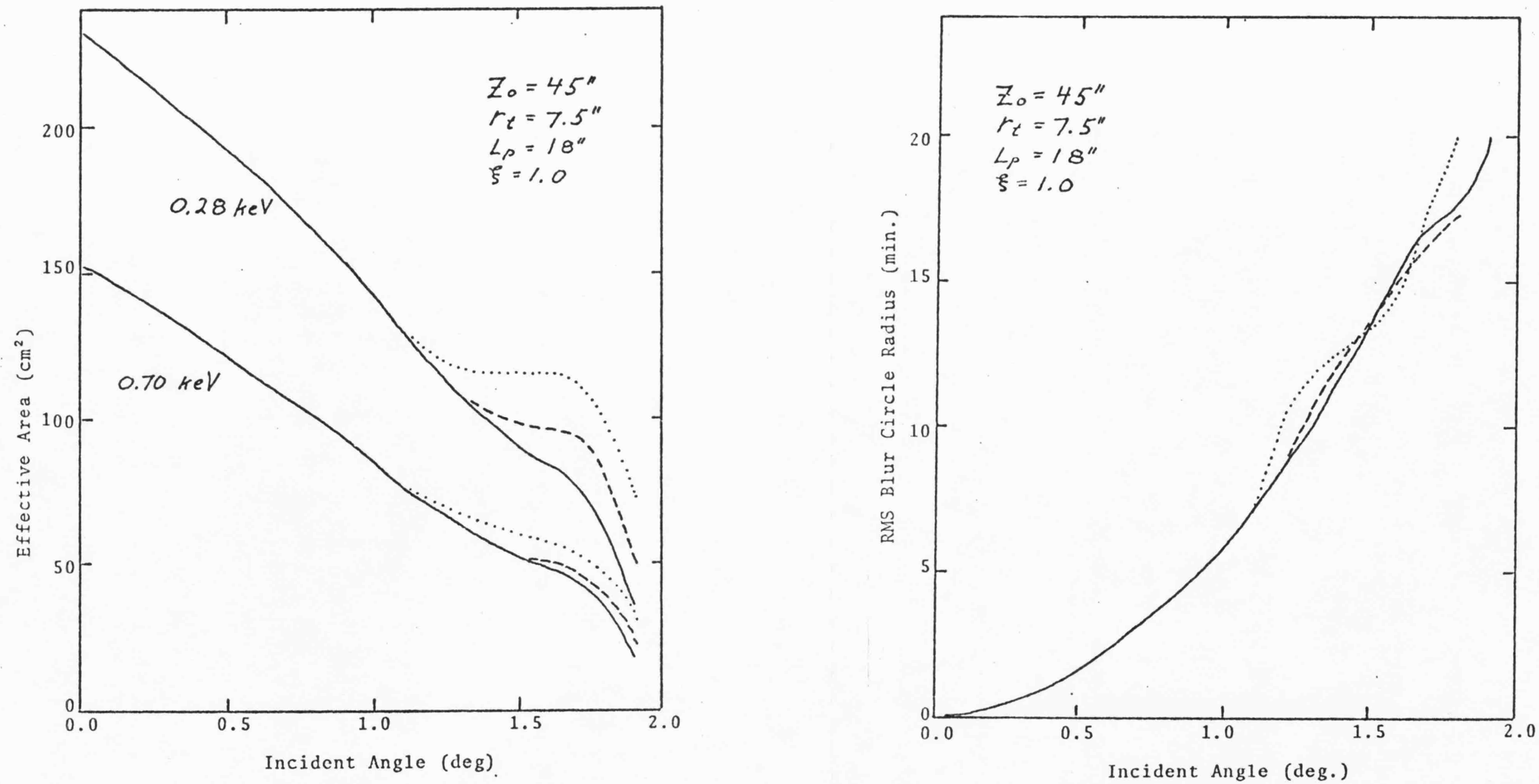

Figure 3.7 Angular resolution vs. incident angle, two nested telescopes. Dotted line: one baffle. Dashed line: five baffles. Solid line: ideally baffled.

Wolter I system, Fig. 3.3, with a diameter just small enough to pass all axial rays which strike the next larger surface, both systems being confocal.

The design details of the MIT Wolter I system are presented in Fig. 3.4 and Fig. 3.5 (Boughan 1977). With the calculated total reflection efficiency from two N_i surfaces (Fig. 3.6), the results of ray-tracing presented by Halpern (1976 are reproduced in Fig. 3.7, for several baffle configurations. The constructed MIT mirror system is shown in Plate 3.1. The nested X-ray telescopes were machined with a numerically controlled lathe (Ober Tool and Die Co., Mass.) out of blocks of forged aluminium. The inside surface of each of the four pieces, (Fig. 3.4), was polished, coated with electroless N_i (90% N_i + 10% P) and repolished.

The performance of the telescopes was measured in the the 215' X-ray facility at A.S and E. (Boston) (Rappaport, Levine and Petre, 1977). X-ray energies of 0.25 keV and 1.5 keV were used to determine both the effective area and angular resolution. A narrow slit (0.012") in front of the mirror system was used to map the shape of the on-axis focussed X-ray beam (incident on a monitor proportional counter). The results of the slit scan across the focussed X-ray beam are reproduced in Fig. 3.8. Superimposed on the data points is the fitted response from a slit detector that was translated across the image of the point source. The empirical resolution function, on-axis, was of the form (Rappaport 1977) :

$$F(r) = C . \frac{e^{-\frac{r^2}{2\sigma^2}}}{r} \qquad (3.1)$$

where $F(r)$ is the radial intensity per unit area and the rms value is given by :

$$(\bar{r^2})^{\frac{1}{2}} = \frac{\int_0^\infty F(r) . r^2 \; 2\pi r \; dr}{\int_0^\infty F(r) . \; 2\pi r . \; dr}$$

$$\therefore \quad (\bar{r^2})^{\frac{1}{2}} = \sigma \qquad (3.2)$$

Plate 3.1   The Wolter I two-nested mirror system.

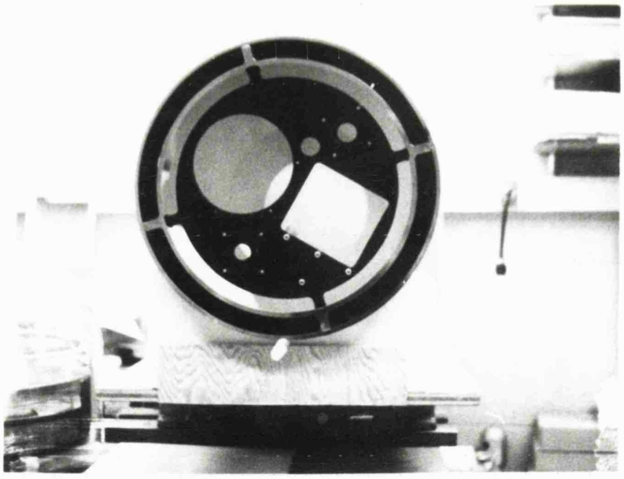

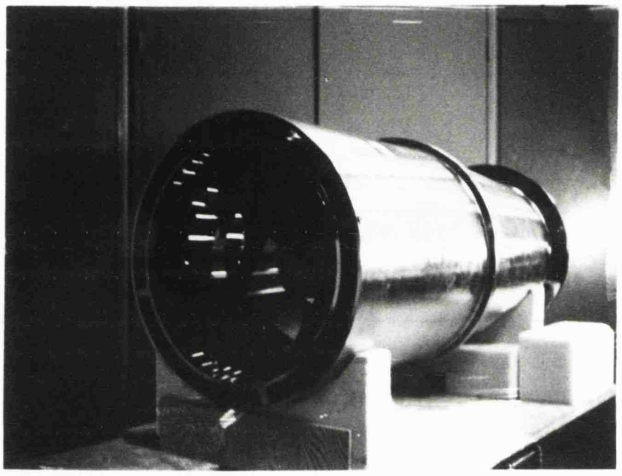

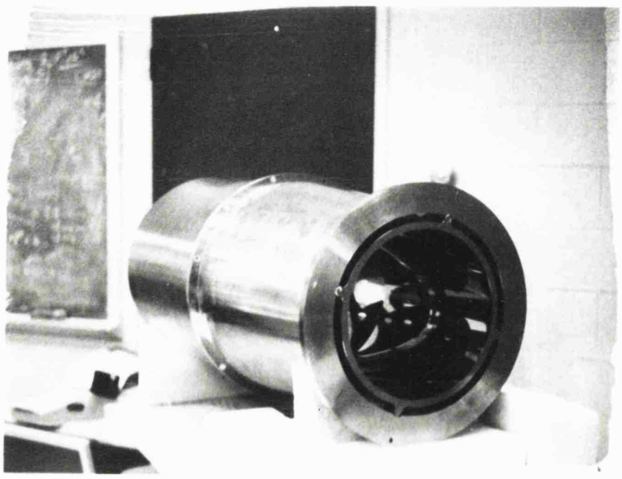

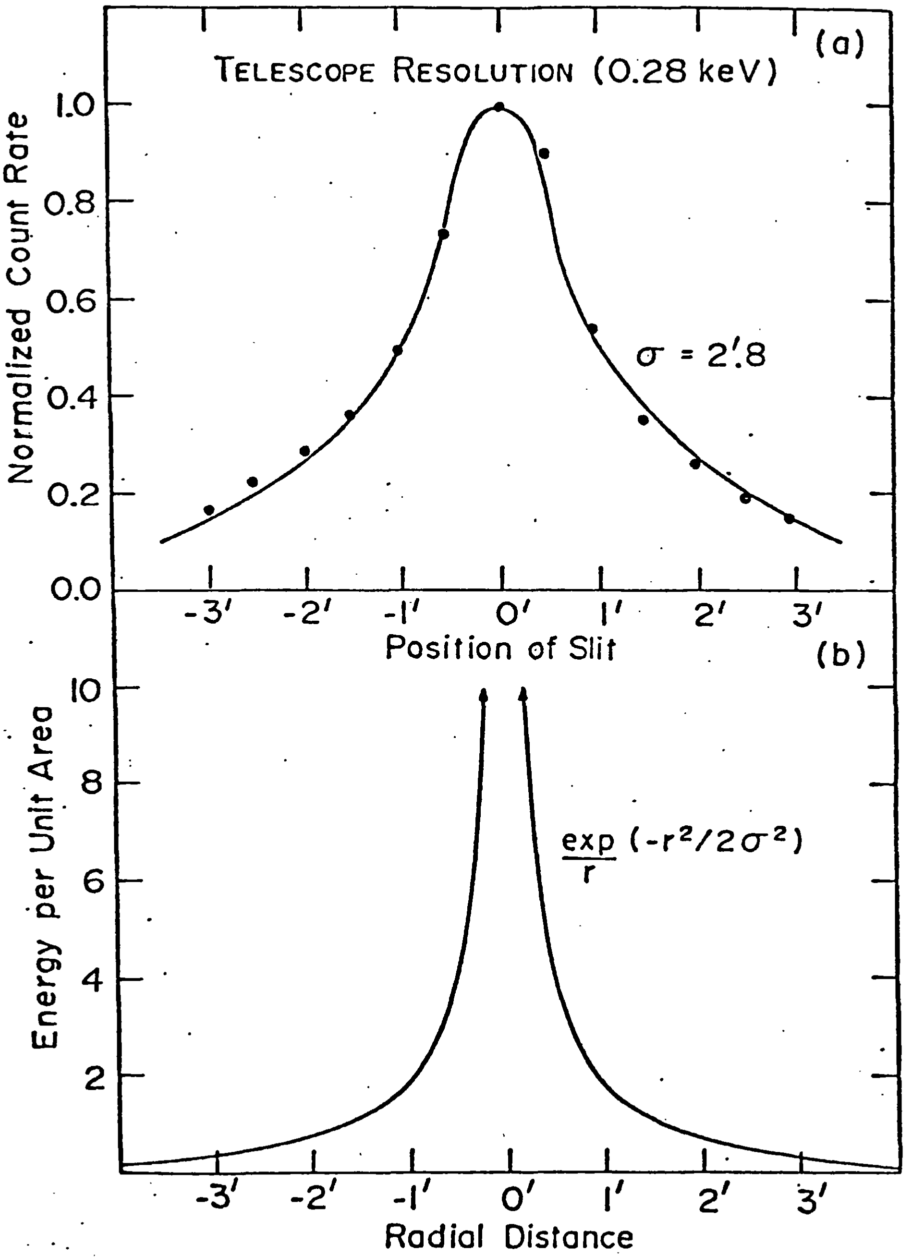

Fig. 3.8. Results of MIT Wolter I system angular resolution measurements.
(Rappaport, Levine and Petre 1977)

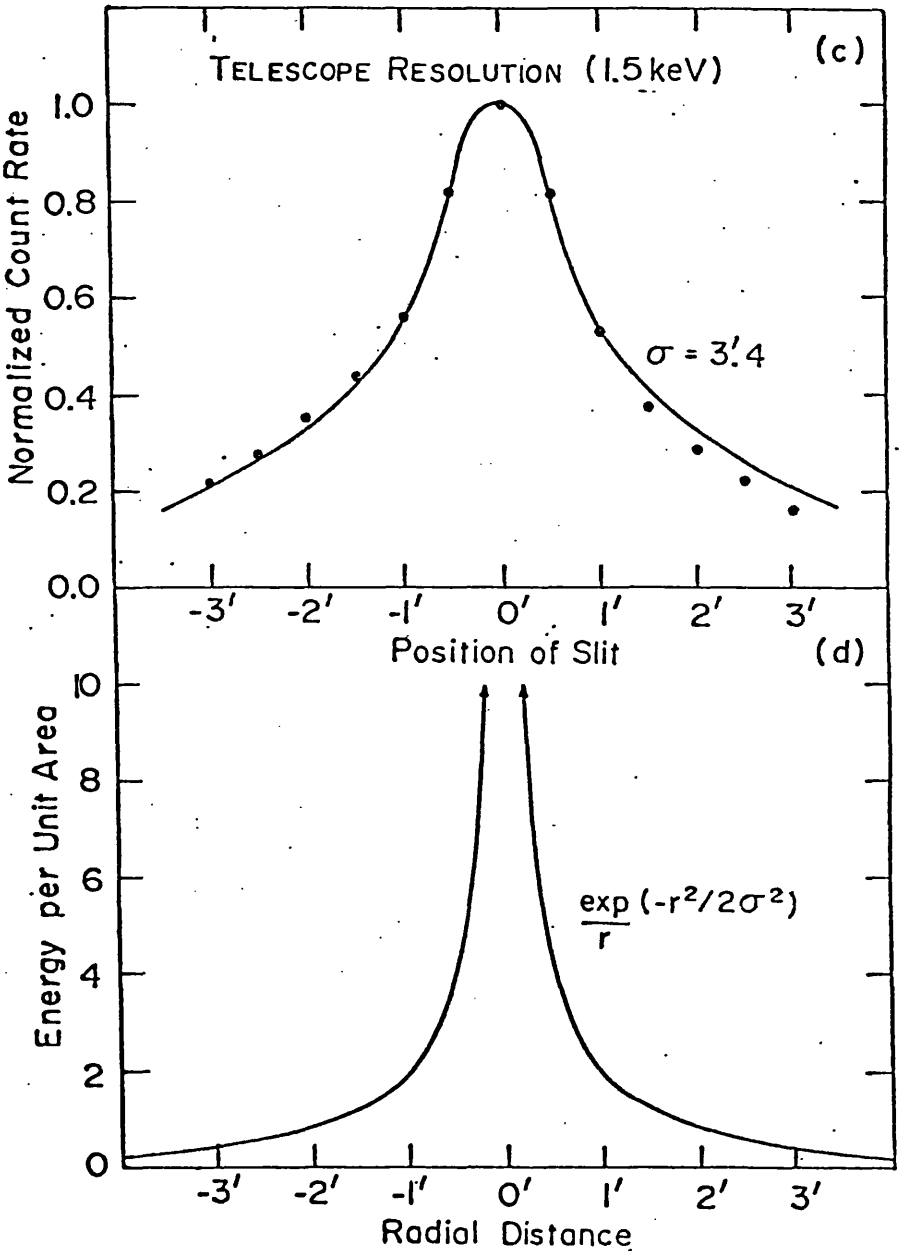

(c)
TELESCOPE RESOLUTION (1.5 keV)
Normalized Count Rate
1.0
0.8
0.6
0.4
0.2
0.0
σ = 3.′4
-3′
-2′
-1′
0′
1′
2′
3′
Position of Slit
(d)
Energy per Unit Area
10
8
6
4
2
0
exp (-r²/2σ²) / r
-3′
-2′
-1′
0′
1′
2′
3′
Radial Distance

Fig. 3.8. cont'd.

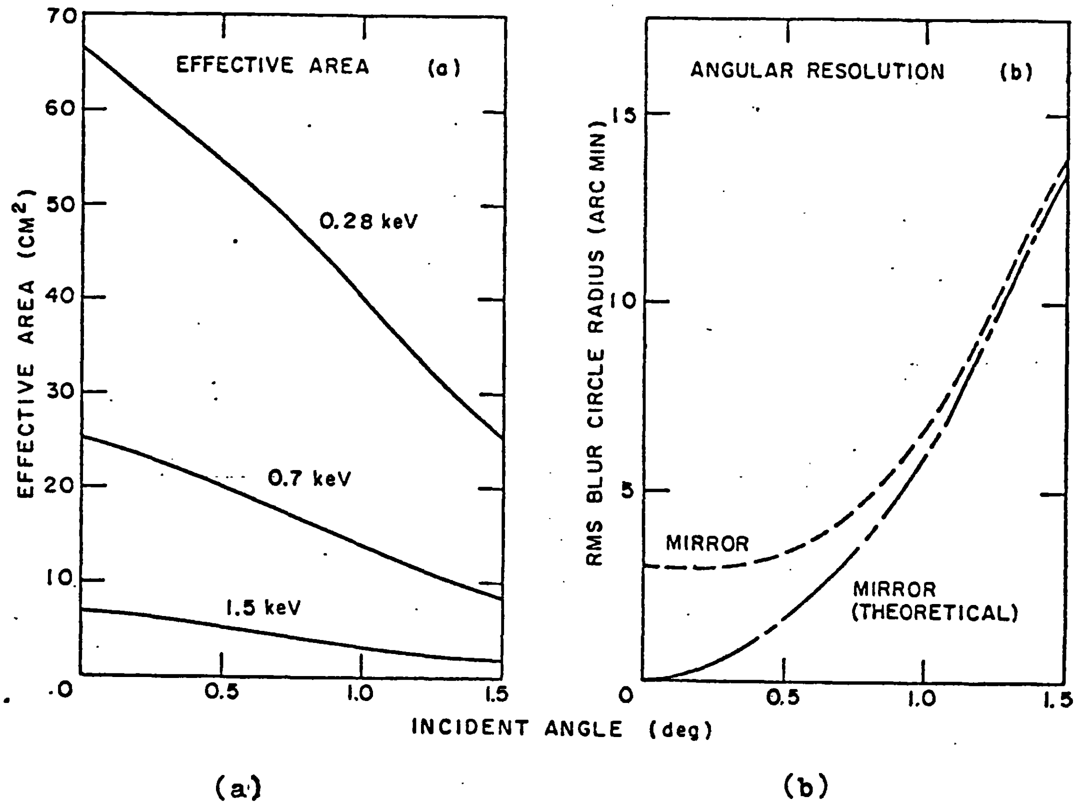

Fig. 3.9. Measured MIT Wolter I system performance.

(a) The overall effective area. The values are convolved with a 1 μ proportional counter window efficiency (~ 70% at .28 keV).

(b) The overall angular resolution with the 3' limit being set by errors of surface figure, leading to zonal aberrations.

In Fig. 3.9, the overall mirror system performance from the A.S and E. measurements, is summarised. The deduced overall reflective efficiences were 36% and 31% of the theoretical curve (Fig. 3.6) at 0.28 keV and 0.7 keV, respectively. The modified N_i efficiency curve has also been plotted in Fig. 3.6.

The overall MIT Wolter I mirror parameters are summarised below, in Table 3.1.

TABLE 3.1

Summary of Wolter I system parameters.

Reflecting surface material	N_i
Focal length	114.3 cm
Focal plane dispersion	3'/mm
Total projected frontal area	$\sim$ 350 cm^2
Effective area (0.28 keV)	$\sim$ 90 cm^2
Maximum glancing angle	2^o
Beam convergence	9^o
Useable field of view	$1.5^o \times 1.5^o$
Angular resolution (0.28 keV, on-axis)	$\sim$ 3' (RMS)

3.3.2 Design and characteristics of the imaging proportional counter (IPC) and associated systems.

The closely approximating aplanatic images, formed by the Wolter I system within a frame size of 6 cm. x 6 cm., were recorded by a two - dimensional, position - sensitive, gas - filled, proportional counter. The advantages on utilising an imaging proportional counter for the envisioned X-ray astronomy experiment would be (Parkes 1974, Gorenstein et al. 1975) :

(1) A high gas gain (10^4 - 10^6) leading to output charges of $\sim$ 10^7 electrons ($\sim$ 1 pC) per photon.

(2) Adaptability, in that the size and shape were variable; and that a large number of anodes and cathodes could be incorporated.

(3) Provided electrical tracking or breakdown were avoided by use of moderate fields, the operation would be noiseless apart from the ambient background radiation. The low capacitance ($\sim$ 10 - 50 pF) between anode and cathode would enable particular use with linear, charge - sensitive preamplifiers at minimum noise characteristics.

(4) An operational lifetime of $\sim$ 10^{10} integrated pulses.

(5) Moderate energy resolution ($\sim$ 45 - 50% FWHM at 0.93 keV) providing some identification of the photon spectrum, when imaging.

(6) Good quantum detection efficiency ($\sim$ 70% at 0.28 keV for a $\sim$ 1μ polypropylene entrance window).

(7) Count rate capability of $\sim$ 10^4 pulses / s. over 1 mm of the anode.

(8) Negligable power consumption.

(9) Good detection area / weight ratio.

Considerations of the main disadvantages would have to include :

(1) The active gas depth and considerations of the track length for the primary photoelectron (perhaps negligable, i.e a 1.5 keV photoelectron has an effective track length of $\sim$ 150μ in argon at STP) and diffusion of secondaries (the jitter of the centroid of the electron cloud, becomes important for X-ray energies, $\varepsilon_X \lesssim$ 0.5 keV) may indicate increased positional uncertainty.

(2) The output charge per photon is proportional to the incident photon energy. A counter operating over an order of magnitude in energy ($\sim$ 0.1 - 1 keV) would give $\sim$ 1/10 the charge at the lower end of the range than it does at the upper end. Thus, the positional resolution may also vary by $\sim$ 10. The counter design

would have to be biased towards the lower energies.

A proportional counter relies for its operation on the localised multiplication of the primary ionization released by the photon to be detected. Different methods for determining the position of the avalanche, in one dimension, were investigated :

(1) By using an electrode (anode) of high resistivity in the detector and observing the amplitude (Kuhlmann et al., 1966, Miller et.al., 1971) or pulse risetime (Borkowski and Kopp 1968).

(2) By using a multi-wire anode in the counter with a separate electronic channel connected to each wire (Charpak et. al., 1968, Charpak et. al., 1970).

For the developments of one - dimensional position sensitive detectors for X-ray astronomy, the pulse risetime sensing method has been particularly utilised, (Smith 1977) but the less flexible pulse amplitude sensing method (charge division) has also been used (Desai and Holt 1972).

Multi - wire proportional chambers (MWPC) were first developed at CERN (Charpak 1970 and references therein) and two - dimensional position sensitive MWPC have since been developed (primarily for particles) (Charpak 1974, Charpak et al., 1978). Borkowski and Kopp (1970, 1972, 1975) first reported the development of a two - dimensional, position sensitive, hard X-ray ($\sim$ 1 - 150 keV) MWPC. The basic elements comprising the imaging proportional counter, are shown in Fig. 3.10. The avalanche centroid position (Borkowski and Kopp 1968) on one anode wire was detected by the positively induced pulses (Charpak et. al., 1970) formed on the orthogonal cathode wire grids above, and below, and capacitively coupled to, the anode grid. The total resistance between each cathode output was R and the total capacitance between each anode and cathode, C . For the signal flow, the cathodes behaved as two, lumped element RC lines. The RC line termination impedances Z_L were rational fraction approximations of the characteristic impedance of the cathode RC lines. The cathode RC lines performed independently and the

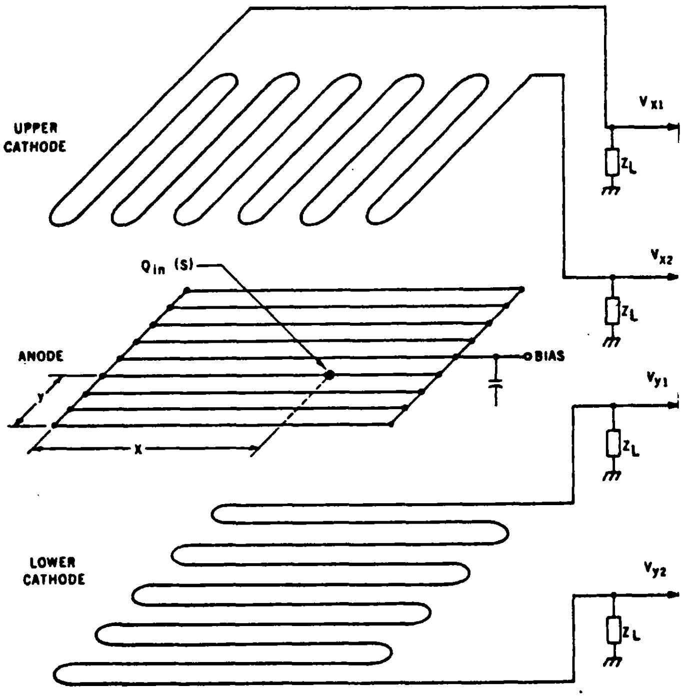

In the following discussion the position-signal flow is described for a single photon detected at a point with coordinates x and y. In the detection process a localized electron avalanche is produced in the vicinity of the anode wire closest to y. The positive ions produced in the avalanche move toward the cathode planes and induce a displacement current in each cathode.

In each cathode the displacement currents divide into two equal parts and flow through portions of the cathode RC lines and through the termination networks to ground. The shapes of the currents in the termination networks and, therefore, the shapes of the voltages V_{x1}, V_{x2}, V_{y1}, and V_{y2} are functions of the length of RC line between the point of induction and cathode output. Therefore, if L is the total length of the cathode RC lines, the shapes of V_{x1} and V_{x2} are proportional to x and L − x, respectively; and the shapes of V_{y1} and V_{y2} are proportional to y and L − y, respectively. The shapes of these voltages are measured by crossover timing.

Fig. 3.10. Electrode configuration for the imaging proportional counter of Borkowski and Kopp (1972).

two signals from each cathode were processed by the pulse risetime position sensing method consisting of pulse shaping and consequent time - difference measurements (Borkowski and Kopp 1970), Fig. 3.11. The signals from each cathode were electrostatically shielded from the other cathode by the anode grid. The output signals from the upper cathode determined the x co-ordinate of α_{in} and the output signals of the lower cathode determined the y co-ordinate of α_{in} .

To determine the position of the avalanche centroid to better than the anode wire spacing, a linear drift field was incorporated in the region above the upper cathode, of Fig. 3.10, to produce large electron clouds of effective diameters extending over several anode wires. In this way, charge sharing between anode wires occurred and enabled displacements of the avalanche centroid, smaller than the anode pitch, to be detected.

The requirements for a space - qualifiable IPC were largely satisfied by the advantages offered by the Borkowski and Kopp stacked electrode grid configuration :

(1) Support of the anode and cathode wire planes by three independent frames (of rigid structure) enable simple constructional procedure.

(2) The frame size would be a variable parameter ensuring removal of any edge distortion in the required image area (6 cm. x 6 cm.)

(3) The distance between the anode and cathode planes would be easily adjustable (using spacers).

(4) The wire spacing of the anode and cathodes could be determined accurately with reference pins.

(5) Only one connection to the anode grid and two electrical connections to each cathode grid would be required (for the timing method).

(6) Assembly / re-assembly time would be short.

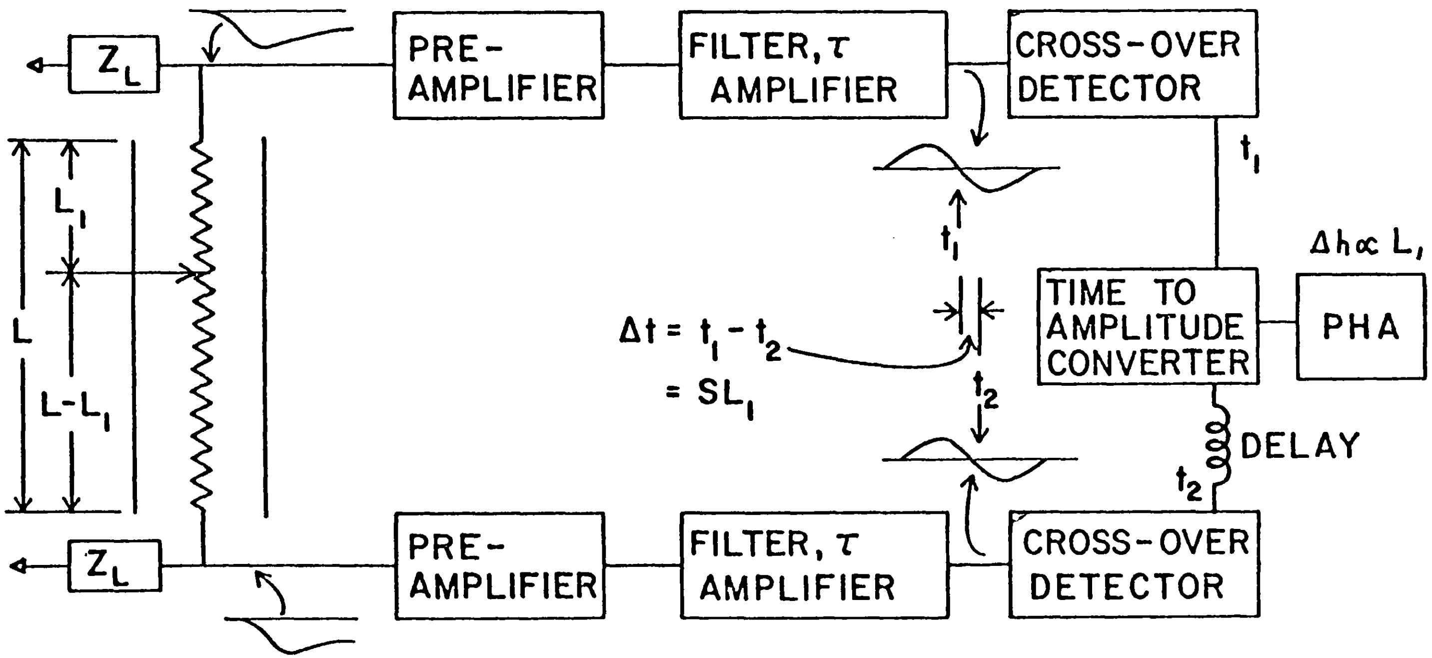

Fig. 3.11. The timing method for position sensing used by Borkowski and Kopp (1968, 1970, 1972) is shown schematically. For each cathode RC line in each axis, the position L_1 of the centroid of the induced pulses was determined from the difference between the cross-over times of the shaped pulses at the two ends of each cathode.

Since the output terminals of the two cathode grids would be interconnected such that the x co-ordinate signals were independent of the y co-ordinate signals then discussion on RC position encoding in an IPC may be reduced to a discussion of two, independent, orthogonal, linear, one - dimensional position sensitive proportional detectors. The one - dimensional, position sensing performance of a capacitively terminated RC line of the form shown in Fig. 3.12 has been studied by Mathieson et. al., (1971, 1974, 1975a, 1975b), in several limiting cases. The results assumed that the electronic noise in the line was the only cause of position uncertainty and that the position decoding networks were limited to RC differentiators and integrators. The effects on position resolution of random processes in the detector (i.e random charge collection time or random electron diffusion) were not considered and hence optimised position decoding filters could not be determined (Nowlin 1976). However, the work of Mathieson et. al., has enabled close optimisation of the encoder RC transmission lines suitable for the required IPC design. In Fig. 3.12, the essential features of the risetime mode system are shown. The line, total resistance R and total capacitance C is terminated at each end with capacitance C_d , used to shunt charge sensitive preamplifiers. The filter systems produce the zero - crossing bipolar pulse. The special case where $S_1 = S_2 = T$ is of special interest, for which the filter circuit has been optimised in signal / noise.

Since electronic noise contributes to the position resolution of such a system, in practise, to obtain acceptable linearity, it is necessary to measure the difference in cross - over times between filter outputs at each end of the line.

For charge q_0 injected at a position $x \leq 1$ along the line, $t(x)$ is the zero - cross time, expressed in units of RC/π^2, of the filter output waveform, $v_0(t)$ (Fig. 3.12). The difference zero - cross time is :

$$T(x) \equiv t(x) - t(1-x) \tag{3.3}$$

and the positional sensitivity :

$$S(x) \equiv \frac{d\,T(x)}{dx} \tag{3.4}$$

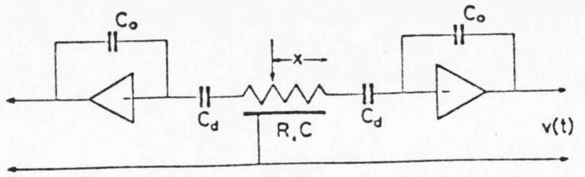

(a)

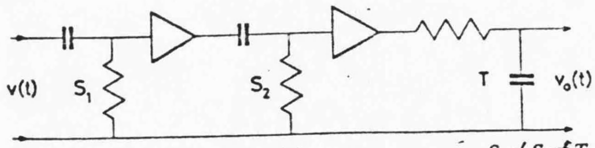

(b) $S_1 \neq S_2 \neq T$.

(a) Transmission line, total resistance R and total capacitance C, symmetrically terminated in capacitance C_d, used as input elements to shunt feedback amplifiers, feedback value C_0. (b) The filter configuration used

For a uniform line of total resistance R and total capacitance C the line propagation constant γ and characteristic impedance Z_0 are given by:

$$\gamma = \pi\sqrt{s},$$

and:

$$Z_0 = R/\pi\sqrt{s},$$

where s is the complex frequency (with time normalised to units of RC/π^2).

Consider the line to be terminated at both ends in capacitance C_d, and suppose that a current impulse $q_0\,\delta(t)$ is injected at fractional distance x from one end. The voltage waveform developed across the near-terminating capacitance C_d is amplified by an amount A_v, say, and shaped with passive, non-interacting, integrating, and doubly differentiating circuits of (normalised) time constants T, S_1, and S_2, respectively. The output signal from this system is then given by:

$$\begin{aligned} v_0(t) = A_v \frac{q_0}{C_d} \sum_{n=0}^{\infty} & \frac{p\cos\pi\alpha_n(1-x) - \alpha_n \sin\pi\alpha_n(1-x)}{\alpha_n(1+p\pi)\sin\pi\alpha_n + [\frac{1}{2}\pi(\alpha_n^2 - p^2) - p]\cos\pi\alpha_n} \times \\ & \times \frac{S_1 S_2 \exp[-\alpha_n^2 t]/\alpha_n^2}{(S_1 - 1/\alpha_n^2)(S_2 - 1/\alpha_n^2)(T - 1/\alpha_n^2)} - \\ & - A_v \frac{q_0}{C_d} \sum_{i=1}^{3} \frac{\sin\pi S_i^{-\frac{1}{2}}(1-x) - pS_i^{\frac{1}{2}}\cos\pi S_i^{-\frac{1}{2}}(1-x)}{(1-p^2 S_i)\sin\pi S_i^{-\frac{1}{2}} - 2pS_i^{\frac{1}{2}}\cos\pi S_i^{-\frac{1}{2}}} \times \\ & \times F_i \exp[-t/S_i], \end{aligned}$$

where:

$$F_1 = \frac{S_1 S_2}{(S_1 - S_2)(S_1 - T)},$$

$$F_2 = \frac{S_1 S_2}{(S_2 - S_1)(S_2 - T)},$$

$$F_3 = \frac{S_1 S_2}{(S_1 - T)(S_2 - T)},$$

$$S_3 = T,$$

$p = C/\pi C_d$ and α_n are the roots of the subsidiary equation:

$$\tan\pi\alpha = 2/(\alpha/p - p/\alpha).$$

Fig. 3.12.

Parameters defining the system performance include δ_x, the rms non - linearity in $T(x)$, and $(\Delta x)_m$, the rms positional uncertainty due to system noise, with the subscript m indicating a mean value taken over a central 85% portion of the line. The position resolution may be determined as follows . The rms voltage fluctuation Δv_0 in the output waveform $v_0(t)$ due to the noise in the system results in uncertainty in the cross - over times

$$\Delta t(x) = \frac{\Delta v_0}{g(x)} \tag{3.5}$$

where $g(x)$ is the negative scope at cross - over. Neglecting correlation between the two noise outputs (which may have a non - negligable effect - the correlation coefficient is at present being investigated, Evans 1978) the mean square fluctuation in difference cross - over time, $T(x)$ is

$$\Delta^2 T(x) = \Delta^2 v_0 \left\{ \frac{1}{g^2(x)} + \frac{1}{g^2(1-x)} \right\} \tag{3.6}$$

The rms uncertainty in position determination due to electronic noise is then

$$\Delta x = \frac{\Delta T(x)}{S(x)} = \frac{\Delta v_0 \left\{ \frac{1}{g^2(x)} + \frac{1}{g^2(1-x)} \right\}^{\frac{1}{2}}}{S(x)} \tag{3.7}$$

Referring the system noise to the line termination, if q_n/C_d is the voltage step which, when applied to the line termination yields an output pulse of height equal to the rms noise, then

$$\Delta v_0 = 0.231 \frac{A_V q_n}{C_d} \tag{3.8}$$

where A_V is the voltage gain of the system and the factor 0.231 is the amplitude response to a unit step function of a passive CR - RC - CR filter. Since $v_0(t)$ and hence $g(x)$ can be expressed with $A_V q_0/C_d$ as a factor, then from (3.7) it follows that Δx normalised with respect to signal / noise ratio can be calculated from the form for $v_0(t)$, without reference to the specific origin of system noise.

$$\Delta x \, q_0/q_n \quad \equiv \quad D\left(x, T, \; C_d/C\right) \tag{3.9}$$

The quantity $D = \frac{0.231}{S(x)}\left\{\frac{1}{g^2(x)} + \frac{1}{g^2(1-x)}\right\}^{\frac{1}{2}}$ is a dimensionless resolution parameter (of general application to linear imaging systems). $D_m \equiv (\Delta x)_m \; q_0/q_n$ is the mean value over a central portion of the line and is a function of T and C_d/C only. For small values of C_d/C, $D \sim C_d/C$ and when $D_m . C_d/C$ is plotted against T, a minimum occurs for $T \sim 0.5 - 2$ (Mathieson et. al., 1975).

The total system noise is the resultant of the two (uncorrelated) components, q_l (line noise) and q_a (amplifier noise) :

$$q_n^2 \quad = \quad q_l^2 \; + \; q_a^2 \tag{3.10}$$

The formal expression for q_l has been given (Mathieson 1971, Mathieson et. al., 1975) :

$$q_l \quad = \quad C^{\frac{1}{2}}\left(kT_e\right)^{\frac{1}{2}} \mu\left(T, \; C_d/C\right) \tag{3.11}$$

where μ is a dimensionless line noise parameter and $\mu \sim C_d/C$
The form for μ is :

$$\mu = \frac{C_d/C}{0.231}\left\{2\pi \int_0^1 \int_0^\infty \left|H(i\omega')\right|^2 \left|P(x,\omega')\right|^2 d\omega' dx\right\}^2$$

where

$$P(x,\omega') = \frac{\cosh \gamma'(1-x) + 3_d \sinh \gamma'(1-x)}{2\cosh \gamma' + \left(3_d + 1/3_d\right) \sinh \gamma'}$$

$$3_d = \frac{1}{\gamma' . C_d/C} \qquad ; \qquad \gamma' = \pi\sqrt{i\omega'}$$

and for a double differintiating, singly integrating filter of time constants equal to T the filter response is :

$$\left|H(i\omega')\right|^2 \; = \; \frac{(\omega' T)^4}{\left\{1 + (\omega' T)^2\right\}^3}$$

$$\omega' = \omega/(Rc/\pi^2)$$

Then the rms position resolution is given by :

$$\Delta x = \frac{D}{q_0}\left\{ kT_e . C \mu^2 + q_a^2 \right\}^{\frac{1}{2}} \qquad (3.12)$$

and the mean uncertainty over 85% of the line is :

$$(\Delta x)_m = \frac{D_m}{q_0}\left\{ kT_e . C \mu^2 + q_a^2 \right\}^{\frac{1}{2}} \qquad (3.13)$$

The limiting cases considered by Mathieson et. al., (1974, 1975a, 1975b) for C finite, non - zero, involved the short - circuit case, $C_d \rightarrow \infty$, the open - circuit case, $C_d \rightarrow 0$, together with the charge equilibrium case, C_d finite, non - zero and $C \rightarrow 0$. In all cases, for near - coincident minima in non - linearity δx and position uncertainty $(\Delta x)_m$, $T \sim 1-2$. The open circuit and charge equilibrium cases produce the smallest values of δx ($\sim$ 0.1%) and $(\Delta x)_m$ ($\sim$ 0.1% RMS of the line length) with a reduced degradation in $(\Delta x)_m$ towards the ends of the line.

In practise, the design of the IPC RC line was influenced by prior, preliminary investigations of the case $C_d \sim C$, in the context of the above discussion, indicating further reduction in δx and $(\Delta x)_m$, with $T \sim 1$, for the respective minima. For the IPC position processing electronics, a filter centre frequency corresponding to $T_a = 2 \mu s$ was chosen, thus determining the position sensitivity of the cathode RC lines. Each cathode grid resistance R was chosen to be $R = 50 K\Omega$. With the T_a and R values set, the values of C_d and hence the RC line performance parameters $T(x)$, $S(x)$, δx and $(\Delta x)_m$ could be determined, once the distributed line capacitance C was measured.

The cathode RC lines and anode grids constructed for the IPC are shown in Plate 3.2. Each cathode grid contained 90 wires, separated 1mm (the non - accumulated error was 89 $\pm$ 0.1mm) and each, 10 cm in length. A thick film resistance strip, deposited on ceramic cards (EMI, Hayes Middlesex) and in contact with the electro - deposited finger strips upon which the wires were soldered, provided a wire resistivity of 5.6 Ω /mm. The ceramic (96% alumina ceramic) cards were epoxyed onto fibre - glass (G10 fibre - glass, epoxy laminated)

Plate 3.2 The IPC anode grid (top) and the cathode RC transmission line, one of two used for position sensing the centroid of each avalanche occurring in the anode plane.

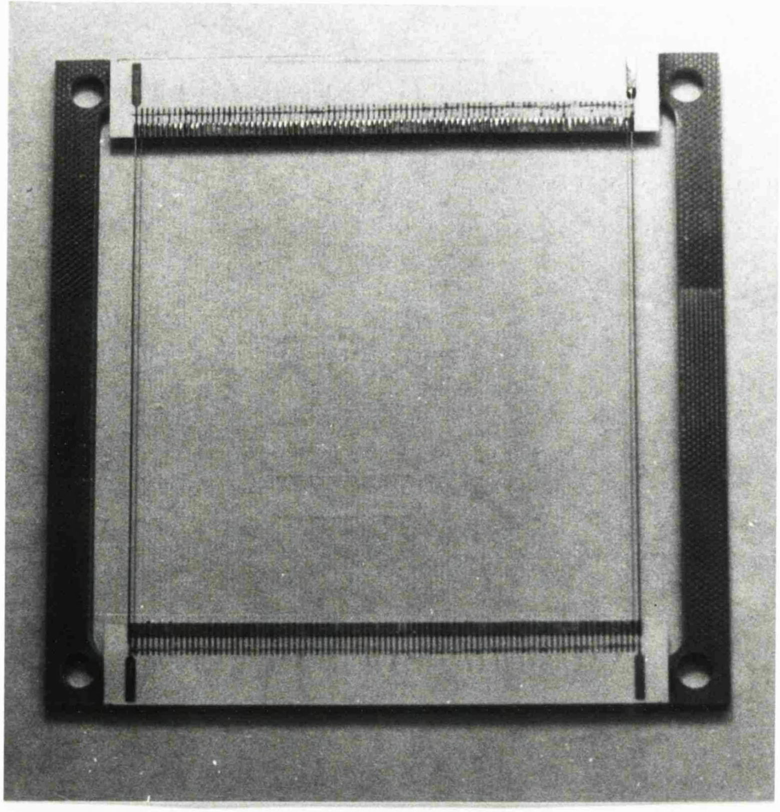

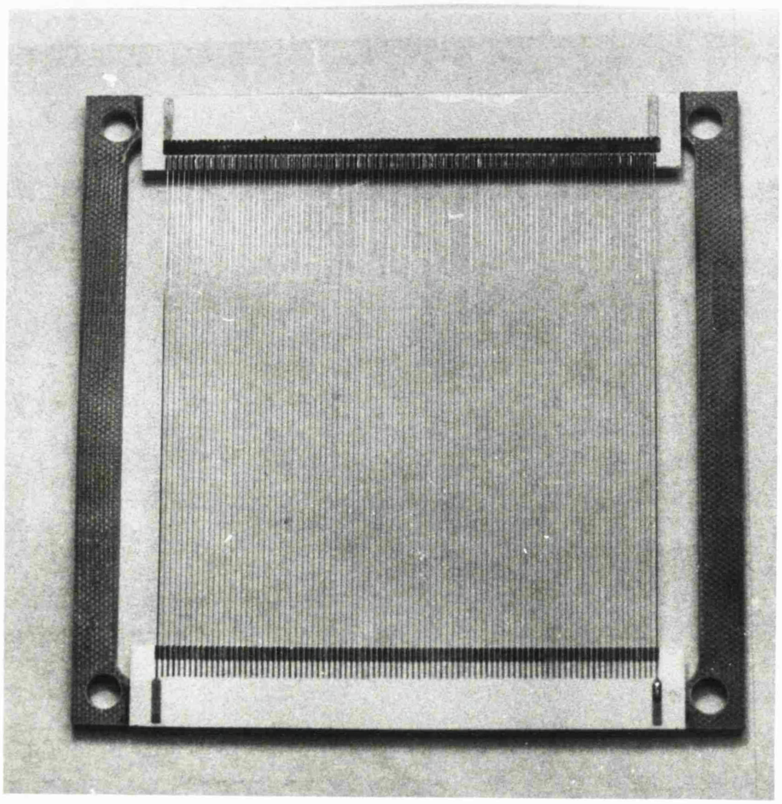

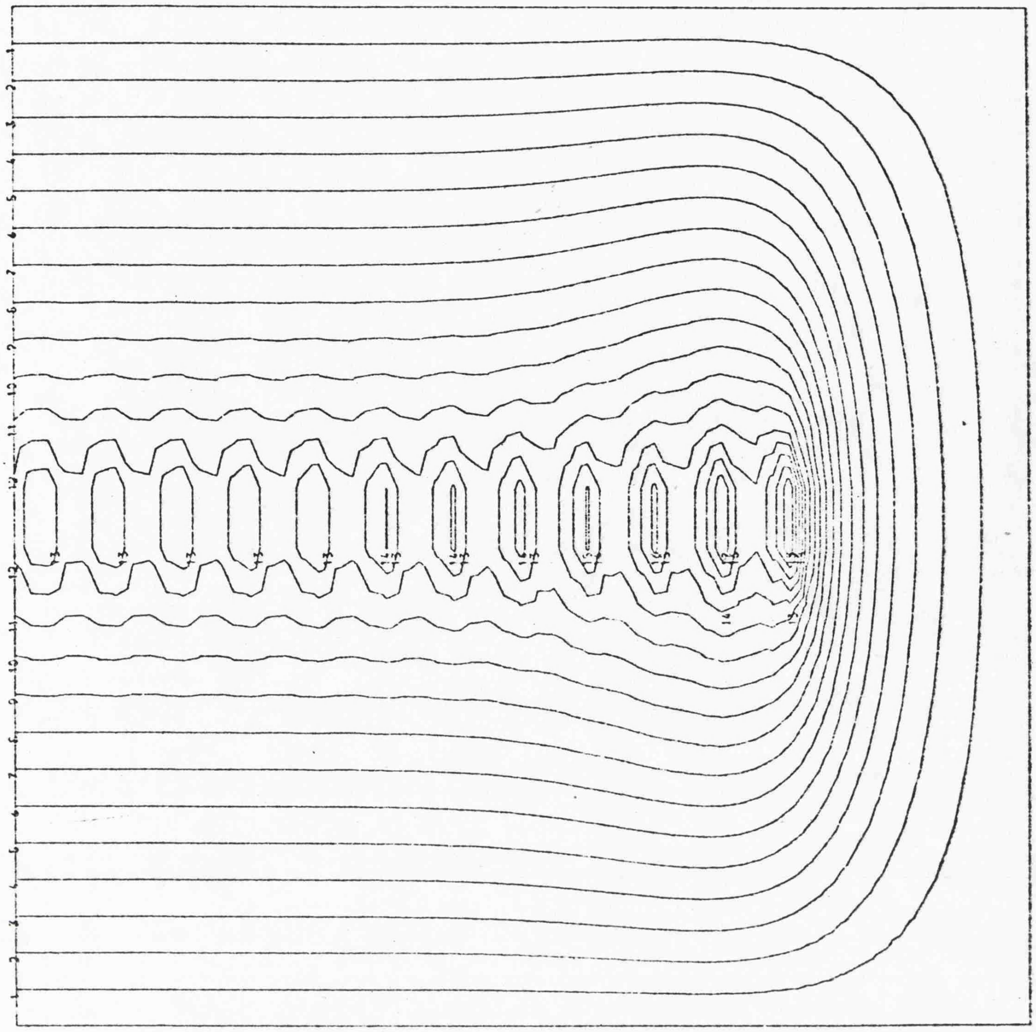

Fig. 3.13 Electric field configuration of the anode grid. The decrease in field strength towards the edge due to successively larger diameter wires is shown.

frame. The resist strip cards were produced having values $50 \pm 0.7\ K\Omega$. The cathode Cu-Be wires (Goodfellow Metals Ltd, Cambridge) were $125\,\mu$ in diameter and connected through the resist strip at one end.

The anode grid contained 45 wires, separated by 2 mm, each 10 cm. long. The wires were shorted on one ceramic card. The high voltage plane consisted of 37 x $15\,\mu$ diameter Au-plated tungsten wires (Lumas, Vic Steels, London) with successively larger diameter wires moderating the electric field around the anode grid edge, (Fig. 3.13).

All the sets of wire grids were z-wound on a wire winding rig which could accommodate both 1 mm. and 2 mm. pitch planes, over 20 cm. in width. Tension was applied to each wire uniformly through gas pressurised pistons to which reference pins at one end were connected. For mechanical stability against electrostatic forces, and hence for spark-free operation, the anode wire tensile force had to satisfy the relation (Trippe 1969) :

$$T_w > 1.1 \times 10^{-8} \left\{ \frac{V \ell}{2\pi L} \right\}^2 \text{ grm. wt.} \qquad (3.14)$$

where ℓ is the wire length, L the anode - cathode spacing and V the anode voltage. For V = 4 KV, ℓ = 10 cm. and L = 0.4 cm, $T_w \gtrsim$ 3 grm. wt.

The complete design of the IPC is presented in Fig. 3.14 and Fig. 3.15, and comprised the following features :

(1) For significant soft X-ray flux, the IPC window was $\sim 1\,\mu$ polypropylene, facilitating the use of a replenishing gas supply to overcome the gas effusion through the window. The IPC was positioned over a gas pack enabling gas flow (A) at a constant rate.

(2) The linear drift region (B) was directly below the entrance window. The drift depth was chosen to be 2.5 cm. by optimising the effective absorption depth for high detection efficiency for $\varepsilon_x < 1$ keV and length required to drift secondary electron clouds to form effective

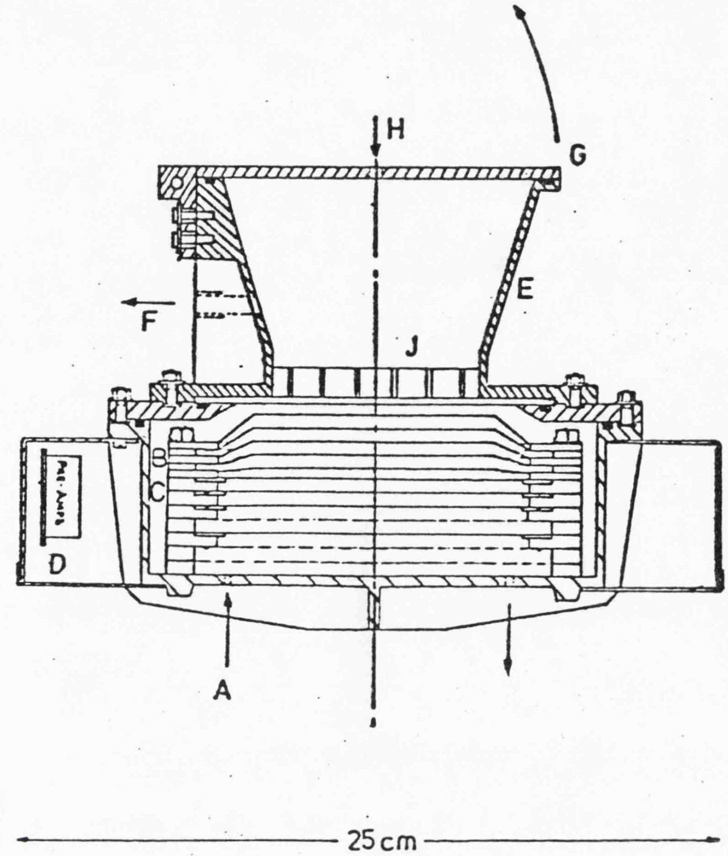

Fig. 3.14. Mechanical design of the IPC.

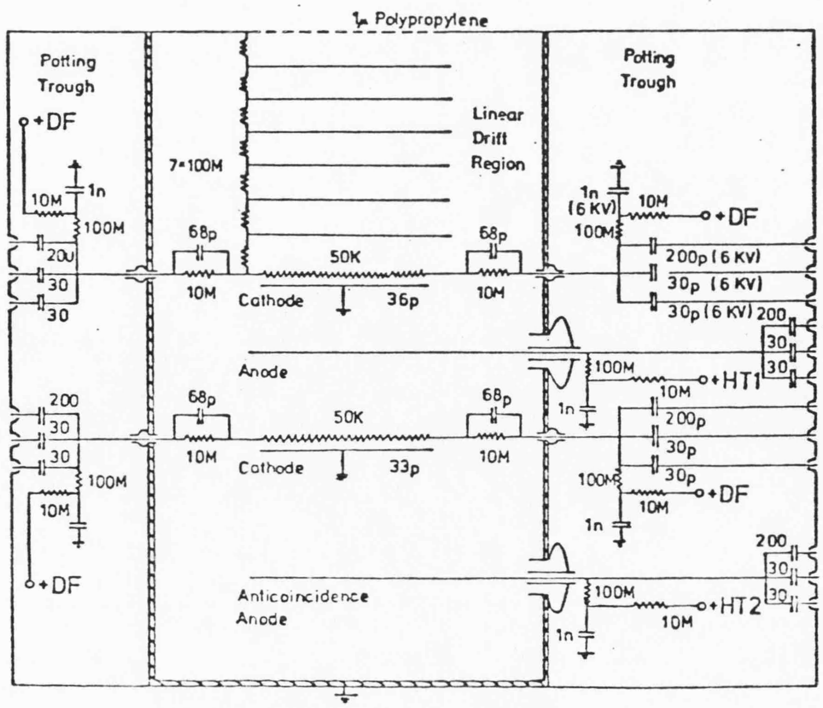

Fig. 3.15. Detail of high voltage filter circuits and low voltage signal circuits.

diameters of several mm. (for negligable charge centroid jitter). For X-ray, $\varepsilon_X \sim 0.5$ keV converging at 9° off the mirror, the 1/e depth in argon would give a lateral spread $<$ 0.1 mm. The effective diameter of the consequent electron cloud, after drifting h in time t is given by (Huxley and Compton 1974, Palladino and Sadoulet 1975) :

$$d_{eff} = 6 \cdot \{ 2 D t \}^{\frac{1}{2}} \qquad (3.15)$$

assuming a Maxwellian distribution of electron velocities, D is the electron lateral diffusion coefficient and if η is the characteristic energy

$$\frac{D}{\mu} = \eta \cdot \frac{kT}{e}$$

where k is Boltzmann's constant, T is the gas temperature and μ is the electron mobility. For a linear field E, the electron drift velocity w is :

$$w = \mu E$$

Thus, $D = \eta \left(\frac{kT}{e}\right) \frac{w}{E}$ and $t = \frac{h}{w}$ then

$$d_{eff} = 6 \left\{ \frac{2h}{E} \left(\frac{kT}{e} \right) \eta \right\}^{\frac{1}{2}}$$

$$\therefore \quad d_{eff.} = 13.4 \left\{ \frac{h}{E} \eta \right\}^{\frac{1}{2}} \text{ mm.} \qquad (3.16)$$

where $[h]$ is cm. and $[E]$ is V/cm. Hough (1972) presented an approximate method for calculating $\eta = \eta(E)$ for A/CH_4 gas mixtures (10% - 85% CH_4) using the electron diffusion data of Cochran and Forrester (1962), Cottrell and Walker (1965) and English and Hanna (1953). Direct measurements were made on $\eta = \eta(E)$ for propane by Cottrell and Walker (1967). From a series of gas physics studies in drift chambers, the gas mix A/CH_4 : 25% / 75% was chosen for the IPC to maximise both $d_{eff.}$ (hence position determination of the avalanche centroid) and

X-ray energy resolution ($\sim$ 50% FWHM (0.93 keV) for A/CH_4 : 25% / 75% compared with $\sim$ 86% FWHM (0.93 keV) for A/CH_4 : 90% / 10%) for constant h = 2.5 cm. For A/CH_4 : 25% / 75%, for $E \sim$ 76 V/cm - 300 V/cm, $\eta \sim$ 2.2 - 5.5 giving $d_{eff} \sim$ 3.6 - 2.7 mm.

The jitter of the centroid of the diffusing cloud would ultimately limit the IPC position resolution. The statistical uncertainty in the mean position of the cloud centroid is given by :

$$\sigma_m = \frac{\{2Dt\}^{\frac{1}{2}}}{\sqrt{n}} = \frac{d_{eff.}}{6\sqrt{n}} \qquad (3.17)$$

where $n = \varepsilon_x / w_i$ with w_i , the mean energy per ion pair, and generally, $n \sim$ 35 - 45 e^-/keV. Hence, for $\varepsilon_X \lesssim$ 0.28 keV, $\sigma_m \sim 200\mu$.

(3) The stacked grids were positioned as shown in Fig. 3.15, region (C). Each fibre-glass frame was 4 mm. thick, for the anode and cathodes, giving L = 4 mm. An anode of pitch 9 mm. was placed below (C) to act as a counter in geometrical anti-coincidence with the first anode.

Electrical connections from the anode and cathodes ran through the pressure shell via glass-to-metal seals, to (D), the potting trough, containing the high voltage filters and preamplifier inputs. In this way the preamplifier leads were as short as possible to reduce stray capacitance (i.e a load impedance tending to increase the signal processing time). Fig. 3.15 shows the complete wiring configuration. With the anodes and cathodes positioned as shown, the cathode distributed capacitance C was measured in situ (with the anode grid earthed), and a value $C \sim$ 30 pF found. Hence, $T = T_a/(RC/\pi^2)$ = 13.2 and a preferred value of C_d = 68 pF was used, to limit the maximum difference in cross-over times to $\sim$ $3\mu s$. The relatively large value of T ensured that any further shaping within the preamplifiers or cables would have no effect on each RC line resolution, since $(\Delta x)_m$ only slowly varies with increasing T , away from the minima near $T \sim 1 - 2$. The predicted behavior of each cathode RC position sensing line is summarised in Fig. 3.16 (Fraser 1978), which graphs the zero-cross times $t(x)$, difference zero-cross time $T(x)$, the gradient at zero-cross $g(x)$ and sensitivity $S(x)$, for a central 85% ($0.0725 < x < 0.925$). Over the central 6 cm. of the line ($0.2 < x < 0.8$), the rms non-linearity $\delta x \leqslant 0.1\%$ and $\overline{S(x)} = 4 = 61$ ns/mm. A comparable value of positional sensitivity of 41 ns/mm had been previously measured for each cathode line. Measurements of q_a for the preamplifiers enabled a value for $(\Delta x)_m$ to be calculated below.

(4) The window section (E), Fig. 3.14, of the IPC comprised an evacuated cone (with vacuum line (F)) with a spring loaded lid (G). Prior to launch of the experiment, the cone section (E) would be evacuated and when sufficient altitude had been reached, the lid (G) would open to admit X-rays to the IPC. The section (E) would serve to protect the fragile window during launch. Directly before launch, X-ray calibration of the IPC would be observed using a Po^{210} AL-K X-ray (1.49 keV) fluorescent source at (H). The source geometry is shown in Fig. 3.17. The window support (J) consisted of 1 cm. ribbed sections, spaced 11.3 mm. apart. Directly below was a fine woven tungsten mesh 80 lines / inch (Buckby Mears Co., U.S) having optical transparancy $\sim$ 86%. Mounted on the same frame was a $\sim$ 1μ polypropylene window (Hayakawa et. al., 1970), $(C_3H_6)_n$ (no O-K edge), which had been biaxially stretched from $\sim$ 25μ unorientated sheet (to give a maximum thickness variations of $\sim$ 20% over an area $\sim$ 300 cm^2), then coated, using a dipping technique (Backmann 1977), with carbon solution (Dag 154 + Isopropanol, 1 : 10 PBW). Consistent thicknesses of 14 μg/cm^2 could be produced, giving consequent reduced UV (1216 A) transmission $\sim$ 0.002 (with $\sim$ 13.5% transmission for white light).

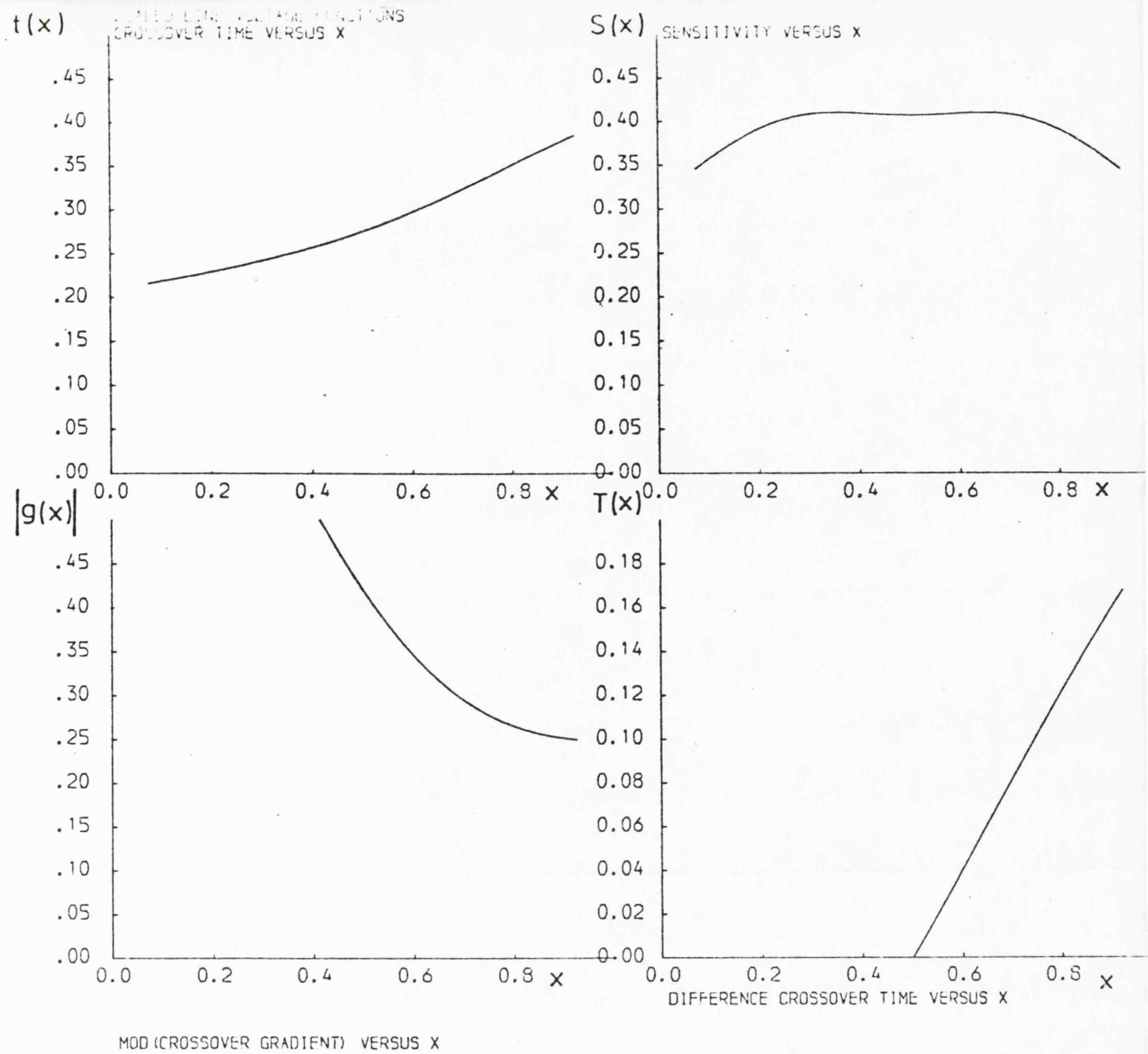

Fig. 3.16. Predicted characteristics of the IPC cathode RC lines for $T_a = 2\mu s$, $C_d = 68pF$, $C = 30pF$, $R = 50K\Omega$.

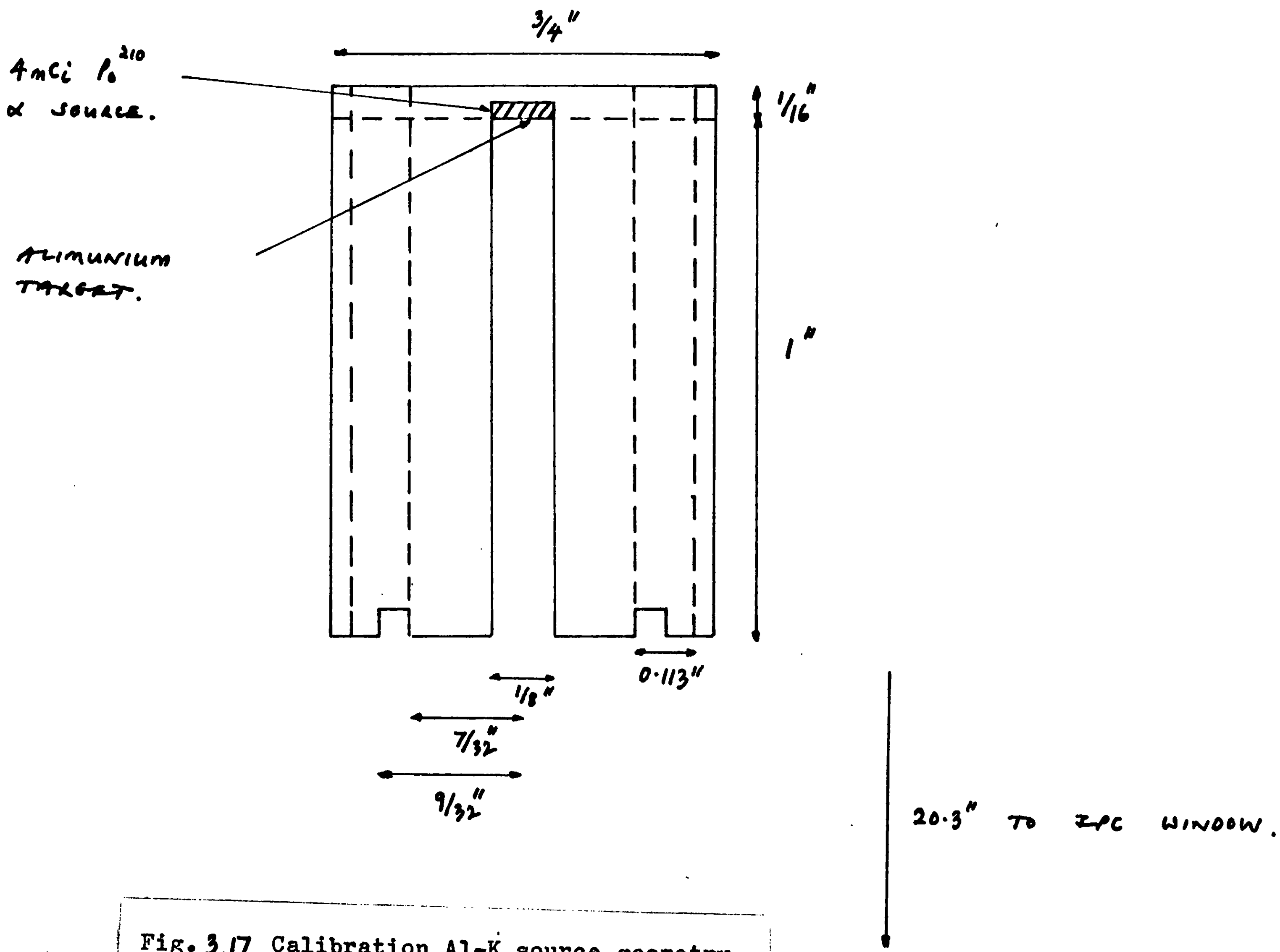

Fig. 3.17. Calibration Al-K source geometry.

(5) The charge sensitive preamplifiers were connected as shown in Fig. 3.18 and a circuit diagram, based on a design by Blalock (1965) is shown in Fig. 3.19. The preamplifier risetime was ~ 50ns , fall-time ~ 100 μs with recovery time ~ 1.5ms. Input capacitance was $<$ 20 pF, output impedance ~ 100 Ω . With the series resistor and two shunt diodes connected for protection against high voltage transient, the equivalent noise charge was measured to be ~ 350 electrons, on average.

Except for input pulse polarity, the same preamplifiers were used with the negative pulses from the anode and anti-coincidence anode and the positive pulses from the cathodes. The preamplifiers were trimmed to give charge conversion gains of 1V/pC (Fig. 3.20). Plate 3.3 shows detail of the linear drift field electrode system, which had an internal area 7 cm. x 7 cm, so that electric field irregularities around the edges, extending to $<$ 1 mm. inwards, were outside the image frame of 6 cm. x 6 cm. Also shown is the stacked grid electrode configuration. The upper cathode was orthogonal to both the anode and cathode grids. The ceramic insulators and spacers are clearly seen at each corner. Connections were made as shown, from the ceramic strip edge fingers, through the glass-to-metal seals to the preamplifier inputs. Plate 3.4 shown the layout of the high voltage (6KV) seals and filters, in the IPC potting troughs. A comparison has been given between the cathode seals (~ 2KV) and the anode seals (~ 6KV) with increased surface area against tracking. Plate 3.5 shows the method of mounting the preamplifiers around the potting troughs, to shorten the signal cable length. The preamplifiers were easily demountable. Table 3.2 summarises the constructional details of the IPC. The IPC was internally coated with N_i to further reduce UV flux.

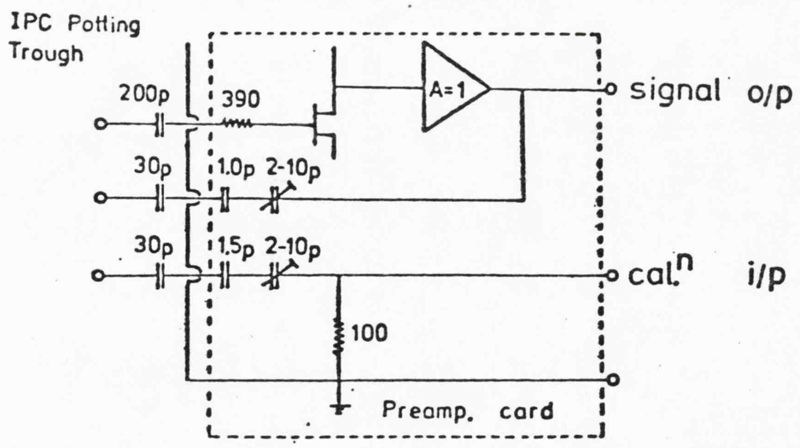

Fig. 3.18. Preamplifier card connections (see Plate 3.5)

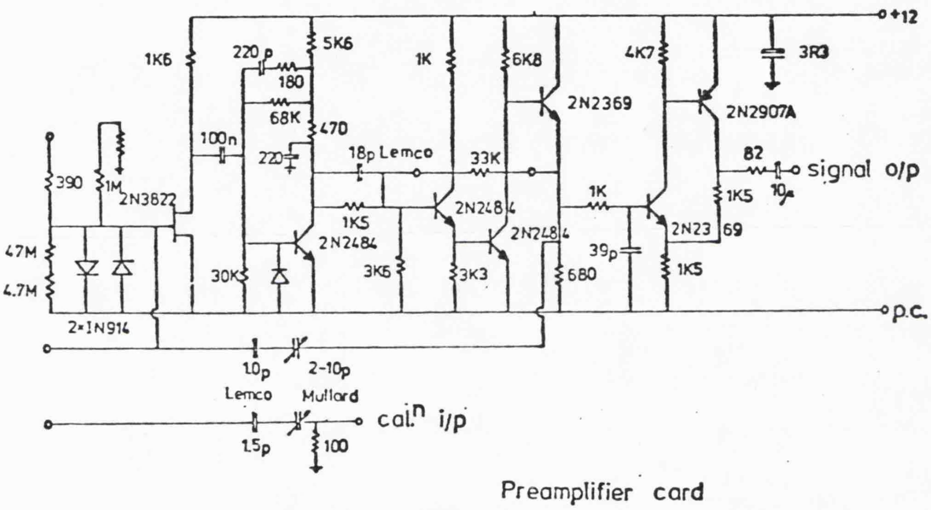

Fig. 3.19. Anode/cathode charge sensitive preamplifiers (with biassing according to input pulse polarity).

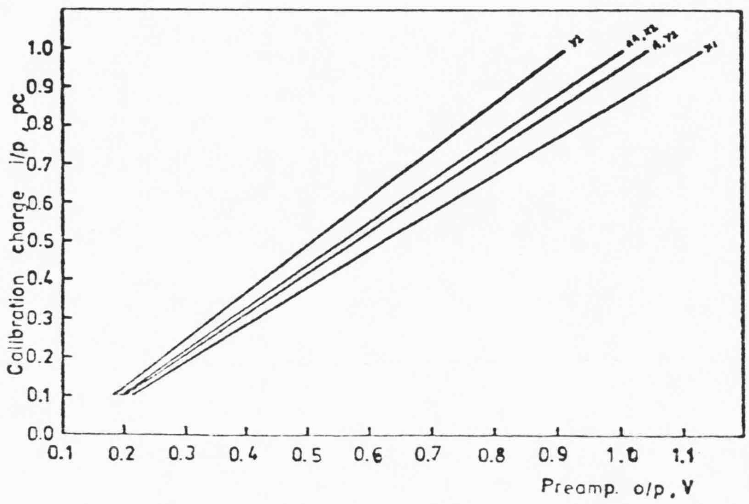

Fig. 3.20. Linearity of preamplifier conversion gains.

Plate 3.3 The drift field electrode configuration (top) used in the IPC.

The configuration of the cathode and anode wire grids within the IPC (bottom). The upper cathode RC line was orthogonal to the anode and lower cathode RC line.

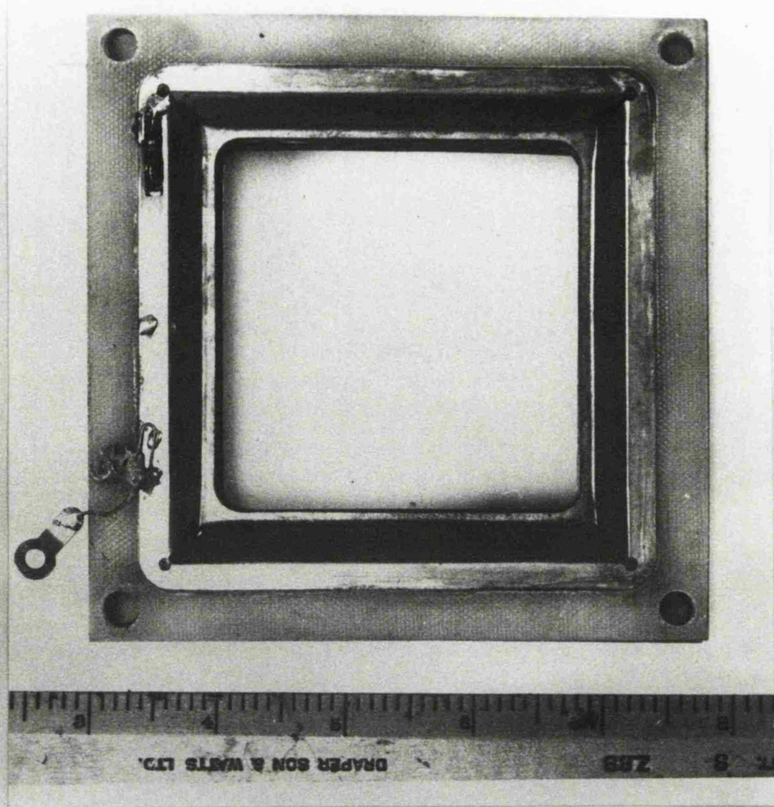
DRAPER SON & WATTS LTD.

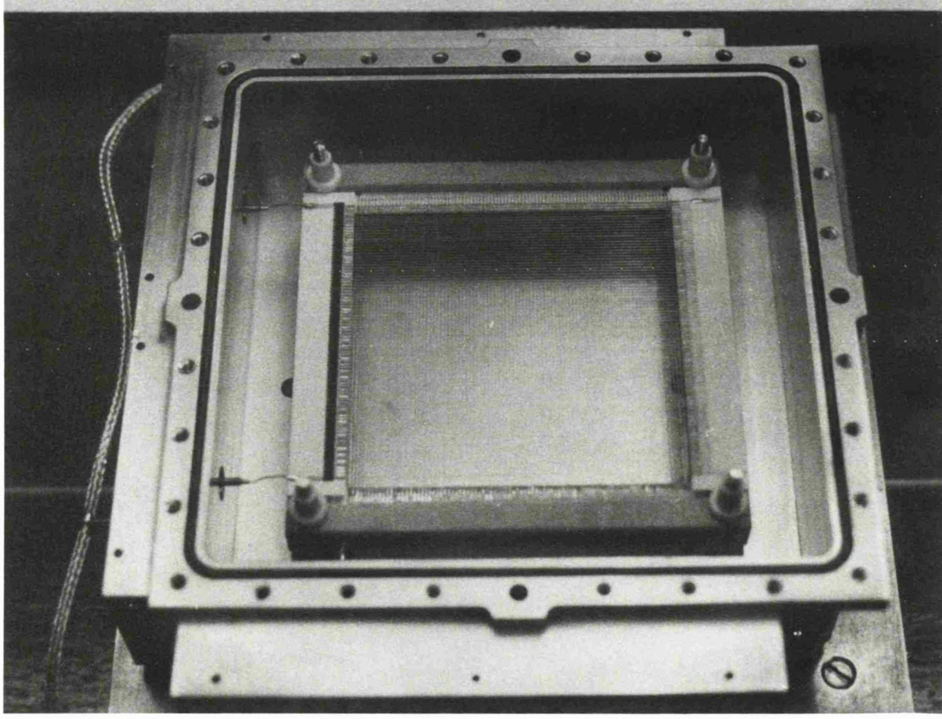

Plate 3.4 Detail of the high voltage filter layout within the potting troughs of the IPC (top).

Comparison between the glass-to-metal seals uesd for the cathode (left) and anode (right) signals.

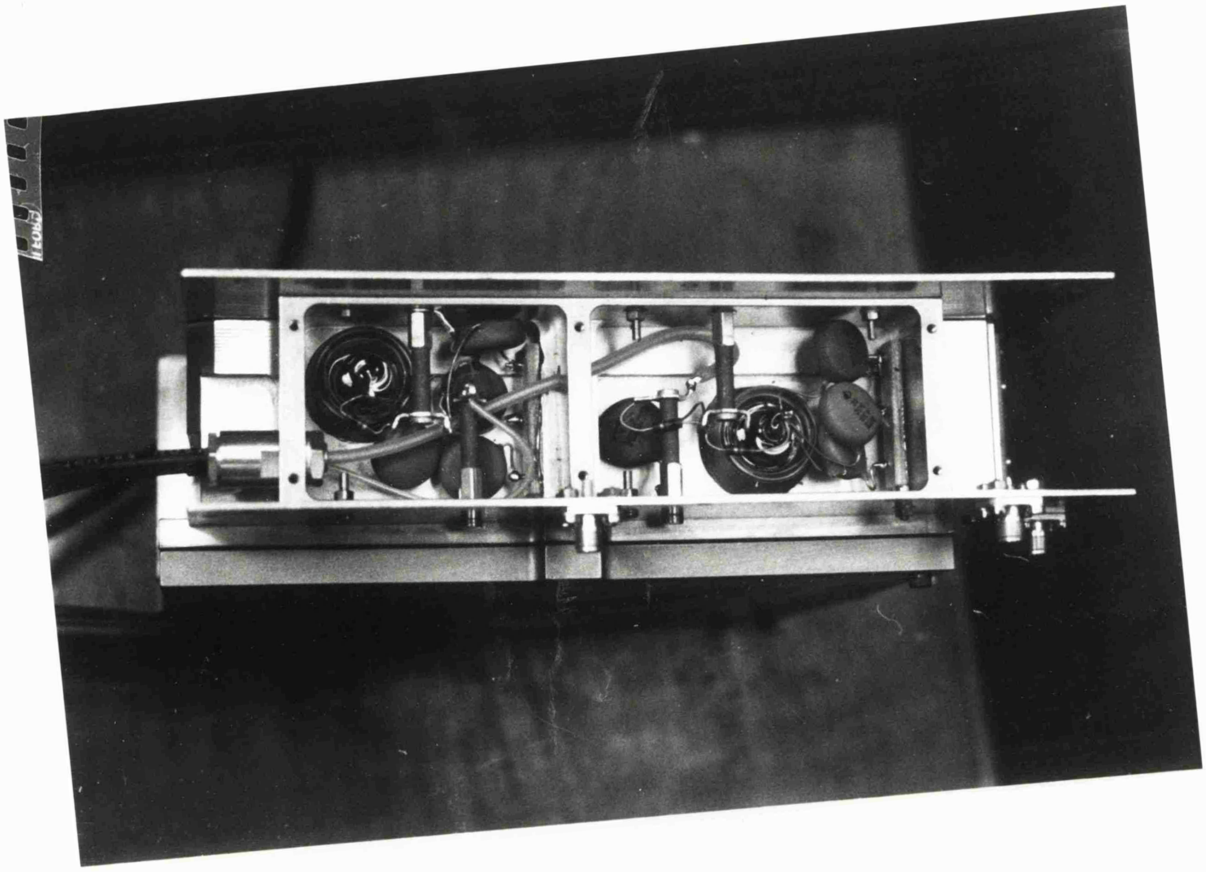

Plate 3.5 Detail of the method used to mount the IPC preamplifiers.

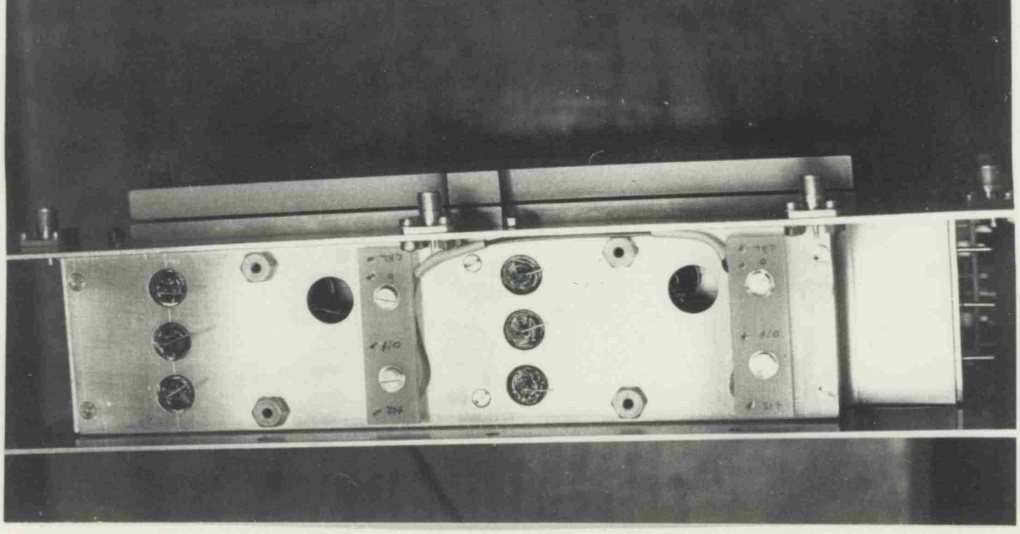

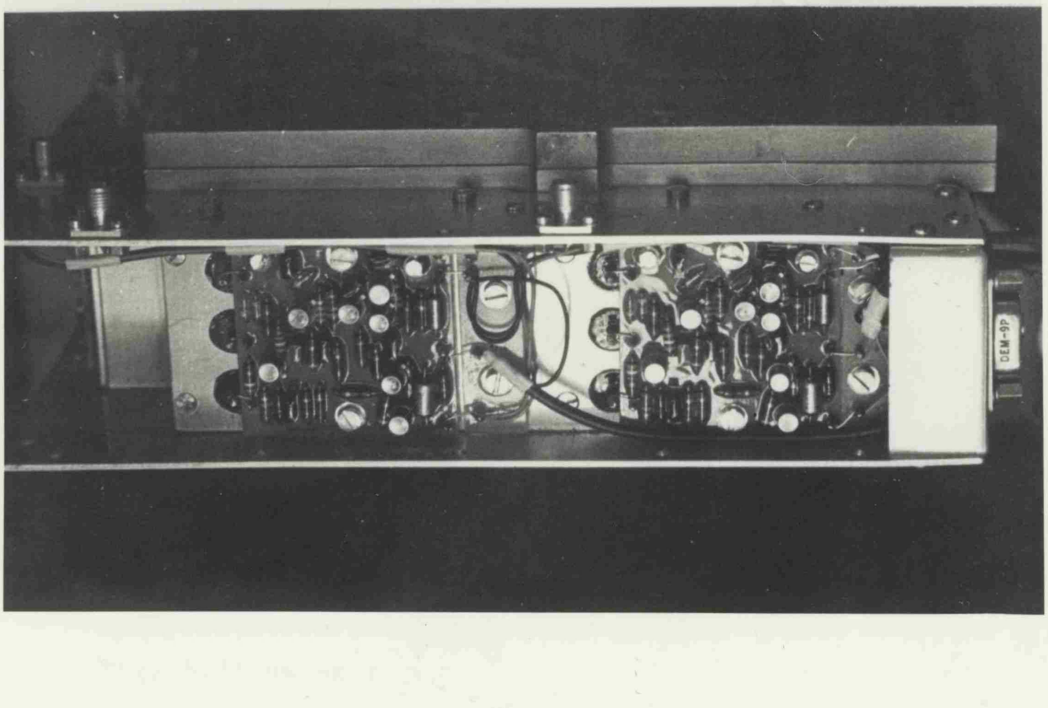
DEM-9P

TABLE 3.2

IPC parameters.	
Sensitive area	6 cm x 6 cm.
Counter window	1 μ polypropylene + 14 $\mu g/cm^2$ carbon
Counter gas mixture	A/CH_4 : 25% / 75%
Counter gas pressure	1 atm.
Active gas volume	0.25 l.
Depth of drift region	2.5 cm.
Anode wire grid pitch	2 mm.
Anode wires	37 x 15 $\mu \phi$ ($T_\omega \sim$ 15 grm.wt)
Cathode wire grid pitch	1 mm.
Cathode wires	90 x 125 $\mu \phi$ ($T_\omega \sim$ 15 grm.wt).
Anti-co. anode grid pitch	9 mm.
Anti-co. anode wires	8 x 15 $\mu \phi$ ($T_\omega \sim$ 15 grm.wt).
Anode - cathode spacing	4 mm.
Cathode RC line :	
Line length	100 mm.
R	50 KΩ
C	30 pF
C_d	68 pF
T_a	2 μs.

The performance of the IPC was evaluated with the timing analysis electronics and image display system shown in Fig. 3.21 using :

(1) A 300 cm. long, 20 cm. diameter vacuum line with a vacuum tube Al/K X-ray source (1.49 keV) (20th Century Electronics Ltd., Croydon), for linearity and resolution

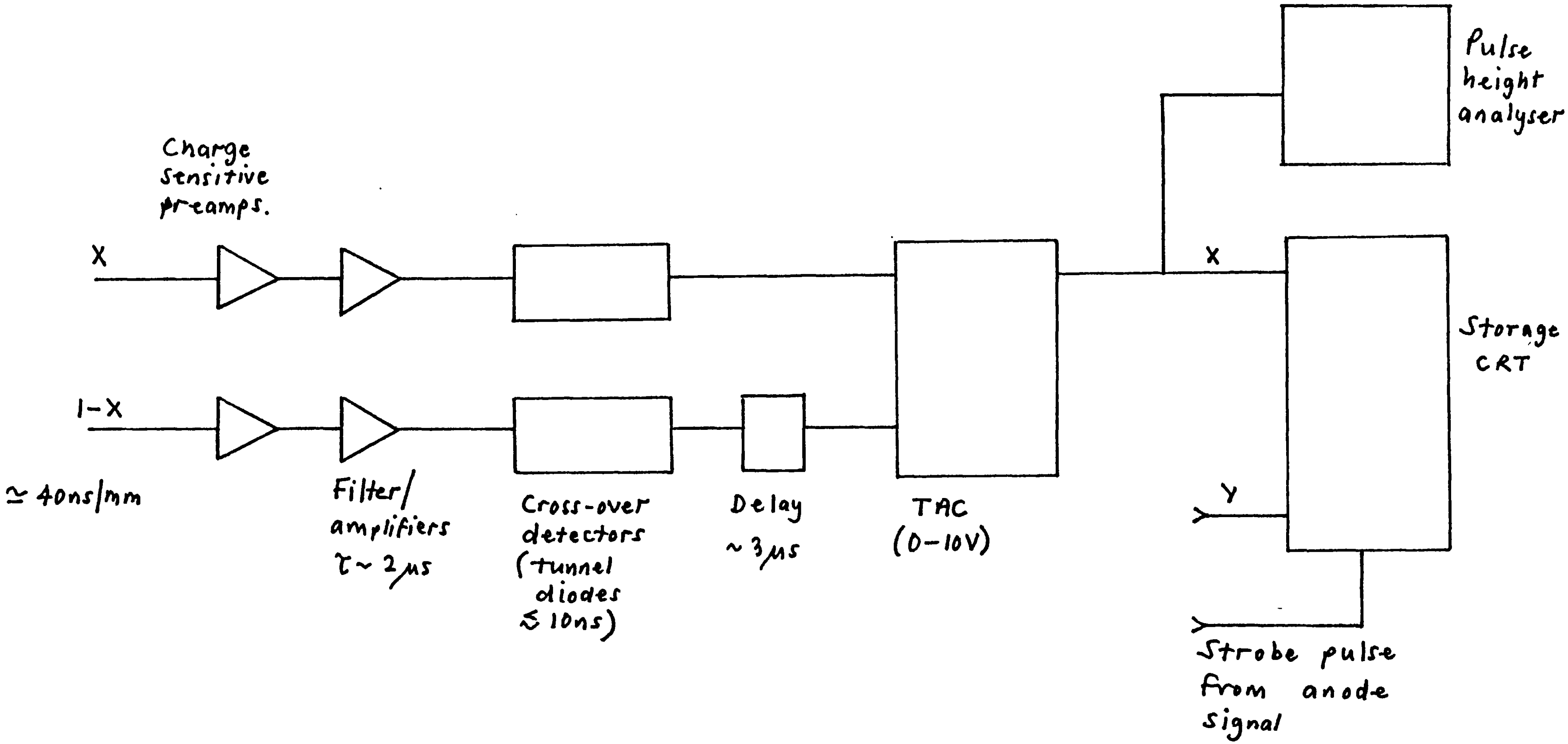

Fig. 3.21 Laboratory set up for performing linearity and resolution tests on the IPC.

tests. A series of test masks were placed directly in front of the IPC window and the resulting image recorded together with the two one-dimensional line scans. The overall IPC linear response to the test mask of Fig. 3.22 is shown in Fig. 3.23. Samples of the recorded image and line scans are presented in Plates 3.6 - 3.8 for varying anode gain, hence q_0 . The effect of uneven illumination is evident. The maximum deviation from linearity was $\sim$ 2% on comparing the image and mask.

With a narrow slit mask, the drift field was varied to maximise electron transmission through the upper cathode grid (Bunemann et.al., 1949) and to minimise the effect of anode wire binning (the modulation due to the anode wire spacing) for constant anode voltage. The observed minimum modulation was $\lesssim$ 10%, the expected result for charge sharing between anode wires by a Gaussian electron cloud of $\sim$ 4 mm. diameter, together with a Gaussian - shaped IPC point spread function of FWHM $\sim$ 1 mm. An approximate description of the anode charge sharing process has been given by Mathieson (1976). For a Gaussian cloud undergoing lateral diffusion in a linear drift field, and having rms width α , the detected position of the centroid in a direction orthogonal to the anode wires, of pitch s , is given by

$$\bar{y} = s \sum_{n=0}^{N} n \, . \, f_n \qquad (3.18)$$

where f_n is the fraction of the total electron cloud collected on the n^{th} anode wire and

$$f_n = \frac{1}{2} \left\{ \operatorname{erf}\left(\frac{n + \frac{1}{2} - \frac{y}{2}}{\sqrt{2}\, \alpha / s} \right) - \operatorname{erf}\left(\frac{n + \frac{1}{2} + \frac{y}{2}}{\sqrt{2}\, \alpha / s} \right) \right\}$$

The recorded positional error $(y - \bar{y})$ is zero at $y = \pm\frac{s}{2}$ and at $y = 0$ and a maximum at $y = \pm\frac{s}{4}$. Since each event would be systematically recorded in an incorrect position, the output pattern exhibits intensity modulation

$$m = \frac{I_{max} - I_{min}}{I_{max} + I_{min}} \qquad (3.19)$$

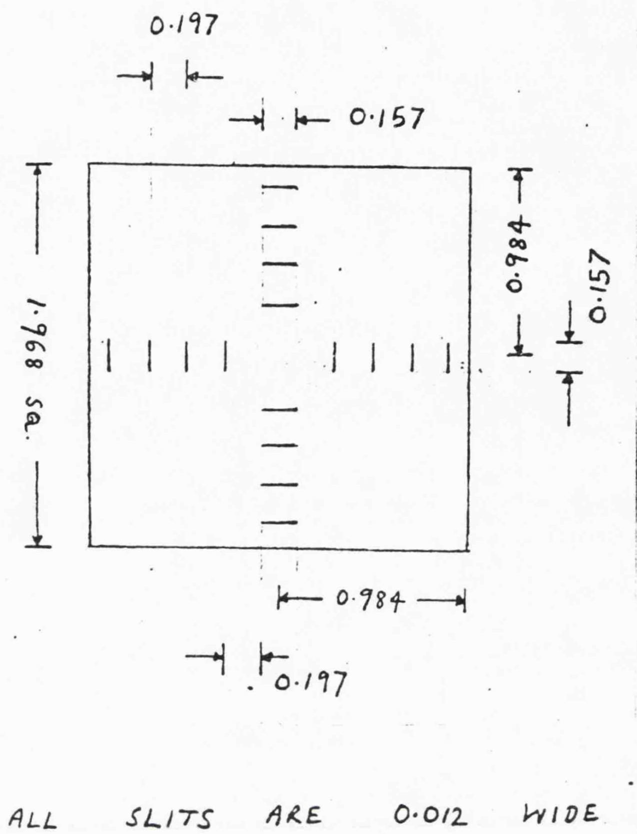

Fig.3.22 IPC aluminium test mask.
Dimensions in inches.

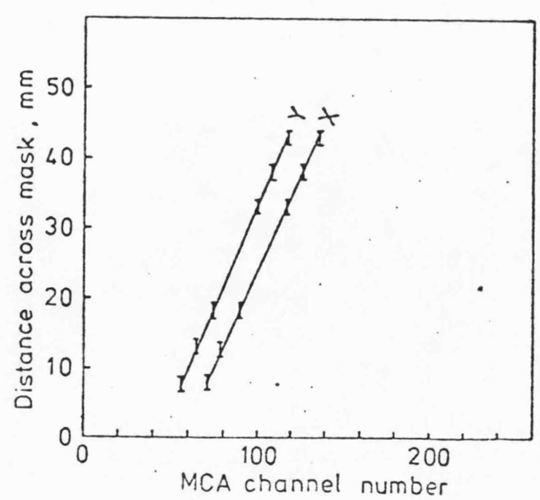

Fig.3.22 IPC linear response in the X and Y axes to I.49 keV X-ray transmission through the test mask above.

Plate 3.6

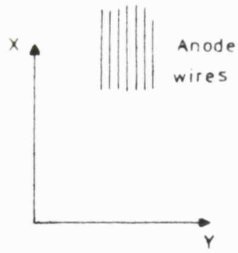
X
Anode
wires
Y

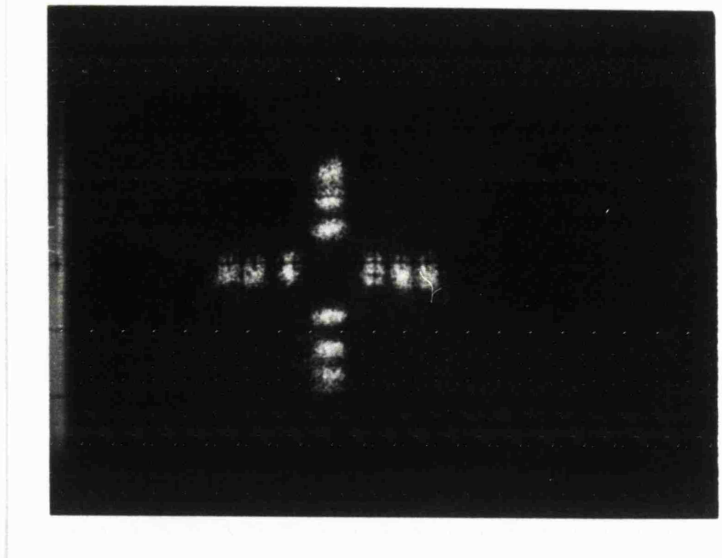

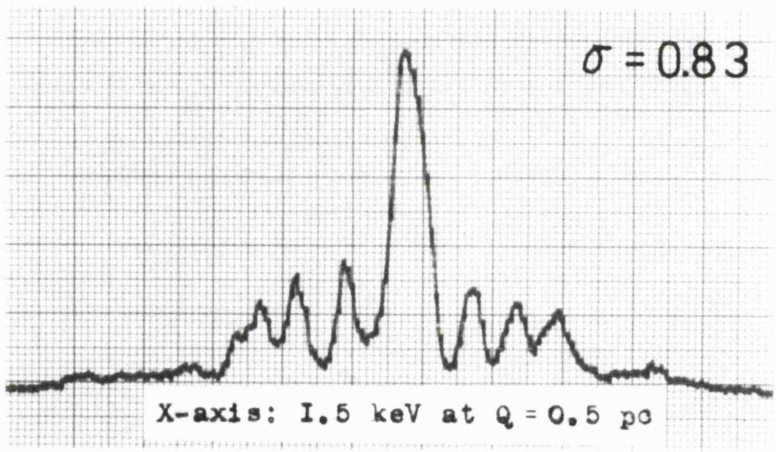
σ = 0.83
X-axis: I.5 keV at Q = 0.5 pc

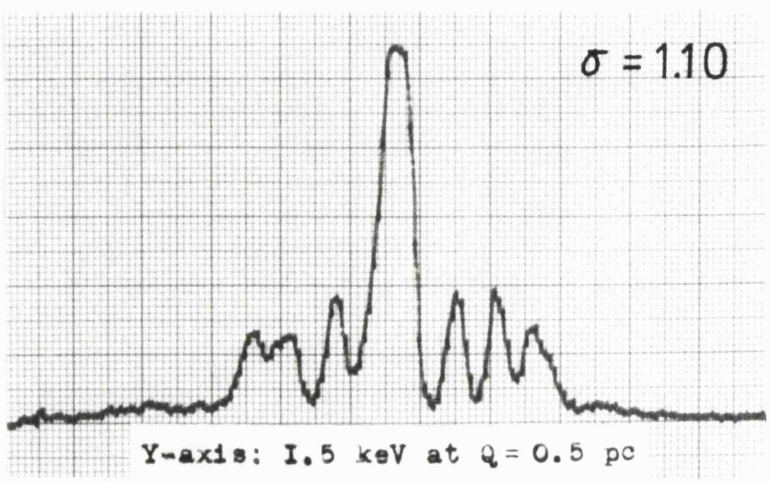
σ = 1.10
Y-axis: I.5 keV at Q = 0.5 pc

Plate 3.7

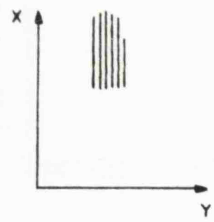
X
Y

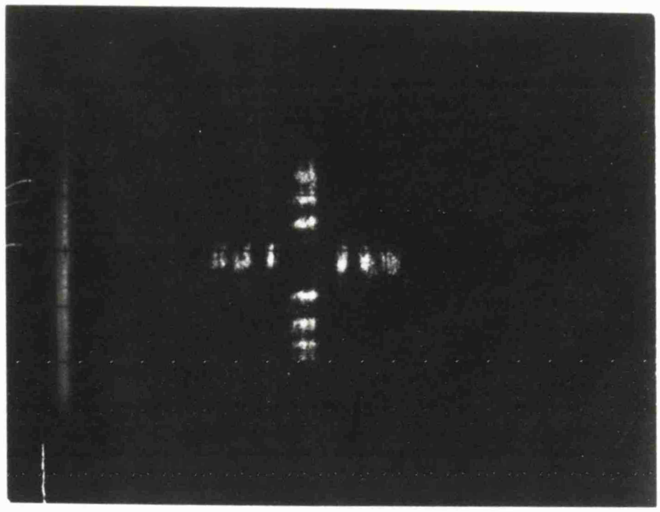

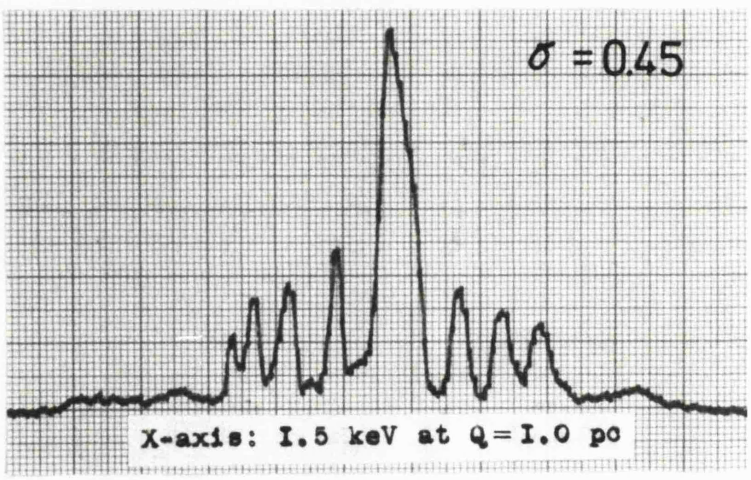
σ = 0.45
X-axis: I.5 keV at Q = I.0 pc

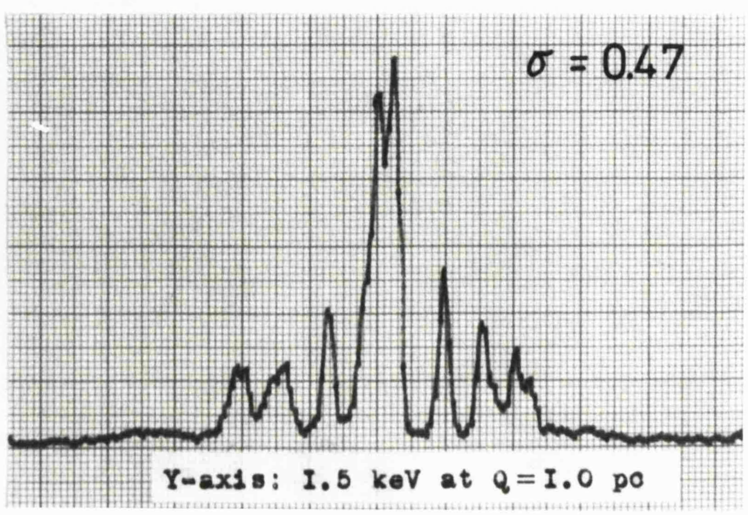
σ = 0.47
Y-axis: I.5 keV at Q = I.0 pc

Plate 3.8

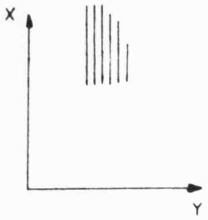
X
Y

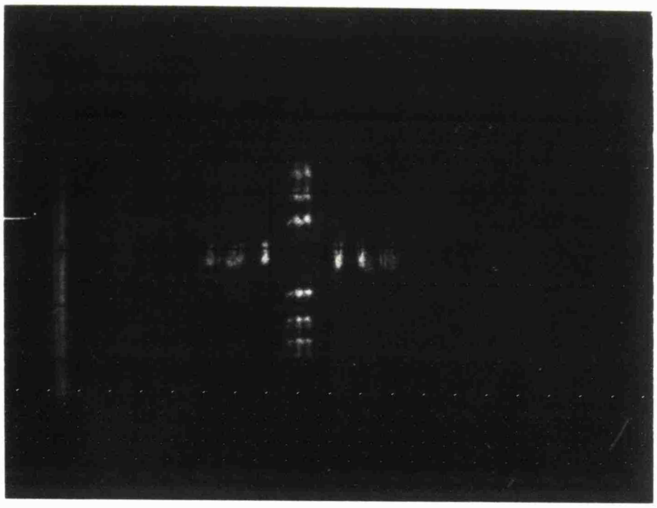

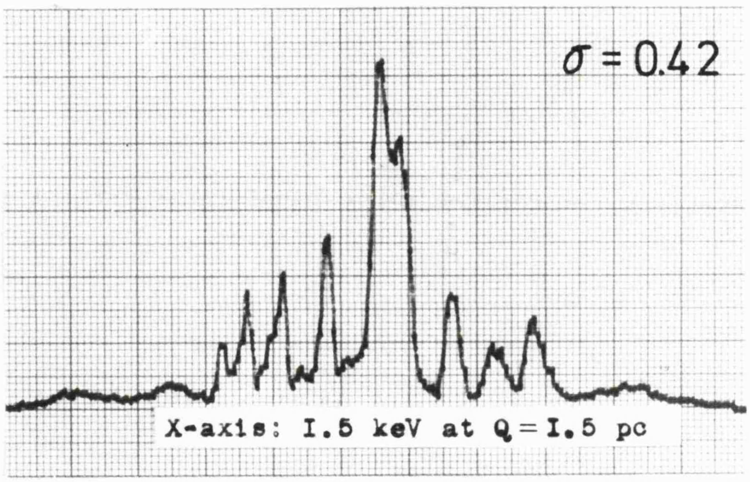
σ = 0.42
X-axis: I.5 keV at Q = I.5 pc

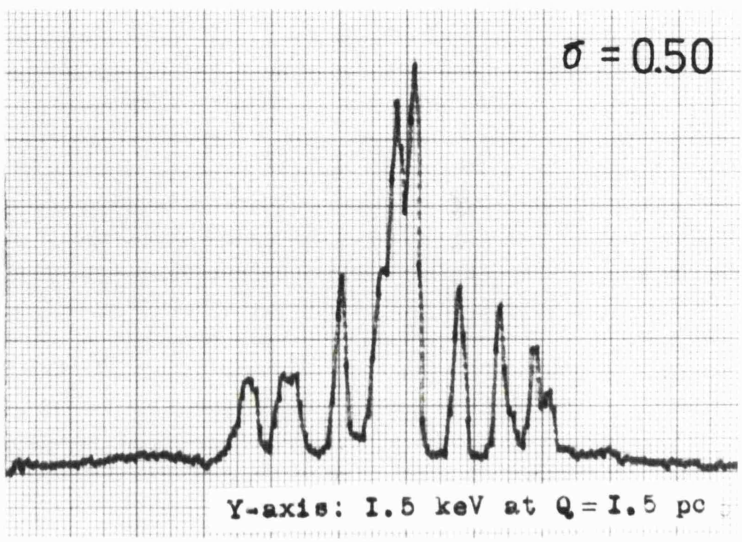
σ = 0.50
Y-axis: I.5 keV at Q = I.5 pc

where for mean value intensity I_0

$$I_{max} = I_0 \left(\frac{dy}{d\bar{y}} \right)_{y=0}$$

$$I_{min} = I_0 \left(\frac{dy}{d\bar{y}} \right)_{y=S/2}$$

Including the effect of finite IPC resolution where the IPC line spread function may be closely approximated by :

$$F(y) = \frac{1}{\sqrt{2\pi\sigma^2}} e^{-\frac{y^2}{2\sigma^2}} \qquad (3.20)$$

where σ is the line spread rms width. The Fourier transform is

$$\tilde{F}(k) = e^{-\frac{\sigma^2 k^2}{2}} \qquad (3.21)$$

where $k/2\pi = 1/S$ is the spatial frequency. The ratio of the observed modulation to the intrinsic modulation is then :

$$\frac{m_{obs}}{m} = e^{-2\pi^2 \cdot \frac{\sigma^2}{S^2}} \qquad (3.22)$$

For a value of m_{obs} , σ, m may be found, and (3.20) solved to find α .

For each one - dimensional line scan of Plates 3.6 - 3.8, a measure of the position uncertainty, for variable V_0 , was made as follows. Each line spread function was the result of a convolution with the mask of Fig. 3.22, of finite slit width W = 0.3 mm, and the IPC point spread function, which to a good approximation, was Gaussian shaped. Hence, the image $I(x,y)$ produced by an object $O(x,y)$ by an instrument with point spread function $S(x,y)$ is :

$$I(x,y) = \iint O(x',y')\, S(x-x', y-y')\, dx'dy' \qquad (3.23)$$

For a long, narrow slit

$$I(x) = \int O(x')\, S(x-x')\, dx'$$

For

$$S(x) = \frac{1}{\sqrt{2\pi\sigma^2}} e^{-\frac{x^2}{2\sigma^2}}$$

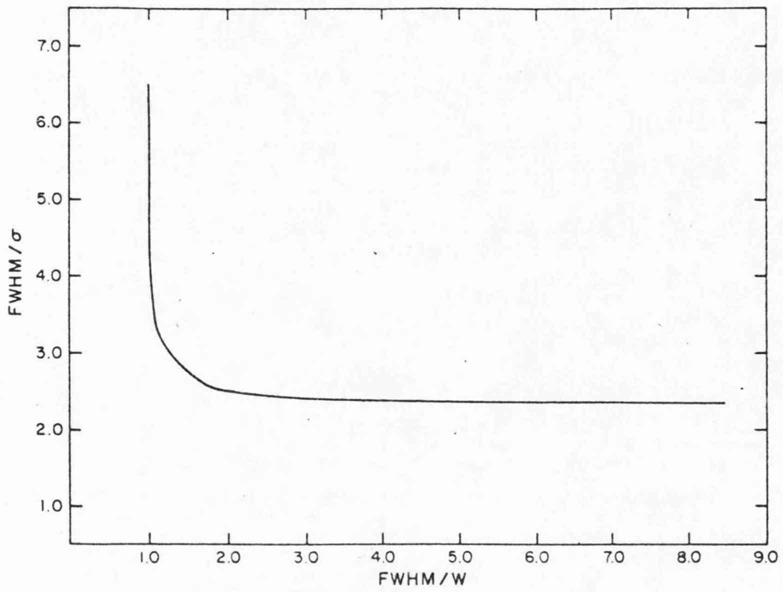

Fig. 3.24. Plot of the fullwidth at half-maximum of the image of a slit divided by the resolution as a function of the fullwidth at half-maximum divided by the width of the slit, assuming a Gaussian point spread function.

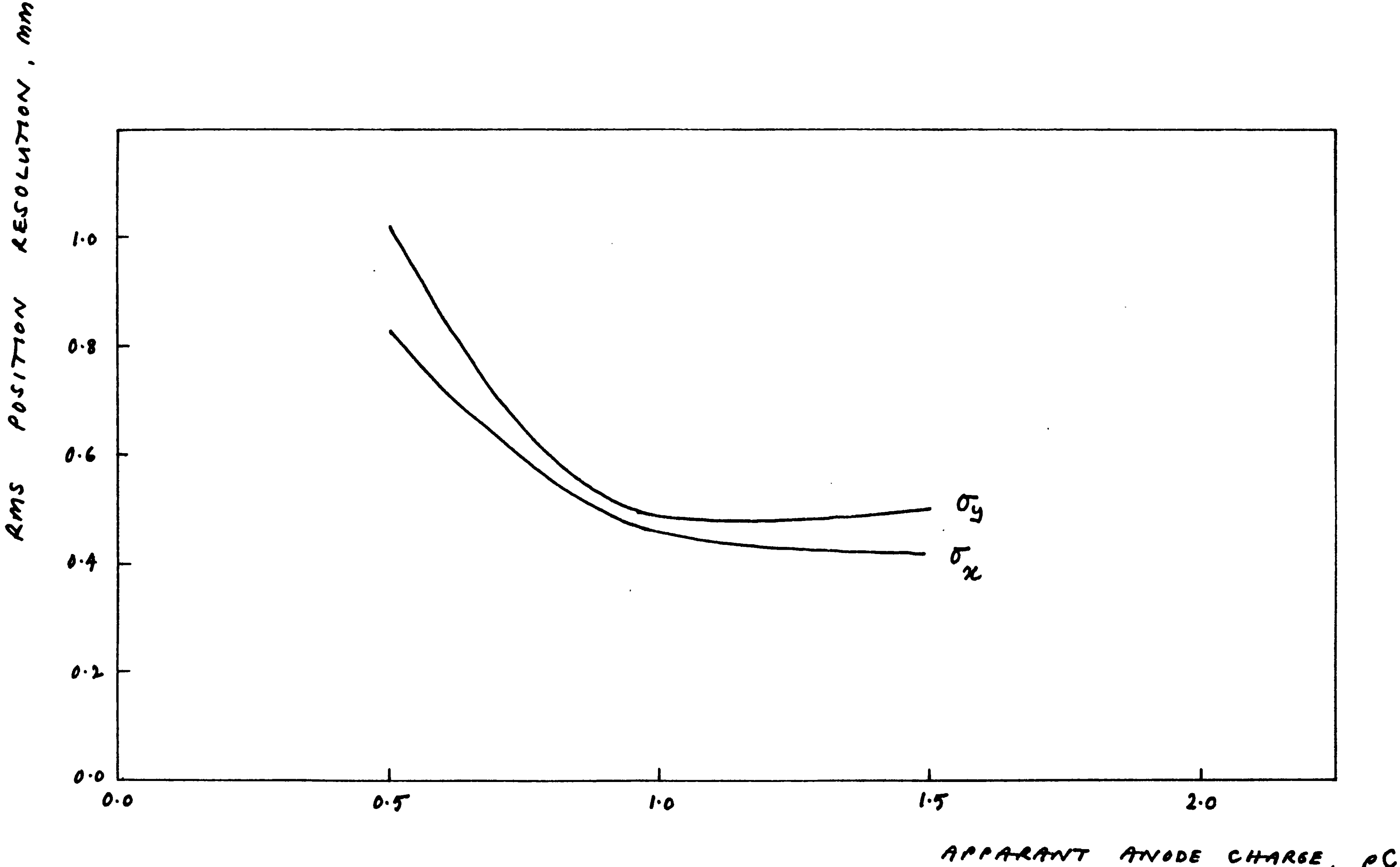

Fig. 3.25. RMS position measured at 1.49 keV for the upper cathode RC line (Y-axis) and lower cathode RC line (X-axis).

$$I(x) = \frac{1}{\sqrt{2\pi\sigma^2}} \int_{-W/2}^{W/2} e^{-\frac{(x-x')^2}{2\sigma^2}} dx'$$

$$\therefore \quad I(x) = \frac{1}{2}\left\{ \mathrm{erf}\left(\frac{W/2 - x}{\sqrt{2}\,\sigma}\right) + \mathrm{erf}\left(\frac{W/2 + x}{\sqrt{2}\,\sigma}\right) \right\} \qquad (3.24)$$

The solution is graphed in Fig. 3.24 (Kellogg et. al., 1976). By measuring the FWHM of each slit image, in each direction, the width of the IPC point spread function could be found, Fig. 3.25.

(2) A vacuum rig ~ 15" in diameter and 15" deep with a tunable X-ray source, enabling measurements of the IPC point spread width at C - K (0.28 keV) and Cu - L (0.93 keV) as a function of anode charge. Using an opaque mask containing two slits 1 mm. and 50μ wide, separated by 3 mm, the IPC point response was fitted with a Gaussian curve of variable width. The observed widths are plotted in Fig. 3.26. Also plotted is the calculated cathode RC line noise limited position resolution. From (3.13)

$$(\Delta x)_m = \frac{D_m}{n q_0}\left\{ kT_e . C\mu^2 + q_a^{\,2} \right\}^{\frac{1}{2}} \qquad (3.25)$$

where the factor n represents the fraction of charge contained in the anode avalanche, induced on the upper and lower cathodes. For the upper cathode $n \sim 0.66$ and the lower cathode $n \sim 0.33$. For $T_a = 2\mu s$, $C_d = 68pF$ $C = 30pF$, $R = 50k\Omega$, $q_a = 500$, line length 10 cm. and $[q_0] = pC$ then (Fraser 1978)

$$(\Delta x)_m = \frac{0.1}{n . q_0} \quad mm\ (RMS) \qquad (3.26)$$

For anode charge q_0 = 2 pC, the IPC point spread width for 0.93 keV was ~ 0.3 mm. (RMS) in both axes with a corresponding value for 0.28 keV of ~ 0.6 mm. (RMS). For $q_0 \lesssim$ 1.5 pC, $\sigma_x \sim \sigma_y$ and the overall IPC point response function was well represented by

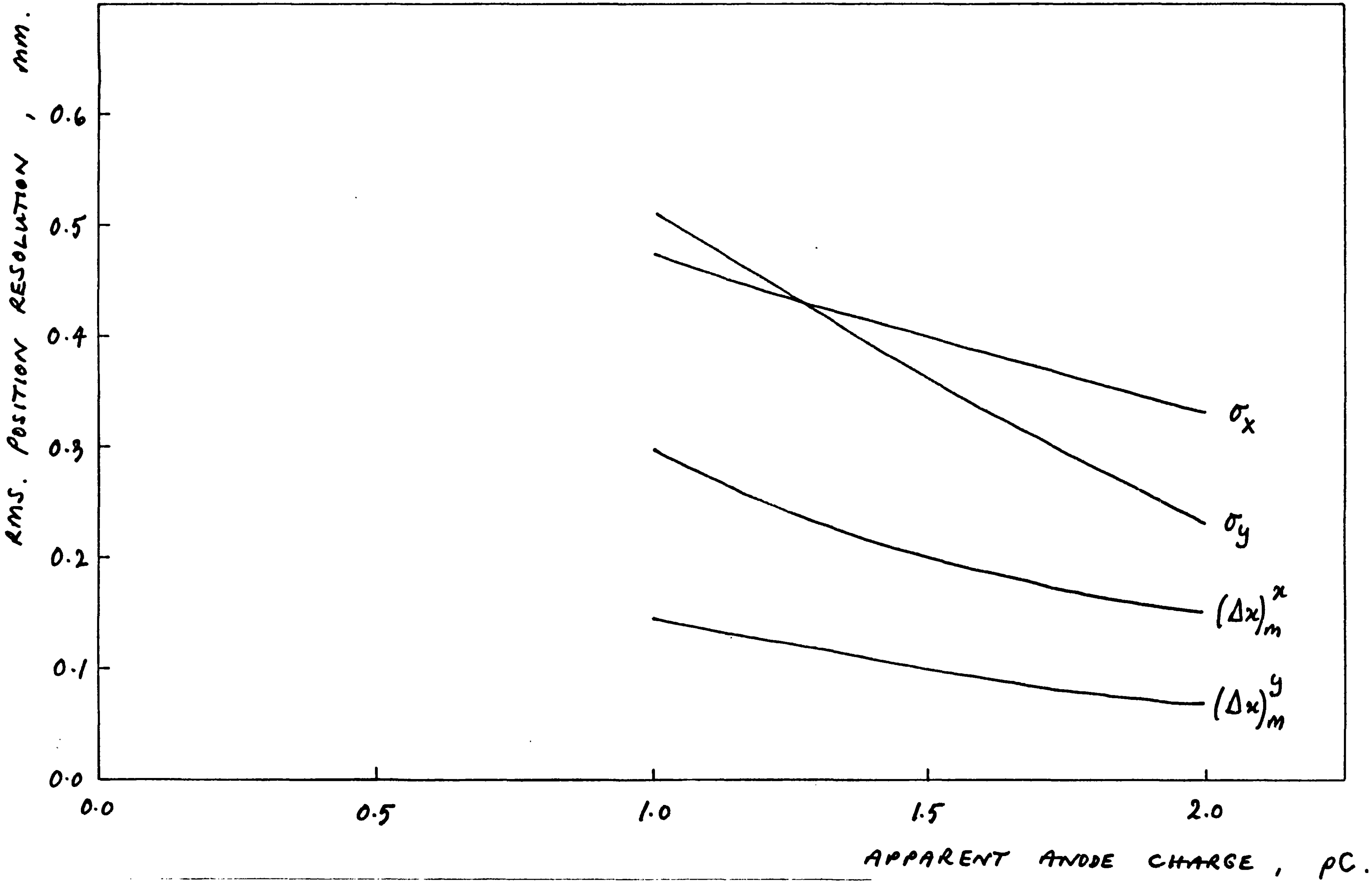

Fig. 3.26. RMS position resolution measured at 0.93 keV for the upper cathode RC line (Y-axis) and the lower cathode RC line (X-axis). The calculated line noise limited resolution is also shown for the upper and lower cathode RC lines ($(\Delta x)_m^y$ and $(\Delta x)_m^x$, respectively).

$$F(r) = C.\ e^{-\frac{r^2}{\sigma^2}} \qquad (3.27)$$

where $F(r)$ is the radial intensity per unit area.

The anode charge was estimated using the pulse matching method (Hendricks 1973).

Details of the IPC rocket payload pulse position sensing electronics (Boughan 1977) are shown in Fig. 3.27 - Fig. 3.30. For the anode / anti-coincidence anode measurement chain, the lower level threshold of each peak stretcher was trimmed to 300 mV = 120 eV using an Al-K source. The corresponding levels for the upper and lower cathodes were 300 mV = 80 eV and 300 mV = 40 eV respectively, taking into account the fraction of anode charge induced on each cathode. Similar measurements were performed on the IPC, as discussed above, trimming the flight electronics to give near identical results. All the measurements were performed using the IPC gas supply system, Fig. 3.31. The gas pack principally comprised two 300 cm^3 stainless steel gas tanks which could accommodate A/CH_4 up to 1500 p s i . From the reservoirs the gas flowed through a 5μ filter into a two stage mechanical pressure regulator then into the IPC. A flow restrictor on the gas exhaust provided a steady flow of gas through the counter during flight. Since the leak rate through the 1μ polypropylene window was $\leqslant$ 0.5 psi/hr, over $\sim$ 40 cm^2, the flow rate was set at $\sim$ 10 cm^3/hr., for the IPC volume of $\sim$ 0.5l. An additional flow valve enabled an external gas supply to be used for purging the IPC over long periods. A pressure relief valve located between the gas system and IPC prevented the counter pressure from exceeding 22 psi. A pressure transducer continuously monitored the IPC gas pressure. A pressure change of $\sim$ 1% effected a change of the IPC anode gain of $\sim$ 3%. Plate 3.9 shows the IPC after space enviroment testing (vacuum and vibration tests). Detail of the IPC / gas pack

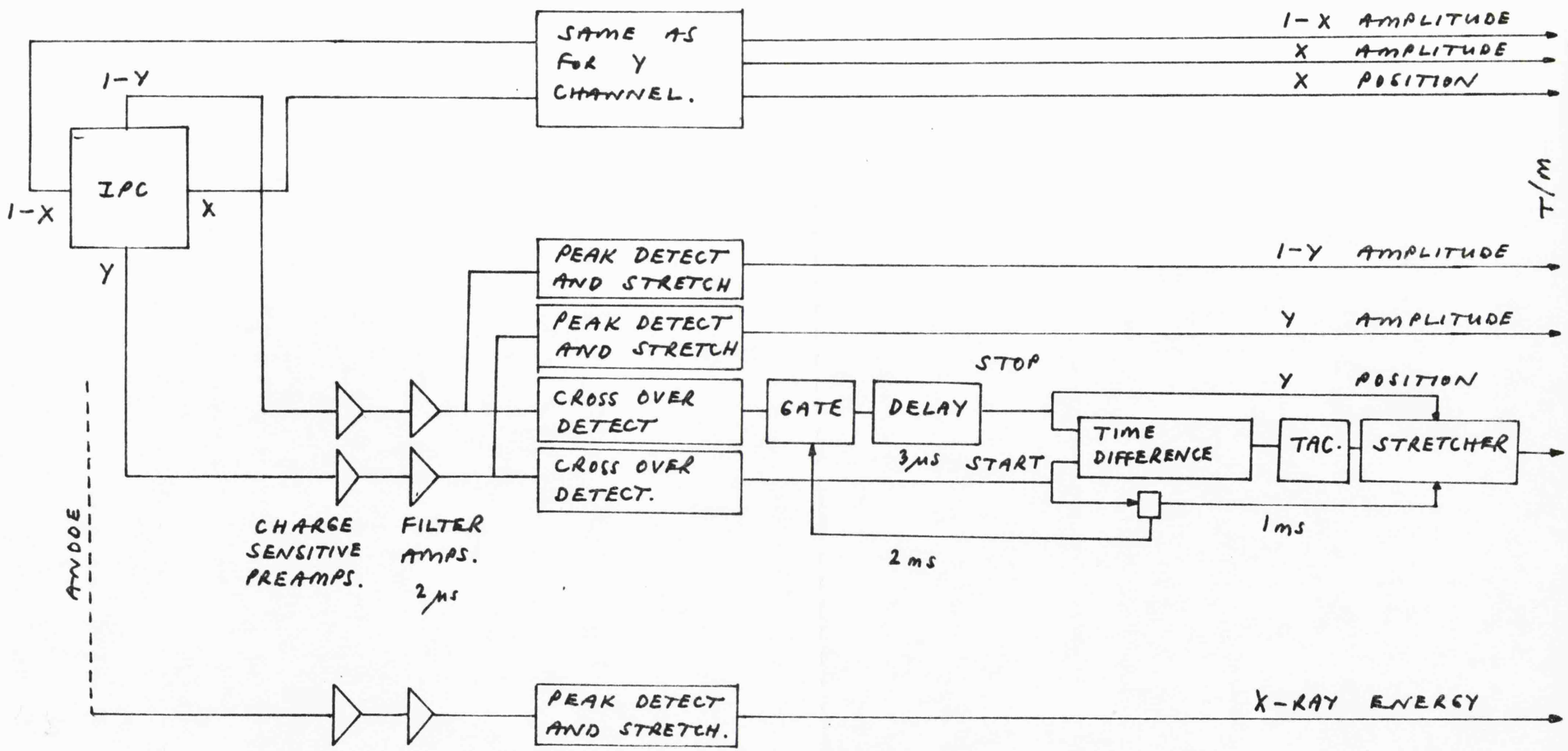

Fig. 3.27. Schematic diagram of IPC pulse position sensing electronics with simultaneous X-ray energy readout.

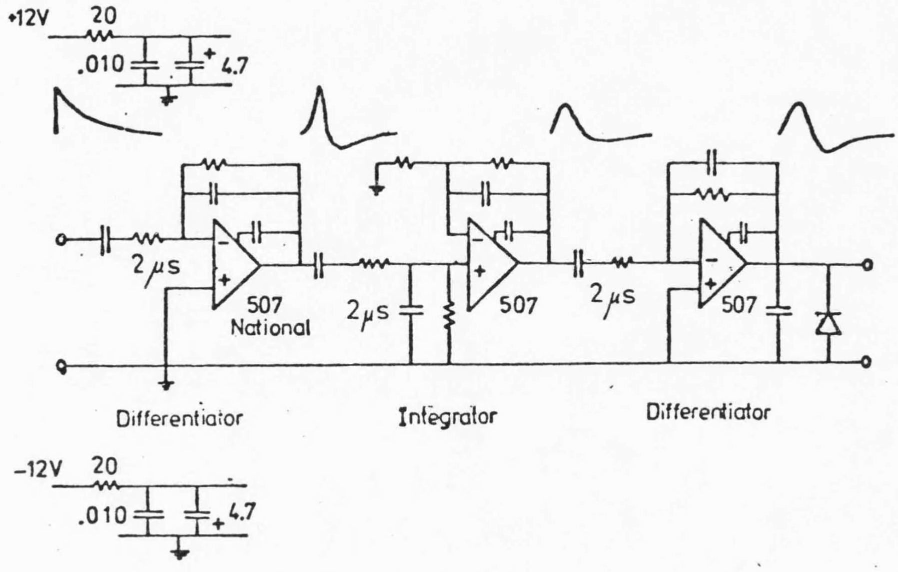

Fig. 3.28. Anode/cathode pulse shaping circuit.

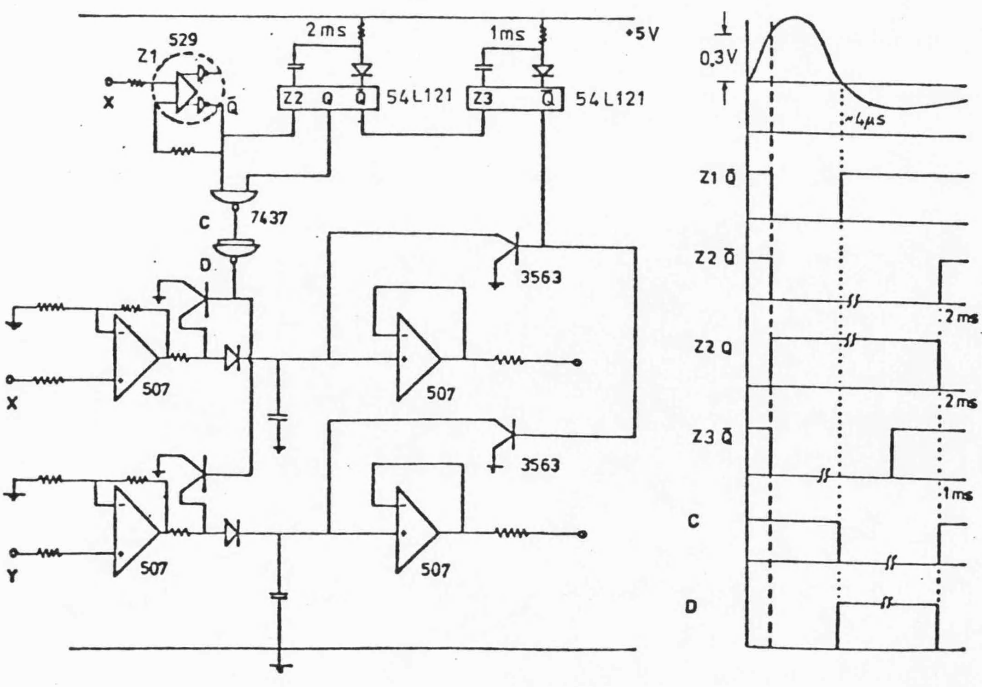

Fig. 3.29. Anode/cathode pulse stretching circuit.

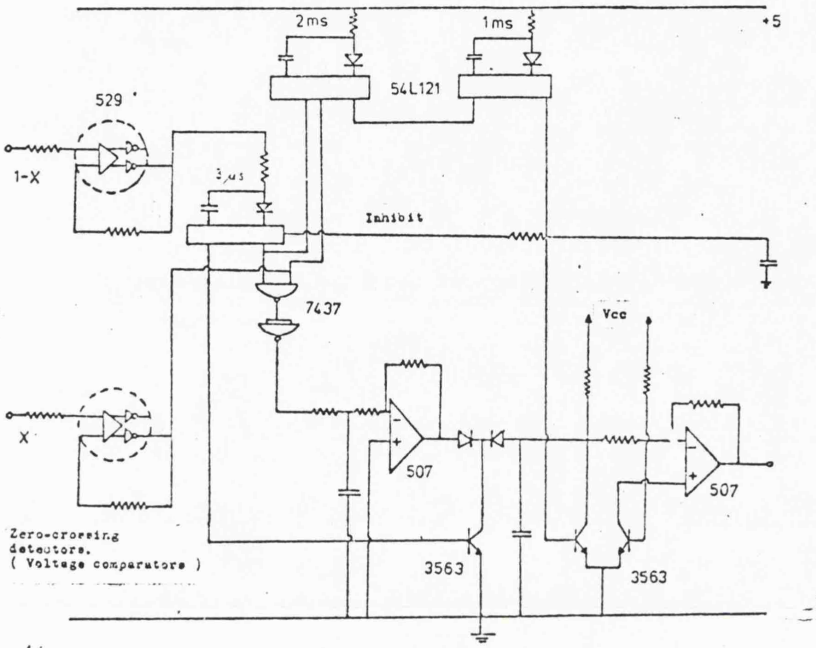

Fig. 3.30. Cathode pulse position sensing circuit.

Fig. 3.31

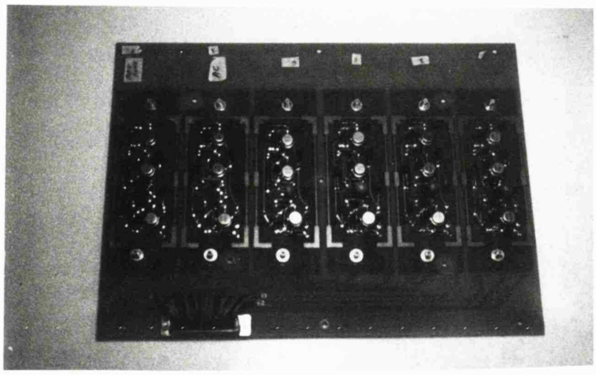

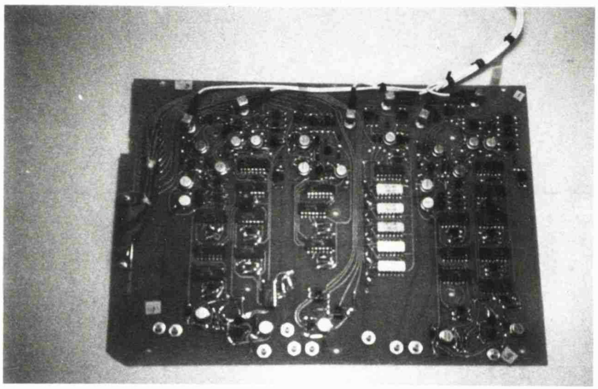

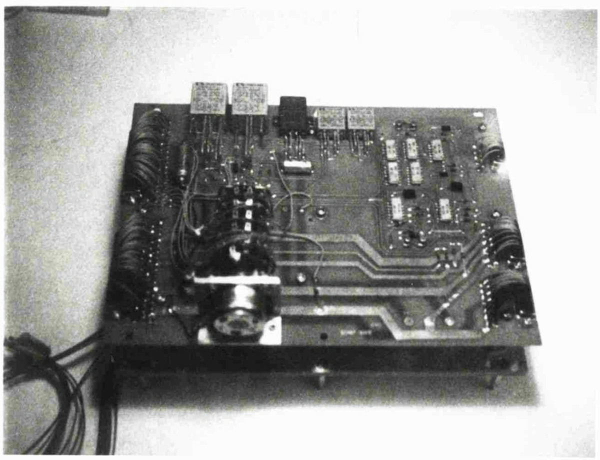

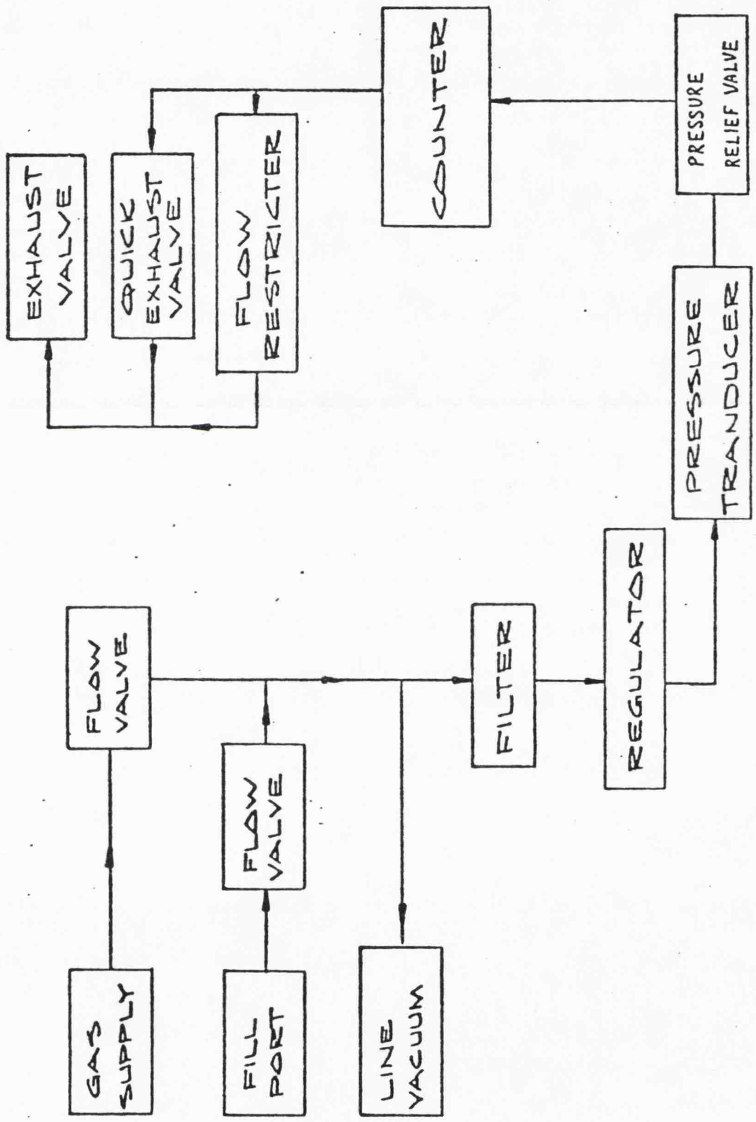

Fig. 3.31. Schematic diagram of the gas pack configuration.

Plate 3.9 The IPC (top) and detail of the IPC/gas pack integration (bottom).

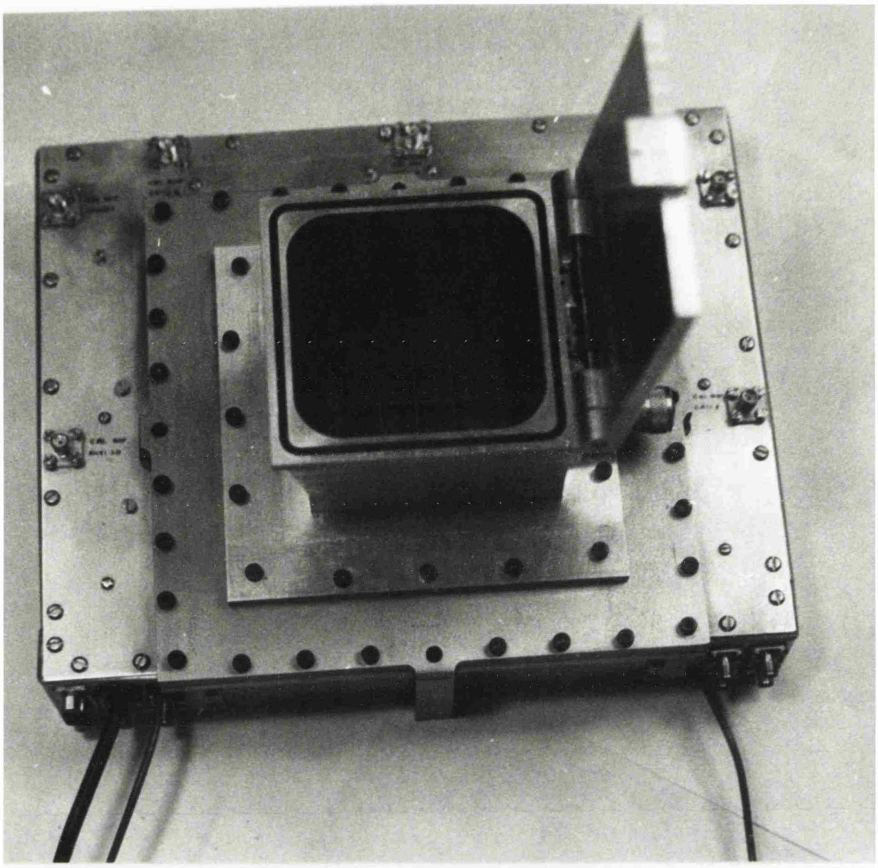

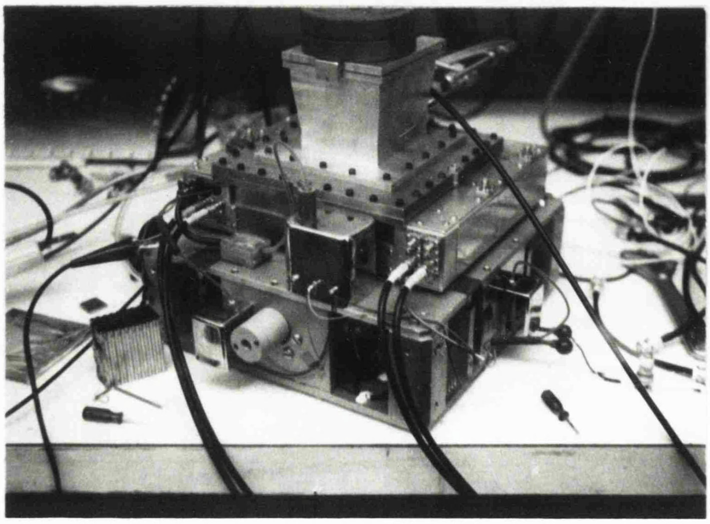

integration is also shown. The three Velonex high voltage power supplies are seen positioned around the IPC.

A summary of the IPC operational characteristics is presented in Table 3.3.

TABLE 3.3

Summary of IPC system parameters.

Anode EHT	3.6 KV
Anode charge conversion gain	1pC/keV
Drift field HT	400 V
Anti-co. anode EHT	2.7 KV
Anti-co. anode charge conversion gain	1 pC/keV
Photon detection efficiency (0.28 keV)	76%
X-ray energy resolution (1.49 keV)	43% (FWHM)
Maximum positional non-linearity	2%
Positional resolution (0.93 keV)	0.5 mm. (RMS)

The X-ray energy resolution ,gain curve and proportionality are illustrated in Fig. 3.32. For measurements 0.1 keV $\leq \varepsilon_X \leq$ 6 keV, the IPC X-ray energy resolution was well represented by

$$R(\varepsilon) = C.\ e^{-\frac{\varepsilon_X^2}{2\Sigma^2}} \tag{3.28}$$

where $\Sigma = 0.21\ \varepsilon_X^{-0.5}$

The IPC system parameters pertaining to X-ray image and energy information directly before and during the X-ray astronomy observation (of the Cygnus Loop) are presented in Tables 4.6 and 4.7.

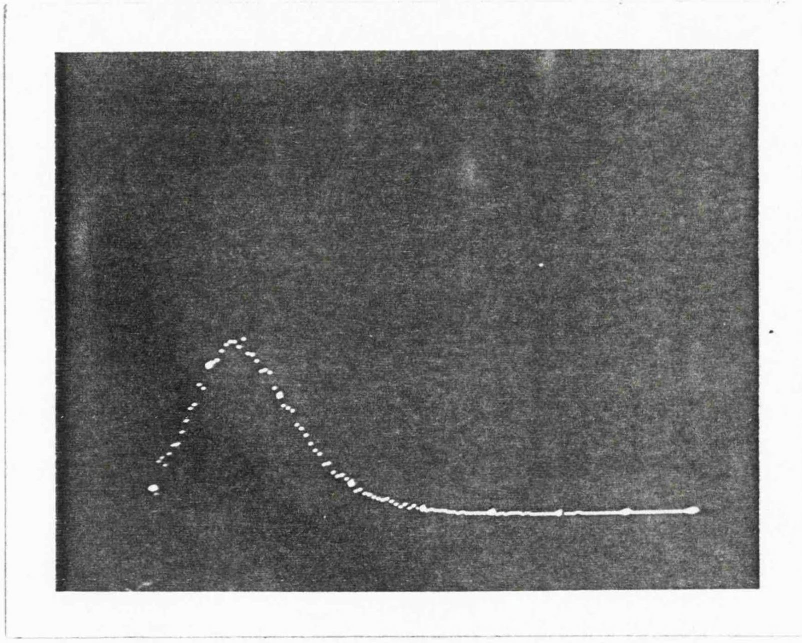

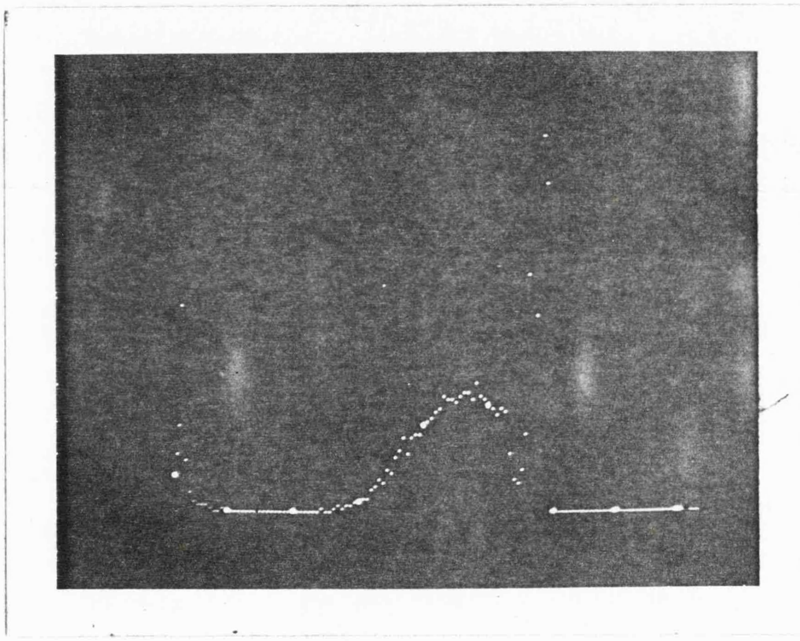

Fig 3.32

(a) Energy response of IPC to 0.28 keV and 1.5 keV X-rays (top)

(b) IPC gain curves and proportionality (right)

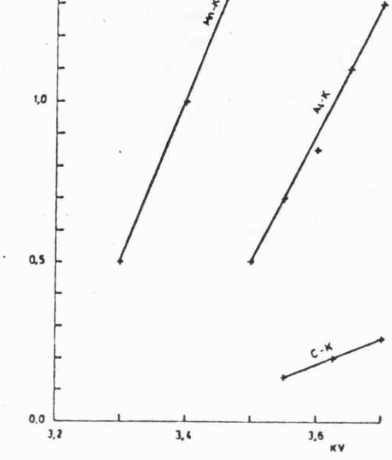

3.3.3. Overall X-ray telescope parameters and payload configuration.

The integrated X-ray telescope rocket payload is shown in Fig. 3.33. The overall payload length was $\sim$ 7.5' by 17" wide. A star field camera, a 16 mm. movie camera, (57° field of view, Multidata, Giannini Sci. Co.) and a star sensor (GSFC - Ball Brothers) were mounted in the front baffle of the Wolter I mirror system (Plate 4.1). The final alignment between the centre of the field of view of the star field camera and the centre of the IPC window (mirror axis) was measured to be $\sim$ $\pm$ 3', using an optical flat placed near the star field camera. To compensate for possible changes in the alignment during flight, a fiducial light system, placed in the star field camera field of view, was used to mark the position of a fixed point in the focal plane, relative to the mirror axis. Thus, with a subsequent star sensor alignment, with the centre of the star field camera field of view, of $<$ 1', the final X-ray images produced by the X-ray telescope would contain a maximum positional error of $\pm$ 3' on the sky, for any relative motion between the telescope and the source. Also, the maximum non-linearity (3.3.2) present in the images would amount to $\sim$ 2% = 1.2 mm. $\sim$ 4'.

Besides the limiting pointing accuracy and non-linearity contained in subsequent X-ray images, image blurring would occur through the finite telescope angular resolution. Contributions to the overall telescope resolution limit of $\sim$ 6' (RMS) are summarised in Table 3.4.

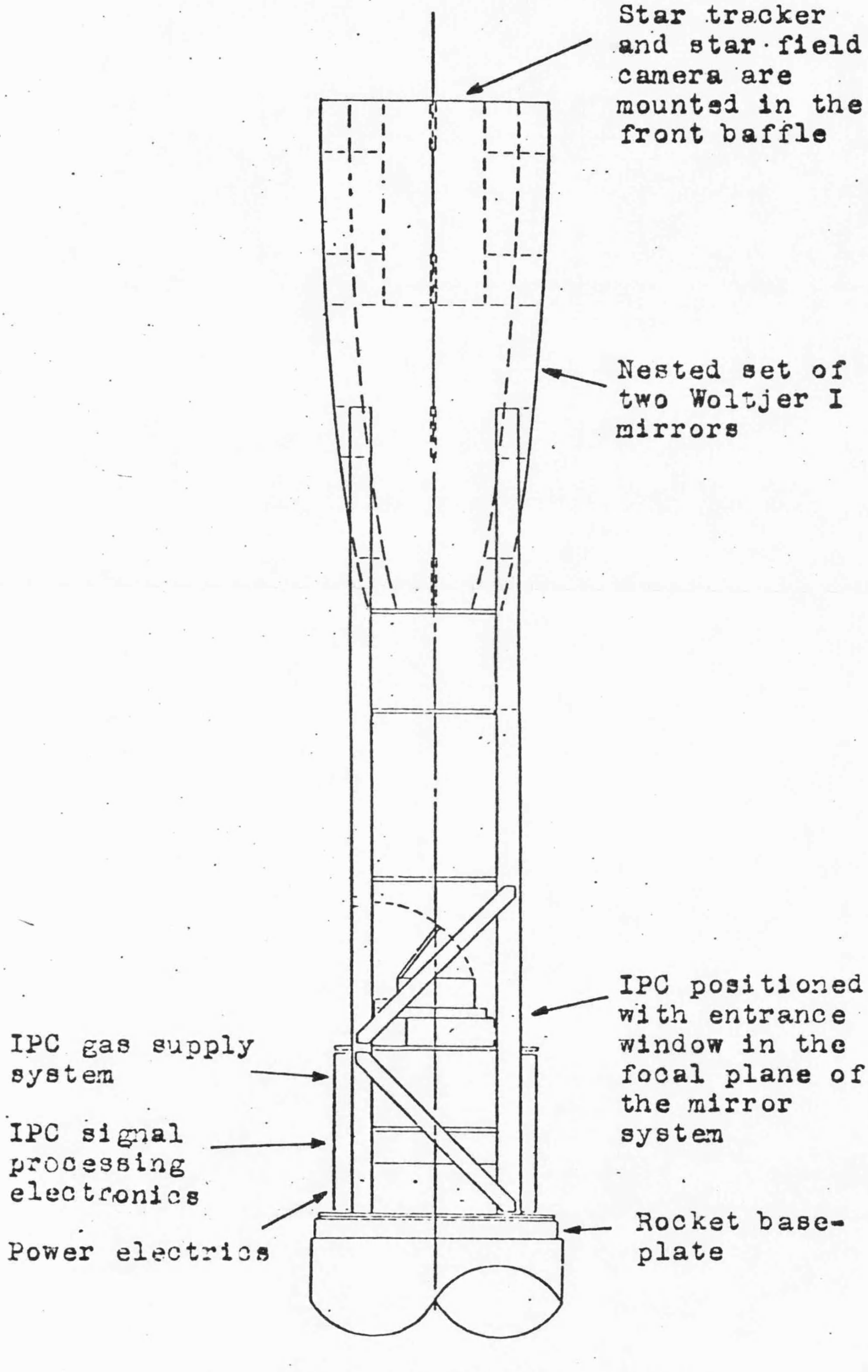

Fig. 3.33. X-ray telescope configuration.

TABLE 3.4

X-ray telescope component point spread functions.

Origin	Radial intensity per unit area	Typical value
X-ray mirror, on-axis scattering	$F_m(r) = \sqrt{\frac{2}{\sigma_m^2}} \cdot \frac{e^{-\frac{r^2}{2\sigma_m^2}}}{2\pi r}$	$\sigma_m \sim 3'$ (0.28 keV)
IPC, X-ray attenuation in the drift region (gas spreading)	$F_g(r) = \frac{1}{\sigma_g} \cdot \frac{e^{-\frac{r}{\sigma_g}}}{2\pi r}$	$\sigma_g = \frac{1}{\mu} \sin 9^\circ \sim 0.4'$ (0.5 keV)
IPC, avalanche location (wire response)	$F_w(r) = \frac{1}{2\pi\sigma_w^2} \cdot e^{-\frac{r^2}{2\sigma_w^2}}$	$\sigma_w \sim 4'$ (0.93 keV)
Convolution of above		$\sigma \sim 6'$ (0.4 keV)

The sensitivity of the X-ray telescope may be defined as the flux in photons / cm^2.s in a given energy interval ΔE, that gives rise to a fluctuation of three standard deviations in the background counting rate. The limiting sensitivity of the telescope to discrete sources, due to the cosmic ray and diffuse soft X-ray background is :

$$S \propto \left\{ A_{eff.} \, \sigma \right\}^{\frac{1}{2}} \tag{3.29}$$

where $A_{eff.}$ is the telescope effective area for $\Delta\mathcal{E}$ and σ is the telescope angular resolution in units of solid angle. If A is the telescope geometric area, η the overall telescope efficiency (the product of the mirror and detector efficiencies) in $\Delta\mathcal{E}$, D the IPC wall area, γ the background reduction factor, C_B the particle count rate and I_{DX} the diffuse X-ray flux, then for discrete sources,

$$S_{\Delta\mathcal{E}} = \frac{3 \cdot \left\{ C_B . D . \gamma + I_{DX} . (\eta A)\, \sigma \right\}^{\frac{1}{2}}}{(\eta A)\, t^{\frac{1}{2}}} \qquad (3.30)$$

For the diffuse soft X-ray component

$$S_{\Delta\mathcal{E}} = \frac{3 \cdot \left\{ C_B . D . \gamma \right\}^{\frac{1}{2}}}{(\eta A)\, t^{\frac{1}{2}} . \sigma} \qquad (3.31)$$

Davidsen et. al., (1972) give a thermal Bremsstrahlung, with unit Gaunt factor, fit to the diffuse soft X-ray background, $\mathcal{E}_X < 1$ keV :

$$I_{DX} = 300 \cdot \frac{e^{-\frac{\mathcal{E}_X}{0.2}}}{\mathcal{E}_X} \quad ph./cm^2.s.sr.keV \qquad (3.32)$$

giving an integrated flux of $\sim 3 \times 10^{-8}$ erg / cm^2.s. sr (0.1 - 1.0 keV) i.e $\sim$ 20 ph / cm^2.s. sr. For $0.2 < \mathcal{E}_X <$ 2.0 keV, $C_B \sim 0.01$ counts / cm^2.s. keV (Ricketts 1973). For the MIT-UL telescope, A = 350 cm^2, D = 160 cm^2, γ = 0.8, $\eta \sim 0.05$ (0.1 - 0.8 keV) $\sigma \sim 3 \times 10^{-6}$ sr (0.1 - 0.8 keV). Table 3.5 gives the approximate X-ray telescope sensitivity for an observation time t = 200 s, a typical time for a rocket observation.

TABLE 3.5

Sensitivity for discrete sources (0.1 - 0.8 keV) $ph / cm^2.s$	Sensitivity for the diffuse, soft X-ray component (0.1 - 0.8 keV) $ph / cm^2.s\ sr$
3.7×10^{-2}	1.2×10^{4}

In conclusion, the design and operating characteristics of the MIT-UL X-ray telescope may be compared with two other existing, space qualified, X-ray imaging telescopes. In Fig. 3.34, a summary of the details of the SAO rocket payload (Gorenstein et. al., 1975) is shown. The mirror configuration utilised, has a larger geometric area but reduced field of view. The angular resolution of each telescope is comparable. The imaging properties of the SAO telescope have been clearly demonstrated with the observation of the point source, Algol (Harnden et. al., 1977). From a background pointing position during an observation of the Virgo cluster of galaxies, a uniform background distribution of counts equivalent to only 0.3 counts / 4' x 4' in a 120 s observation time, was detected.

The HEAO-B observatory, due for launch in late 1978 and designed to operate for 6-12 months, has been described by Schreier (1977). Fig. 3.35 and Fig. 3.36 summarise the design parameters. The telescope consists of a four nested set of Wolter I mirrors with confocal length 3460 mm, with a plate scale of 1' / mm. The imaging detectors comprise the small angle, high resolution ($\sim$ 2") micro-channel plate array (16 μ diameter tubes) (Kellogg et. al., 1976) and the wide angle, low resolution ($\sim$ 2') IPC (Humphrey et. al., 1978).

Characteristics of Large Area Focusing Collector

For Aerobee 350

Focal Length	180 cm
Number of Plates	25 Front (10" x 20" x 0.1") 18 Rear (14.5" x 20" x 0.1")
Total Geometric Area	16" x 10" ~ 1000 cm^2
Effective Area of Assembly	185 cm^2 ($\theta = 0$, $\lambda = 10$ Å) 264 cm^2 ($\theta = 0$, $\lambda = 44$ Å)
Detector Efficiency	.65 ($\lambda = 10$ Å) .55 ($\lambda = 44$ Å)
Net Effective Area	120 cm^2 ($\theta = 0$, $\lambda = 10$ Å) 145 cm^2 ($\theta = 0$, $\lambda = 44$ Å)
Field of View	40 ARC MINUTES, RADIUS, FWHM
Angular Resolution	3 arc min x 3 arc min

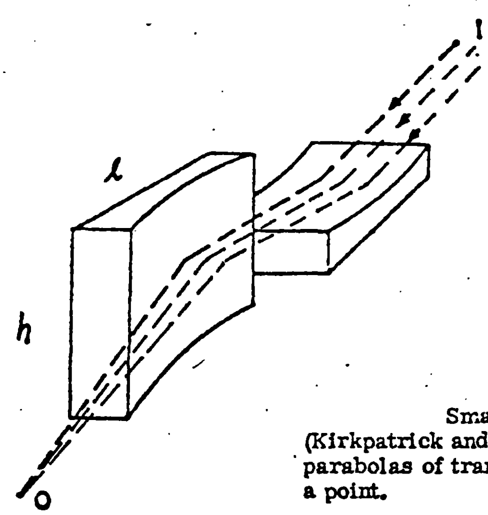

Small angle reflection by two orthogonal curved surfaces (Kirkpatrick and Baez). If surfaces have the proper curvature, e.g. parabolas of translation, a parallel beam of radiation is focused to a point.

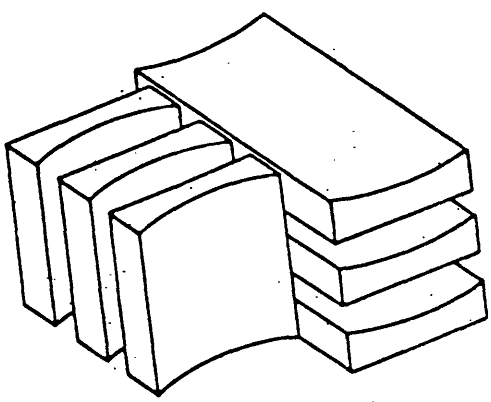

Fig. 3.34. Summary of the characteristics of the SAO X-ray imaging rocket payload (Gorenstein et al. 1975)

HEAO-B EXPERIMENT CONFIGURATION

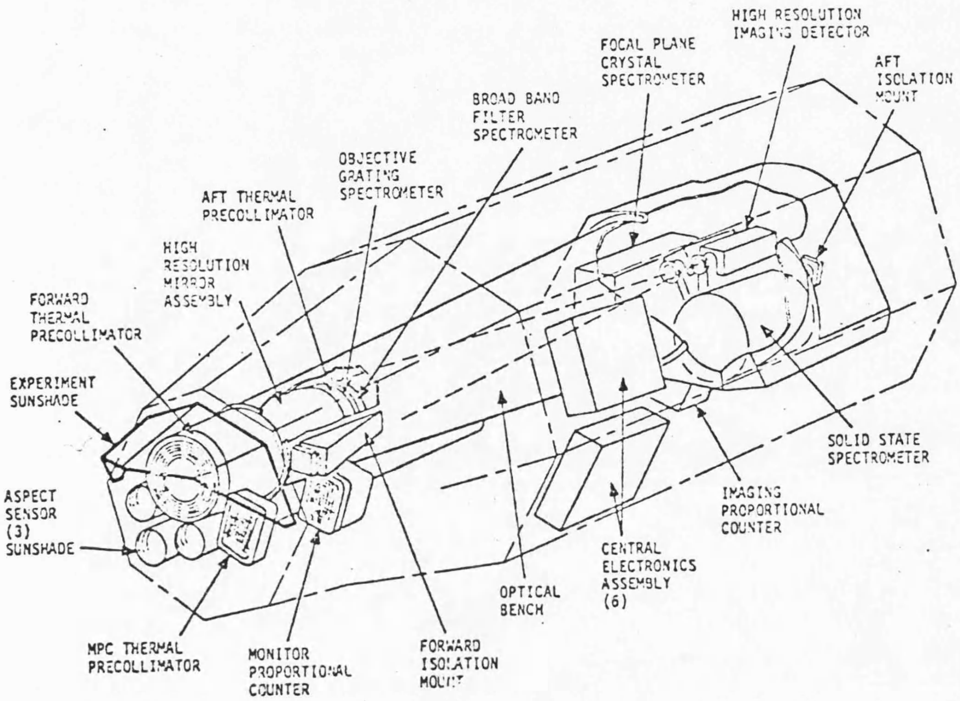

HEAO-B INSTRUMENT PARAMETERS SUMMARY

Instrument	Field of View	Spatial Resolution	Effective Area	Energy Resolution ($E/\Delta E$) (Range)	Time Resolution	Background
High Resolution Imager	25' Diam.	2" within 5' of axis (determined by mirror response)	$\sim$ 20 cm^2 at $\frac{1}{4}$ keV $\sim$ 10 cm^2 at 1 keV $\sim$ 5 cm^2 at 2 keV	3 color w/BBFS* 50-10 w/OGS** (0.15-3.0 keV)	8 μsec	5×10^{-3} cts/arcmin^2-sec
Imaging Proportional Counter	75' x 75'	1'	$\sim$ 100 cm^2	0.7 at $\frac{1}{4}$ keV 3-4 at 1.5-4 keV (0.15-4.0 keV)	63 μsec	3×10^{-3} cts/arcmin^2-sec
Solid State Spectrometer	6' Diam.		200 cm^2	3-25 (0.4-4.0 keV)	2 μsec - 5 msec	10^{-2} cts/sec
Focal Plane Crystal Spectrometer	6' Diam. 1' x 20' 2' x 20' 3' x 30'		1 cm^2 at $E < .28$ keV 0.1-1 cm^2 at $E > .28$ keV	50-100, $E < 0.4$ keV 100-1000, $E > 0.4$ keV	8 μsec	5×10^{-3} cts/sec
Monitor Proportional Counter	1.5° x 1.5° FWFM Collimated		600 cm^2	5 at 6 keV (1.5-20 keV)	1 μsec for $\Delta t < 64$ μsec $\Delta t/100$ for $\Delta t > 64$ μsec	10 cts/sec

* BBFS = Broad-Band Filter Spectrometer

** OGS = Objective Grating Spectrometer

Fig. 3.35. Summary of the characteristics of the X-ray imaging satellite payload, HEAO-B (Schreier 1977).

IPC Efficiency Parameters

(a) Entrance window	77% transmissive mesh
	0.2 μm carbon dag
	2 μm polypropylene, det. A
	0.4 μm lexan, det. A
	3 μm mylar, det. B
(b) Absorbing gas	800 torr, STP
	4 cm deep
	Composition
	Argon 84%
	Xenon 6%
	CO_2 10%
(c) Active area	7.62 x 7.62 cm, total window
	3.8 x 3.8 cm, unobstructed area
(d) Sensitivity	1 count sec^{-1} per UFU or
	1 count sec^{-1} per 4×10^{-11} erg cm^{-2} sec^{-1}
	(0.1 - 4 keV, Crab spectrum)
(e) Non-X-ray background	1.5×10^{-3} counts mm^{-2} sec^{-1}, 0.1-1.5 keV
	1.5×10^{-3} counts mm^{-2} sec^{-1}, 1.5-4 keV

IPC Performance Parameters

(a) Spatial resolution*:	1 arcmin, 1.5 keV and above
	2 arcmin, 0.28 keV
	10 bits per coordinate
(b) Energy resolution (32 channel PHA)	≤ 50% FWHM, 1.5 keV and above
	140% FWHM, 0.28 keV
(c) Temporal resolution	63 μ seconds
(d) Count rate capacity	125 per second, telemetry limit
(e) Background rejection	background counter provides anticoincidence veto signal

*2σ of an assumed Gaussian point-spread function.

The resolution becomes limited by the mirror performance at the edges of the field of view.

Fig. 3.36. Summary of the HEAO-B IPC characteristics.

It is clear that both the SAO and MIT-UL X-ray imaging rocket payloads, each of moderate angular resolution, and low background sensitivity, are able to provide, in the pre - HEAO-B era, highly significant astronomical X-ray images, to provide deeper insight into high energy astrophysical processes and to contribute to enabling a detailed observing programme for HEAO-B to be assembled, along with associated computer image processing packages.

3.4 Summary

Details of the design and operating characteristics of a wide angle ($2^o \times 2^o$), moderate resolution (6' (RMS)) imaging X-ray telescope have been given. The nominal operational wavelength band is (0.1 - 1.8 keV) and the limiting sensitivity for discrete source detection is approximately 5×10^{-11} erg / cm^2.s (0.2 - 0.8 keV).

The X-ray telescope was subsequently integrated aboard an Astrobee sounding rocket and an observation of the Cygnus Loop SNR was performed, together with an observation of the stellar source, Sco. X-1. The telescope flight and performance parameters are reported in Chapter 4.

References.

Backmann, D., 1977. Private communication, MIT.

Blalock, T., 1965. Oak Ridge National Laboratory Report, ORNL-TM-1055.

Borkowski, C. and M. Kopp, 1968. Rev. Sci. Instr., 39, 1515.

Borkowski, C. and M. Kopp, 1970. IEEE Trans. Nucl. Sci., NS-17, 340.

Borkowski, C. and M. Kopp, 1972. IEEE Trans. Nucl. Sci., NS-19, 161.

Borkowski, C. and M. Kopp, 1975. Rev. Sci. Instr., 46, 751.

Boughan, E., 1977. Private communication, MIT.

Bunemann, O., T. Cranshaw and J. Harvey, 1949. Can. J. Phys. 27, 192.

Charpak, G., R. Bouchier, T. Bressani, J. Favrier and C. Zupancic, 1968. NIM, 62, 235.

Charpak, G., 1970. Ann. Rev. Nucl. Sci., 21, 196.

Charpak, G., D. Rahm and H. Steiner, 1970. NIM, 80, 13.

Charpak, G., 1974. IEEE Trans. Nucl. Sci., NS-21, 38.

Charpak, G., G. Petersen, A. Policarpo and F. Sauli, 1978. NIM, 148, 471.

Christie, P., K. Evans, J. Griffiths, E. Mathieson and P. Murphy, 1975b. NIM, 130, 279.

Cochran, L. and D. Forrester, 1962. Phys. Rev., 126, 1785.

Compton, A., 1923. Phil. Mag., 45, 1121.

Compton, A. and S. Allison, 1963. X-rays in theory and experiment. D. Van Nostrand Co., NY.

Cottrell, T. and I. Walker, 1965. Trans. Faraday, Soc., 61, 1585.

Cottrell, T. and I. Walker, 1967. Trans. Faraday, Soc., 63, 549.

Davidsen, A., S. Shulman, G. Fritz, J. Meekins, R. Henry and H. Friedmann, 1972. Ap.J., 177, 629.

Desai, U. and S. Holt, 1972. IEEE Trans. Nucl. Sci., NS-19, 592.

English, W. and G. Hanna, 1953. Can. J. Phys., 31, 764.

Evans, K., 1978. Private communication, University of Leicester.

Fraser, G., 1978. Private communication, University of Leicester.

Giacconi, R. and B. Rossi, 1960. J. Geog. Res., 65, 773.

Giacconi, R., W. Reidy, G. Vaiana, L. Van-Speybroeck and T. Zehnpfennig, 1969. Sp. Sci. Rev., 9, 3.

Gorenstein, P., H. Gursky, F. Harnden, A. DeCaprio and P. Bjorkholm, 1975. IEEE Trans. Nucl. Sci., NS-22, 616.

Gorenstein, P., D. Fabricant, K. Topka, W. Tucker and F. Harnden, 1977. Ap. J. (Lett.), 216, L99.

Gorenstein, P., D. Fabricant, K. Topka, F. Harnden and W. Tucker, 1978. CFA preprint.

Gursky, H. and D. Schwartz, 1974. X-ray Astronomy. ed. R. Giacconi and H. Gursky, D. Reidel Publ. Co., Dordrecht, NL.

Halpern, J., 1976. B.S. Thesis, MIT.

Harnden, F., D. Fabricant, K. Topka, B. Flannery, W. Tucker and P. Gorenstein, 1977. Ap. J., 214, 418.

Hayakawa, S., T. Kato, F. Makino, H. Ogawa, Y. Tanaka and K. Yamashita, 1970. Jap. J. Appl. Phys., 9, 542.

Hendricks, R., 1973. NIM, 106, 579.

Hough, J., 1972. NIM, 105, 323.

Humphrey, A., R. Cabral, R. Brissette, R. Carroll, J. Morris and P. Harvey, 1978. IEEE Trans. Nucl. Sci., NS-25, 445.

Huxley, L. and R. Crompton, 1974. The diffusion and drift of electrons in gases. Wiley-Interscience, London.

Kellogg, E., P. Henry, S. Murray and L. Van Speybroeck, 1976. Rev. Sci. Instr., 47, 282.

Kirkpatrick, D. and A. Baez, 1948. J. Opt. Soc. Am., 38, 766.

Kuhlmann, W., K. Lauterzung, B. Schimmer and K. Sistemich, 1966. NIM, 40, 118.

Magnus, J. and J. Underwood, 1969. Appl. Opt., 8, 95.

Mathieson, E., 1971. NIM, 97, 171.

Mathieson, E., K. Evans, W. Parkes and P. Christie, 1974. NIM, 121, 139.

Mathieson, E., K. Evans, K. Cole and R. Everett, 1975a. NIM, 126, 199.

Mathieson, E., 1976. Internal memo, University of Leicester.

Miller, G., N. Williams, A. Senator, R. Stensgaard and J. Fisher, 1971. NIM, 91, 389.

Nowlin, C., 1976. Rev. Sci. Instr., 47, 684.

Palladino, V. and B. Sadoulet, 1975. NIM, 128, 323.

Rappaport, S., K. Pounds, H. Bradt, C. Canizares, G. Clark, D. Hearn, P. Joss, W. Lewin, K. Evans, E. Mathieson, B. Cooke and R. Griffiths, 1974. Proposal to NASA for a soft X-ray imaging telescope to be launched from a Scout vehicle.

Rappaport, S., A. Levine and R. Petre, 1977. Private communication, MIT.

Rappaport, S., 1977. Private communication, MIT.

Ricketts, M., 1973. Thesis, University of Leicester.

Schreier, E., 1977. CFA preprint.

Smith, A., 1977. Thesis, University of Leicester.

Trippe, T., 1969. CERN NP Intern. Rep. 69 - 18.

Underwood, J., 1975. Sp. Sci. Instr., 1, 289.

Underwood, J., J. Milligan, A. deLooch and R. Hoover, 1977. Appl. Op., 16, 858.

Van Speybroeck, L. and R. Chase, 1972. Appl. Op., 11, 440.

Wolter, H., 1952a, Ann. Physik, 10, 94.

Wolter, H., 1952b. Ann Physik, 10, 286.

Chapter 4. FLIGHT AND PERFORMANCE OF THE X-RAY TELESCOPE.

Chapter 4. FLIGHT AND PERFORMANCE OF THE X-RAY TELESCOPE.

4.1 Flight preparation.

4.1.1 Attitude control system (ACS)

A nominal ACS pointing accuracy of $\pm$ 20' for the Cygnus Loop observation (together with $\pm$ 30' for the Sco. X-1 observation) was required to ensure a successful X-ray imaging astronomy experiment, taking into account the characteristics of the X-ray telescope (3.3). Pointing to $\pm 1^{\circ}$ would give a marginally successful result. A satisfactory pointing system was the NASA - GSFC STRAP IV ACS. The STRAP IV unit (stellar Tracking Rocket Attitude Positioning) is a 3-axis stabilised, cold gas reaction jet system, with a star sensor and auxiliary low-thrust jet system, capable of achieving a limit-cycle performance of $\sim$ 30" for 3rd magnitude objects. The worst case pointing alignment on a first target is $\pm 3^{\circ}$ in all three axes (pitch, yaw and roll) and 1% of the manoeuvres to each additional target. The star sensor updates the two control axes to a few arc min. The worst case pointing mis-alignment (in the third axis) then is $\theta . \sin 3^{\circ}$, where θ is the angle from the update star to the target, and $\theta \lesssim 5^{\circ}$. To update the third axis, the STRAP IV unit manoeuvres to a second star by one of the update axes, and measures the miss-angle in the second updated axis. This angle is then transferred to the third axis. The worst case third axis alignment becomes $\sim 1.5^{\circ}$ if a pitch manoeuvre is used between the two stars, and $\sim$ 47' if a yaw manoeuvre is used. The target miss-angle, $b \sim \sin(\sin B . \sin a)$ where B is the third axis mis-alignment angle and a is the angle between the last update star and the target (Lau 1977) Hence, for small third axis mis-alignment and small update star - target angle, the miss-angle is also small.

The actual STRAP IV unit used for the X-ray telescope rocket payload had previously been flown successfully three times before (Lau 1977).

The update stars chosen, in view of the ACS constraints above, were ε Cyg. for the first target (Cygnus Loop SNR) and ζ Oph. for the second target (Sco. X-1). Details of these update stars are given in Table 4.1. ε Cyg. is 3.1° away from the Cygnus Loop centre (RA(1950) $\sim$ $20^{h}49^{m}.5$, Dec. (1950) $\sim$ $30^{\circ}.7$) and ζ Oph. is 7° away from Sco. X-1, and are the only $\sim$ 3^{rd} magnitude stars within the search areas for each target.

TABLE 4.1

ε Cyg. (Gienar)

Epoch (1900)

α	δ	d (pc)	m_v [a]	B-V [a]	Sp [a]
$20^{h}42^{m}10^{s}$	$+33^{\circ}36'$	23	2.5	+1.03	KOIII

ζ Oph.

Epoch (1900)

α	δ	d (pc)	m_v [b]	B-V [b]	N_H [bd]	n_H [be]	Sp [c]
$16^{h}31^{m}39^{s}$	$-10^{\circ}22'$	190	2.57	+0.02	4.2	0.8	09.5Ve

[a] Allen (1973)

[b] Jenkins (1970)

[c] Conti and Leep (1974)

[d] Units of 10^{20} cm^{-2}

[e] Units of cm^{-3}

The first update star, ε Cyg., is a cool giant. ζ Oph. is an O-B runaway (Blaauw 1961), singly rotating, early-type

Plate 4.1 View of the star field camera (top centre), alignment mirror (left) and star tracker (red), positioned in the front baffle of the nested mirror system.

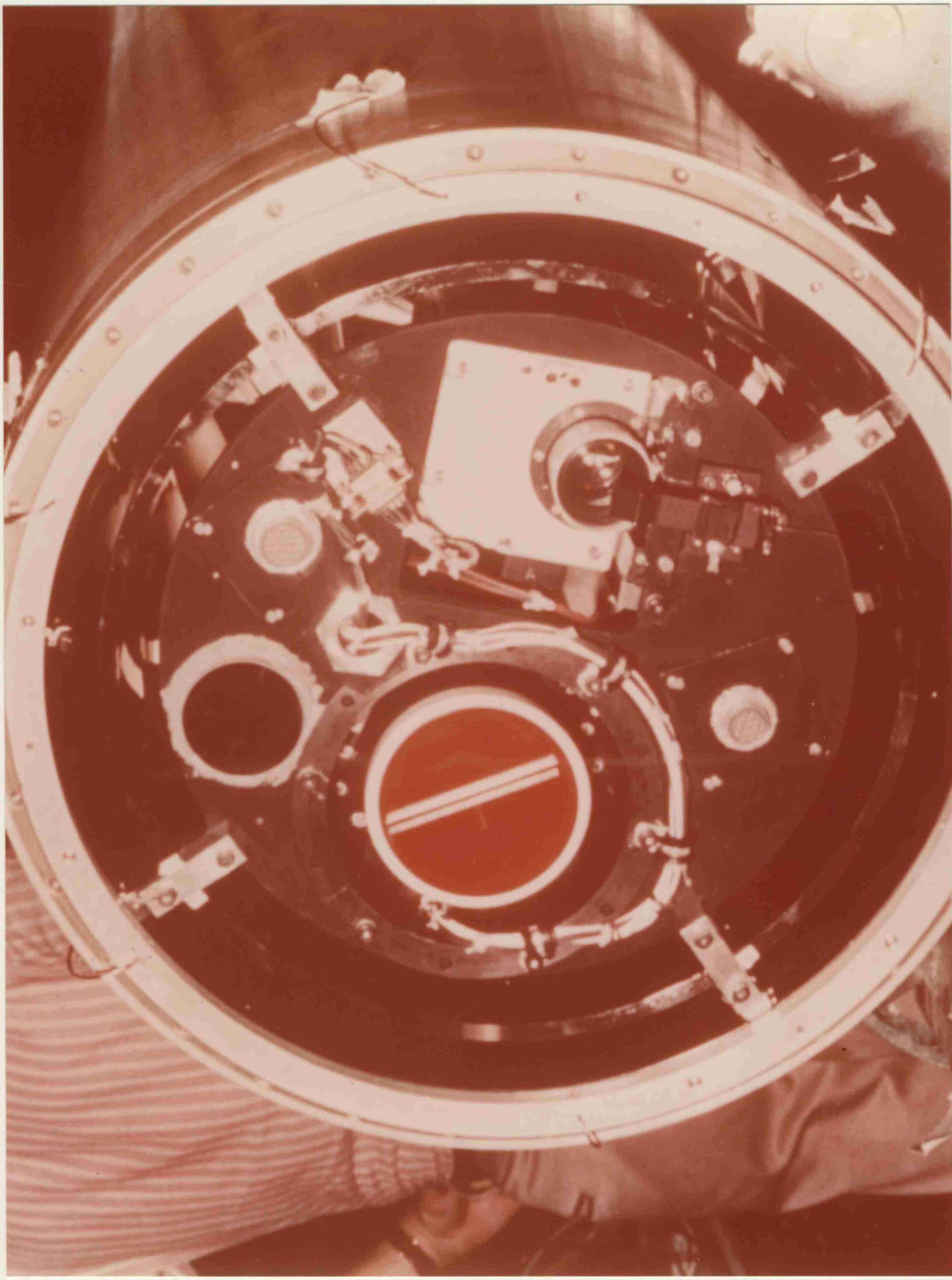

TABLE 4.2

Summary of experiment data TM channel designations.

Programme designation		Experiment data
2 - 0 - 0	IPC	ΔX TAC (X position)
3 - 0 - 0	IPC	X
4 - 0 - 0	IPC	1 - X
5 - 0 - 0	IPC	Antico. rate.
6 - 0 - 0	Gas pack	Pressure transducer.
7 - 0 - 0	IPC	Anode pulse height.
8 - 0 - 0	IPC	ΔY TAC (Y position)
9 - 0 - 0	IPC	Y
10 - 0 - 0	IPC	1 - Y
11 - 0 - 0	Aspect Camera	Camera and sync. pulse.

The PCM unit encoded the IPC X and Y, 0 - 5V, digital position pulses into 512 levels. Each level was equivalent to 9.5 mV. From laboratory calibrations (3.3.2), the average position voltage conversion gain of the X and Y axes, was $\sim$ 50 mV / mm, hence each PCM level corresponded to $\sim$ 0.2 mm, a factor of $\sim$ 5 up on the measured linear resolution of the IPC at Cu - $L_{\alpha_1 \alpha_2}$ (0.93 keV), $\sim$ 1 mm (FWHM).

4.1.3 Rocket payload configuration.

The complete rocket payload is shown in Fig. 4. 1 (a) and (b). A final determination of the mass properties of the payload enabled the ACS yaw and pitch regulators to be set to perform, in timed sequences according to the flight plan. For the first time for an Astrobee experiment, a three fin configuration (instead of the usual four) was to be used. This entailed placing extra weights in the nose cone. Due to the proximity of the X-ray optics, these weights were made of brass (low out - gassing characteristics). Fig. 4.2 (a) and (b) show the relative orientation of the IPC X and Y axes

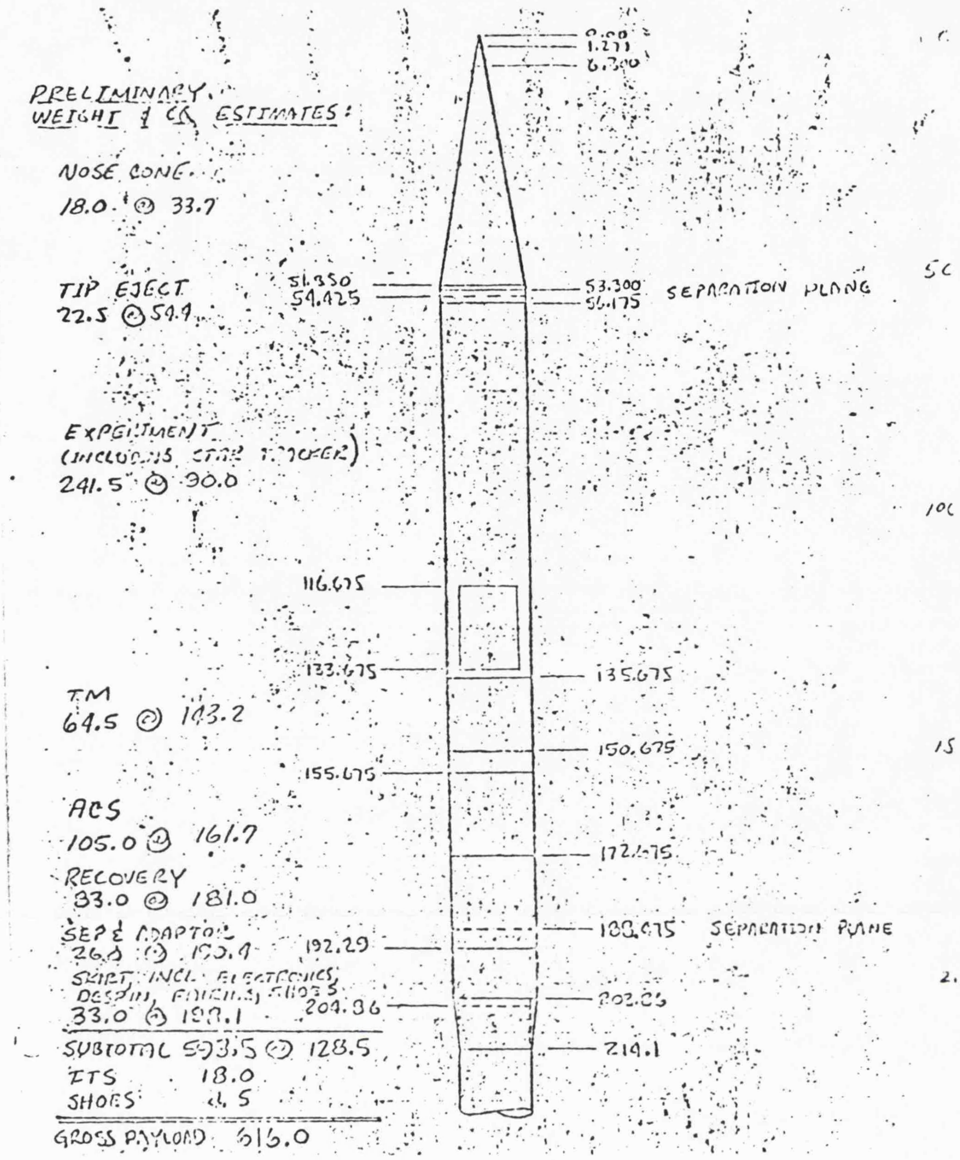

Fig. 4.1 (a) Rocket payload configuration.

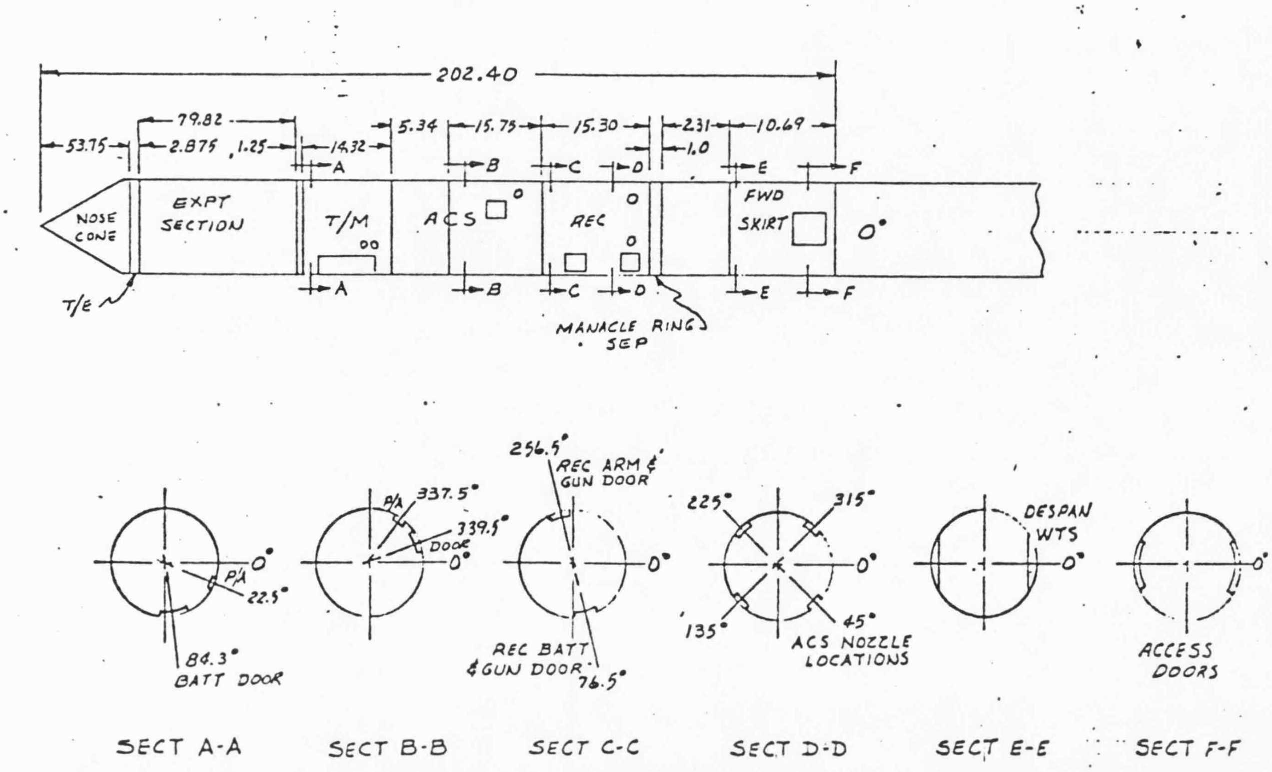

Fig. 4.1 (b) ACS configuration.

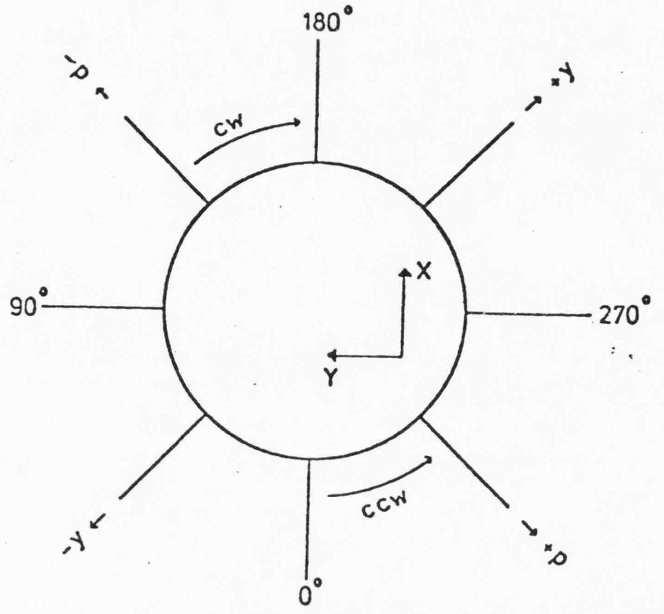

(a)

Fig. 4.2. (a) Relative orientation of the IPC X and Y axes with respect to the ACS control axes: view down the payload towards the ground.

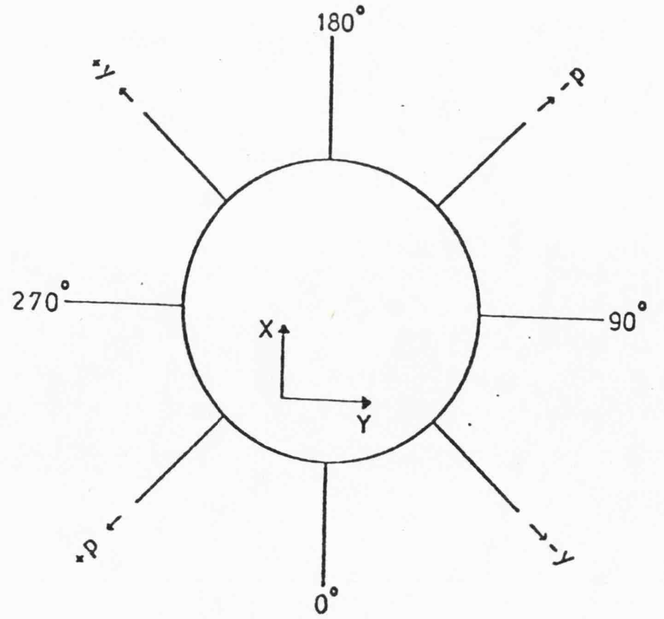

(b)

Fig. 4.2. (b) Relative orientation of the IPC X and Y axes with respect to the ACS control axes: view up the payload towards the sky.

with respect to the ACS control axes. Plate 4.2 presents a view of the IPC, gas pack and electronic boards. The head and motor have been integrated in the launch tower and in the period before launch the IPC was continiously evacuated with the gas pack used in external mode (3.3.2). An envelope of polythene around the head (experiment section including the nose cone) was continiously filled with dry N_2 to protect the X-ray optics from condensing particle - laden water vapour.

4.1.4 Pre - launch experiment calibrations.

Fig. 4.3 shows the IPC energy and line responses, in two - dimensions, to the centrally located Al - K flourescence source (3.3.2), at $\sim$ 37 c/s, immediately prior to launch, with the experiment powered by the flight batteries and gas pack in internal mode. Table 4.3 shows the IPC characteristics directly before launch.

TABLE 4.3

Pre - launch IPC characteristics.

IPC anode charge conversion gain	0.6 pc/keV
IPC X-ray energy resolution at 1.49 keV	43.1%
IPC gas mix	23.1%A + 76.9%CH_4
IPC X position voltage conversion gain	40.5 $\pm$ 5 mV/mm
IPC Y position voltage conversion gain	63.3 $\pm$ 5 mV/mm
IPC average background count rate	4 c/s
IPC average antico. rejection efficiency	75%

The quoted limits for the X and Y position voltage gain values were derived from the estimated systematic error in the measurement procedure.

IPC linear resolution in each axis could not be directly determined by the method adopted for pre-launch X-ray calibration, but the X and Y position voltage conversion gain values could be monitored. The Al-K flourescent X-ray source appeared as a local line source in front of the IPC

Plate 4.2 View through the payload access door of the IPC, gas pack and electronic boards. The rocket is standing in the launch tower at White Sands Missile Range.

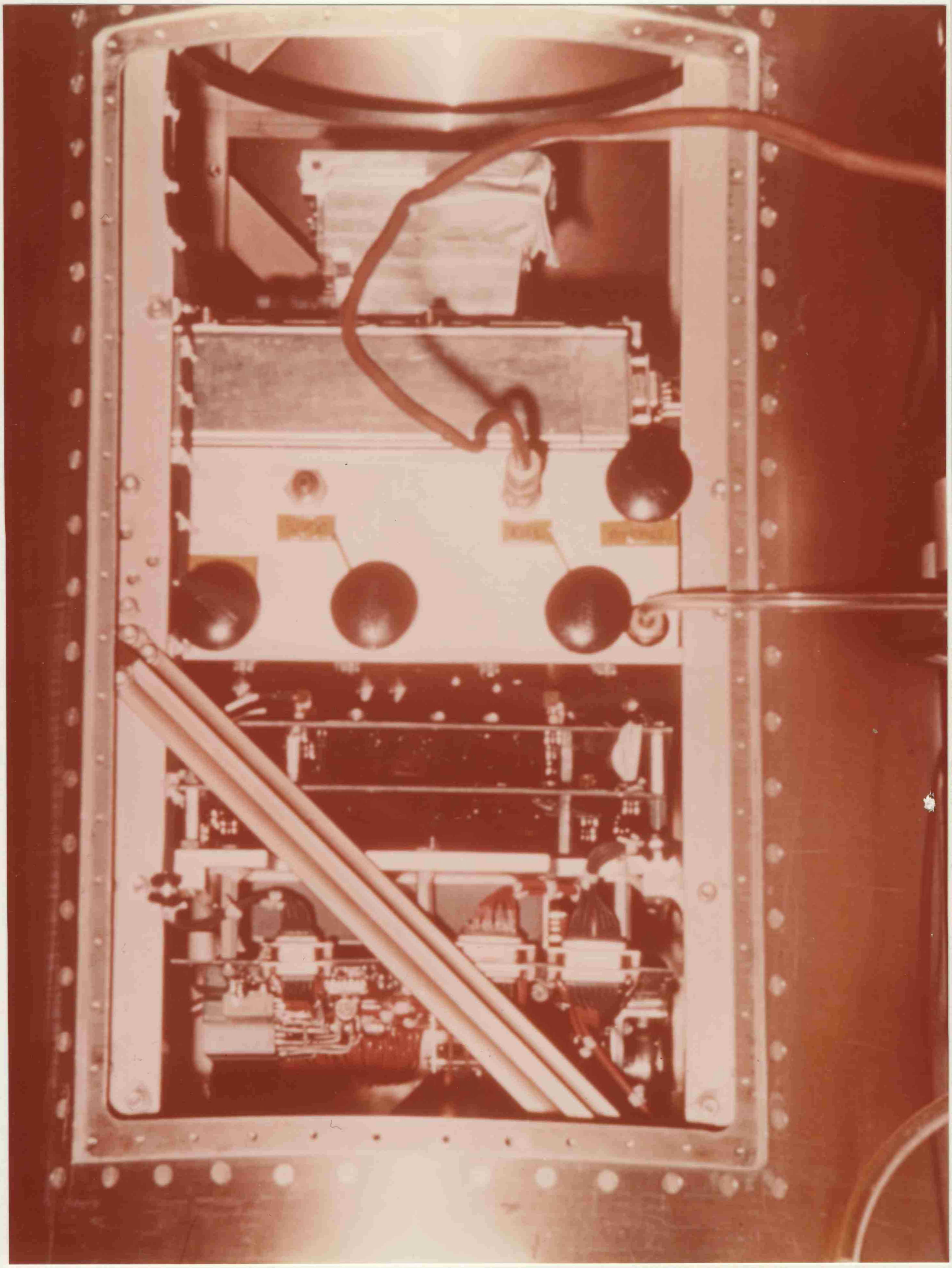

window with the X-rays contained in a disc size, incident on the window, of $\sim$ 21.4 mm (3.3.2 for source geometry). For X and Y position voltage conversion gains of $\sim$ 40 mV/mm and $\sim$ 60 mV/mm, respectively, the expected X and Y position spectra would have base widths $\sim$ 900 mV and 1300 mV respectively. Since the IPC window support cross-section spacing was 11.3 mm, the position spectra were expected to show a shadowing effect due to one support in each IPC axis. These voltage widths and shadowing effects were observed in the pre-launch position spectra.

4.2 Flight details.

4.2.1 ACS and experiment programme.

The primary target, the Cygnus Loop SNR is an optically diffuse, extended object of $\sim 3^{\circ}$ angular diameter, comparable with the maximum field of view of the telescope. Since the r m s width of the telescope point response was $\gtrsim$ 20' for off-axis angles $\gtrsim 1.5^{\circ}$, two parallel scan manoeuvres for the rocket payload were required for the SNR observation, to produce an X-ray image of $\sim$ 10' resolution. The planned scan paths (for the telescope axis) ran southward through 4.7°, at a rate of 0.05°/s, across the eastern half of the SNR, passing within 1° of the apparent centre, and northward, across the western half, $\sim 2^{\circ}$ away from, and parallel to, the first scan path and at the same scan rate. Each scan manoeuvre would take 94 s to complete. These scan manoeuvres would erase the IPC window support response and wire binning effects (3.3.2) from the X-ray image, together with effectively correcting for the overall telescope non-linear response (3.3) and ensuring a more uniform exposure across the extended SNR.

Following the Cygnus Loop observation the telescope would image Sco. X-1 to perform an in-flight point response calibration.

The launch window for July was calculated (A. Levine 1977) taking into account the ACS launch constraints (4.1.1) and the following constraints imposed by considerations of telescope

X-ray sensitivity :

(1) Sun - zenith angle for negligable flux of scattered solar X-rays in the upper atmosphere (Hayakawa et al. 1971) $\geqslant 130^{\circ}$

(2) Cygnus Loop - zenith angle for short ACS acquisition time. $\leqslant 30^{\circ}$

(3) Sco. X-1 - zenith angle for negligable soft X-ray absorption in the upper atmosphere (i.e $< 5\%$ at $N\text{-}L_{\alpha_1,\alpha_2}$ edge) $\leqslant 70^{\circ}$

In practise, after several days of severe magnetic storms (a no-go situation for the ACS) the telescope was launched aboard the Astrobee F sounding rocket designated NASA R25.021 UHX, (Plate 4.3), on July 27th 1977 at $05^{h}35^{m}00^{s}$ UT from the White Sands Missile Range, New Mexico. Details of the launch site parameters and solar, lunar and target positions, at launch, are given in Table 4.4.

Plate 4.3 Launch of X-ray telescope, July 27th 1977, 05^{h} 35^{m} 00^{s} UT.

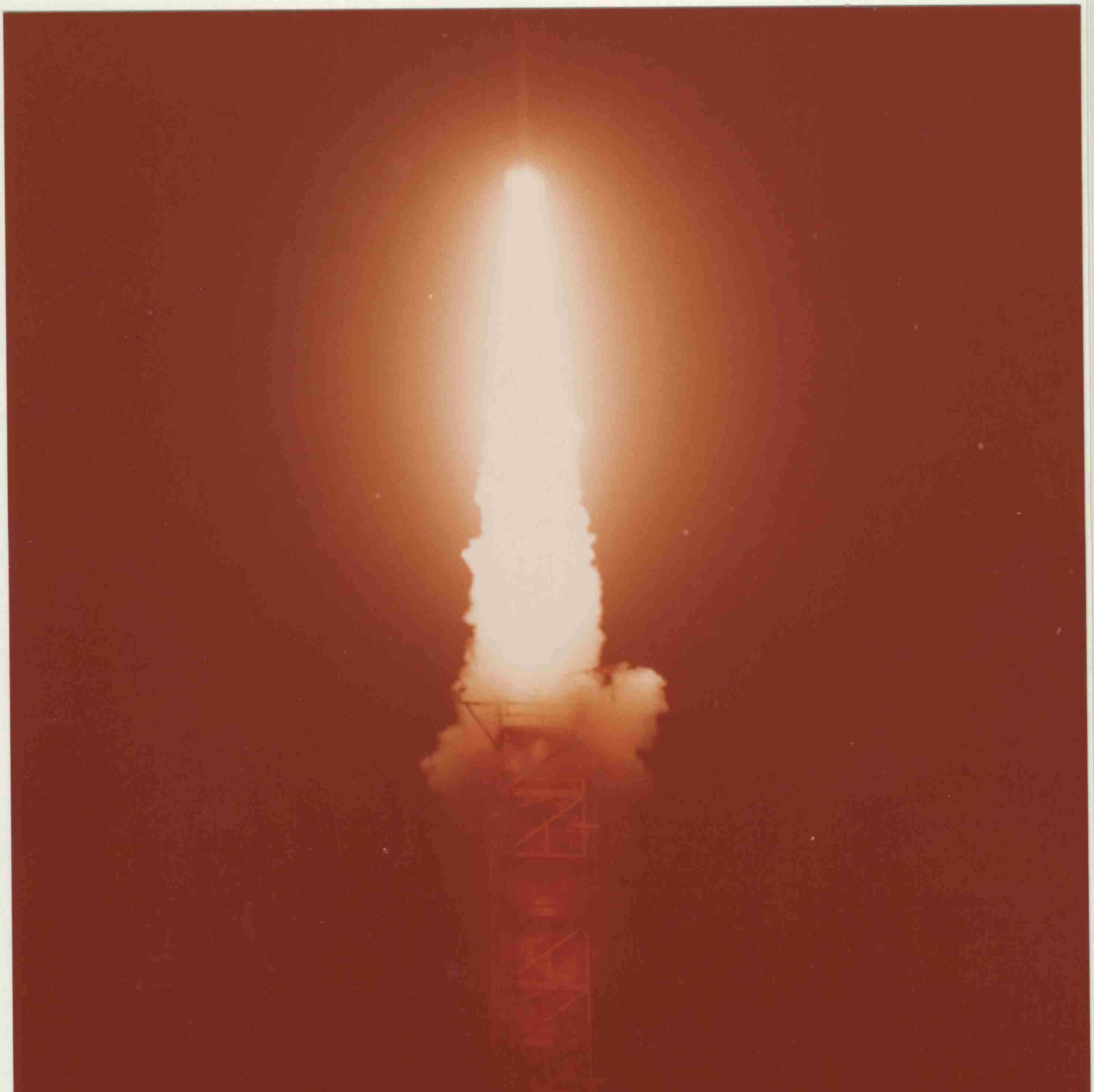

TABLE 4.4

Launch site parameters.	
Local siderial time	$18^h\ 48^m\ 47^s$
'A' tower : longitude	$7^h\ 05^m\ 22^s$ W
lattitude	$+ 32.418^\circ$
Yaw azimuth	315°
Sun, moon and target zenith angles.	
Sun - zenith angle	121.5°
Moon - zenith angle	71.7°
ε Cyg. - zenith angle	24.3°
ε Cyg. - moon angle	71.9°
Cygnus Loop - zenith angle	25.7°
ζ Oph. - zenith angle	58.5°
ζ Oph. - moon angle	13.1°
Sco. X-1 - zenith angle	60.1°

The payload flight operations and experiment programmes are shown in Fig. 4.4 and the ACS times for manoeuvres in Table 4.5. A peak altitude of 187.2 km was achieved, 240 s into the flight. The payload was successfully recovered after the flight.

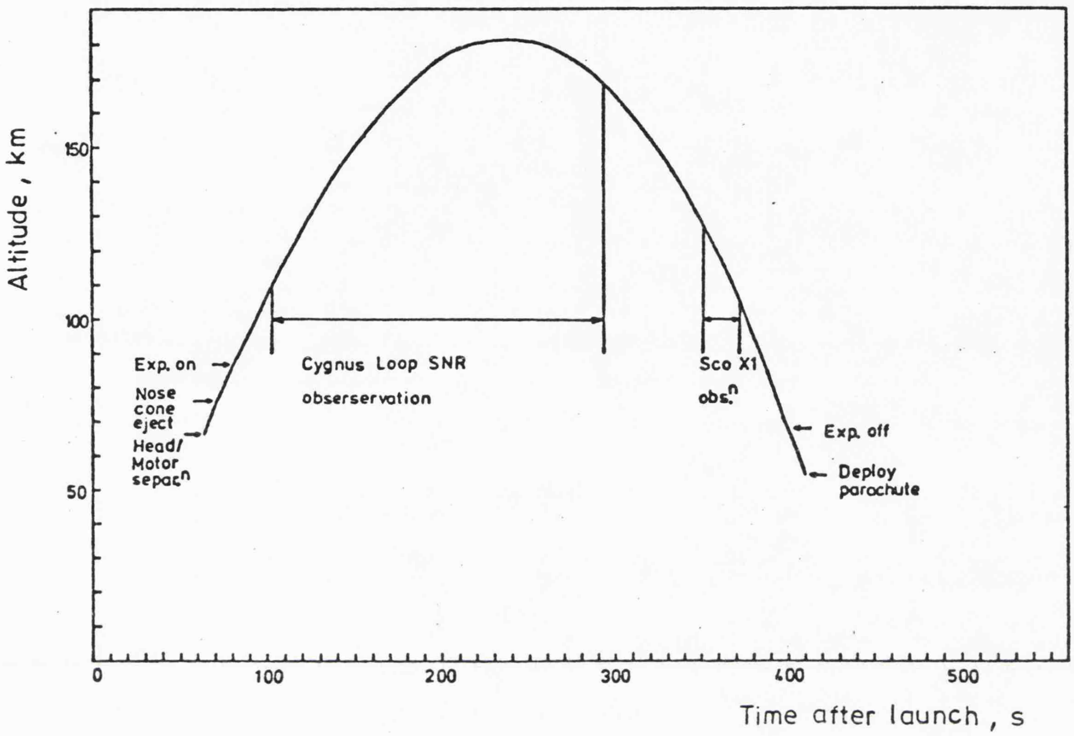

Fig. 4.4. The free-flight trajectory of the X-ray telescope after being launched aboard an Astrobee sounding rocket.

TABLE 4.5

ACS manoeuvre	Time into flight (s)
Update on ϵ Cyg.	93.0
Intermediate mode on ϵ Cyg.	96.0
Fine mode on ϵ Cyg.	100.0
Begin Cygnus Loop scan (along positive pitch axis)	102.6
Fine mode on first scan	103.0
Move to second scan start position (along negative yaw axis)	196.6
Begin second Cygnus Loop scan (along negative pitch axis)	199.3
Fine mode	204.0
End Cygnus Loop scan	293.3
Update on ϵ Cyg.	294.8 - 302.2
Yaw to ζ Oph.	319.0
Intermediate mode on ζ Oph.	322.0
Yaw to Sco. X-1	344.0
Arrive within 1.2^{o} of Sco. X-1	346.2
Pitch to Sco. X-1	348.9
Rig capture	349.3
On Sco. X-1	351.0
Fine mode	352.0 - 372.0

The 16mm film from the aspect camera revealed the locus of the fiducial light image (hence roll axis) moving in the star fields photographed throughout the flight. TM data, recorded in time on UV paper chart, yielded the timing information of the film exposures (2 per second) together with the light marker clutch pulse (every 16 exposures), for synchronizing the time and exposure number. With templates containing star positions (SAO - 4 Star Catelogue) overlaid on the magnified film exposures, the RA and Dec. of the fiducial light image as a function of time was determined,

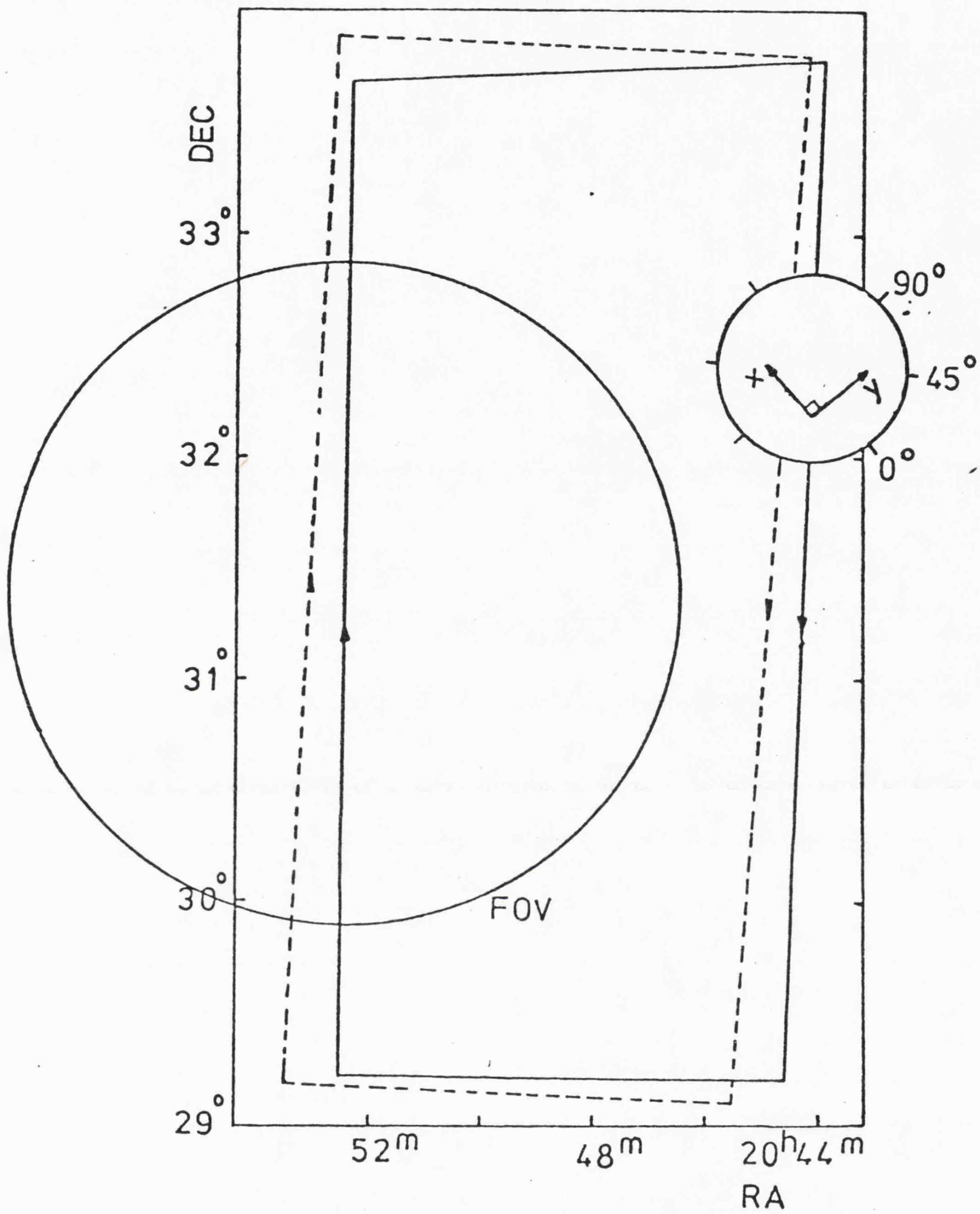

Fig. 4.5 ACS planned maneuvers (----) and the actual flight scan paths (———) in RA and Dec.. Also shown are the X-ray telescope field of view (FOV) and orientation of the IPC axes. The IPC axes are at ± 45° with respect to the scan paths, which are parallel and at 1.07° from due North-South. The scan rate was 3'/s through ~ 5°.

to within 1' and hence the telescope optical axis pointing, in time, was determined with a limiting accuracy of $\sim$ 3' due to the pre-flight procedures (3.4).

For the Cygnus Loop observations, the equation of motion of the telescope axis (for each scan) was transformed off the celestial sphere onto a tangent plane at the Cygnus Loop centre, with the projections of the great circle of the yaw axis with the roll axis, and the projection of the great circle of the pitch axis with the roll axis, defining the rectangular co-ordinate system. The linear least squares fit of the telescope axis motion is shown in Fig. 4.5, together with the planned ACS manoeuvres, plotted in RA and Dec., in the region of the Cygnus Loop. The flight scan paths were parallel to one another and separated by 1.75^{o} in the east-west direction. The orientation of the IPC X and Y axis are shown, positioned at $\pm 45^{o}$ with respect to the scan paths. The equations of motion of the telescope axis, in sky co-ordinates, for each scan manoeuvre enabled a transformation of X-ray events in the IPC co-ordinates, to sky co-ordinates, to form an image matrix of the Cygnus Loop, with the bin size an adjustable parameter (5.2).

For the Sco. X-1 observation, a stationary pointing position, 34' away from Sco. X-1 for $\sim$ 20s, forming an X-ray image and revealing the telescope in-flight off-axis point response for X-ray energies in the bandwidth of the telescope.

The analogue magnetic tape of the telescope TM digitised at GSFC, was converted, on tape, to event blocks of times X and Y pulse heights and positions, anode pulse heights and anti-co. binary flags at MIT (A. Levine 1977), by conventional computational techniques. Tape was also formatted to be read by the CDC Cyber 72 at Leicester. The initial criteria for selecting pulses for further analysis were as follows :

(1) There must be an X and Y pulse height greater than the lower level discriminator values for the X and Y axis electronics, for each X and Y position pulse height.

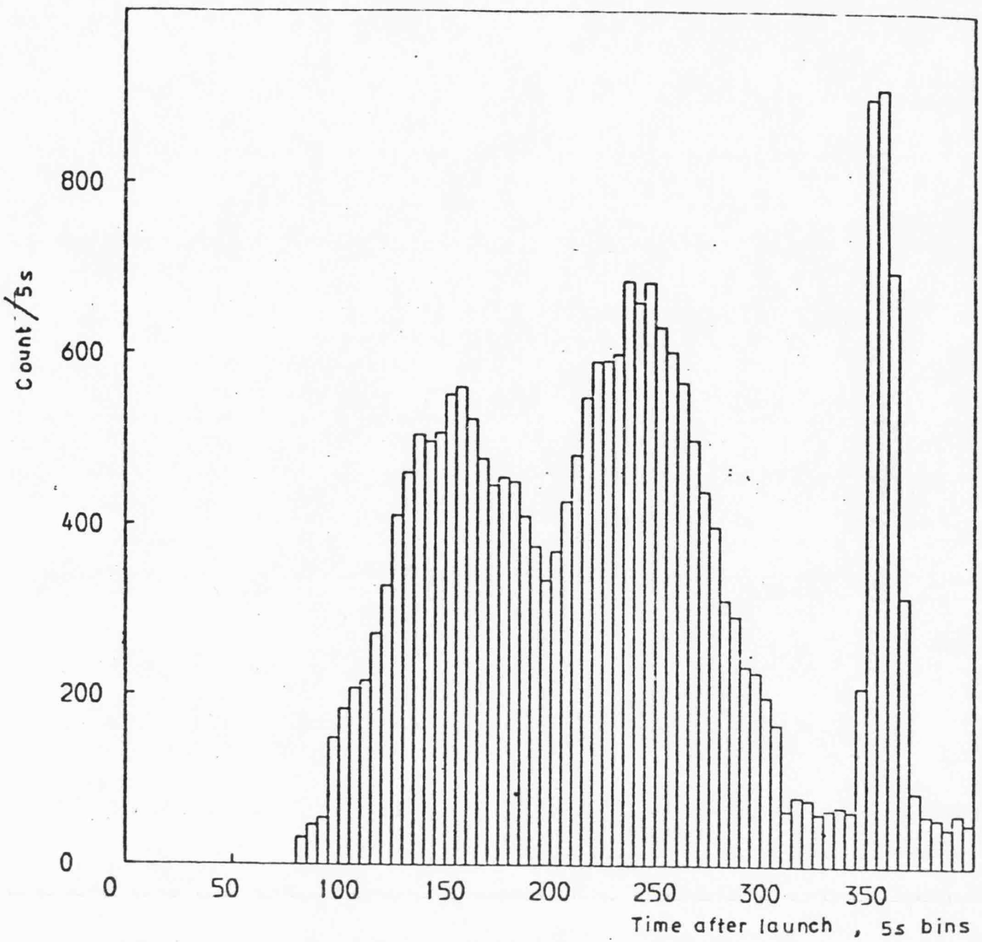

Fig. 4.5 (a) IPC anode count rate for Cygnus Loop SNR and Sco XI observations: no anti-co.

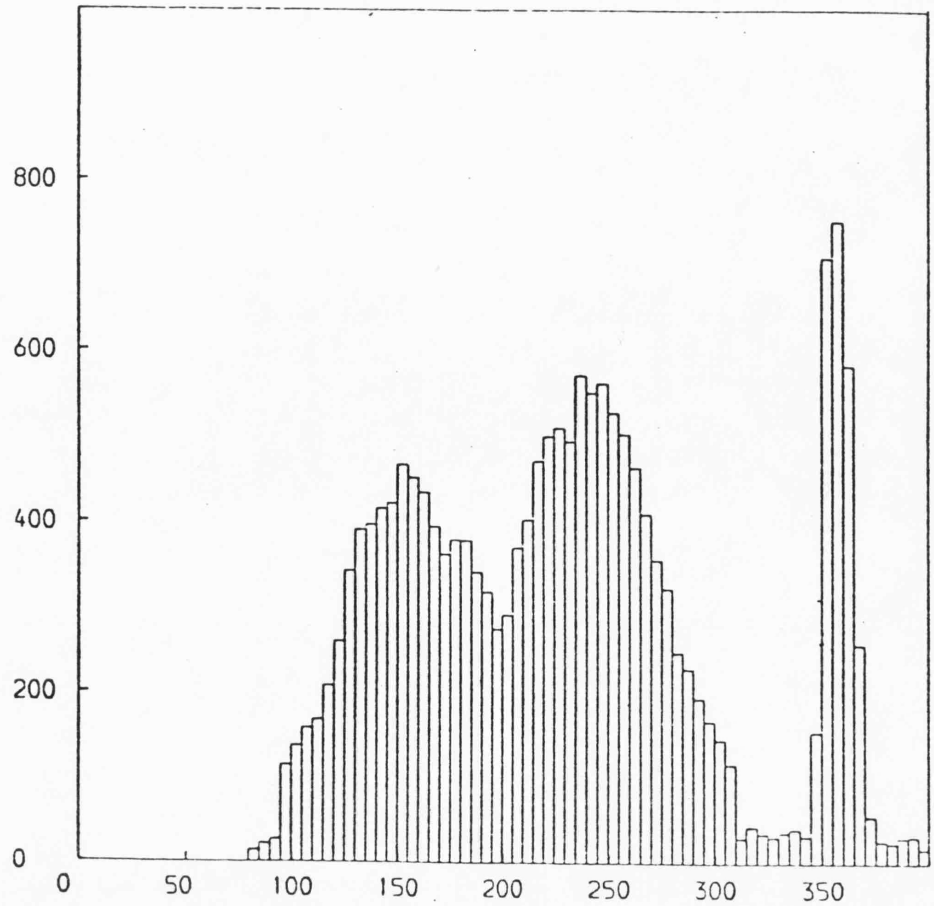

Fig. 4.5 (b) As for (a) above but including the anti-co.

(2) The X and Y pulses must occur within 1 ms.

(3) The X and Y position pulses must be above the lower level electronic thresholds.

(4) There must be an anode pulse height above the lower level electronic threshold, to within 1 ms, for each X and Y position pulse.

(5) There must be no antico. count for the anode and X and Y pulses.

The counting rate data for the entire flight over the maximum field of view and telescope bandwidth, is shown in Fig. 4.5 (a) for the anti-coincidence inactive and (b) for the anti-coincidence active. In Fig. 4.5 (b), the Cygnus Loop observation produced $\sim$ 16000 counts and Sco. X-1 $\sim$ 2500 counts.

4.2.2 Preliminary results of Cygnus Loop observation.

The anode pulse height distribution for the Cygnus Loop observation (100s - 300s after launch) is shown in Fig. 4.6 (a), plotted in 0.01V bins, with lower and upper thresholds of 0.03V and 5.00V respectively. Detailed X-ray spectral analysis of parts of the Cygnus Loop, is reserved for Chapter 6. For the present, it is remarked that earlier (Gorenstein et al. 1971, Borken et al. 1972, Bleeker et al. 1972, Stevens et at. 1973, Rappaport et al. 1974, Gronenschild et al. 1976) have convolved X-ray source emission models (continuum and line emission from hot, isothermal, optically thin plasmas) with their respective instrument energy responses, to hield a range of values for the plasma parameters describing the emission from the entire SNR. The convolved X-ray spectrum (Fig. 4.6 (a)) is similar to these earlier results, but it is shown in Chapter 6 that there is evidence for significant plasma parameter variations over the SNR region.

In Fig. 4.6 (b) and (c), the X and Y position pulse height distributions (100s - 300s after launch) are shown (0.01V bin) and subject to the constraints that the anode pulse heights are between 0.03V and 5.00V and that each of the position pulse heights are between 0.05V and 5.00V. The

Fig. 4.6 (a) Anode pulse height distribution for the Cygnus Loop observation (100s - 300s after launch), in 0.01 V bins.

Fig. 4.6 (b) X position pulse height distributions.

Fig. 4.6 (c) Y position pulse height distributions.

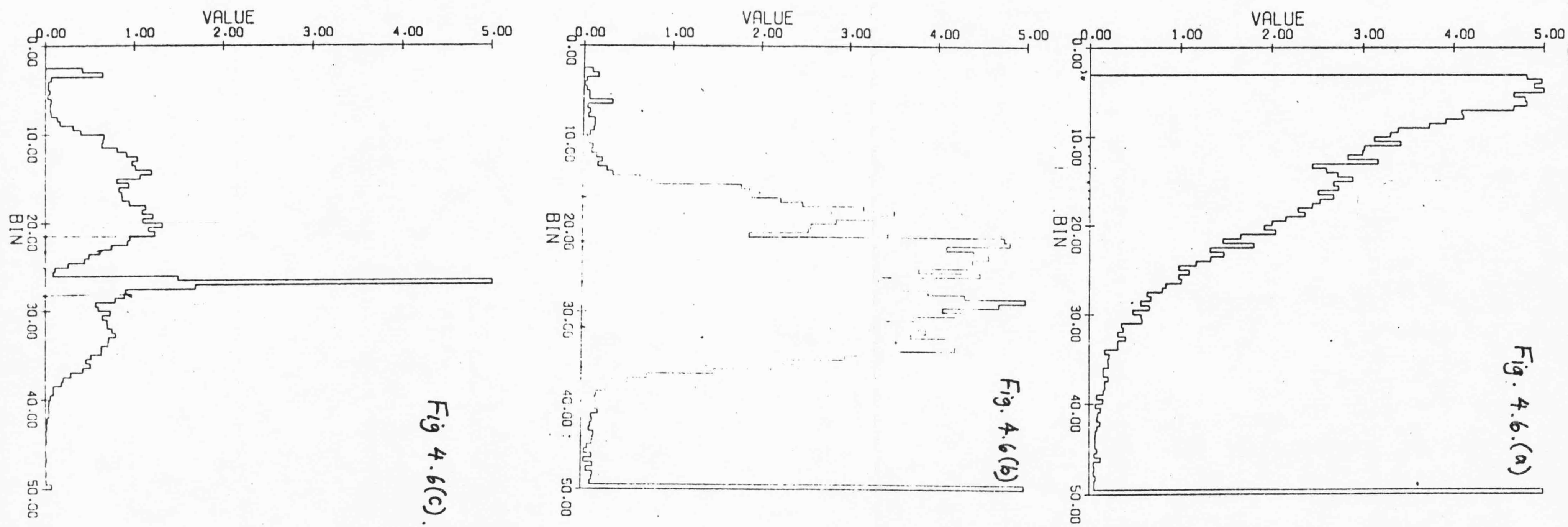

spectra exhibit the expected responses to the effective area roll-off of the X-ray optics, and to the IPC window support as the telescope moved across the extended X-ray source. However, a malfunction in the on-board position processing electronics affected X-ray events occuring in a localised region at the IPC centre, particularly in the Y-axis electronics. This fault was subsequently investigated in order to prepare the payload for a re-flight (to image Puppis A and IC443 SNR) and was explained as follows :

Each X and Y axis position processing electronics had common earth lines. For the Y-axis, the fault was most marked, the effect increasing for decreasing X-ray energy. Transients on the fast, front edge of the (1-Y) delay pulse (3.2.2) caused distortion of the Y bipolar pulse falling edge, occuring near or at the cross-over point, for low energy X-ray events localised aroung the Y-axis centre. In a direction away from the centre (to the right in Fig. 4.6 (c)) the Y bipolar pulse distortion triggered the Y zero - crossing sensing comparator, prematurely (at exactly the same time as the (1-Y) bipolar pulse cross-over time), placing Y X-ray event near the centre. This state of affairs persisted until Y X-ray events, sufficiently far away from the Y-axis centre, under-went no further significant bipolar pulse distortion, effecting the action of the comparators. Since the distortion was caused by the front edge of the (1-Y) delay, X-ray events to the left of centre (Fig. 4.6 (c)) were not effected, since the Y bipolar pulse cross-over point occurred before the (1-Y) bipolar pulse cross-over point. Higher energy X-ray events ($\gtrsim$ 0.5 keV) remained un-effected by this cross-talk, the bipolar pulse cross-over times remaining undistorted (any pulse distortions occurred high up on the bipolar falling edge).

The cross-talk was, for the most part, removed from the Y-axis by re-earthing the Y and (1-Y) channels separately. (Smith 1978).

For the Cygnus Loop observation, Y position pulse heights in the range 1.00 - 2.20V and 2.75V - 3.7oV were accepted for further X-ray image analysis (Chapter 5).

For the X-axis, the cross-talk was much less marked probably because of a slightly different layout. The X-axis cross-talk was subsequently reduced in a similar manner as for the Y-axis. For the Cygnus Loop observation X position pulse heights in the range 1.60 - 1.90V and 2.25V - 3.70V were accepted for further X-ray image analysis.

Post-flight calibrations and one-dimensional simulations of the Cygnus Loop data, in the form shown in Fig. 4.6 (b) and (c), including the effects of the effective area roll-off the X-ray optics and IPC linear resolution (from laboratory measurements) yielded values for the X and Y position voltage conversion gains of 43.5 ± 1.8 mV/mm and 54.6 ± 0.6 mV/mm respectively, with centre co-ordinates for the X and Y axis of 2.65 ± 0.02 V and 2.33 ± 0.05 V respectively (Rappaport 1978).

4.2.3 Preliminary results of Sco. X-1 observations.

The anode pulse height distributions for Sco. X-1 observation (356s - 365s after launch) is shown in Fig. 4.7 (a), in 0.01V bins with upper and lower thresholds as for Fig. 4.6 (a) In Fig. 4.7 (b) and (c) the X and Y position pulse height distributions (356s - 365s after launch) are shown (0.01V bins), subject to the same constraints as Fig. 4.6 (b) and (c). With the pointing of Sco. X-1 $\sim \frac{1}{2}^{o}$ away from the IPC centre, the Sco. X-1 X and Y position spectra were not affected by the position processing electronic cross-ralk (4.2.2) and enabled an in-flight telescope point response calibration to be made. From (4.2.2), for the X-axis position voltage conversion gain of 43.5 mV/mm, together with the X-ray optics angular dispersion of 3'/mm, the X-axis line response from Sco. X-1 yielded a width of 200 mV = 13.8' (FWHM) while for the Y - axis, the Sco. X-1 time response width 240 mV = 13.2', over the telescope X-ray energy range.

Analysis of the Sco. X-1 point response is reported in Chapter 5.

4.3 Conclusions on telescope performance.

4.3.1 IPC performance.

The in-flight performance of the IPC was stable, at the pre-launch measured characteristics (4.1.4). Analysis of

Fig. 4.7 (a) Anode pulse height distribution for Sco X - 1 observation (356s - 365s after launch), in 0.01 V bins.

Fig. 4.7 (b) X position pulse height distribution.

Fig. 4.7 (c) Y position pulse height distribution.

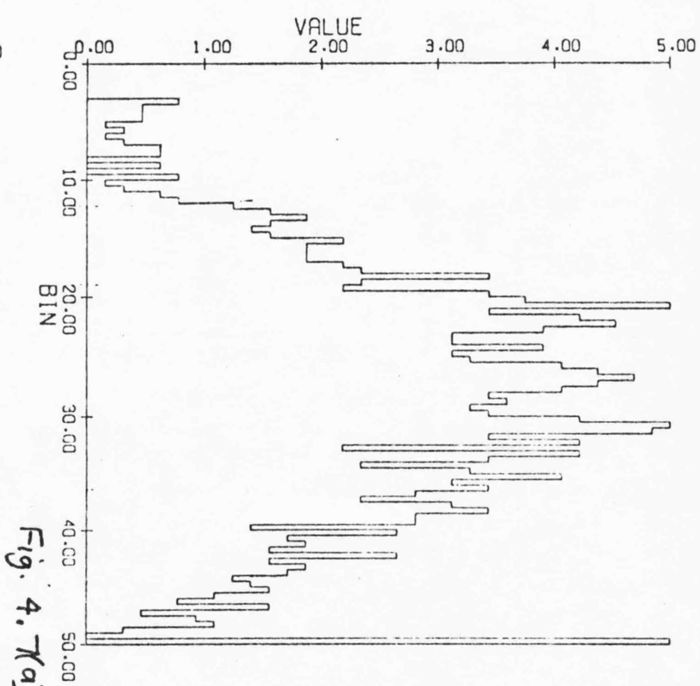

Fig. 4.7(a)

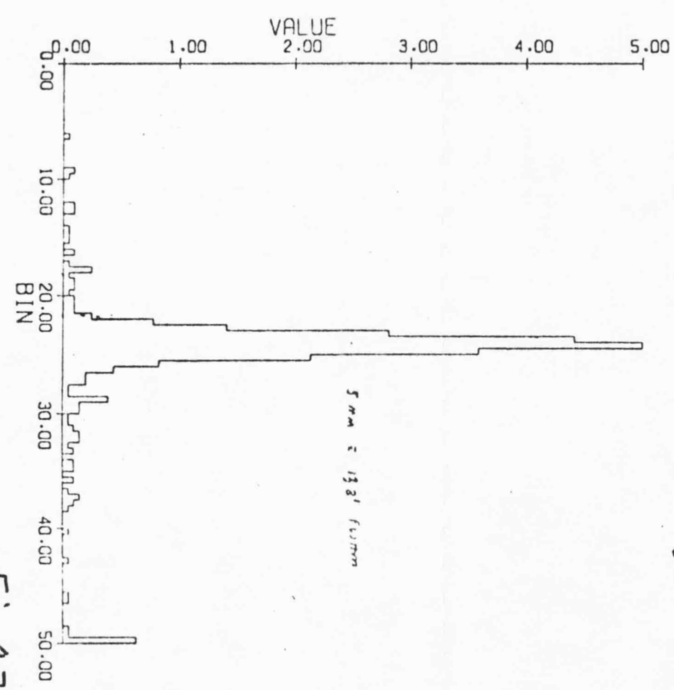

Fig. 4.7(b)

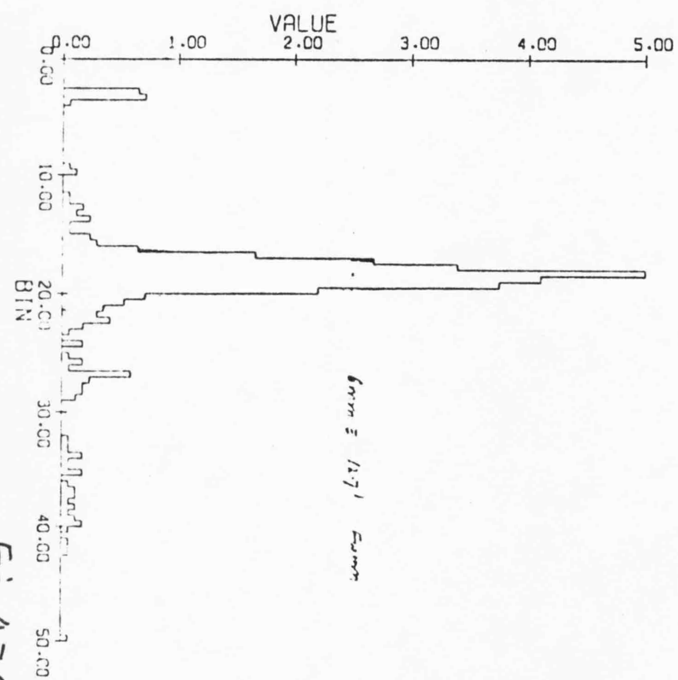

Fig. 4.7(c)

the pressure transducer TM data gave the result that the gas pack operated as expected with no significant ($<$ 1%) gas pressure variations. (IPC gain constant to within 3% for pressure dependance from section 3.2.2. Together with the absence of spark or corona discharge, voltage variations and the fact that there was no significant temperature change of the payload, it is inferred that the IPC in-flight anode charge conversion gain remained constant at the pre-launch value of 0.6 pc/keV, to within 3%. No direct in-flight observation of the IPC X-ray energy resolution was performed but again it is inferred from the stability of the pressure transducer data, that the X-ray energy resolution did not change significantly during flight.

In section 4.3.3, the result of utilising the IPC (and mirror) in-flight parameters, to convolve with previously reported Sco. X-1 X-ray energy spectra, supports the above discussion and that of section 4.3.2 below.

4.3.2 Mirror performance.

The pre-launch precautions taken to prevent contamination of the mirror surfaces (4.1.3) were effective. Post-flight optical calibrations showed the mirror axis to have maintained its pre-launch alignment in flight. There was no evidence for significant leakage of X-ray flux, undergoing reflection at one surface only, for events less than 2° off-axis, consistant with previous ray-tracing results (3.3.1). For the Cygnus Loop observations, X-ray events $\leq 1.5^{\circ}$ off-axis were accepted for further X-ray image analysis of $\sim$ 10' resolution.

4.3.3 Overall telescope performance.

Application of the IPC and mirror constraints for acceptance of X-ray events, yielded a total of $\sim$ 7000 events, which were selected for further X-ray image analysis (Chapter 5). From sections 4.2.2 and 4.2.3 and 3.3. Table 4.6 summarises the telescope in-flight parameters required for X-ray image analysis. Table 4.7 summarises the telescope in-flight parameters required for X-ray energy spectral analysis. The measured IPC flight window efficiency is shown in Fig. 4.8.

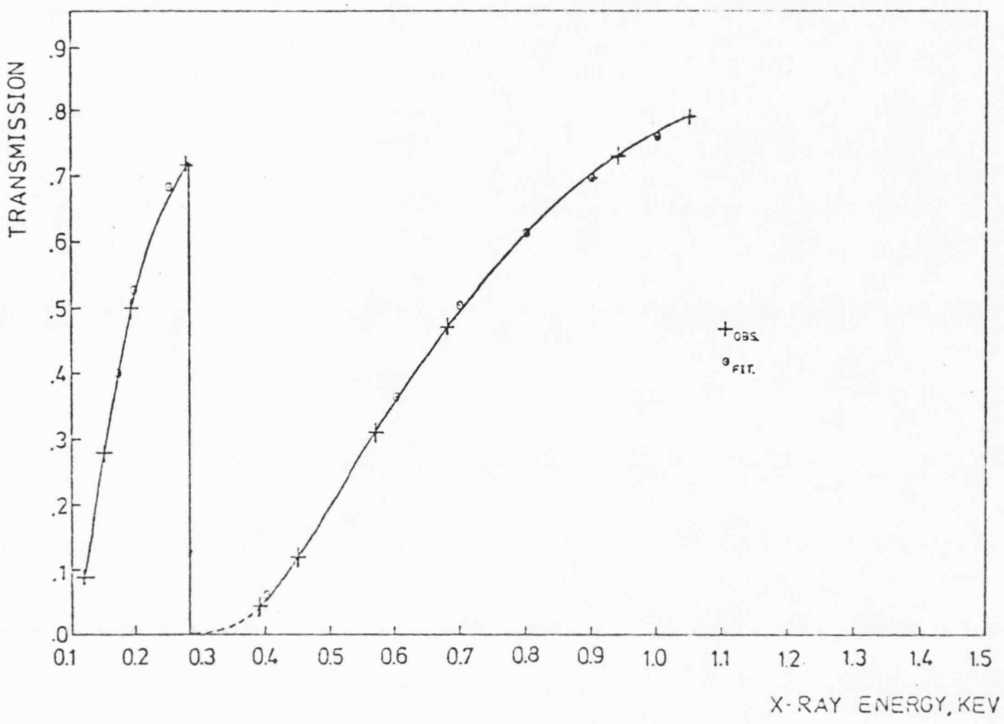

Fig. 4.8 IPC quantum efficiency.

TABLE 4.6

Summary of telescope parameters for X-ray event position analysis.

Focal plane angular dispersion	3'/mm
IPC X-axis centre	2.65 ± 0.02V
IPC X-axis position voltage conversion gain	14.5 ± 0.6mV/'
IPC Y-axis centre	2.33 ± 0.05V
IPC Y-axis position voltage conversion gain	18.2 ± 0.2mV/'

TABLE 4.7

Summary of telescope parameters for X-ray spectral analysis.

IPC X-ray energy/TM channel conversion	1 keV = 2.799 V
IPC X-ray energy resolution RMS function	$\sigma = 0.21\, \mathcal{E}_x^{0.5}$
IPC flight window X-ray transmission :	
$0.15 \leq \mathcal{E}_x \leq 0.28$ keV	$\mu/\rho = 0.095\, \mathcal{E}_x^{-2.42}$
$0.28 \leq \mathcal{E}_x \leq 1.49$ keV	$\mu/\rho = 2.029\, \mathcal{E}_x^{-2.53}$

The mirror efficiency for on-axis X-rays (Fig. 3.3) was convolved with the IPC window efficiency and the IPC energy resolution function (3.3.2) and Table 4.7) to produce the overall telescope quantum efficiency curve (for on-axis X-rays), Fig. 4.9. This curve is essentially the non-linear telescope spectral response (for unit mirror geometric collecting area) to an incident, uniform X-ray photon spectrum.

The stability of the telescope parameters during the Cygnus Loop and Sco. X-1 observations may be inferred from detailed considerations of the Sco. X-1 pulse height spectrum observed.

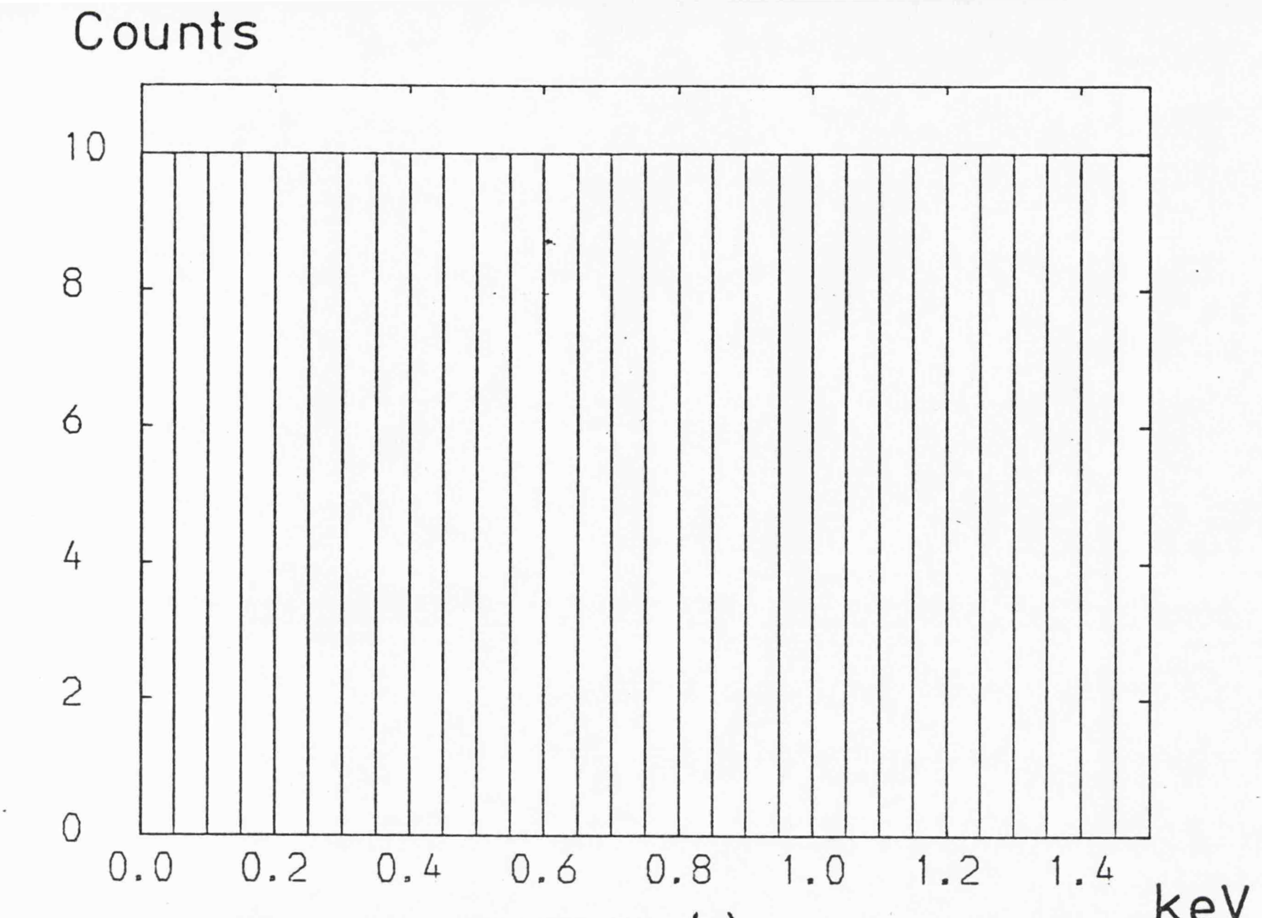

(a)

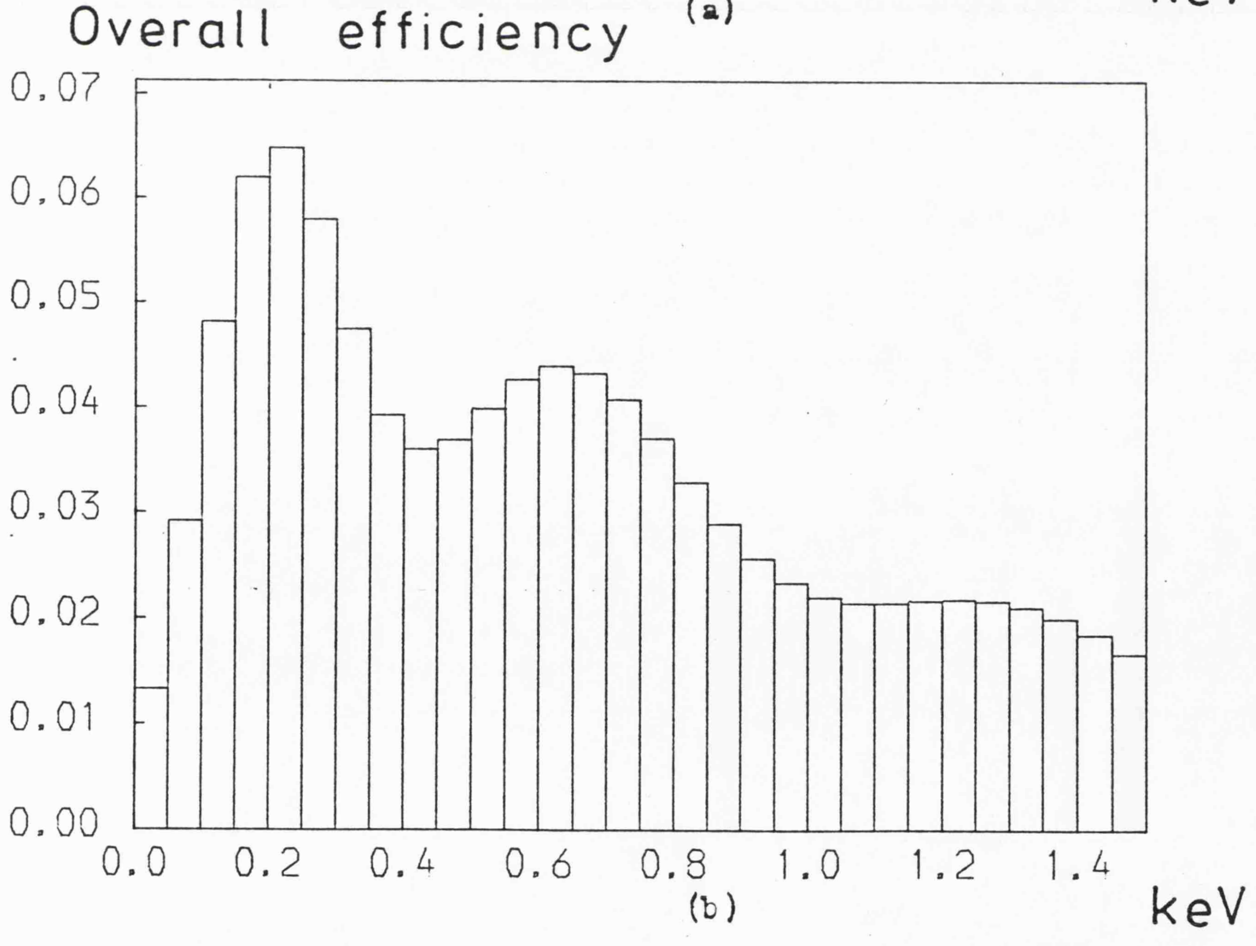

(b)

Fig. 4.9 (a) Uniform field photon spectrum incident on the X-ray telescope.
(b) Non-linear spectral response of the X-ray telescope to (a). The mirror response is convolved with the IPC spectral response. The IPC window C-k edge (.28 keV) and mirror Ni-l edge (.85 keV) effects are observed.

The on-board digital TM system had a limited capacity of 500 c/s, which was not sufficient to cover counting rates due to an observation of very bright X-ray sources such as Sco. X-1 (i.e $\sim$ 2000 c/s (1-6 keV) Canizares et al. 1973). Thus, only a fraction of the observed photons was telemetered during the Sco. X-1 observation, and consequently used for spectral analysis. Since the dead time per telemetered event was independant of the pulse height (or energy) of the observed photons, the spectral shape was not affected by system saturation.

The physical properties of the X-ray, optical and radio emission from Sco. X-1 have been reviewed recently (Miyamoto and Matsuoka 1977). Table 4.8 lists optical and X-ray details of Sco. X-1 taken from Miyamoto and Matsuoka (1977) and references therein.

Sco. X-1 has the following general features attributed to compact X-ray sources :

(1) The compact X-ray source accompanies a high temperature plasma responsible for X-ray emission and whose energy source is considered to be derived from the gravitational energy imparted to gas accreting onto a compact star. Sco. X-1 is associated with such a high temperature plasma.

(2) Sco. X-1 is a close binary system with a period of 0.787 days. In an X-ray emitting close binary system, the primary star supplies the gravitational material for accretion onto the compact star. However, the amplitude of the binary period of Sco. X-1 is only 0.22 mag. (optical) and there is no indication of the periodic variation in the X-ray region, due probably to a pole-on position, or a small inclination of the orbital plane of the binary system.

(3) Sco. X-1, like some compact X-ray sources, emits weak and variable non-thermal radio flux, and simultaneous radio, optical and X-ray observations reveal complicated features of their variations.

Fig. 4.10 Compilation of Sco X - 1 X-ray data (Miyamoto and Matsuoka (1977)).

(a) Column densities deconvolved using free - free spectrum with variable Gaunt factor and absorption coefficient.

(b) The corresponding values of kT for free - free spectra.

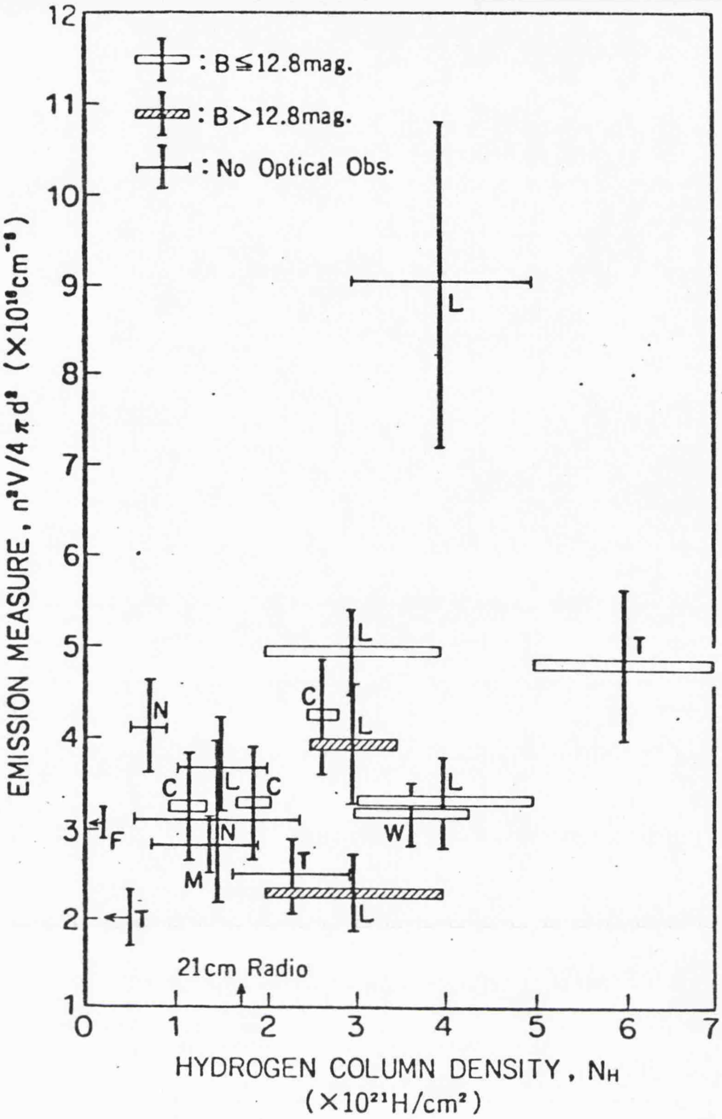

The hydrogen column density vs emission measure. C; Moore *et al.*, 1973; F: Fritz *et al.*, 1968; L: Burginyon *et al.*, 1970; M: Rapaport *et al.*, 1969; N: Deerenberg *et al.*, 1973; T: Matsuoka *et al.*, 1974; W: Bunner *et al.*, 1972.

Fig. 4. 10 (a)

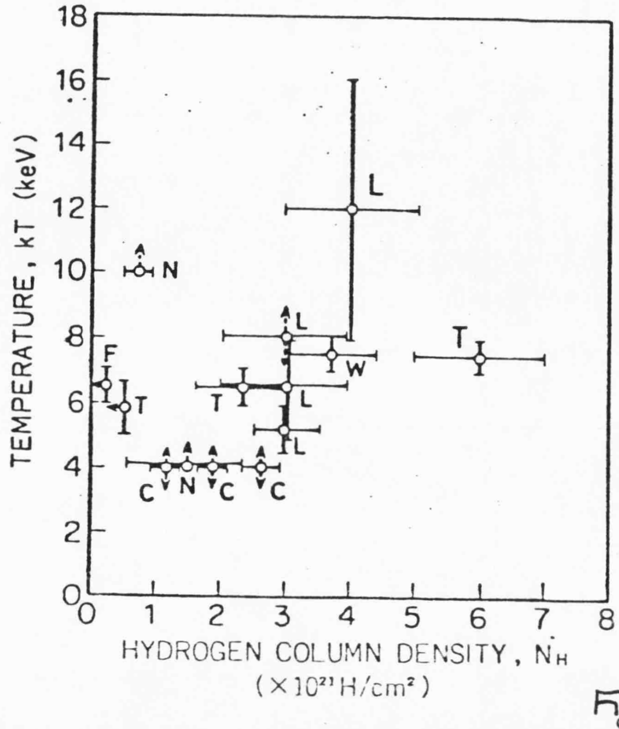

Fig. 4. 10 (b)

The hydrogen column density vs temperature.

TABLE 4.8

Optical/X-ray properties of Sco. X-1.

Star	α(1950)	δ(1950)	d(pc)	X-ray intensity (variable) at 2keV (ph/cm^2.s)	M_V (vari)	E_{B-V}	Period (optical)	X-ray behavior
V818 Sco. (F8)	$16^h17^m4.3^s$	$-15^\circ31'13''$	500	12-30	12.4-14.0	0.6-0.7	0.787^d	No eclipses Flaring.

The soft X-ray spectrum ($<$ 2 keV) from Sco. X-1 may be approximately described by considering thermal bremsstrahlung radiation from a hot, sperical, isothermal, optically thin hydrogenic plasma cloud (Kitamura et al. 1971, White et. al. 1976). For radius r , distance d , with electron/ion temperature T and electron density n , the X-ray spectral shape is (Karzas and Latter 1961, Allen 1973) :

$$I(\varepsilon) = \frac{3.0\times10^{-15}}{4\pi d^2}\int_V n^2 . \bar{g}(\varepsilon,T) . \frac{e^{-\frac{\varepsilon}{kT}}}{\varepsilon(kT)^{\frac{1}{2}}}\, dV \quad ph./cm^2.s.keV. \qquad (4.1)$$

Where the temperature averaged Gaunt factor is approximated by (Karzas and Latter 1961, Tucker 1975) :

$$\bar{g}(\varepsilon,T) = 0.84 . \left\{\frac{kT}{\varepsilon}\right\}^{0.3} \qquad (4.2)$$

Temperature uniformity gives :

$$I(\varepsilon) = \frac{3.0\times10^{-15}}{(kT)^{\frac{1}{2}}} . \int_V \frac{n^2\, dV}{4\pi d^2} . \bar{g}(\varepsilon,T) . \frac{e^{-\frac{\varepsilon}{kT}}}{\varepsilon} \quad ph./cm^2.s.keV. \qquad (4.3)$$

$$\therefore \quad I(\varepsilon) = C . \bar{g}(\varepsilon,T) . \frac{e^{-\frac{\varepsilon}{kT}}}{\varepsilon} . \quad ph./cm^2.s.keV.$$

where

$$C = \frac{3.0\times10^{-15}}{(kT)^{\frac{1}{2}}} . \left\{\frac{n^2 V}{4\pi d^2}\right\} .$$

$$V = \frac{4}{3}\pi r^3$$

where $[r]$ and $[d]$ are cm., $[n]$ cm^{-3}, and the photon energy $[\epsilon]$, plasma temperature $[kT]$ are keV. Variability in both kT and C (emission measure) have been observed, Fig. 4.10 (a) and (b), along with hydrogen column density. The spectral form of (4.1) was convolved with absorption in the interstellar medium in the form $exp\{-\sigma(\epsilon).N_H\}$ where $\sigma(\epsilon)$ is the energy dependent absorption cross-section (Brown and Gould 1970). The values of the Sco. X-1 parameter from Matsuoka et. al. (1974) for the flaring and non-flaring states, were folded through the telescope response (Fig. 4.9) to yield the results in Table 4.9, compared with the observed spectrum (for 356 s - 365 s), in 0.25 keV bands.

TABLE 4.9

Comparison of predicted and observed Sco. X-1 X-ray spectra.

X-ray energy band (keV)	Observed spectrum (counts/s.bin)	Predicted spectrum non-flaring mode (counts/s.bin) *a	Predicted spectrum flaring mode (counts/s.bin) *b
0.25-0.50	5.5 ± 2.3	3.3	27.3
0.50-0.75	19.9 ± 4.5	5.9	23.4
0.75-1.00	31.9 ± 5.6	24.3	23.2
1.00-1.25	30.0 ± 5.5	28.7	16.6
1.25-1.50	21.4 ± 4.6	25.5	11.5

* Normalised to the total count of the observed spectrum.

a $\frac{n^2V}{4\pi d^2} = 4.5 \times 10^{16}$ cm^{-3}, $N_H = 6.0 \times 10^{21}$ cm^{-2}, $kT = 7$ keV

b $\frac{n^2V}{4\pi d^2} = 3.3 \times 10^{16}$ cm^{-3}, $N_H = 2.2 \times 10^{21}$ cm^{-2}, $kT = 6.2$ keV

The values for $\sigma(\varepsilon)$ were approximated (to within $\sim$ 10%) by :

$$\sigma(\varepsilon) = 6.0 \times 10^{-20} \left\{ \frac{0.1}{\varepsilon} \right\}^{3} \ \mathrm{cm}^{2} \qquad \varepsilon < 0.53 \ \mathrm{keV} \qquad (4.4)$$

$$\sigma(\varepsilon) = 2.0 \times 10^{-22} \left\{ \frac{1}{\varepsilon} \right\}^{2.5} \ \mathrm{cm}^{2} \qquad 0.53 \lesssim \varepsilon \lesssim 5 \ \mathrm{keV}.$$

Given the poor statistics, the Sco. X-1 spectral shape for the non-flaring mode is consistent (in peak response) with the observed spectral shape. The uncertainties in the above values for the Sco. X-1 spectra (Matsuoka et al. 1974) were not included in Table 4.9.

No single temperature, thin plasma model could be made to fit the integrated pulse height spectrum of the Cygnus Loop. The consequences of this fact are discussed in Chapter 6.

4.4 Summary.

Details of an imaging X-ray observation of the Cygnus Loop SNR have been discussed, with particular reference to the flight operation of the X-ray telescope. The pertinent telescope parameters for subsequent X-ray image analysis, together with X-ray spectral analysis, have been presented and their stability during the observation discussed.

The Sco. X-1 in-flight point response was $\sim$ 15' (FWHM) (0.15 - 1.80 keV). The Cygnus Loop observation produced $\sim$ 7000 photons (for off-axis angles $\lesssim$ 90') during the observation times 122s - 194s and 202s - 273s into the flight, valid for the telescope axis equations of motions. Detailed analysis of the X-ray image of the Cygnus Loop is discussed in Chapter 5 and detailed analysis of the partitioned image pulse height spectra in Chapter 6.

References.

Allen, C., 1973. Astrophysical Quantities, 3rd ed. The Athlone Press, London.

Bidlemann, W., 1976. Be and shell stars. IAU Symp. No.70, ed. A. Suttbok, D. Reidel Publ.Co., Dordrecht, NL.

Blaauw, A., 1961. Bull. Astr. Neth. 15, 265.

Bleeker, J., A. Deerenberg, K. Yamashita, S. Hayakawa, and Y. Tanaka, 1972. Ap. J., 178, 377.

Bless, R. and B. Savage, 1970. UV Stellar spectra and related ground-based observations. IAU Symp. No. 36, ed.L.Houziaux and H. Butler, D. Reidel Publ. Co.

Borken, R., R. Doxsey and S. Rappaport, 1972. Ap.J. (Lett.) 178, L 115.

Brown, R and R. Gould, 1970. Phys. Rev. D1, 2252.

Bunner, A., P. Coleman, W. Kraushaar and D. McCammon, 1970. Ap. Lett., 12, 165.

Burginyon, G., R. Grader, R. Hill, W. Hiltner, E. Mannery, R. Price, R. Rodrigues, F. Seward and C. Swift. 1970. Ap. J., 161, 987.

Canizares, C., G. Clark, W. Lewin, H. Schnopper and G. Sprott, 1973. Ap. J. (Lett.), 79, L1.

Conti, P. and E. Leep, 1974. Ap. J., 193, 113.

Deerenberg, A., J. Bleeker, P. DeKorte, K. Yamashita, Y. Tanaka and S. Hayakawa, 1973. Nature, 244, 4.

Hayakawa, S., T. Kato, F. Makino, H. Ogawa, Y. Tanaka and K. Yamashita, 1971. Report of Ionospheric and Space Research in Japan, 25, 1.

Gorenstein, P., B. Harris, H. Gursky, R. Giacconi, R. Novick and P. Vanden Bout, 1971. Science, 172, 369.

Gronenschild, E., R. Mewe, J. Heise, A. Brinkman, A. den Boggende and J. Schrijver, 1976. Astron. Ap. 49, 153.

Jenkins, E., 1970. IAU Symp. No. 36, op. cit.

Karzas, N. and R. Latter, 1961. Ap. J. (Suppl.), 6, 167.

Kitamura, T., M. Matsuoka, S. Miyamoto, M. Nakagawa, M. Oda, Y. Ogawa, R. Takagishi, U. Rao, E. Chitnis, U. Jayanthi, A. Prakasarao and S. Bhandari, 1971. Ap. Sp. Sci. 12, 378.

Lau, F., 1977. Private communication, GSFC.

Levine, A., 1977. Private communication, MIT.

Matsuoka, M., Miyamoto, S., Nishimura, J., Oda, M., Ogawara, Y., Ohtuka, Y., Hayakawa, S., Kasahara, I., Makino, F., Tanaka, Y., Agrawal, P.C., Sreekantan, B.V., Manabe, R., Mikami, Y., Lokanandham,B., Raghavender Rao, C., Sreedhar Rao, S., and Swaminathan R. 1974, Nature 250, 38.

Miyamoto, S. and M. Matsuoka, 1977. Sp. Sci. Rev., 20, 687.

Rappaport, S., 1978. Private communication, MIT.

Rappaport, S., R. Doxsey, A. Solinger and R. Borken, 1974, Ap. J. 194, 329

Stevens, J., G. Riegler and G. Garmire, 1973. Ap. J., 183, 61.

Smith, G., 1978. Private communication, University of Leicester.

Tucker, W., 1975. Radiation processes in astrophysics. The MIT press, Cambridge, Mass.

White, N., K. Mason, P. Sanford, S. Ilovaisky and C. Chevalier, 1976. MNRAS, 176, 91.

Chapter 5. PRODUCTION OF THE X-RAY IMAGES OF THE CYGNUS LOOP SNR.

Chapter 5. PRODUCTION OF THE X-RAY IMAGES OF THE CYGNUS LOOP SNR.

5.1 Introduction.

Following the discussion of details of an X-ray telescope, and a subsequent X-ray observation aboard a sounding rocket, on returning to Fig.3.1 it is seen that the next stage in the X-ray imaging process is that of the actual two-dimensional remapping in sky co-ordinates. Subsequent smoothing, reconstruction and final presentation in different forms of display enable direct comparison with optical and radio maps.

5.2 Preliminary image formation.

5.2.1 Sky co-ordinate images.

For the Cygnus Loop observation, using the telescope axis equations of motion in celestial co-ordinates (4.2.1) and the measured IPC characteristics from Table 4.7 enabled a transformation from the IPC co-ordinate system (in volts) to sky co-ordinates (in degrees) for each X-ray event. The event set was then binned to form an image matrix. The bin size, 4' x 4', that was utilised provided adequate sampling across the telescope point response, $\sim$ 15' (FWHM), given in-flight by the Sco. X-1 observation (4.2.3). Analysis of the Sco. X-1 point response in the X-ray energy bands (0.36-0.72keV (1.08-1.44 keV) and (0.18-1.80 keV), displayed in Fig. 5.1, Fig. 5.2 and Fig. 5.3 respectively in 4' bins and normalised to the X-ray count in each energy band, yielded the result that the telescope response was only weakly dependent on X-ray energy. The exact shape of the overall telescope response was not a Gaussian profile (3.3, 3.4). Deconvolution of the telescope response from the initial Cygnus image matrix assumed a Gaussian profile (3.3 and 5.2.3.1).

After applying the criteria discussed in section 4.2.2 together with constraint that all X-ray events within 90' radius from the telescope axis, the Cygnus Loop image matrix consisted of 6741 counts (0.15-1.12 keV). Fig. 5.4 through Fig. 5.6 show the unfolded Cygnus image matrix in the energy bands (0.15-0.56 keV), (0.56-1.12 keV) and (0.15-1.12 keV), contained in 64 x 64 arrays of 4' x 4' pixels (image elements) with the

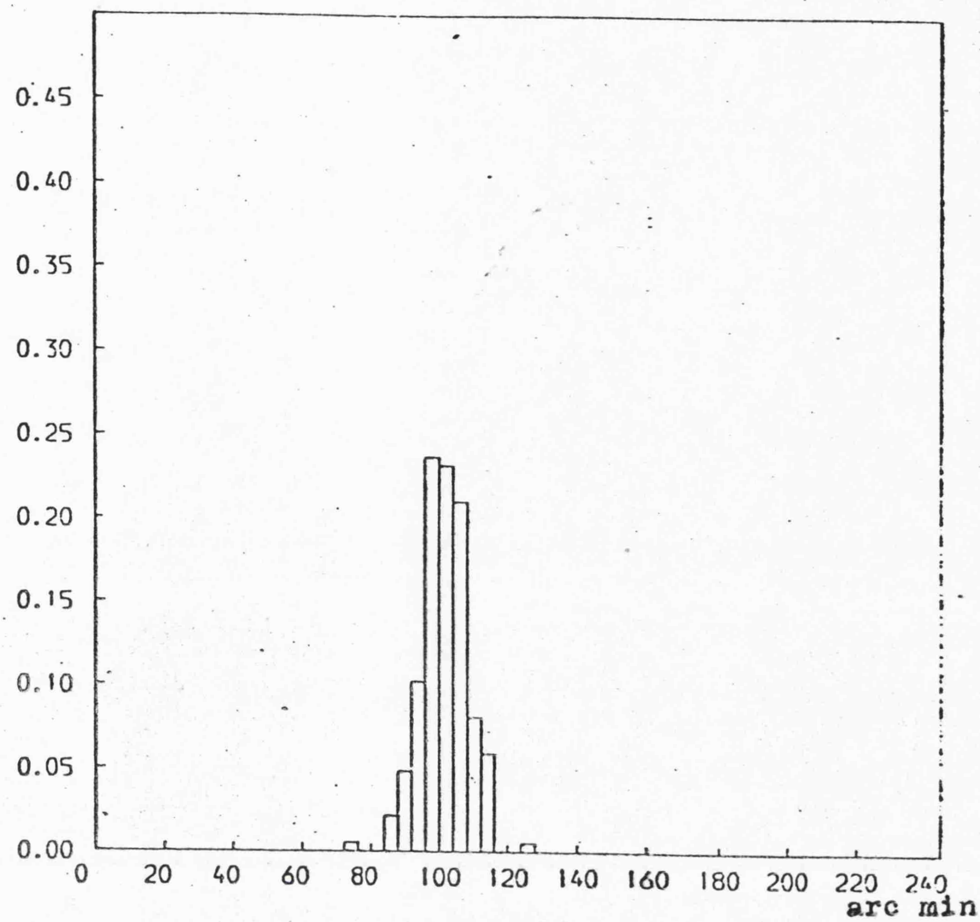

Fig. 5.1 (a) Sco X-I in flight X response
(0.36-0.72 keV, I86 counts).

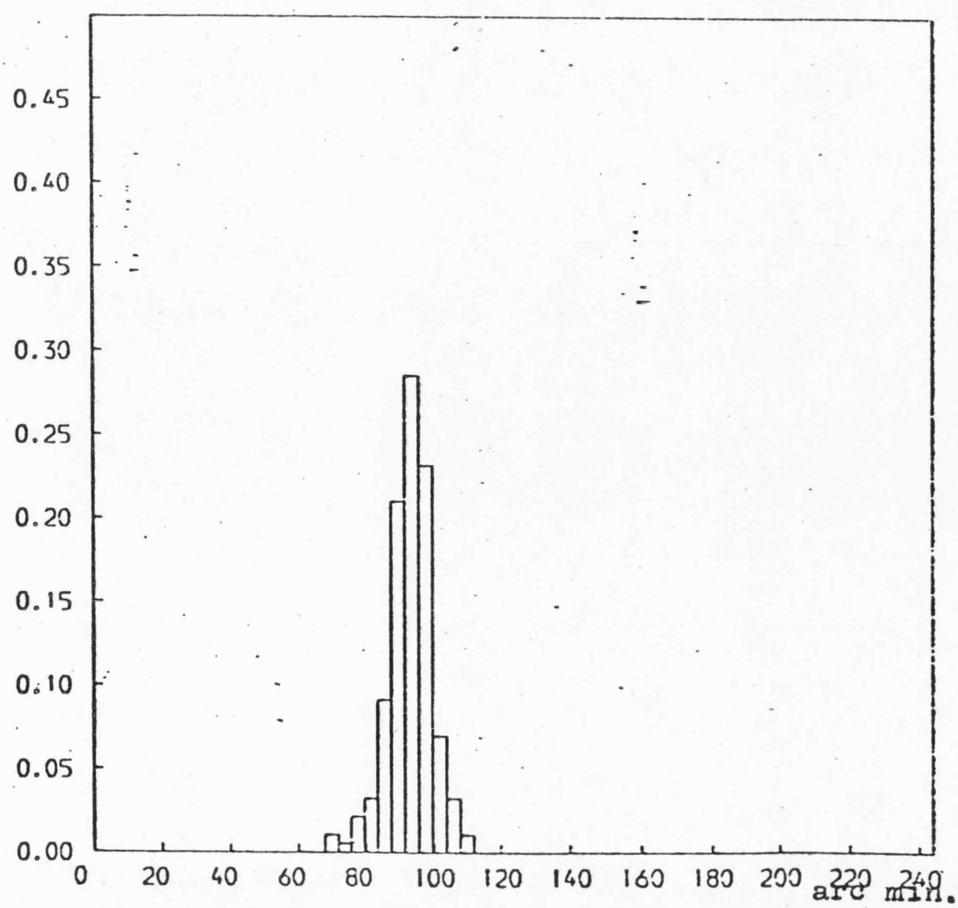

Fig. 5.1 (b) Sco X-I in flight Y response.

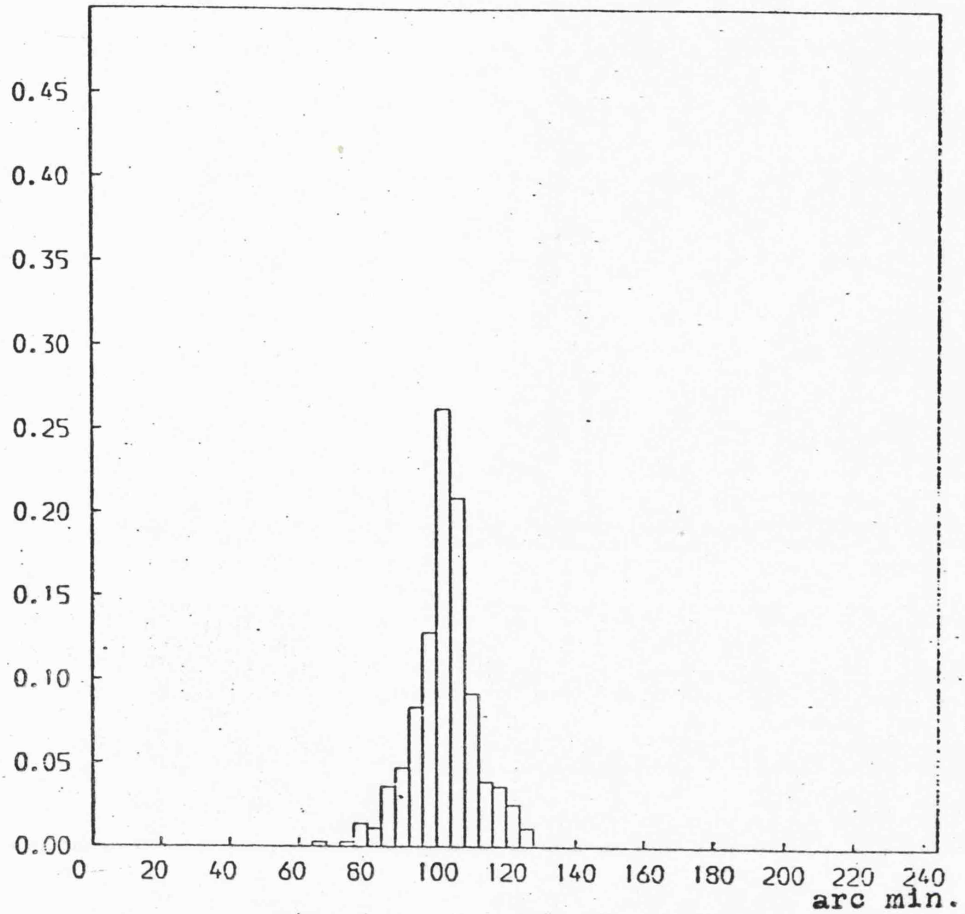

Fig. 5.2 (a) Sco X-I in flight X response
(I.08-I.44 keV, 359 counts).

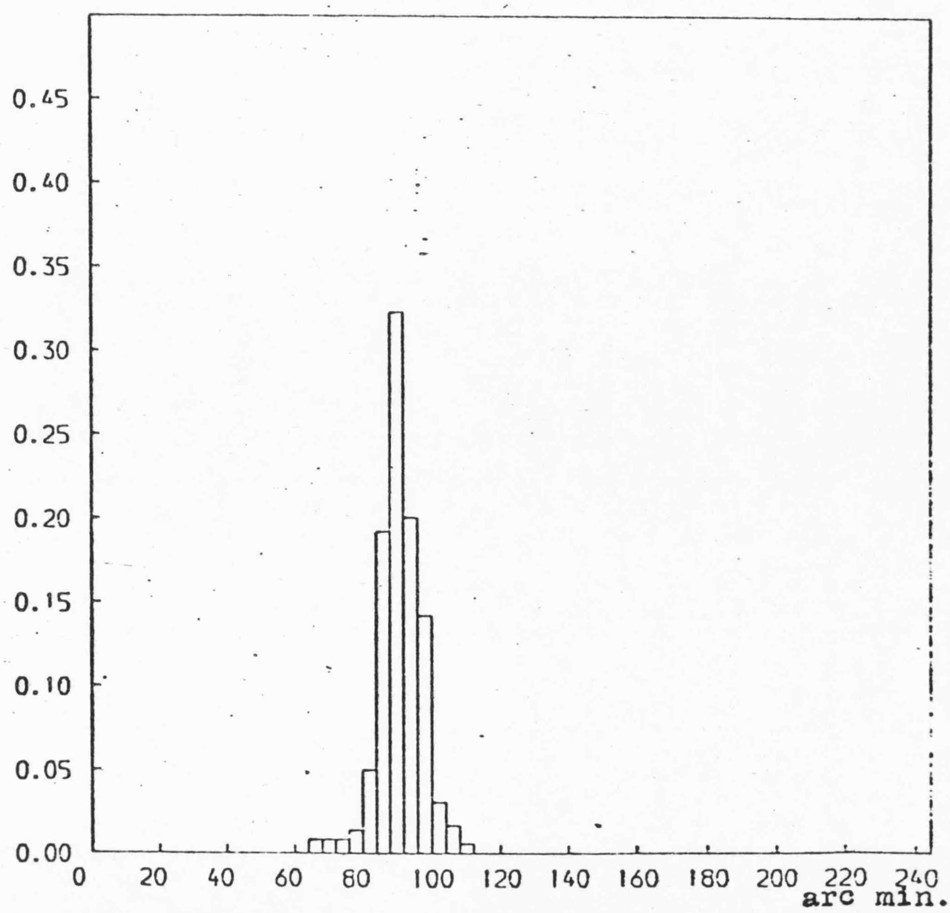

Fig. 5.2 (b) Sco X-I in flight Y response.

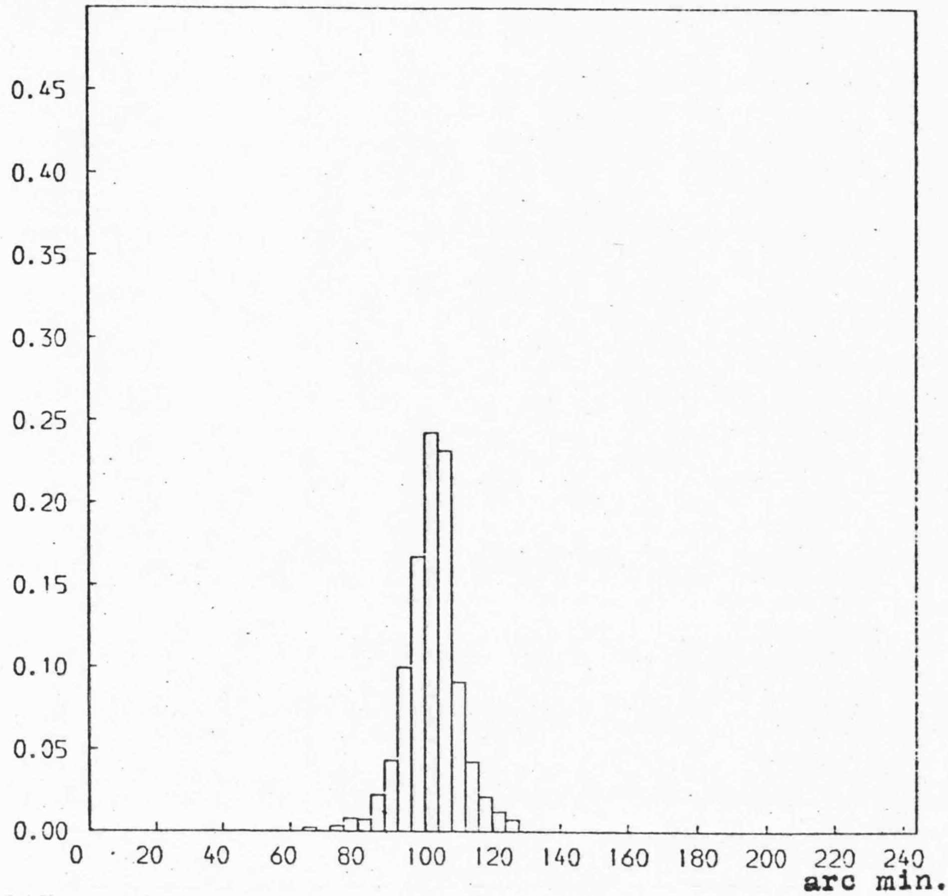

Fig. 5.3 (a) Sco X-I in flight X response (0.I8-I.80 keV, 993 counts).

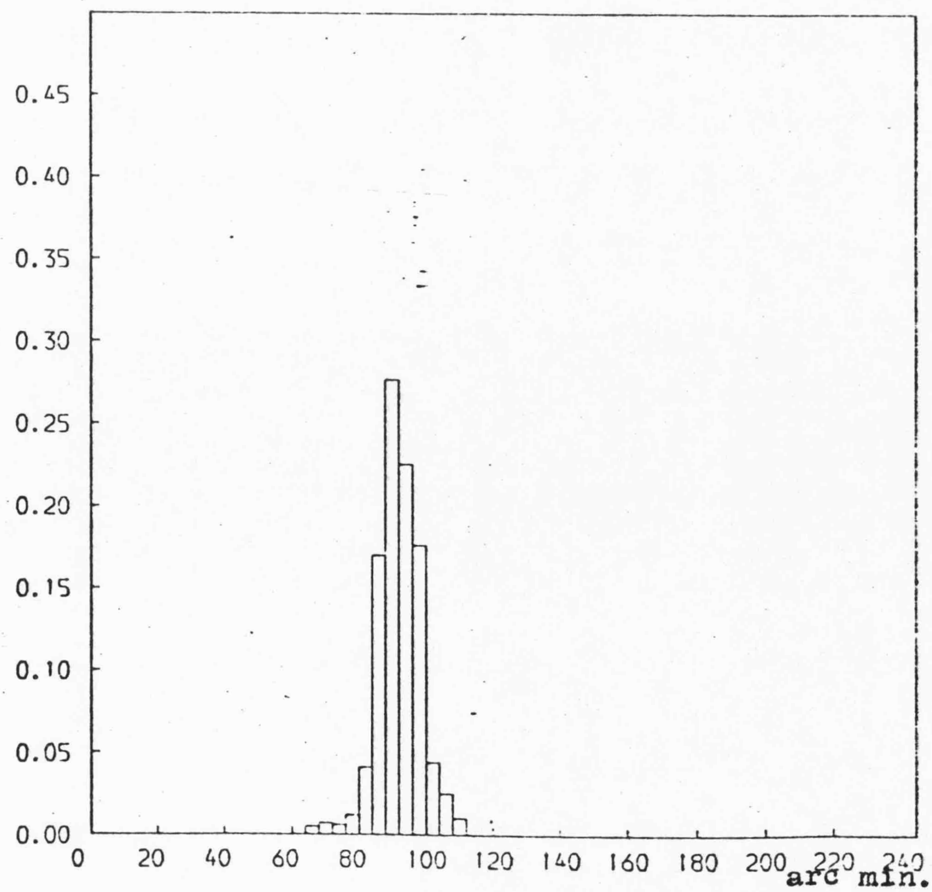

Fig. 5.3 (b) Sco X-I in flight Y response.

pixel (33,33) - origin bottom left hand corner - defining the centre of the SNR at (RA, Dec.) = (312.4^{o}, 30.7^{o}). In Fig. 5.6, discrete, intense features are clearly observable, particularly in the North (NGC 6996) and West (NGC 6990) along with a clearly distinguishable, incomplete, limb-brightening. There is no strong indication of a X-ray emitting stellar remnant in any of the images.

The maximum event count per pixel is 19 (0.15-1.12 keV) but on average there are 1.6 event counts / pixel. The images in Fig. 5.4 - Fig. 5.6 are not corrected for :

(1) Variation in exposure ($cm^2.s$) received per pixel due to the telescope effective area profile (Fig. 3.9) together with the telescope axis scan rate. To correct for apparent surface brightness variations caused by the exposure time, the exposure of each pixel was calculated (5.2.). Since the telescope effective area profile was only slightly energy dependent, individual pixel exposure was ultimately dependent upon one area function (the 0.28 keV curve of Fig. 3.9) and each equation of motion of the telescope axis.

(2) Image degradation (blurring) by the non-linear telescope (the overall point response was spatially variant). However, addition of data from the North-South and South-North scans effectively removed the non-linearity across the images, to enable a single blur (instrument point response) matrix to sufficiently describe the global image blurring.

Systematic errors present in the images of Fig. 5.4 - Fig. 5.6 include :

(1) $\pm$ 3' absolute uncertainty in event position through laboratory measurements of the alignment of the star field camera and telescope axis (3.4).

(2) $\pm$ 4' non-linearity across the images due to the overall estimate derived from the IPC laboratory and in-flight linearity measurements (4.2.2).

Taking the non-Xray background rejection efficiency as 75% (Table 4.3) gives an estimated residual background of 428 events present in the image of Fig. 5.6 which amounts to $\sim$ 0.1

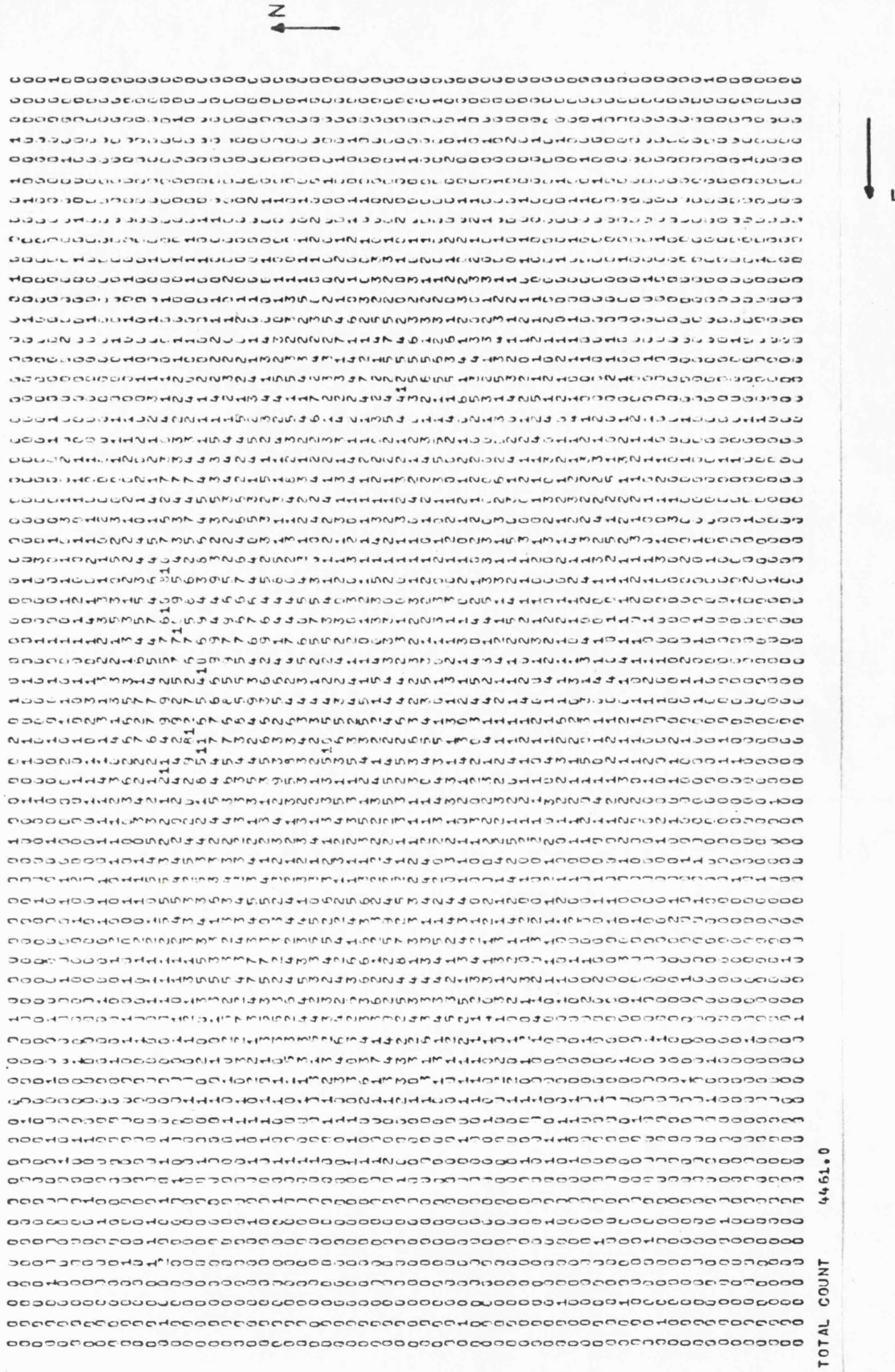

Fig. 5.4. Cygnus Loop X-ray image (.I5-.56 keV plotted in sky coordinates. 446I X-ray events were used to form the image. Each pixel of the 64x64 array is 4'x4' in size. The number of photons detected per pixel is printed out. The image is unsmoothed and is not corrected for exposure variations.

Fig. 5.4. Cygnus Loop X-ray image (0.15-0.56 keV) plotted in sky coordinates. Approximately 4500 X-ray events were used to form the image. The pixel size is 4'x4'. Each cross represents one photon. The image is unsmoothed and is not corrected for exposure variations.

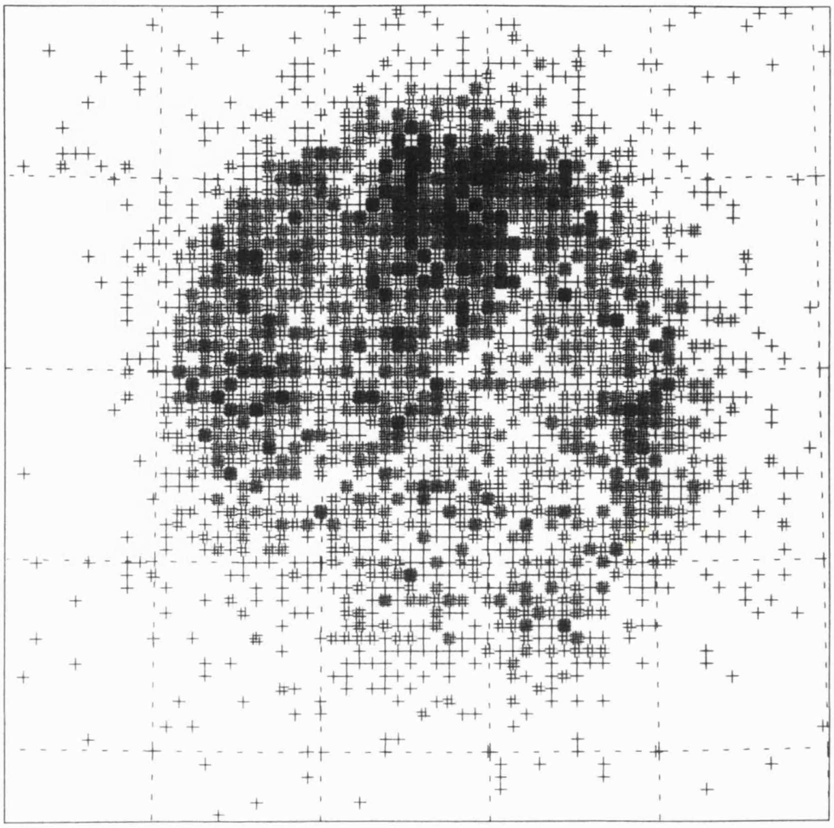

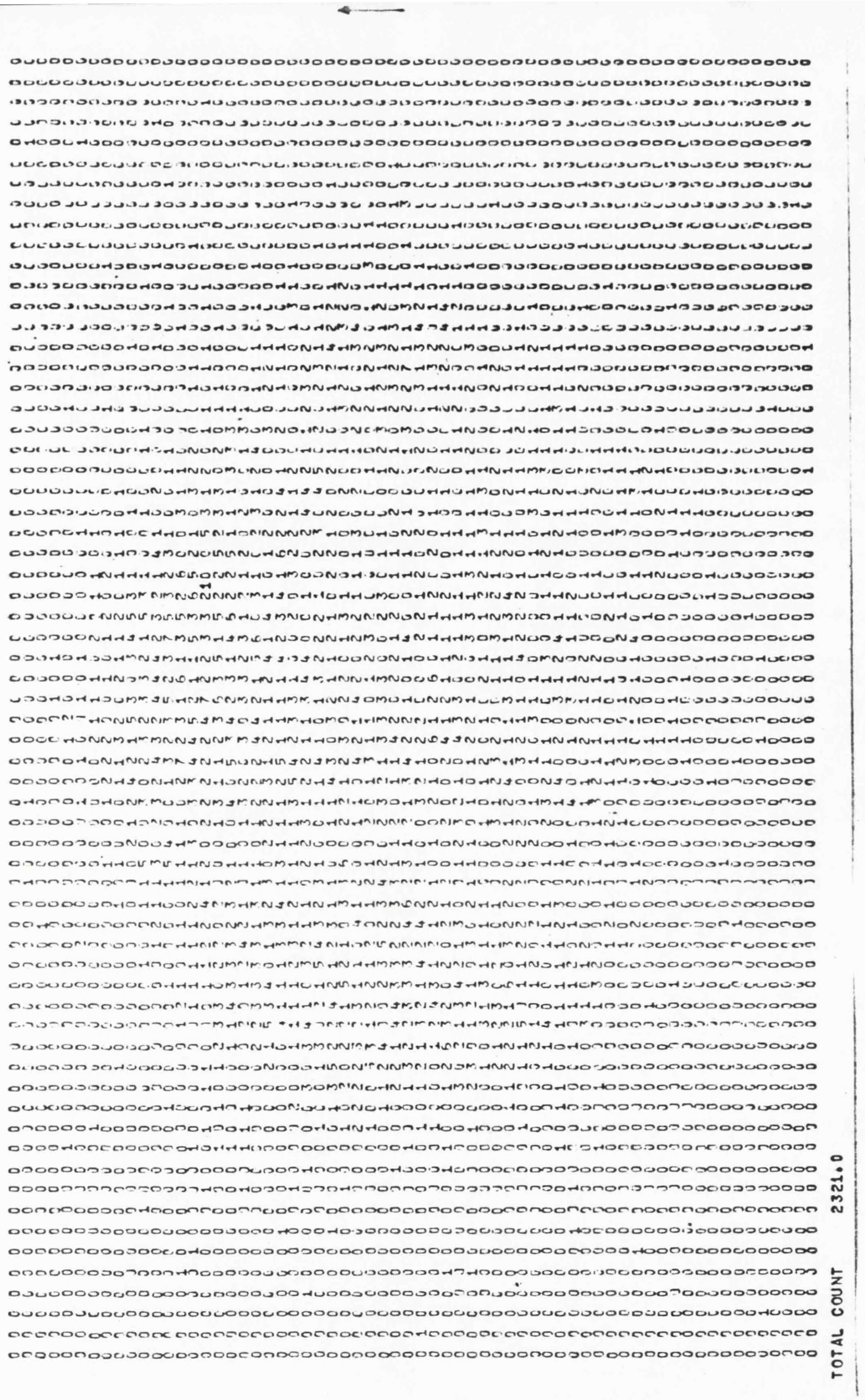

Fig. 5.5 Cygnus Loop X-ray image (.56-I.I2 keV) plotted in sky coordinates. 232I X-ray events were used to form the image. Each pixel of the 64x64 array is 4'x4' in size. The number of photons per pixel is printed out. The image is unsmoothed and is not corrected for exposure variations.

Fig. 5.5 Cygnus Loop X-ray image (0.56-1.12 keV) plotted in sky coordinates. Approximately 2300 X-ray events were used to form the image. The pixel size is 4'x4'. Each cross represents one photon. The image is unsmoothed and is not corrected for exposure variations.

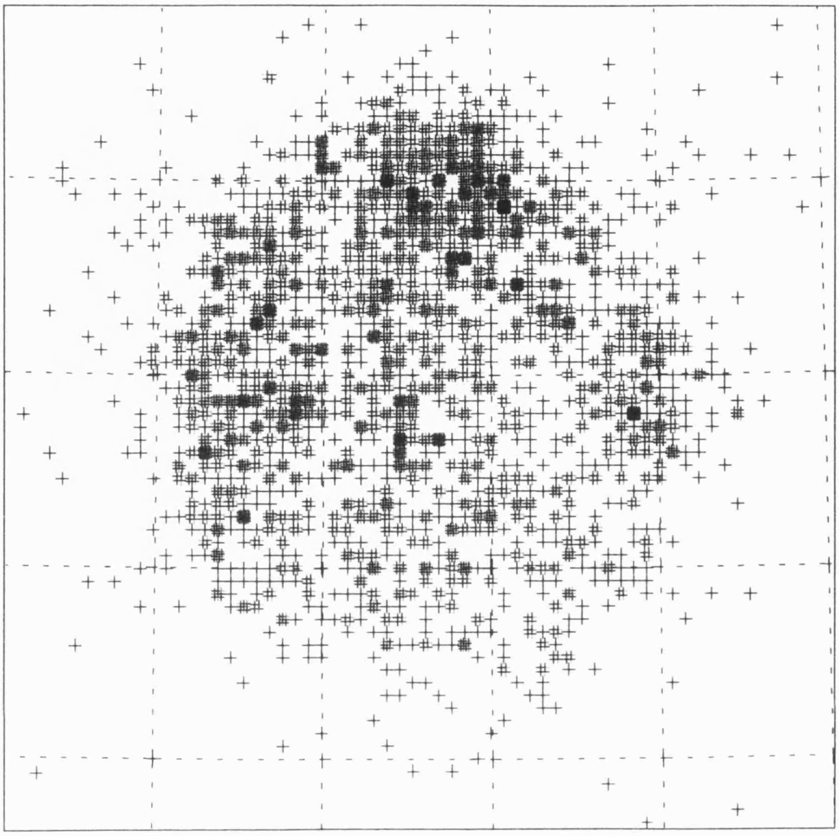

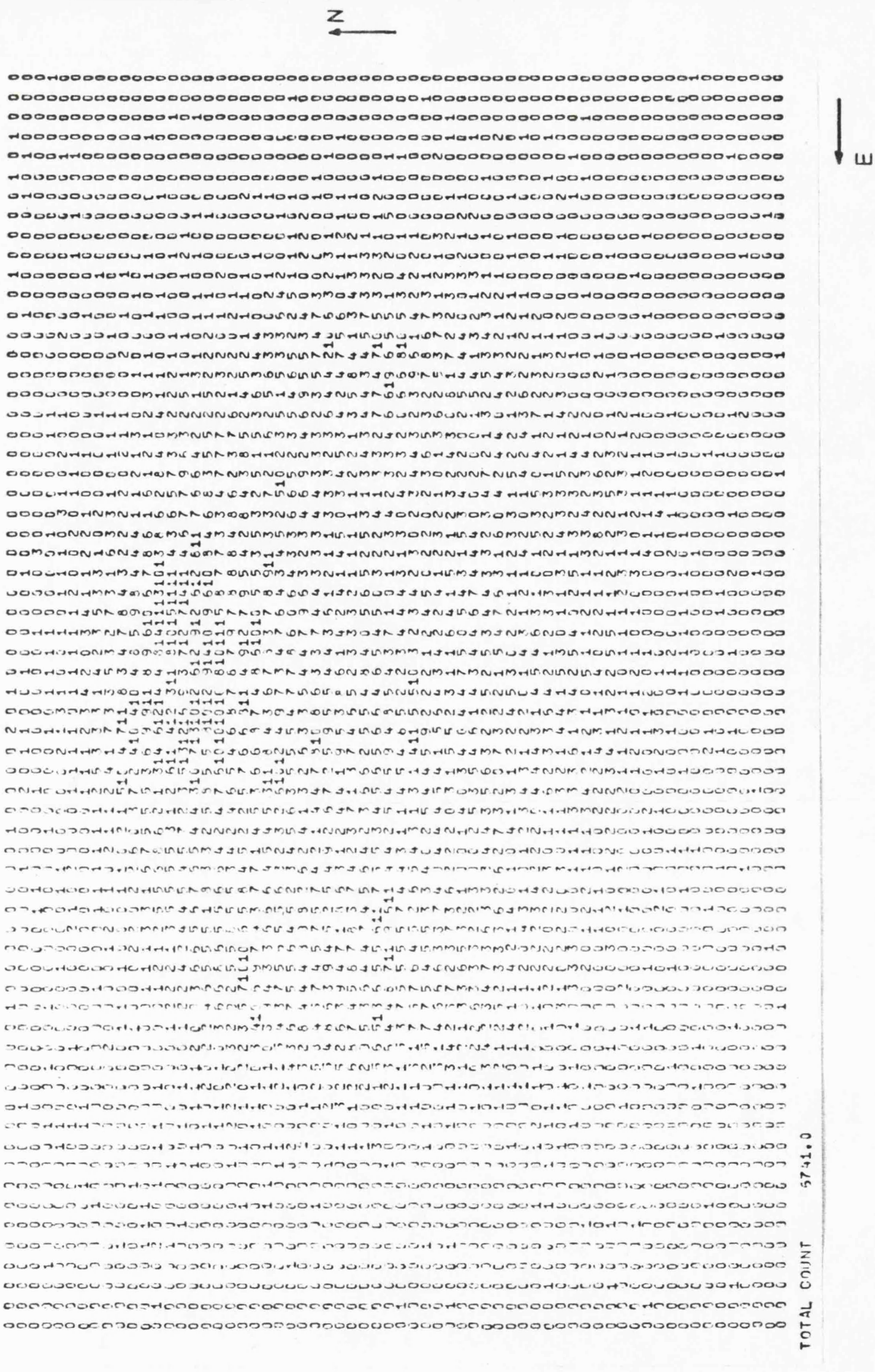

Fig. 5.6. Cygnus Loop X-ray image (.15-1.12 keV) plotted in sky coordinates. 6741 X-ray events were used to form the image. Each pixel of the 64x64 array is 4'x4' in size. The number of photons detected per pixel is printed out. The image is unsmoothed and is not corrected for exposure variations.

Fig. 5.6. Cygnus Loop X-ray image (0.I5-I.I2 keV) plotted in sky coordinates. Approximately 7000 X-ray events were used to form the image. The pixel size is 4'x4'. Each cross represents one photon. The image is unsmoothed and is not corrected for exposure variations.

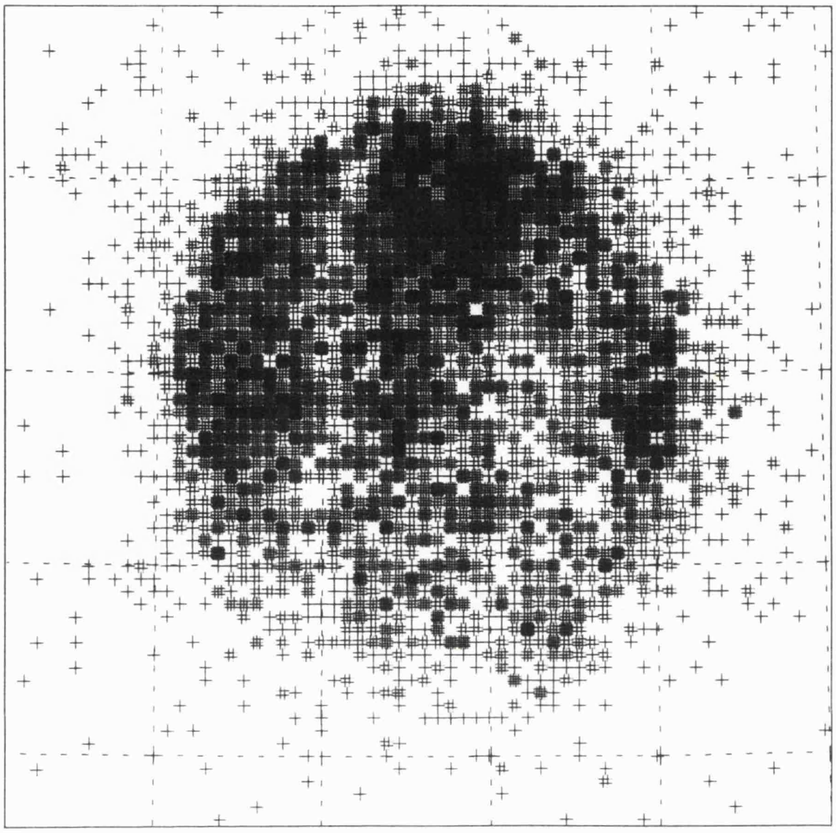

events / pixel. From an observation of the Vela SNR region, Smith (1978) detected a background event count rate of $\sim$ 15/s/keV with a one-dimensional imaging detector of surface area 166 cm^2. If the background event count rate is proportional to counter surface area, then the IPC would detect $\sim$ 15 x (156/166) = 14/s/keV. In the image plane, 6 x 6 cm^2= 3.24×10^4 arc min^2, and the expected background event luminosity would be 4.3×10^{-4}/s. keV arc min^2 in the energy range (0.3-0.8 keV). Hence, the background luminosity detected by the X-ray telescope during the Cygnus Loop SNR is of comparable value, $\sim$ 0.1 events / pixel = 5.0×10^{-4}/s. keV arc min^2 in the energy band (0.15 - 1.12 keV), for 143s observation time.

Hence, the images of Fig. 5.4 - 5.6 are totally source count limited, directly described by Poisson statistics. A pixel count of only 3 events gives a 1 σ signficance above ambient background.

5.2.2 Image smoothing.

With an average pixel X-ray event count of 1.6 for Fig. 5.6, the inherent signed to noise ratio (S/N) of the image is low ($\sim$ 1.3). Noise in an image generally has a higher spatial frequency spectrum than the normal image components because of its spatial decorrelatedness. Hence, simple low pass spatial filtering can be effective for noise smoothing. Simple noise suppression can be achieved by correlation of adjacent pixels in an image I_{xy} by convolution with a regular function with sufficient width, and the most straightforward function to use was a top hat function, T_{ij} , where

$$T = 1 \qquad -\frac{\Delta x}{2} < x < \frac{\Delta x}{2}\ ,\ -\frac{\Delta y}{2} < y < \frac{\Delta y}{2} \tag{5.1}$$

$$T = 0 \qquad \textit{otherwise}$$

The discrete convolution is :

$$I'_{ij} = \sum_{xy} I_{xy}\ T_{i-x\ j-y} \tag{5.2}$$

Normalising, $\sum T_{ij} = 1$

In (5.2) above, conserving the total count,

$$\sum_{ij} I'_{ij} = \sum_{xy} I_{xy} \tag{5.3}$$

For the unsmoothed image

$$\sigma_{xy}^2 = I_{xy}$$

and since the convolution of (5.2) is linear :

$$\sigma_{ij}'^2 = \sum_{xy} \sigma_{xy}^2 \; T_{i-x\; j-y}^2 \qquad (5.4)$$

Before convolution with T_{ij} the S/N of I_{xy} is :

$$\left(S/N\right)_{I_{xy}} = \frac{\sum I_{xy}}{\sum \sigma_{xy}^2} = 1 \qquad (5.5)$$

and after convolution the S/N of I_{ij}' is :

$$\left(S/N\right)_{I_{ij}'} = \frac{\sum I_{ij}'}{\sum \sigma_{ij}'^2} = \frac{N}{\sum_{ij}\sum_{xy} \sigma_{xy}^2 \; T_{i-x\; j-y}^2}$$

$$= \frac{N}{\sum_{xy} \sigma_{xy}^2 \sum_{ij} T_{ij}^2}$$

$$\therefore \quad \left(S/N\right)_{I_{ij}'} = \frac{1}{\sum_{ij} T_{ij}^2} \qquad (5.6)$$

Then the improvement in the S/N after convolution with T_{ij} :

$$\frac{\left(S/N\right) I_{ij}'}{\left(S/N\right) I_{xy}} = \frac{1}{\sum T_{ij}^2} \qquad (5.7)$$

Thus, as T_{ij} increases in width the obvious result is that the noise suppression increases. However, along with an increase in noise suppression, there is a corresponding degradation in resolution, apparent from the top hat modulation transfer function profile, discussed below.

The Cygnus Loop images of Fig. 5.4 - Fig. 5.6 were smoothed with a 3 x 3 pixel wide top hat filter (i.e 12' x 12'), approximating the telescope point response, and the results are shown in Fig. 5.7 - Fig. 5.9. The noise suppression is clearly evident and effective but the resolution has been degraded. The Sco. X-1 response was similarly smoothed and Fig. 5.10 shows the overall effect of the top hat filter. The modulation transfer function profile of the 12' x 12' top hat function,

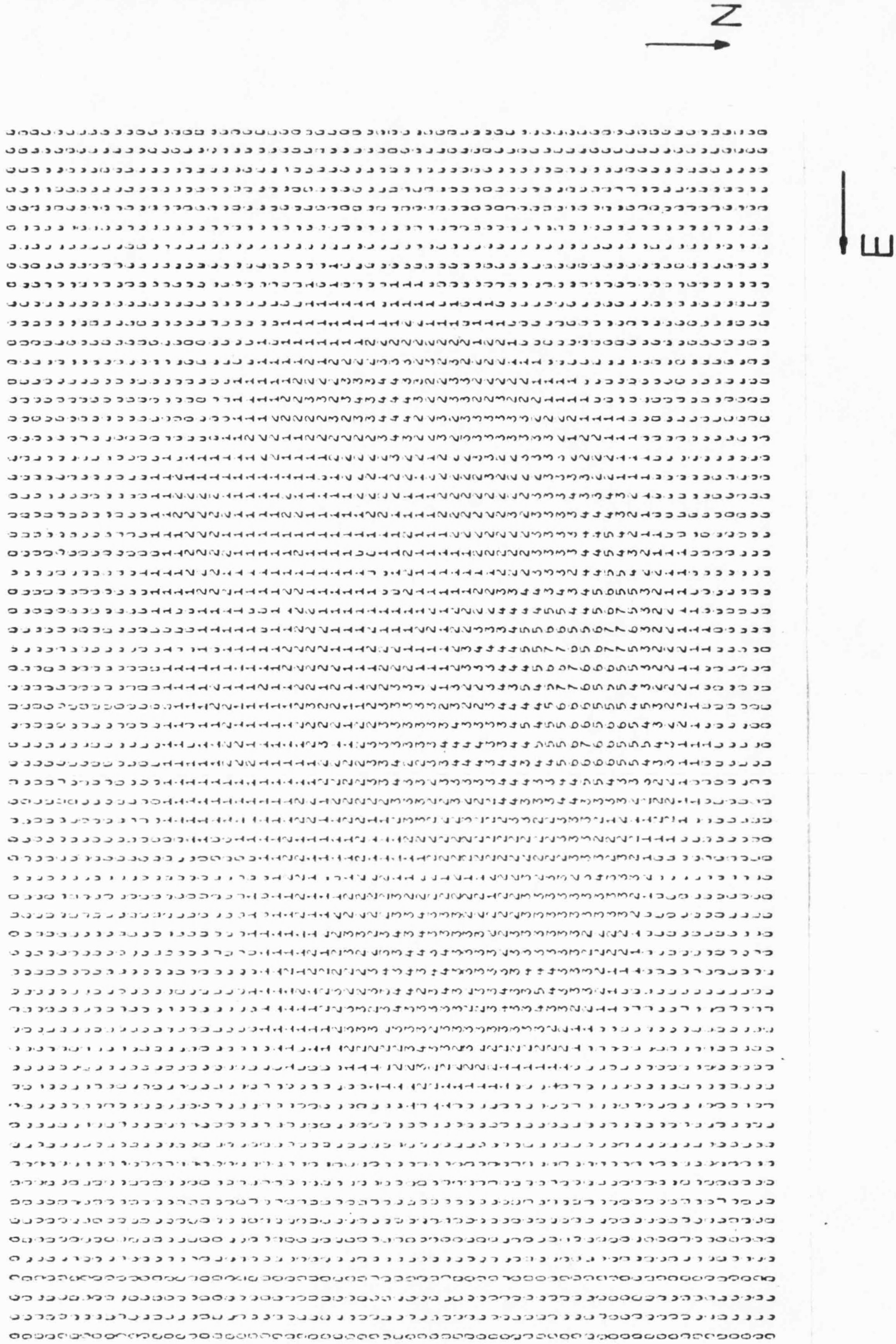

Fig. 5.7 Cygnus Loop X-ray image (.I5-.56 keV) plotted in sky coordinates.
The image has been smoothed with a top hat function, 3x3 pixels in size, to reduce statistical fluctuations. Each cross represents one X-ray event.

Fig. 5.7. Cygnus Loop X-ray image (0.15-0.56 keV) plotted in sky coordinates. The pixel size is 4'x4'. Each cross represents one X-ray event. The image has been smoothed with a top hat function, 3x3 pixels in width, to reduce statistical fluctuations. There is no correction for exposure variations.

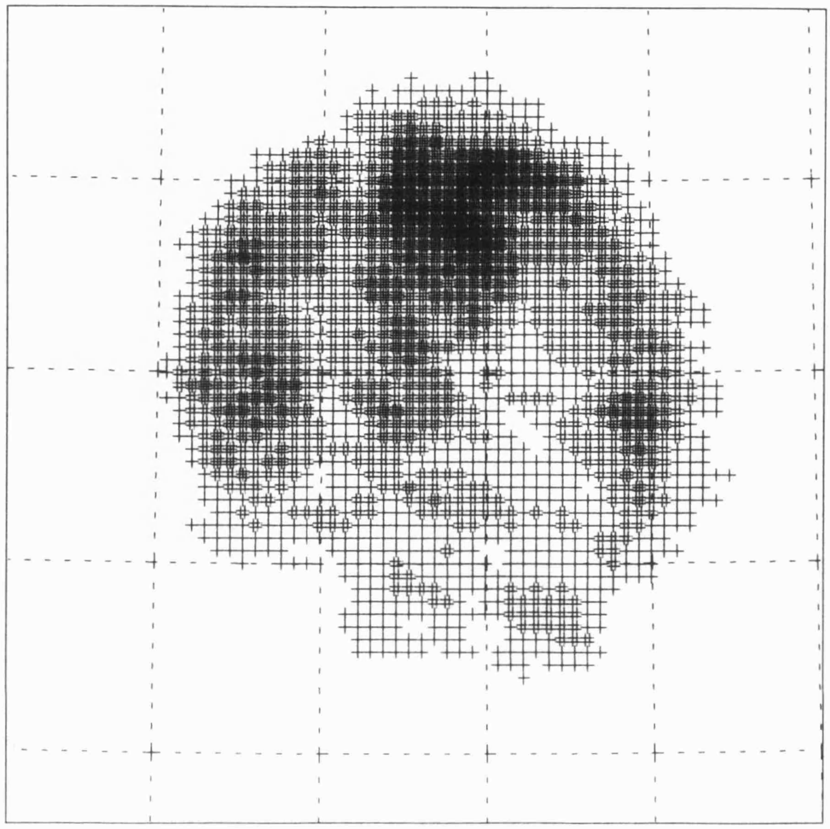

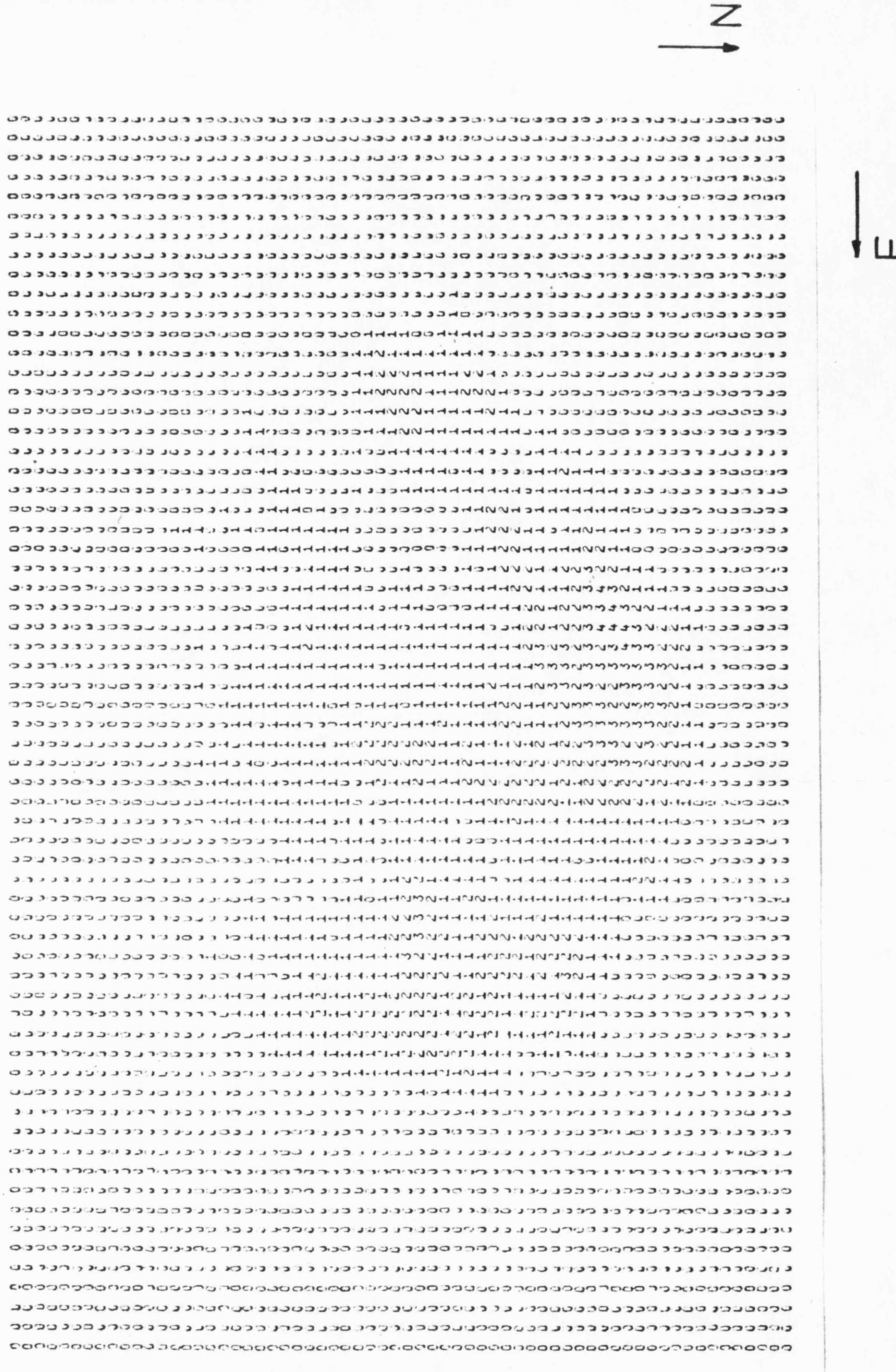

Fig.5.8. Cygnus Loop X-ray image (.56-I.I2 keV) plotted in sky coordinates.
The image has been smoothed with a top hat function, 3x3 pixels in width, to reduce statistical fluctuations. Each cross represents one X-ray event.

Fig. 5.8. Cygnus Loop X-ray image (0.56-1.12 keV) plotted in sky coordinates. The pixel size is 4'x4'. Each cross represents one X-ray event. The image has been smoothed with a top hat function, 3x3 pixels in width, to reduce statistical fluctuations. There is no correction for exposure variations.

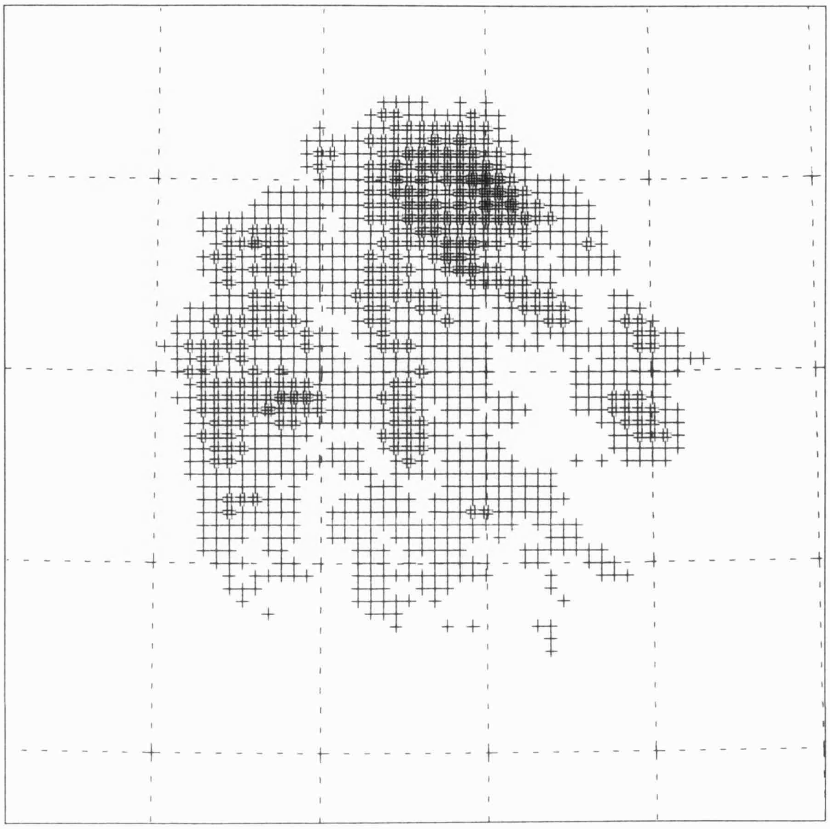

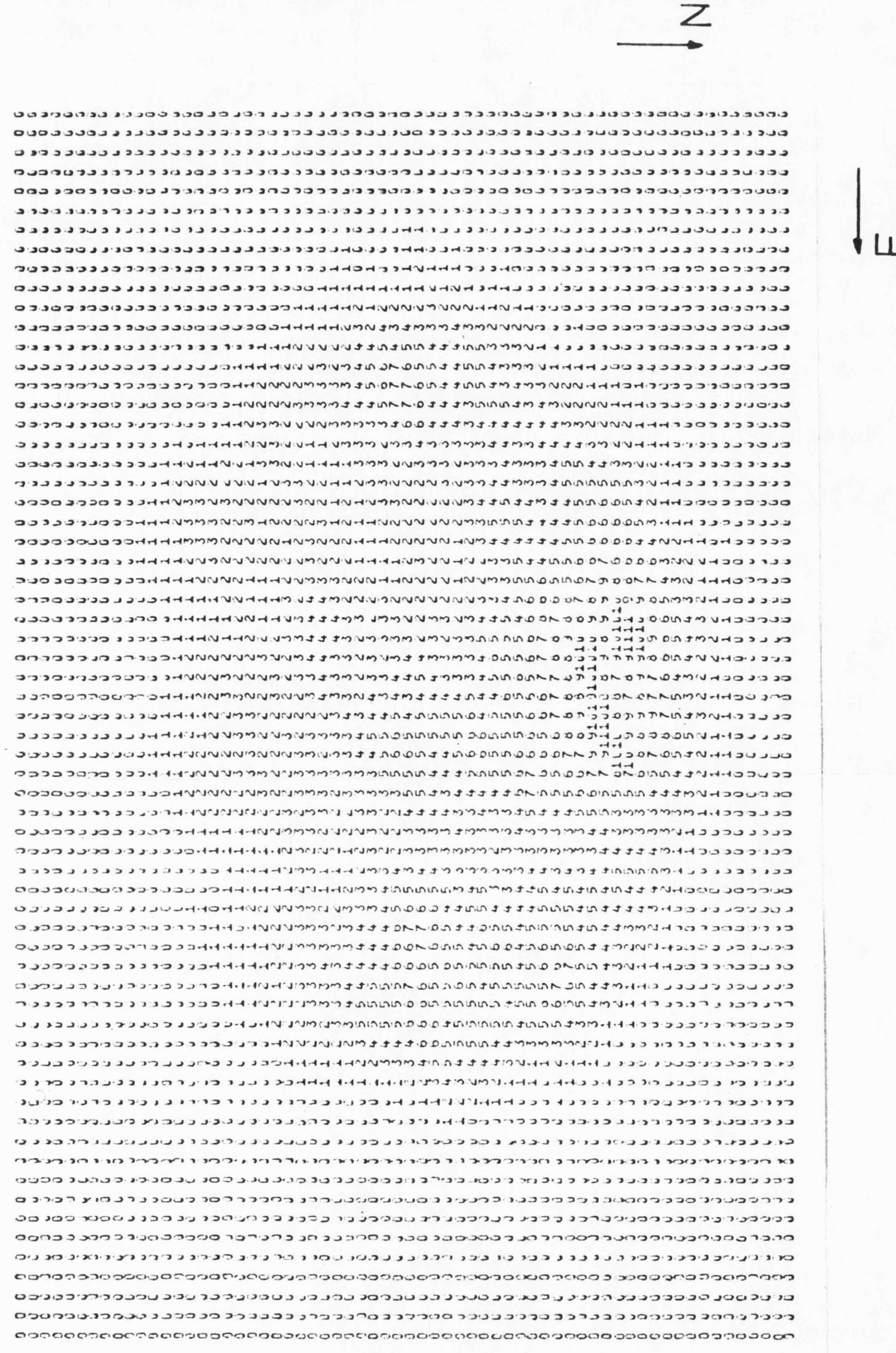

Fig. 5.9. Cygnus Loop X-ray image (.I5-I.I2 keV) plotted in sky coordinates.
The image has been smoothed with a top hat function, 3x3 pixels in width, to reduce statistical fluctuations. Each cross represents one X-ray event.

Fig. 5.9. Cygnus Loop X-ray image (0.15-1.12 keV) plotted in sky coordinates. The pixel size is 4'x4'. Each cross represents one X-ray event. The image has been smoothed with a top hat function, 3x3 pixels in width, to reduce statistical fluctuations. There is no correction for exposure variations.

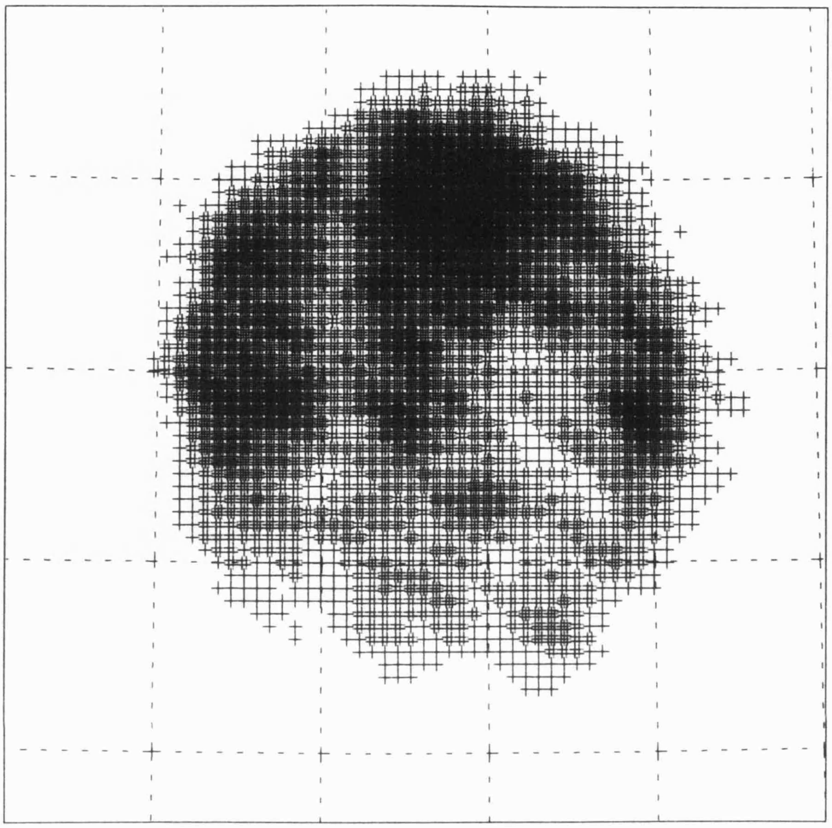

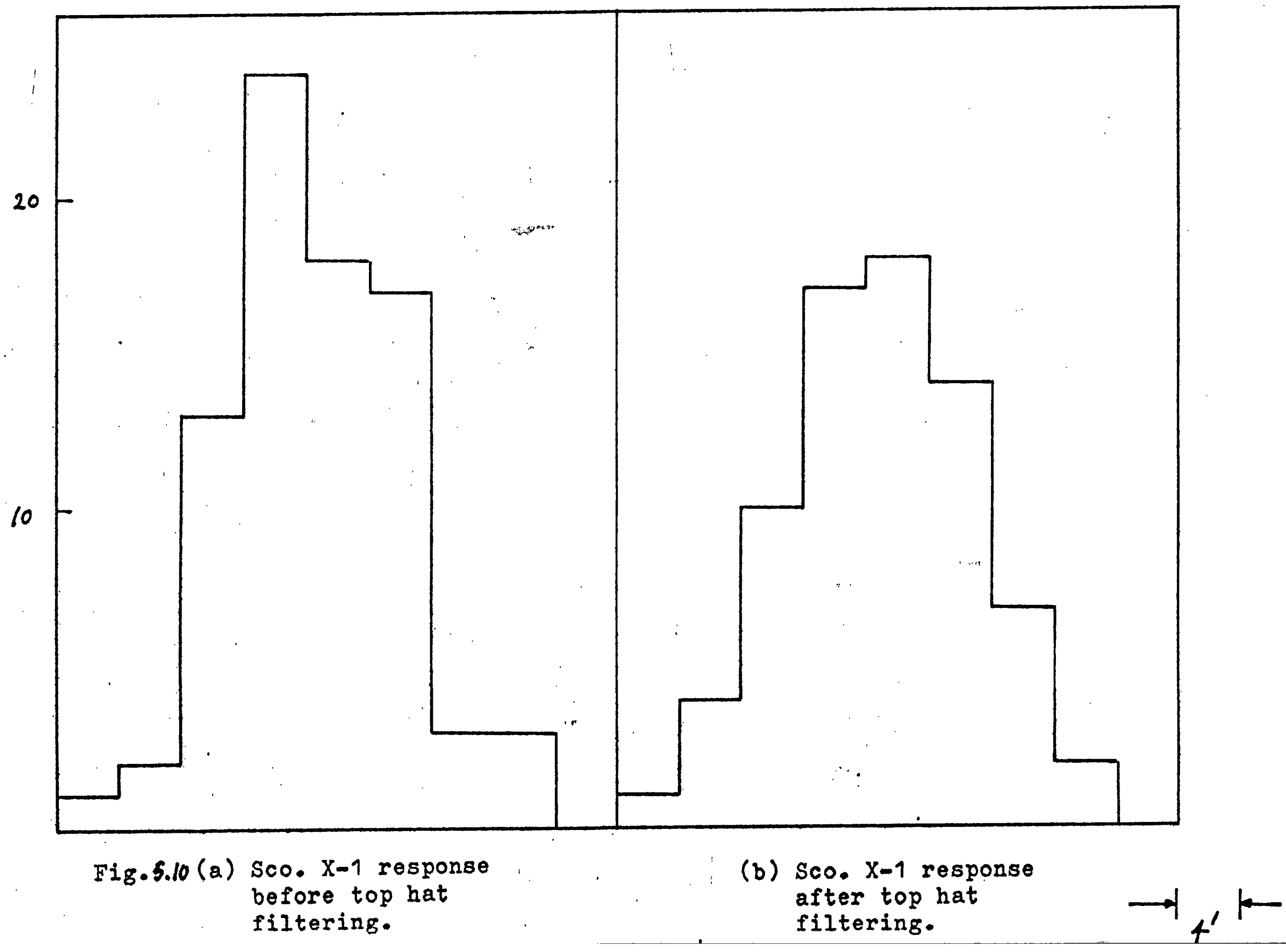

Fig. 5.10 (a) Sco. X-1 response before top hat filtering.

(b) Sco. X-1 response after top hat filtering.

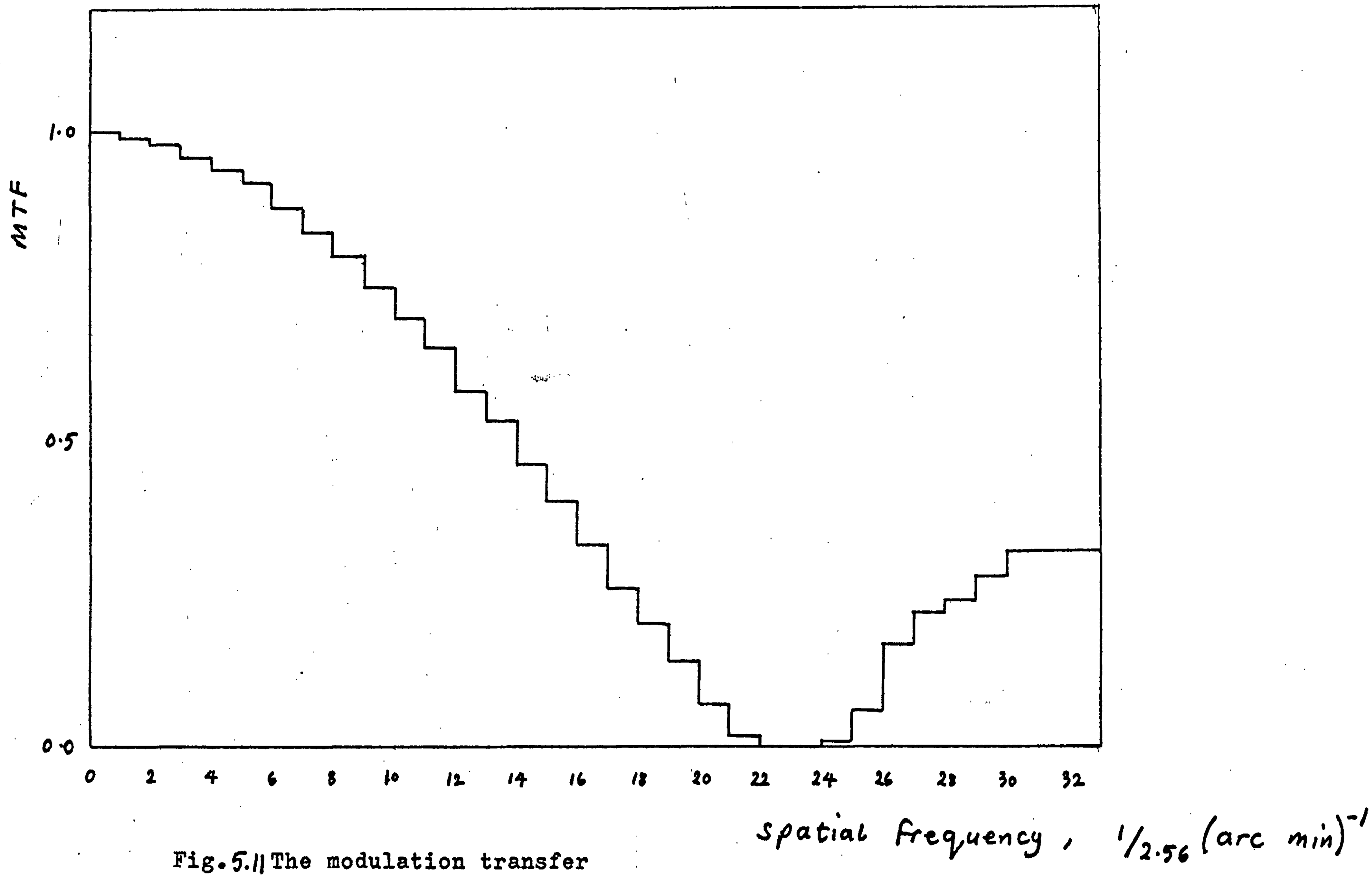

Fig. 5.11 The modulation transfer function profile of the top hat filter, 12'x12' in width.

Fig. 5.11, illustrates the noise suppression region together with the higher spatial frequency lobe which prevents good feature extraction of I_{xy} .

Following the image smoothing, the images of Fig. 5.7 - Fig. 5.9 were exposure corrected. The effective area matrix, in the IPC co-ordinate system, Fig. 5.12, was constructed from Fig. 3. (0.28 keV data) and including the X-ray position analysis criteria of section 4.2.2. The smooth exposure matrix created by integrating Fig. 5.12 along the two scan paths for the Cygnus observation (Fig. 4.4) is shown in Fig. 5.13, which gives a record of the exposure received for each pixel. To correct for exposure variations around the edges, particularly the Southern regions, the event count per pixel per image was inversly weighted by the pixel exposure, and the result normalised to the total event count in the unsmoothed image (to achieve the least mean square difference between the unexposure corrected, unsmoothed image and the exposure corrected, smoothed image). To prevent regions of each image, which experienced low exposure and hence, after exposure correction, being assigned relatively high flux, the exposure matrix only included values above one quarter of the mean exposure (834.6 cm^2.s (0.15 - 0.56 keV)). The images in Fig. 5.14 - Fig. 5.16 have been exposure corrected in the above manner. Each cross in a pixel of Fig. 5.16 represents 1.2 X-ray events detected in the unsmoothed image (Fig. 5.6).

5.2.3 Image reconstruction with feature extraction.

The initial image matrix I_{xy} representing the source brightness distribution, contains the effects of blurring (through finite instrument angular resolution), noise (source associated and non-source associated) and digitisation (of the image field and event energy). The Cygnus Loop X-ray images represent severely degraded (astronomical) pictures and the philosophy of picture processing as a whole may be adopted to these imaging X-ray astronomy results. Picture processing techniques may model the above effects inherent in Fig. 5.4 - Fig. 5.6 to produce final images which are relatively free from errors created by these effects. Willingale (1979) will

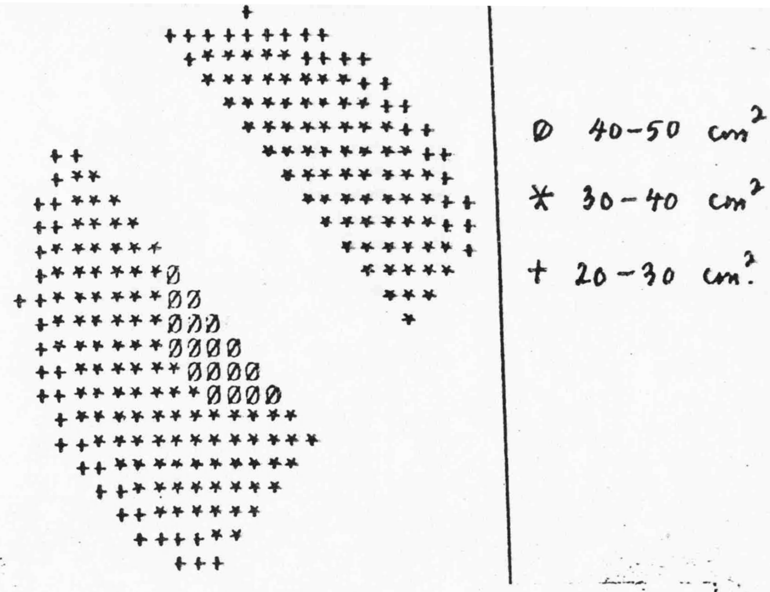

Fig. 5.12 The 90' FOV telescope effective area matrix shape.

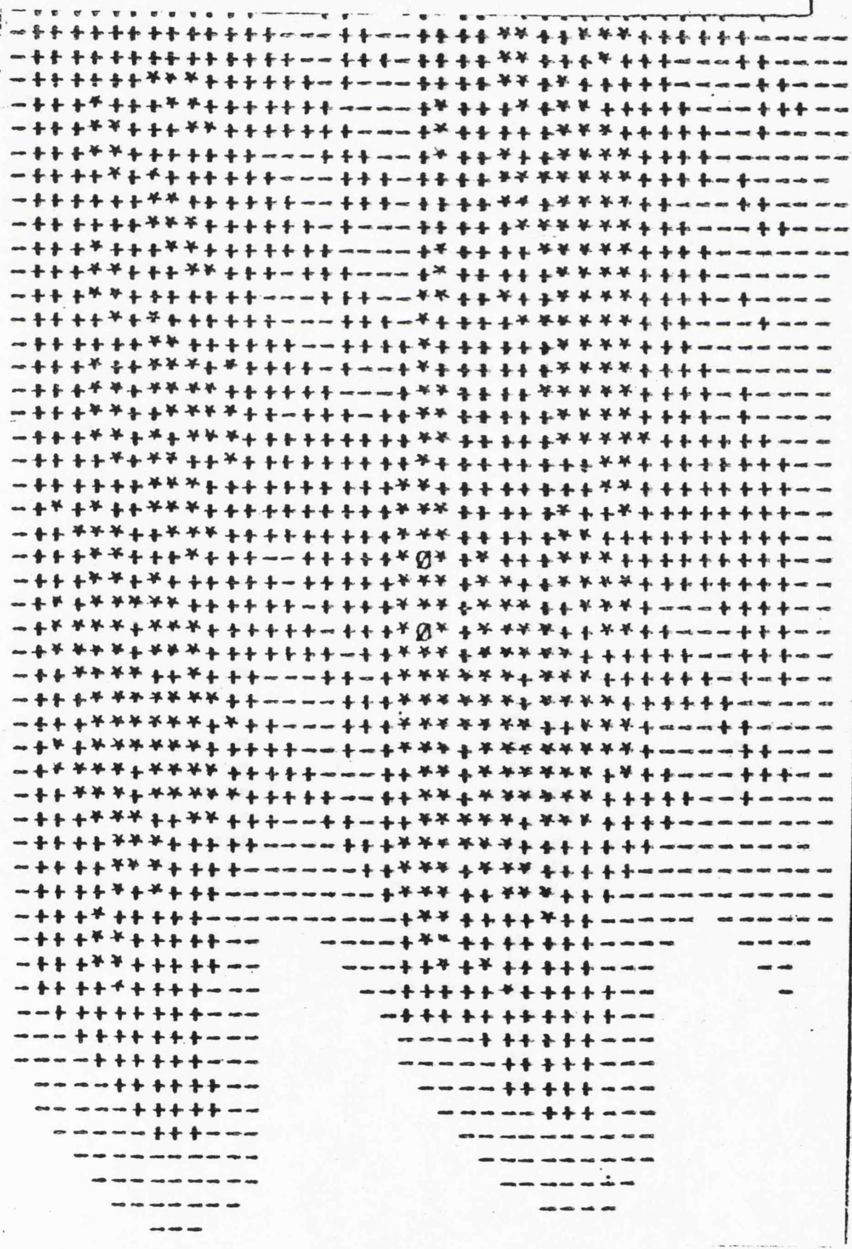

Fig. 5.13 The exposure matrix created by using the telescope axis equation of motion to scan the telescope area matrix over the Cygnus region.

Fig. 5.14 Exposure corrected image
(0.12 - 0.56 keV)

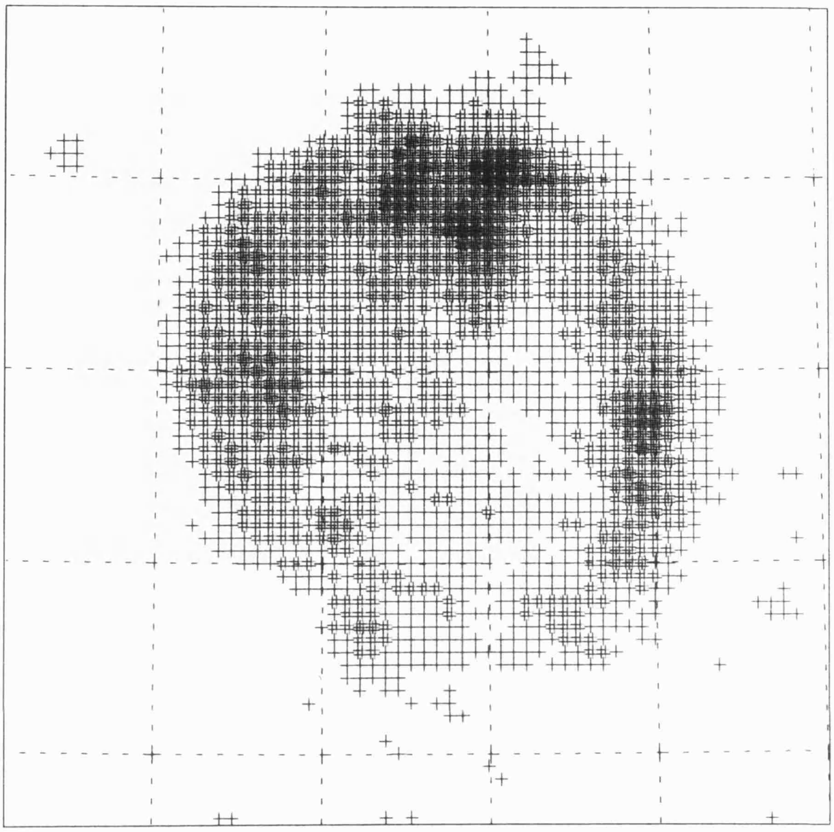

Fig. 5.15 Exposure corrected image (0.56 - 1.12 keV)

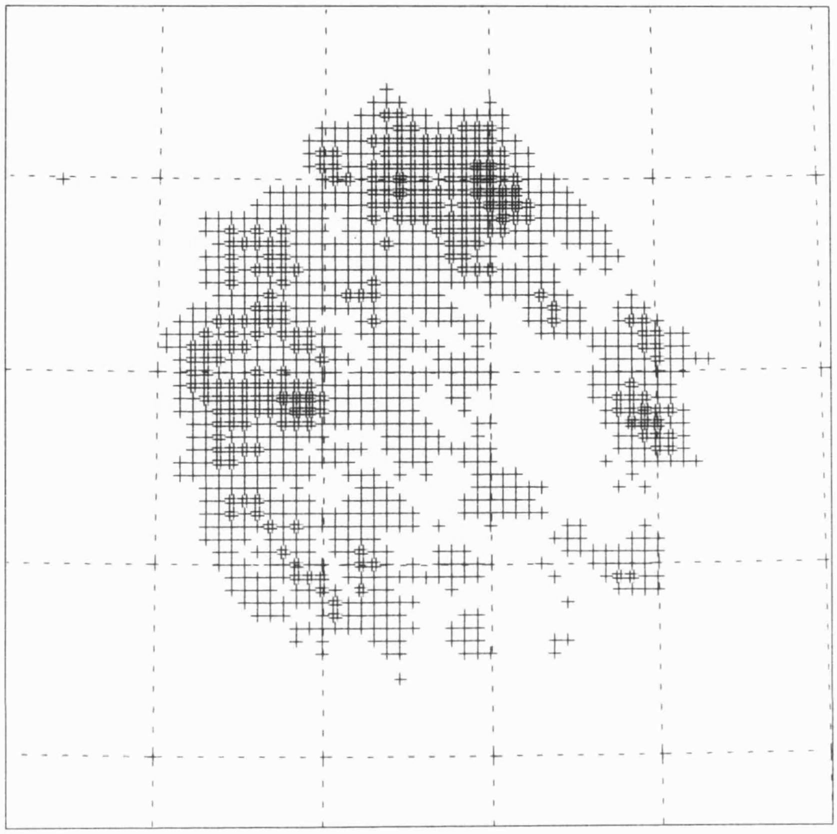

Fig. 5.16 Exposure corrected image (0.12 - 1.12 keV)

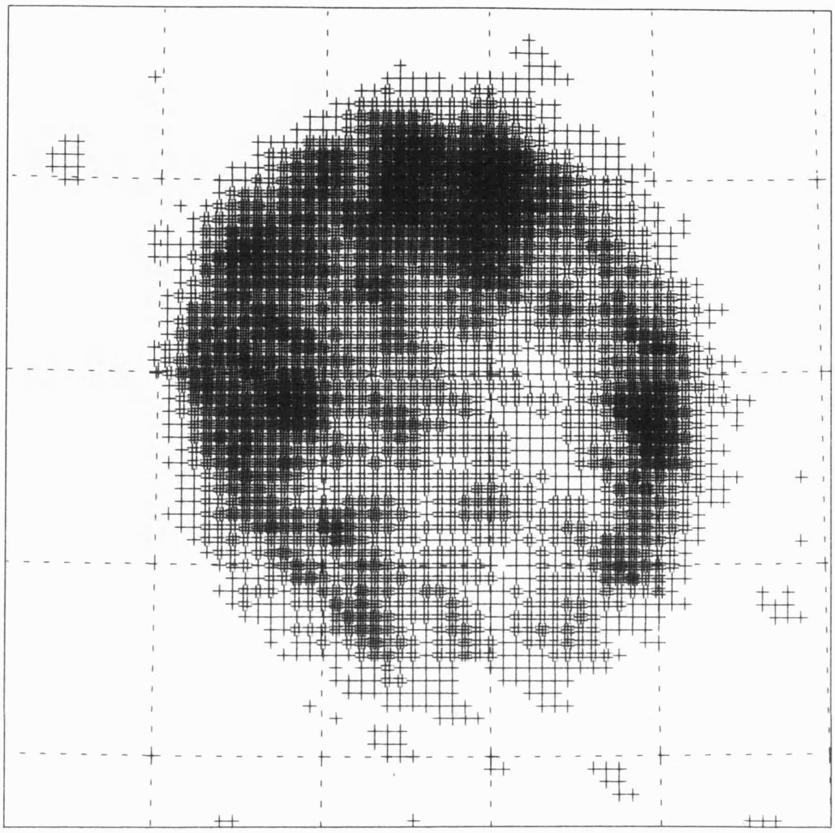

report in detail several techniques of processing X-ray astronomy images. The results of two techniques used to process the Cygnus Loop images, enabling feature extraction and noise suppression are presented below, produced by the linear, non-iterative Wiener filter and the non-linear, iterative maximum entropy reconstruction methods.

5.2.3.1 Discrete filtering - The Wiener filter.

Discrete filtering usually operates on space invariant systems, and is performed in the discrete Fourier transform domain, where a product of a blur matrix, representing the spatially invariant, overall instrument response, and the initial image matrix is performed. Discrete filtering is essentially global. The Wiener filter (Pratt 1972, 1975) was adapted by Willingale (1978) in a first attempt at processing the Cygnus images. Improved reconstruction quality is possible with Wiener filtering techniques, which incorporates apriori statistical knowledge of the image noise field. The application of the Cygnus images first assumed that the noise was white noise with a flat Fourier spectrum (the noise in each pixel being uncorrelated with others). The effectiveness of the Wiener filter is dependent on the ratio of the signal power spectrel density to the noise power spectrel density.

The Wiener filter minimises the least mean square error between the input raw image matrix and the estimated image matrix based on model blur and noise matrices. That is, in continuous image Wiener filtering systems, the impulse response of the restoration filter is chosen to minimise the mean square restoration error :

$$\mathcal{E} = E\left\{ I_{ij} - \hat{I}_{ij} \right\}^2 \qquad (5.8)$$

and the transfer function of the optimum restoration filter is :

$$W_{R_{ij}} = \frac{W_{D_{ij}}^{*}}{\left| W_{D_{ij}} \right|^2 + W_{N_{ij}}} \qquad (5.9)$$

where $\hat{I}$ is the reconstructed image of I and given by :

$$\hat{I}_{ij} = \left[I_{ij} \otimes W_{D_{ij}} + N_{ij} \right] \otimes W_{R_{ij}} \tag{5.10}$$

where $\otimes$ means 'convolved with'. The transfer function of the instrumental blur matrix is $W_{D_{ij}}$ where i and j are the spatial frequencies of x and y , and for the X-ray telescope, consisted of contributions from the mirror (σ_m = 6'), the IPC gas spreading (σ_g = 1') and the IPC wires (σ_w = 3') giving an overall response with σ = 6.7'.

The process above is illustrated in Fig. 5.17. A full description of the Wiener filtering of the Cygnus data (Fig. 5.6) will be given by Willingale (1979). The Wiener filtered, exposure corrected Cygnus images are discussed below (5.3.1).

However, the Wiener filter with additive noise in the above discussion, the white noise filter, had a global nature of suppressing regions of good S/N and enhancing regions of low S/N, giving optimistic feature extraction and poor low frequency band pass (5.3.1). Willingale (1978) included the low spatial frequency correlation of noise with signal, present in the Cygnus images, due to the fact that the image noise was mainly correlated with the source - the non-rejected background (5.2.1) was negligable per pixel - and the roll-off at higher frequencies ($\sim$ 1/15') being the effect of the instrument transfer function. The modified Wiener filter was a more optimum filter for moderate restoration at low frequencies and noise suppression at higher frequencies ($\lesssim$ 1/18'), utilising an overall instrument response of 20' (FWHM).

5.2.3.2 Algebraic methods - The maximum entropy reconstruction.

Albebraic methods, involving iterative procedures are, in general, more adaptable to picture processing.

The principles of the maximum entropy image restoration have been clearly explained by Kikuchi and Soffer (1977) and references therein, who were concerned with the statistics of image formation in determining the optimum

Fig. 5.17 Principle of image reconstruction using a Wiener filter with additive white noise. The instrument point response components are listed in Table 3.4. The image bin size is SR.

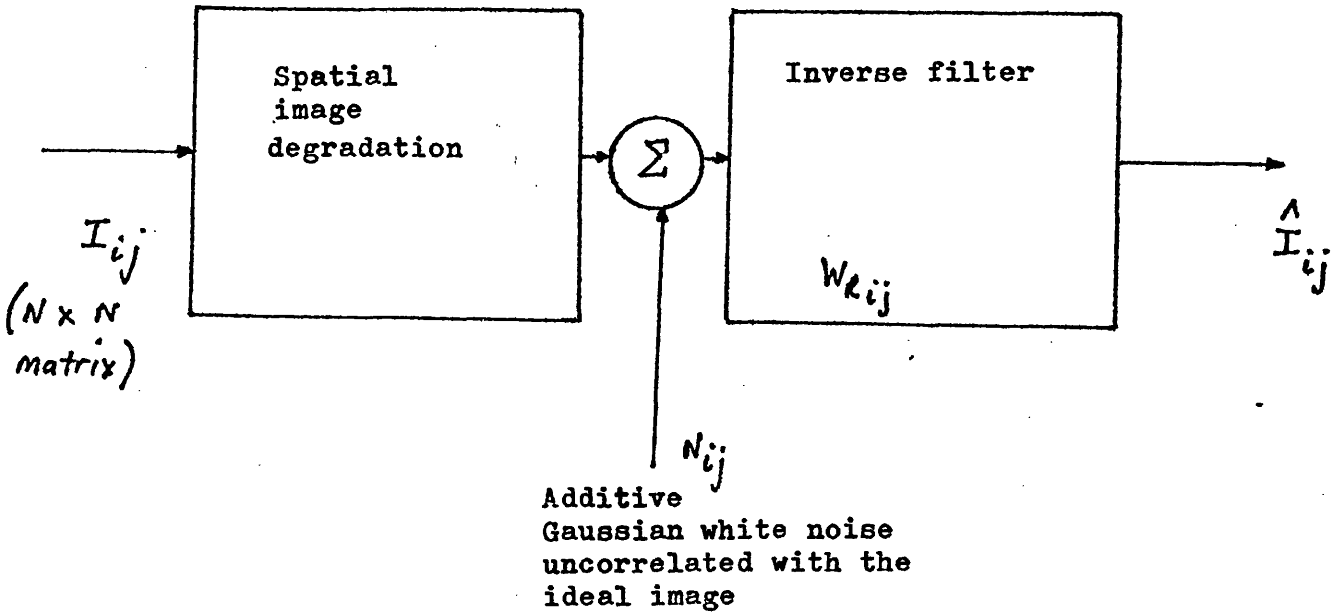

The reconstructed image is given by :

$$\hat{I}_{ij} = \left(I_{ij} \circledast W_{Dij} + N_{ij} \right) \circledast W_{Rij}$$

where the instrument point response matrix is :

$$W_{Dij} = \left(M_{ij} \circledast G_{ij} \right) \circledast W_{ij}$$

and where

$$M_{ij} = \frac{1}{\sqrt{2\pi^2\sigma^2}} \cdot \frac{e^{-\frac{r^2}{2\sigma^2}}}{r} \cdot SR^2$$

$$G_{ij} = \frac{1}{2\pi\sigma} \cdot \frac{e^{-\frac{r}{\sigma}}}{r} \cdot SR^2$$

$$W_{ij} = \frac{1}{2\pi\sigma^2} \cdot e^{-\frac{r^2}{2\sigma^2}} \cdot SR^2$$

$$r = \left\{ \left(i - N/2 - 1 \right)^2 + \left(j - N/2 - 1 \right)^2 \right\}^{\frac{1}{2}} \cdot SR.$$

reconstructed image. For source local brightness B, the entropy expression appropiate to an X-ray image (and an optical image) where the number of degrees of freedom of the field is much greater than the number of photons is (Kikuchi and Soffer 1977, Frieden 1972, 1975) :

$$S = - B \operatorname{Log} B \qquad (5.11)$$

In more detail, $S(\underline{B})$ is defined to be minus the information content of the numbers B_i (intensity in pixel i) :

$$S(\underline{B}) = - \sum_i P_i \operatorname{Log} P_i \qquad (5.12)$$

where $P_i = B_i / \sum B_i$ is the proportion of the total intensity in pixel i. $S(\underline{B})$ gives a measure of uncertainty for the distribution of a given photon intensity among the pixels, given that the pixels produce photons at a rate of B_i, and so measures the uncertainty in predicting where the next photon will come from. Maximum entropy means maximum uncertainty, corresponding to spreading the intensity among pixels in as smooth a manner as possible, in a way consistent with the initial image matrix. Maximum entropy is a smoothness condition. Thus, any feature existing in the processed image are caused by structure existing in the original image.

On application of the maximum entropy technique, S is maximised subject to some particular statistic such as χ^2, taking some value such as the total number of photons detected. In practise, $S - \lambda.\chi^2$ is maximised, where λ is a Lagrange multiplier effecting the constraint. The change in S,

$$\frac{\partial S}{\partial B_i} \propto \operatorname{Log} B_i - \frac{\sum B_i \operatorname{Log} B_i}{\sum B_i} \qquad (5.13)$$

gives a steady increase towards uniformity.

The formulation for the (configurational) entropy expression set down by Kikuchi and Soffer, was adapted by Willingale (1978) to perform two-dimensional image reconstruction and smoothing of the Cygnus Loop data (Fig. 5.4 - Fig. 5.6), and the processed image is discussed in sections 5.3.1 and 5.3.2.

5.3 Final image presentation.

5.3.1 Line density plots in celestial co-ordinates.

In Fig. 5.17 the smoothed (0.15 - 1.12 keV) Cygnus Loop image has been plotted in RA and Dec. Each cross represents 1.2 X-ray events detected in the unsmoothed image. Poisson statistics no longer describe accurately the statistics of the exposure corrected image, but since the exposure matrix (5.2.2) was relatively smooth, then the uncertainty in intensity for any given pixel of Fig. 5.17 may be estimated by the square root of the number of crosses displayed. The only exceptions occur in regions where $\delta \leq 29^{\circ} 30'$, $\alpha \leq 20^{h} 41^{m}$ and $\alpha \geqslant 20^{h} 47^{m}$ where exposure corrections were greater than a factor of 2.

The similarly smoothed Sco. X-1 image is plotted in the inset, with a grey level of one cross $\sim$ 2 X-ray events.

There are several prominent features apparent in the image of Fig. 5.17, which has undergone no restoration (in fact, further blurring - 5.2.2) but significant noise suppression. The image of Fig. 5.17 is discussed in sections 6.3 and 6.4, as are the images presented below.

In Fig. 5.18, the Wiener filtered (0.15 - 0.56 keV), (0.56 - 1.12 keV) and (0.15 - 1.12 keV) images are displayed in RA and Dec. The above discussion for Fig. 5.17 also applies to Fig. 5.18. The discrete features observed in Fig. 5.17 have been further enhanced in Fig. 5.18 along with regions of initial low surface brightness (5.2.3.1). The instrument point response in Fig. 5.18 has 15' (FWHM).

In Fig. 5.19, the maximum entropy reconstruction (0.15 - 1.12 keV) Cygnus image is displayed in RA and Dec. The inherent point response is 20' (FWHM). A smoother image with high noise suppression has been formed. All features observed in Fig. 5.17 and Fig. 5.18 are also reproduced in Fig. 5.19.

All three sets of images show consistent, discrete structure in the X-ray emission from the Cygnus Loop SNR,

Fig. 5.17 Line density plot of the top hat filtered, exposure corrected Cygnus Loop image (0.15-1.12 keV).

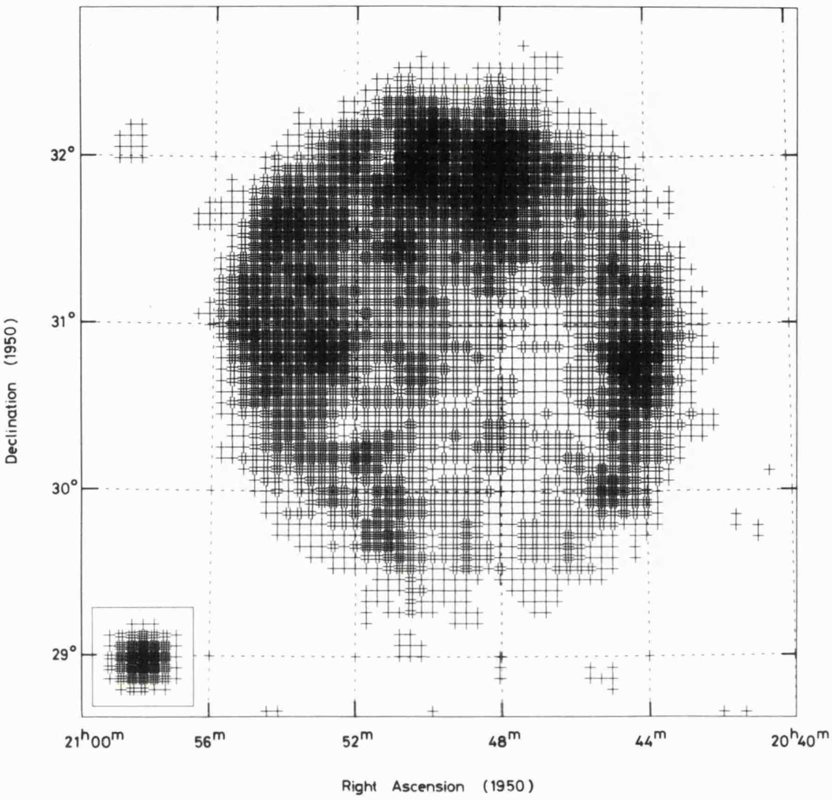
32°
31°
30°
29°
Declination (1950)
21h00m
56m
52m
48m
44m
20h40m
Right Ascension (1950)

Fig. 5.18 Line density plot of the Wiener filtered, exposure corrected Cygnus Loop image (0.15-0.56 keV).

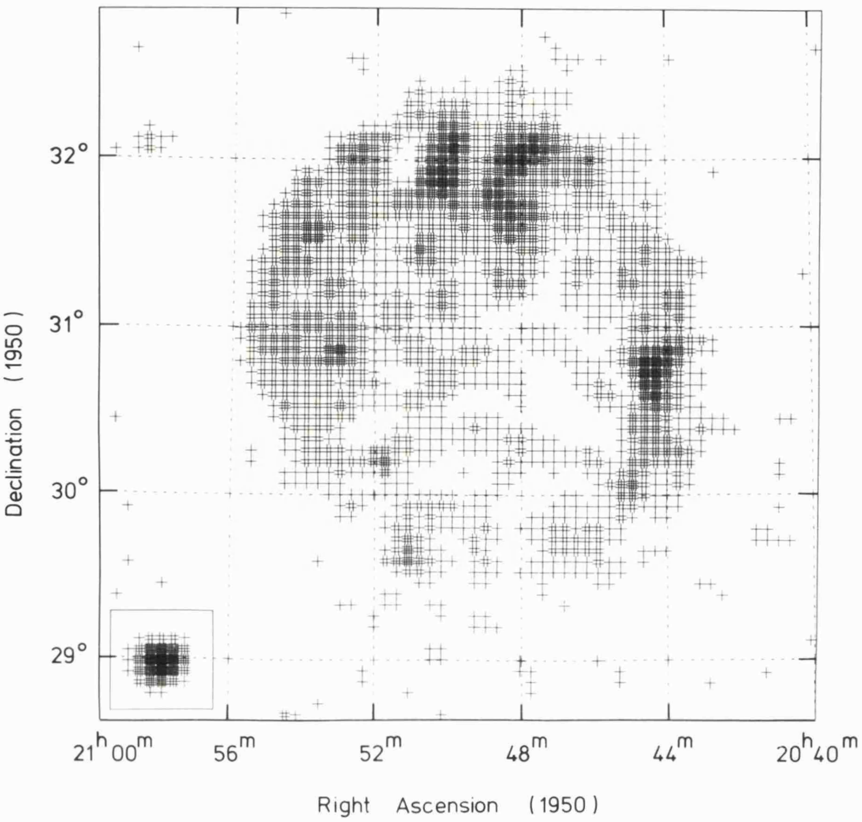
32°
31°
30°
29°
Declination (1950)
21h00m
56m
52m
48m
44m
20h40m
Right Ascension (1950)

Fig.5.18 Line density plot of the Wiener filtered, exposure corrected Cygnus Loop image (0.56-1.12 keV).

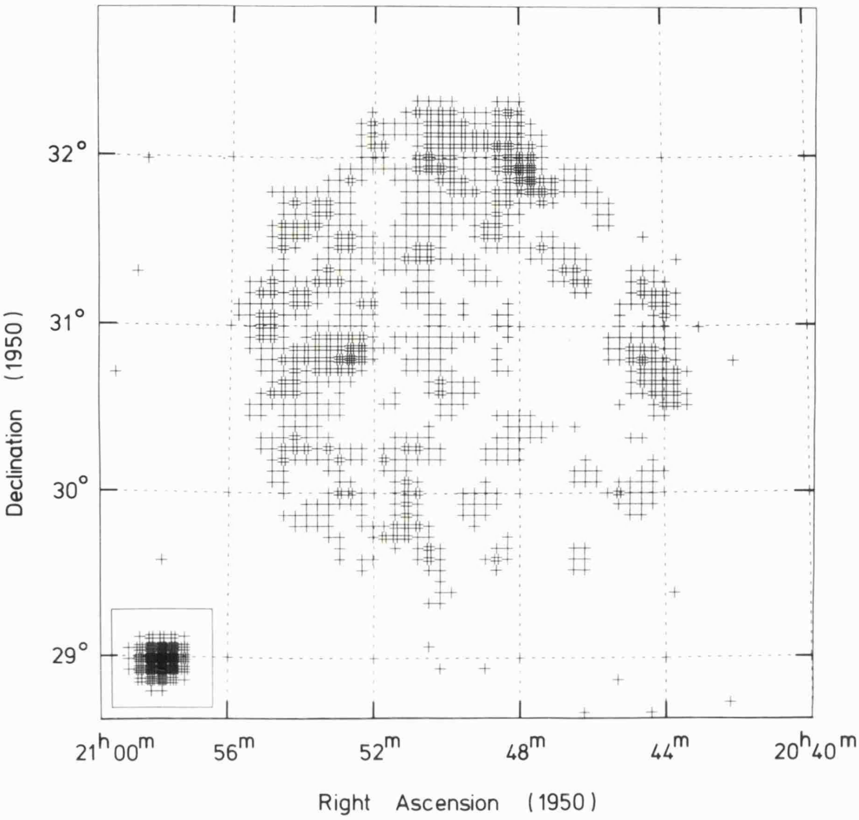
32°
31°
30°
29°
Declination (1950)
21h00m
56m
52m
48m
44m
20h40m
Right Ascension (1950)

Fig. 5.18 Line density plot of the Wiener filtered, exposure corrected Cygnus Loop image (0.15-1.12 keV).

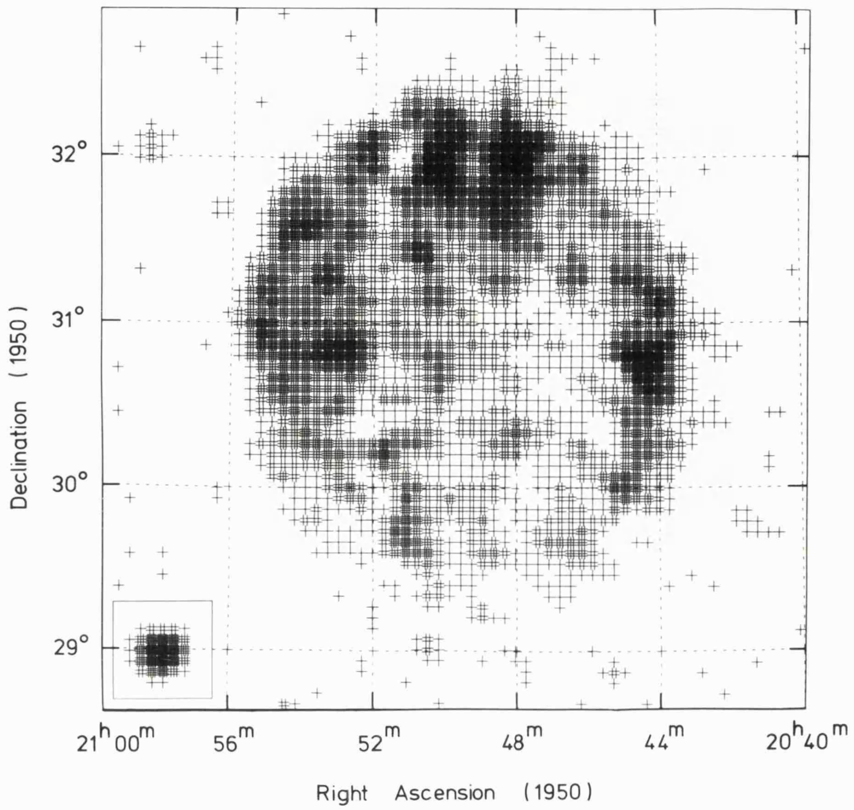

32°
31°
30°
29°
Declination (1950)
21h 00m
56m
52m
48m
44m
20h 40m
Right Ascension (1950)

Fig. 5.19 Line density plot of the maximum entropy reconstruction, exposure corrected Cygnus Loop image (0.15-1.12 keV).

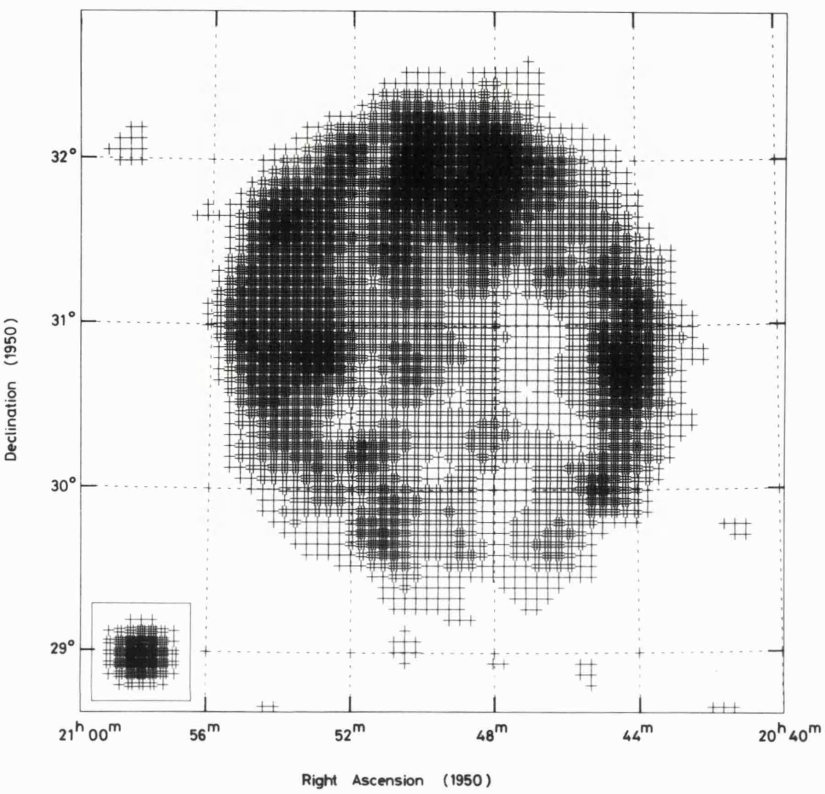

32°
31°
30°
29°
Declination (1950)
21h 00m
56m
52m
48m
44m
20h 40m
Right Ascension (1950)

which have been slightly suppressed (Fig. 5.17) enhanced (Fig. 5.18) and smoothed (Fig. 5.19).

5.3.2 Contour plots in celestial co-ordinates.

Contour plots may give a clearer impression of the intensity and localisation of the discrete features observed in section 5.3.1. In Fig. 5.20, a contour plot of Fig. 5.17 is displayed, with a contour level of 1 event / pixel of Fig. 5.17 ($\sim$ 0.06 photons / cm^2. s. keV arc. min^2.) In Fig. 5.21, a contour plot of Fig. 5.19 is displayed, again with a contour level of 1 event / pixel. Clearer feature extraction again is observed in the maximum entropy image, with the features of Fig. 5.17 being smoothed.

The two contour maps are discussed in detail in sections 6.3 and 6.4.

5.4 Summary.

The final stage of the X-ray image formation of the Cygnus Loop SNR has been briefly discussed. Post processing of the image using three techniques has resulted in localising, consistently, discrete structure in the X-ray emission of the SNR, which has the overall, appearance of a broken, limb - brightened, assymmetrical, thick shell. The image processing techniques, as have been applied to the problem of a corrupted X-ray image, are still being investigated (Willingale 1978). However, the maximum entropy image perhaps gives the best estimate of the true image, consistent with the initial image and the known telescope parameters, by performing a global smoothing and reconstruction, of the initial image.

Fig. 5.20 Contour plot of the top hat filtered, exposure corrected Cygnus Loop image (0.15-1.12 keV)

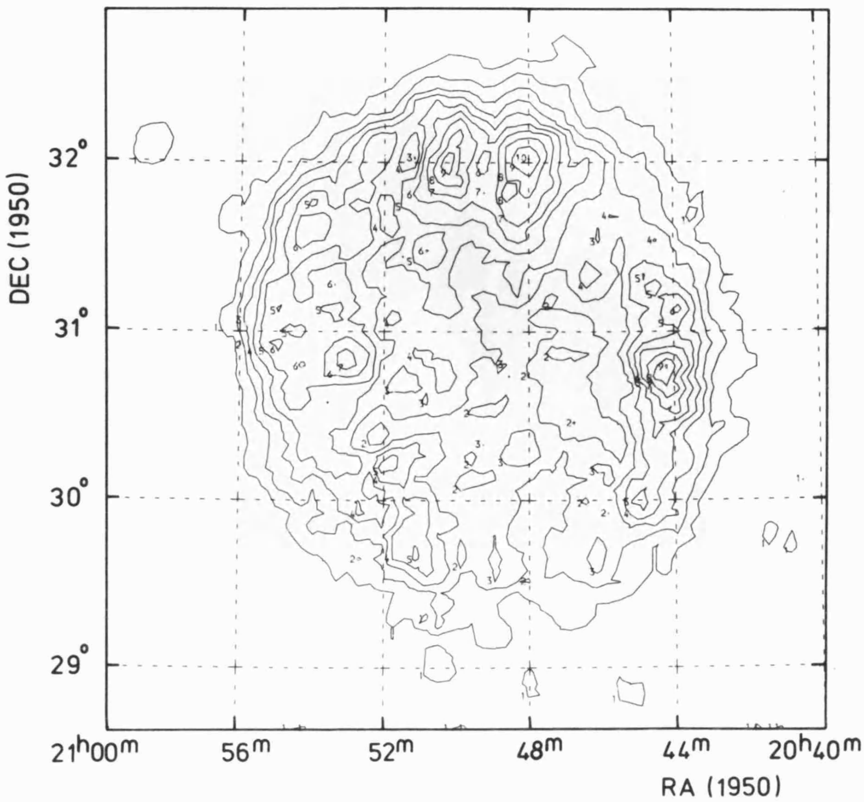
DEC (1950)
32°
31°
30°
29°
21h00m
56m
52m
48m
44m
20h40m
RA (1950)

Fig.5.21 Contour plot of the maximum entropy reconstruction, exposure corrected Cygnus Loop image (0.15-1.12 keV)

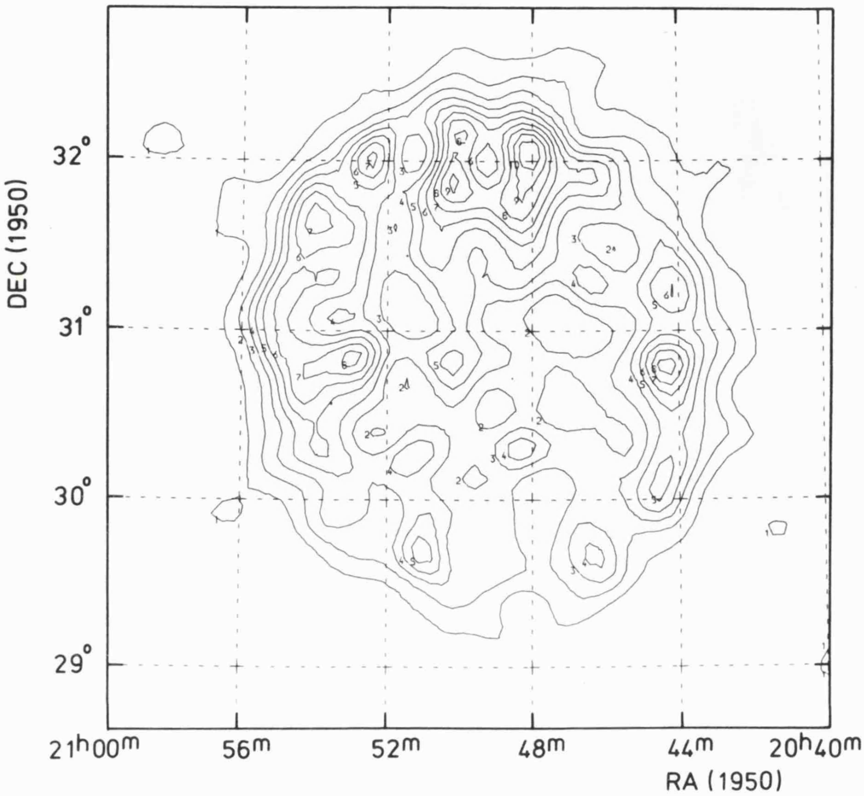

DEC (1950)
32°
31°
30°
29°
21h00m
56m
52m
48m
44m
20h40m
RA (1950)

References.

Frieden, B., 1972. J. Opt. Soc. Am., 62, 511

Frieden, B., 1975. Picture processing and digital filtering, ed. T. Huang., Springer - Verlag.

Kikuchi, R. and B. Soffer, 1977. J. Opt. Soc. Am., 67, 1656.

Pratt, W., 1972. IEEE Trans. Comp., C-21, 636

Pratt, W., 1975. Computer Image Processing, PCL Advanced Technology Series.

Smith, A., 1978. Private Communication, University of Leicester.

Willingale, R., 1978. Private Communication, University of Leicester.

Willingale, R., 1979. Thesis, University of Leicester.

Chapter 6. ANALYSIS AND INTERPRETATION OF THE X-RAY IMAGE OF THE CYGNUS LOOP SNR.

Chapter 6. ANALYSIS AND INTERPRETATION OF THE X-RAY IMAGE OF THE CYGNUS LOOP SNR.

6.1 Introduction.

The features of the Cygnus Loop images presented in Fig. 5. 14 - 19, are discussed and comparison made with earlier X-ray maps and with optical and radio features. Variation of X-ray spectral parameters in the X-ray image are investigated and discussed.

6.2 X-ray spectral analysis.

6.2.1 Spectral hardness map.

From section 4.3, from the Sco X - 1 observation towards the end of the rocket flight, the inferred performance of the X-ray telescope, was that the in - flight parameters remained steady, at the pre - launch calibration values. The Cygnus Loop images, Fig. 5. 17, 18, 19 were examined for gross spectral variations. The unfolded image matrices in the energy bands 0.15 - 0.56 keV and 0.56 - 1.12 keV were binned in 12 x 12 arrays of $32' \times 32'$ pixels, for increased statistical significance per pixel (cf. Fig. 5,4,5) and the ratio of the upper and lower energy matrices, formed. Fig. 6.1 shows the spatial variation of the hardness values were obtained and plotted in celestrial coordinates. Only highly significant $\geqslant 3\sigma$, values for each pixel were plotted, lower values set to zero. The value of σ per pixel was derived from the Poissonian statistic describing the images. If I_{ij}^h and I_{ij}^l are the high and low energy image intensities per pixel, respectively, then the hardness ratio :

$$H_{ij} = I_{ij}^h / I_{ij}^l \geqslant 3\sigma_{ij}$$

$$\sigma_{ij} = \frac{I_{ij}^h}{I_{ij}^l} \left\{ \frac{1}{I_{ij}^l} + \frac{1}{I_{ij}^h} \right\}^{\frac{1}{2}}$$

Fig. 6.1 X-ray spectral hardness map.

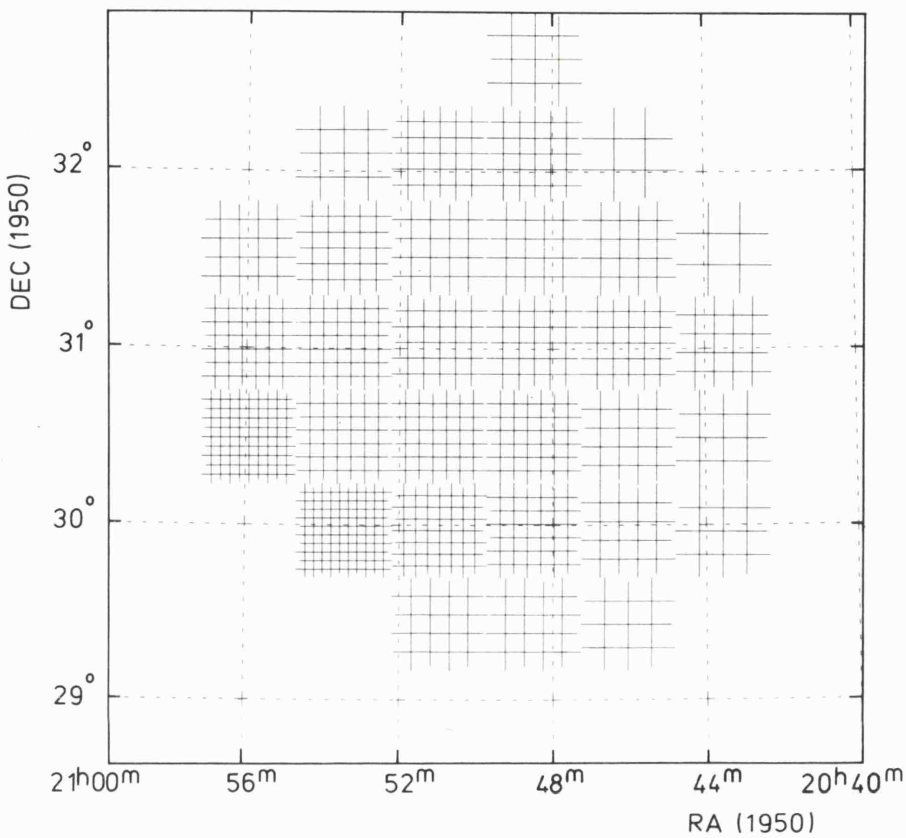

DEC (1950)
32°
31°
30°
29°
21h00m
56m
52m
48m
44m
20h40m
RA (1950)

An overlay of the hardness map on a POSS point of the Loop is shown in Fig. 6.2. Significant spectral variations are observed, in regions $32' \times 32'$ in size (7 pc for the approximate 770 pc distance).

The IPC anode pulse height distributions were analysed in regions delineated as in Fig. 6.2. Generally, the response to an emission function $S(\varepsilon)$, including absorption, of a counter system is given by

$$n_i = \int_0^{\infty} \int_{\varepsilon_i}^{\varepsilon_{i+1}} S(\varepsilon') R(\varepsilon', \varepsilon) \, d\varepsilon \, d\varepsilon'$$

where n_i is the number of counts per pulse height interval and $R(\varepsilon', \varepsilon)$ is the detector response, including the combined effects of X-ray mirror efficiency collimator responses, counter window transmission, gas absorption, gas X-ray fluorescence effects, counter energy resolution and gas gain variations. However, the Fredholm integral transform above may not be solved for $S(\varepsilon')$ since the highly non - linear form of $R(\varepsilon', \varepsilon)$ prohibits a unique deconvolution. The best fit, using an appropiately weighted χ^2 statistic, to a set of observational data, is obtained by assuming a model source spectrum for $S(\varepsilon')$ with variable characteristic parameters (Gorenstein et al. (1968), Cruddace et al. (1972)). Statistical problems on the qualification of models and parameter estimation have been discussed by Lampton et al. (1976). This convolution procedure however, combines the results of modelling the instrument and source emission models. The influence of each stage of the modelling process is then difficult to determine.

A method that has been developed for spectral analysis problems, of a nature discussed above, is that of an iterative maximum entropy solution.

6.2.2.1 Maximum entropy spectral analysis. (M.E.M)

The maximum entropy method provides a conservative estimate for $S(\varepsilon')$, using no priori assumption about the form of $S(\varepsilon')$ and utilising the form for $R(\varepsilon', \varepsilon)$,

Fig. 6.2 Overlay of hardness map onto POSS print of the Cygnus Loop.

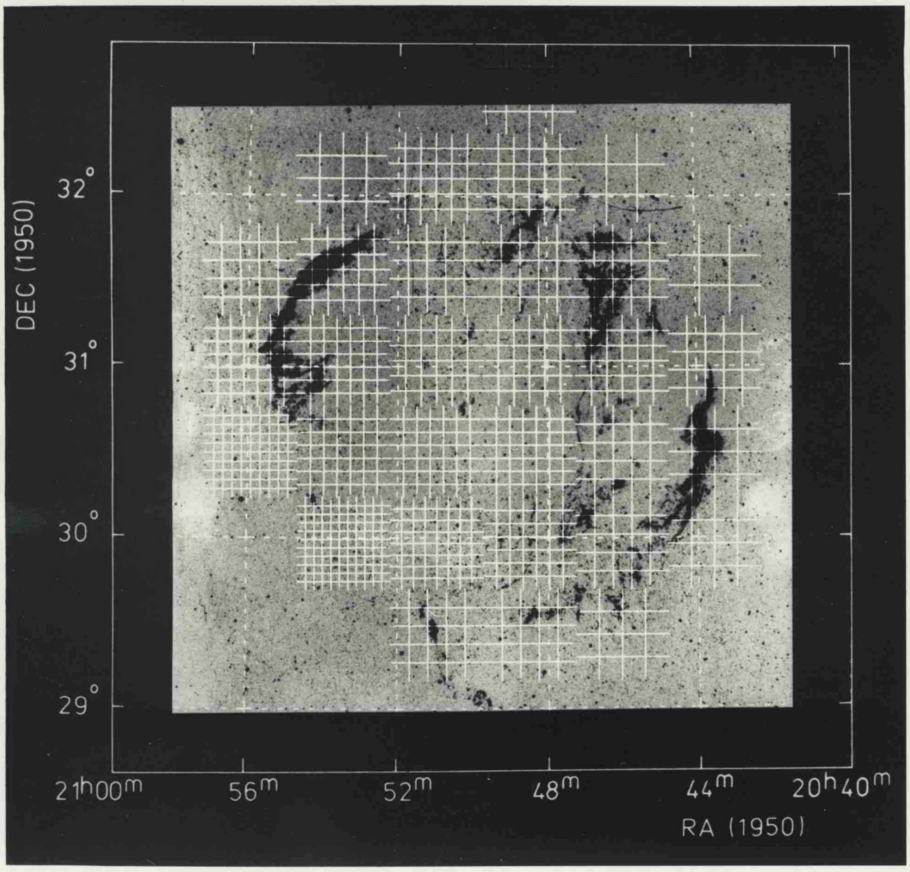

32°
31°
30°
29°
DEC (1950)
21h00m
56m
52m
48m
44m
20h40m
RA (1950)

describing the limitation of the overall instrument performance. Ables (1974) has presented a detailed discussion of the MEM. If $S_0(\nu)$ is the correlation (instrument) function in a finite number of intervals $\tau_n = n\Delta\tau$, then if $S(\nu)$ is the spectral representation of an incident signal over the frequency range $0 \leq \nu \leq \nu_N$; $\nu_N = \Delta\tau/2$, the relative entropy change is given by (in terms of $S(\nu)$ alone - for a uniform spectral density (white) signal passing through a linear filter with power gain function $S(\nu)$) :

$$\Delta H = \int_{-\infty}^{\infty} \mathrm{Log}_e\, S(\nu)\, d\nu$$

Then ΔH is maximised subject to the constraints

$$\int_{-\infty}^{\infty} S(\nu)\, e^{-i\lambda_n}\, d\nu = x_{on} \qquad : \lambda = 2\pi\nu . \Delta\tau$$

for observed spectrum $X_0 = \{x_{01}, x_{02} \ldots x_{0n}\}$ by iteration.

The MEM in the above form was adapted for application to the IPC anode pulse height data, by Willingale (1978). The best estimate of the number of counts received per energy bin $d\varepsilon_i$ was evaluated with the associated statistical weight taken approximately as the value of the Poissonian statistic. In the iteration procedure, the count spectrum was corrected for the overall instrument efficiency (Table 4.7) to obtain the estimated photon spectrum with associated errors, and the χ^2 statistic

$$\chi^2 = \sum_{i=1}^{n} \frac{(x_{0i} - x_i)^2}{x_{0i}}$$

indicating the goodness of fit to the observed spectrum X_0 of the estimated $\hat{X} = \{x_0, x_1 \cdots x_n\}$ was minimised, and so that the reduced $\chi^2 \sim 1$. The stability of the solutions $\hat{X}$ to statistical fluctuations in an observed pulse height distribution was tested by perturbing each data set many times, using a random number generator and re - using the MEM algorithm on each independantly perturbed data set. Mean and variance values could therefore be assigned to each $\hat{X}$ value. It was found that the variance was well approximated by the estimated count x_i and in some cases the variance was considerably less than x_i . The perturbations resulted in slight changes in the $\hat{x}$ solutions, but these were small compared to the gross differences observed between different regions of the hardness map.

The result of MEM for a simulated, uniform photon spectrum incident on the X-ray telescope, are shown in Fig. 6.3. The IPC pulse height interval was set at 0.05 keV, enabling a fine enough spacing to resolve all of the detail in the MEM solution. The small values of χ^2 indicated accurate modelling of the telescope spectral response. The MEM was applied to the observed IPC anode pulse height data in regions delineated as shown in Fig. 6.4 and Fig. 6.5 show the reconstructed incident photon spectra, with error bars representing the rms fluctuations derived from 12 independant perturbations, from three separate regions. Most of the solutions were smooth curves with a single peak which shifted to higher energy in the harder regions. However, one region, W, exhibited a large secondary peak at 0.9 keV. Adjustment of the energy calibration and efficiency parameters within reasonable limits had very little effect on this peak. Furthermore, the perturbation studies indicated that this peak had a significance of 5.2σ. This discrete feature was due to an excess of $\sim$ 40 counts between 0.8 - 1.0 keV which corresponds to a flux of $\sim$ 5 ph./cm^2/s.

6.2.3 Estimates of X-ray spectral parameters.

With the confirmation of the previous X-ray survey results and [Fe XIV] observations (2.4.3) that the X-ray emission from the Cygnus Loop originates from hot, optically thin plasma of near cosmic abundances, the photon spectra of Fig. 6.5 were fitted with thermal X-ray spectra, in order to provide a simple understanding of Fig. 6.2. A thermal bremsstrahlung model, to yield an estimate of effective electron temperature and columnar density for each region was used. A more sophisticated emission line model was not justified since the data were severely photon limited and only a calibration of the hardness map was required. The

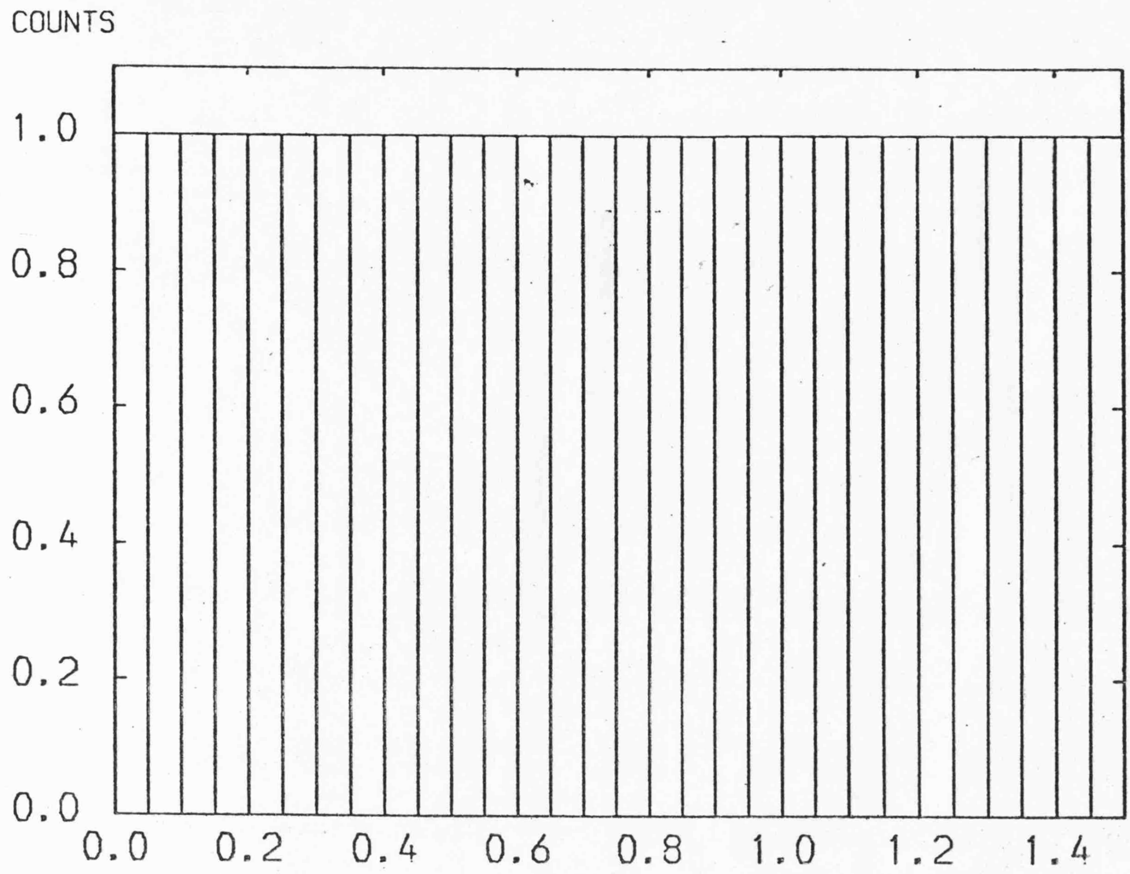

(a)

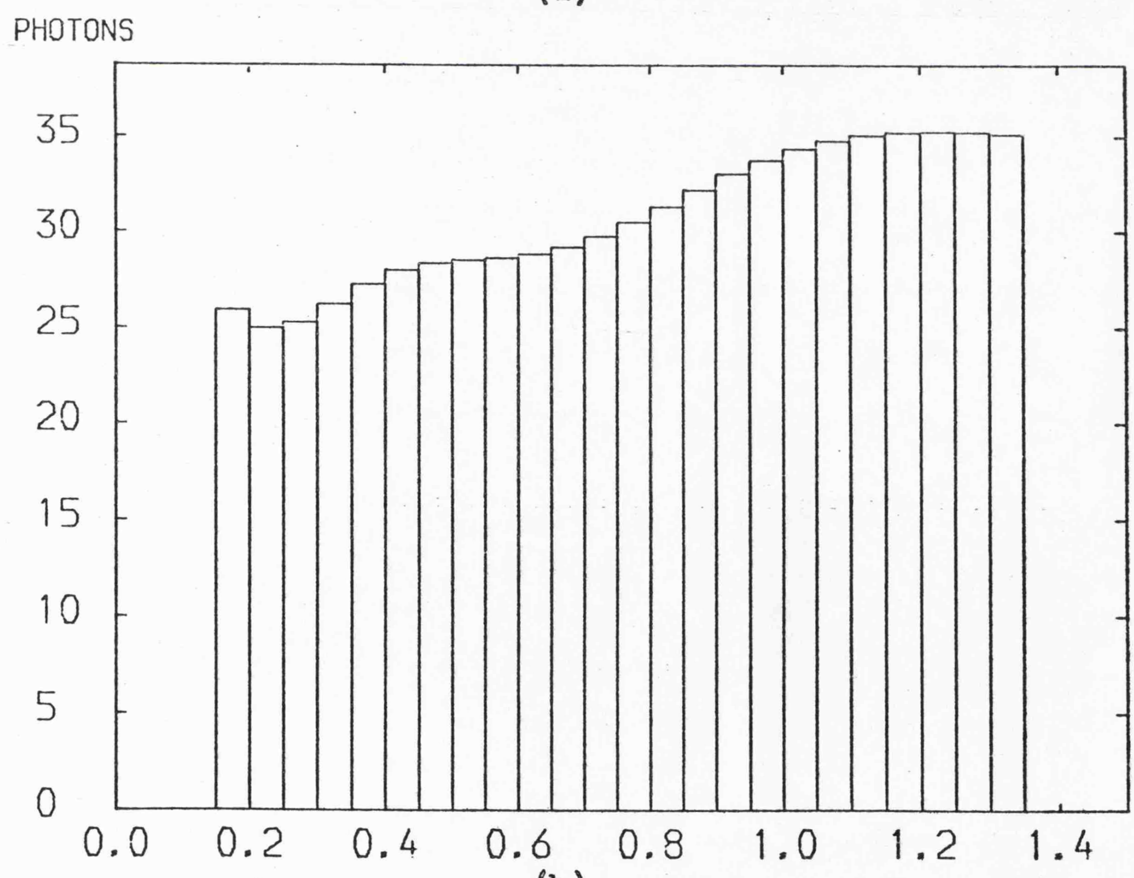

(b)

COUNT 30

CHI-SQUARED 0.177

Fig. 6.3. (a) Uniform field photon spectrum incident on the X-ray telescope.
(b) The Maximum Entropy Reconstruction of (a) using the measured IPC and mirror efficiences.

estimated count was used as the statistical weight for χ^2 fitting. This did not represent the true weight of $\hat{X}$ (6.2.2) but served as a reasonable (although pessimistic) approximation as borne out by the perturbation studies (6.2.2).

The thermal bremsstrahlung function used was of the form (Culhane (1969), Culhane and Acton (1970))

$$\frac{dN}{d\varepsilon} = C\,\bar{g}(\varepsilon, kT)\,\frac{e^{-\frac{\varepsilon}{kT}}}{\varepsilon\,(kT)^{0.5}} \cdot e^{-N_X \sigma(\varepsilon)} \qquad ph./cm^2./keV$$

where ε is the X-ray energy in keV and kT the effective electron temperature of the plasma. Since the absolute detection efficiency of the telescope was unknown to a factor 2, the emission measure was not included as a free parameter, and the model spectra were then normalised to the photon count $\hat{X}$ in each case. The Gaunt factor used was that derived from the Born approximation for free - free collisions in a thermal plasma (Greene (1959)).

$$\bar{g}(\varepsilon, kT) = \frac{\sqrt{3}}{\pi}\, e^{\frac{\varepsilon}{kT}}\, K_0\left(\frac{\varepsilon}{2kT}\right)$$

In the interstellar absorption term, N_X represents the number of equivalent hydrogen atoms in the line of sight (Ryter et al. (1975)) and $\sigma(\varepsilon)$ is the effective absorption cross - section per hydrogen atom. The following fit for based on the calculations of Fireman (1974) was used :

$$\sigma(\varepsilon) = 0.7 \times 10^{-22}\, \varepsilon^{-3} \quad cm^2 \quad : \quad \varepsilon < 0.53 \ keV$$

$$\sigma(\varepsilon) = \left\{ 2 + \frac{3.5}{6.5}\left(\varepsilon - 0.53\right) \right\} \times 10^{-22}\, \varepsilon^{-3} \quad cm^2 \ : \quad 7.1 \geqslant \varepsilon \geqslant 0.53 \ keV$$

The results are shown in Table 6.1. The two limiting, single parameter models, constant column density and constant temperature, were both used to try to explain the simple form of the hardness map.

Fixing the column density at 6 x 10^{20} cm^{-2} gave a reduced $\chi^2 < 1$ for the NW, SE regions and produced a temperature range of

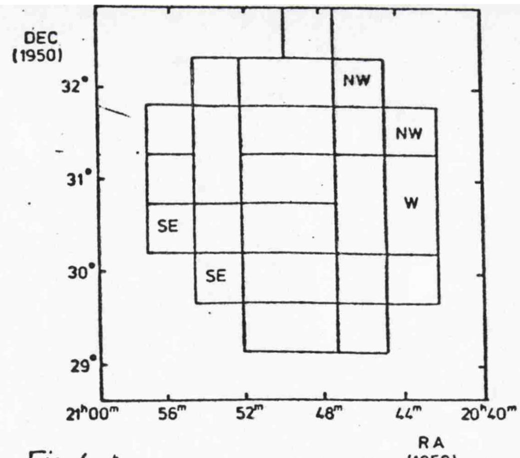

Fig. 6.4.

Regions of the Cygnus Loop SNR used in detailed analysis.

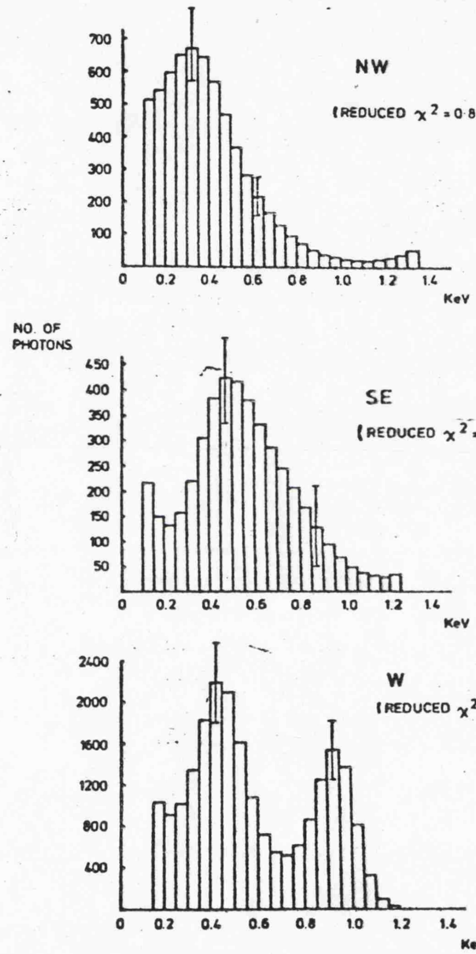

Fig. 6.5.

Photon spectrum estimates from the MEM algorithm for the NW, SE and W regions of the Cygnus Loop.

Spectral fitting results for the Cygnus Loop.

Model	Region	T (10^6K)	N_x (10^{20}atom cm^{-2})	χ^2_ν
Two free parameters	NW	4 (1.6–30)	4 (0.1–8)	0.15
	SE	6 (4–13)	8 (5–10)	0.85
Fixed density	NW	3 (2–5)	6.0	0.49
	SE	8 (5–16)	6.0	0.97
Fixed temperature	NW	5.0	3 (0.6–6)	0.15
	SE	5.0	10 (6–10)	0.95

The ranges quoted are for 90 per cent confidence. The χ^2_ν quoted is for the thermal bremsstrahlung fit to the MEM solution.

$3 - 8 \times 10^6$ K, from NW to SE. These values are in reasonable agreement with previous results, for example Rappaport et al. (1974) reported a density of $5.5 \pm 3 \times 10^{20}$ cm^2 and temperature of $2.9 \pm 0.8 \times 10^6$ K. On the other hand, a high temperature of 5×10^6 K was required for an isothermal model, although a good fit was still obtainable in both the NW and SE yielding a column density range of $3 - 10 \times 10^{20}$ cm^2, NW - SE. This range of densities is high compared to previous X-ray measurements and interstellar reddening (Ryter et al. (1975)), assuming the 770 pc distance.

There is no evidence to corroborate a smooth gradient of column density (Charles et al. (1975), Geiss (1978)) as suggested by an isothermal model and the preferred explanation of the hardness map of Fig. 6.2 must be that it represents a systematic change in temperature across the Loop. Since, for an adiabatic, strong shock

$$T_s = 1.5 \times 10^{-41} \left(\frac{\mathcal{E}_0}{n_0}\right) \cdot \frac{1}{R_s{}^3} \quad \propto \frac{1}{n_0} \qquad (\text{constant } R_s)$$

$$L_X = 4\pi R_s{}^2 \cdot \Delta R_s \, n^2 . P(T) \quad \propto n_0{}^2 \qquad (\text{constant } R_s)$$

$$n = 4 n_0$$

Thus, the X-ray temperature gradient reflects a local density n_0 gradient at the Loop, particularly in a direction perpendicular to the galactic plane (Fig. 6.1) where the more dense regions reach a lower temperature. From Fig. 5. 14-19, the X-ray surface brightness distribution also imply a local density gradient normal to the plane.

The highly significant discrete peak (Fig. 6.5) present in the spectrum from the W region may be direct evidence for X-ray line emission. The IPC energy resolution was insufficient to accurately identify the feature. A possible explanation would be an increase in the abundance of Ne of Fe by an order of magnitude, to sufficiently increase $Ne\,\overline{\underline{IX}}$ or $Fe\,\overline{\underline{XVII}} - \overline{\underline{XVIII}}$ emission to account for the excess in the range 0.8 - 1.0 keV. The anomalous nature of the western limb may be expected, since the Loop appears to be encountering a prominent dust lane and

HI cloud (2.2.2 and 2.2.3) running north - south, just west of NGC 6960. Independant measurements of [Fe X] (2.4.3) indicate an electron temperature of 1 - 2 x 10^6 K, which supports the belief for a low temperature enviroment giving rise to Ne IX or Fe XVII - XVIII emission.

Evidence for the multiple temperature nature of the Loop X-ray emission was discussed in (2.4.3), where Gronenschild (1979) demonstrated that apparent electron temperatures had values 1 - 5 x 10^6 K and Inoye et al. (1979) obtained values of 1 - 10 x 10^6 K. The values obtained above, 3 - 8 x 10^6 K are therefore consistent. Gronenschild (1978) has presented results of estimates of X-ray spectral fits in the energy range 0.16 - 0.284 keV in 30' x 40' cells. Overall, the ANS and present spectral results are in fair agreement : the spectral temperature appears to increase in the NW - SE direction, where the ANS pixel containing the maximum temperature of 5 x 10^6 K is adjacent to the image (hardness map) pixel having apparent temperature 8 x 10^6 K; in the SW regions of the ANS map and present hardness map, the temperatures are lower, with consistent values of $\sim$ 2 x 10^6 K.

Disagreements arise from : the ANS values for the columnar density varied between 1 - 100 cm^{-2} (with the claim that the values may be associated with local HI filaments near the SNR) - the validity of these values was discussed in (2.3.3) and also, above; the ANS observations in the energy band 0.16 - 0.284 keV did not therefore detect any anomalous discrete X-ray emission $\sim$ 0.8 - 1.0 keV in the W limb, but a temperature estimate of 1 x 10^6 K with columnar density 6 x 10^{20} cm^{-2} is consistent, as discussed above.

To summarise so far, the spectral analysis of the soft X-ray image essentially yields effective electron temperature values between 3 - 8 x 10^6 K for the reasonable assumption of constant columnar density, with a fairly smooth temperature gradient existing NW - SE across the Loop. Anomalous discrete X-ray emission 0.8 - 1.0 keV (possibly Ne IX , Fe XVII - Fe XVIII flux at 1 - 2 x 10^6 K) may be associated with the W limb, possibly the site of interaction between the SNR blast wave, and dense cloud. Even though the ANS spectral results were derived through rather ill - fitting conditions (χ^2 with zero degrees of freedom; the relatively small energy band where N_H is the dominant parameter), in comparison with the image analysis results, there is an overall agreement in temperature range and distribution (except in the NW region). However there is no evidence to support the gross N_H changes invoked by the ANS results.

6.3 X-ray image discussion.

6.3.1 General X-ray image features.

Images of the Cygnus Loop were presented in Fig. 5. 14-17. (smoothed with a top hat filter $12' \times 12'$), in Fig. 5. 18 (feature enhancement with a Weiner filter using an instrument response of $15'$ FWHM) and Fig. 5. 19 (smoothing and reconstruction with the MEM, with $20'$ FWHM instrument response). For each image, detailed comparison may be made with the optical $H\alpha$ image, [Fe XIV], [Fe X] observations (2.4.3) together with high resolution, aperture synthesis radio maps and HI observations (2.3.2 and 2.3.3). The features of the Loop images are first discussed below then comparison made with the recent X-ray maps (2.4.2).

(1) The images Fig. 5. 14 - 19 exhibit an incomplete, assymmetrical, thick ($\Delta R/R \sim 0.2 - 0.4$) shell containing discrete, small scale ($\leq 15'$, compared with the shock wave radius of $\sim 90'$) X-ray emitting regions.

(2) From Fig. 5. 14 - 15, 5. 18 the Cygnus images in the energy ranges 0.15 - 0.5 keV and 0.56 - 1.12 keV contain the same features with no indication of decreasing X-ray shell radius with increasing X-ray energy, to within $4'$. However, the Cygnus images have a limited spectral dynamic range of 10 : 1 and contain the systematic errors discussed in (3.3.3 and 5.2.1).

(3) From Fig. 5. 14 - 5. 19, the estimated fraction of the total X-ray flux from each of the regions containing NGC 6990, 6992 - 5, and the northern regions, was $\sim$ 10%.

(4) The images reveal no significant evidence (upper limit $\leq \frac{1}{2}\%$ total X-ray flux) for an X-ray emitting stellar remnant.

Table 6.2 summarises details of the Cygnus Loop images.

TABLE 6.2

Summary of the Cygnus Loop X-ray image characteristics (0.15 - 1.12 keV)

Parameter	Symbol	Value
X-ray centre	α (1950)	$20^h\ 49.75^m$ } $\pm\ 0.2^\circ$
	δ (1950)	$30^\circ\ 53'$
Mean outer X-ray radius	R_{xo}	1.3°
Mean inner X-ray radius	R_{xi}	0.9°

Discrete features	Position α (1950)	Position δ (1950)	Diameter
	$20^h\ 45^m$	$30^\circ\ 44'$	$0.53^\circ \pm 0.1^\circ$
	$20^h\ 48.4^m$	$31^\circ\ 56'$	$0.67^\circ \pm 0.1^\circ$
	$20^h\ 50^m$	$32^\circ\ 00'$	$0.60^\circ \pm 0.1^\circ$
	$20^h\ 52.4^m$	$30^\circ\ 56'$	$0.33^\circ \pm 0.1^\circ$

Previous X-ray maps were reviewed in (2.4.2). Comparing with Fig. 5. 14 - 19, the images confirm the general limb brightened nature of the soft X-ray emission. The images contain the same gross features associated with the limbs but the inherent increased sensitivity (a factor $\gtrsim$ 4 over the most sensitive ANS map) produce a more complete, filled shell with more feature definition overall. The reported discovery of the X-ray central source (2.4.2) may now be explained. About 5% total X-ray flux is contained within $\sim \frac{3}{4}^{\circ}$ diameter circle near the centre, e.g. Fig. 5. 17. This central region is partially surrounded by regions of somewhat lower intensity which were apparently exaggerated in the ART map (2.4.2) so as to enhance the discrete appearance of the central radiation. With the advantage of uniformity of exposure, the X-ray images reveal more distributed X-ray emission between the E, W, and N regions, each region containing $\sim$ 10% total flux, compared with the ANS result of $\sim$ 55% total flux from the N, NW regions. In the images, the significance of the feature near NGC 6990 is higher than the ANS result. More structure is observed in the image around NGC 6992 - 95, and the X-ray minimum in this region confirms the ANS result.

To summarise so far, the soft X-ray images contain the same gross structure as presented in the X-ray maps (2.4.2), but through higher sensitivity and uniformity of exposure, more feature definition. Particularly, the features associated with the X-ray limbs are $\lesssim 15'$, equivalent to $\sim$ 5 pc in size, at the Loop, likely indications of inhomogeneities in the local interstellar medium. The X-ray images support the view that the SNR may be described, on the large scale, by the Sedov adiabatic blast wave model, but also show that small scale ($1' - 10'$) correlations in particular regions, with observations at optical and radio wavelengths, must take account of the effects of non - uniform expansion of the blast wave through the local medium inhomogeneities.

6.3.2 X-ray/optical comparisions.

The contour plots of Fig. 5. 20 - 21 are superimposed on an $H\alpha$ POSS image of the Cygnus Loop, Fig. 6. 6 - 7. The X-ray contours reveal more clearly the close association between X-ray intensity and optical density of the filaments particularly for NGC 6992 - 5 and 6990. The X-ray emission is seen to fall off sharply (within 10' response) at the optical boundaries in these regions. However, in the northern regions there appears to be a weaker association and particularly so for the larger triangular shaped nebulosity to the NW. To the south (where the overall X-ray/optical emission is comparable with the central regions) again there is a close association with optical nebulosity.

The contours of X-ray emission at $\alpha \sim 20^h 45^m$, $\delta \sim 30^\circ.8$ exhibit extremely close correlation with the apparent curvature of the upper part of NGC 6990. Observations have been reviewed (2.2.2., 2.3.3) that indicate the presence in the region, of a dense cloud possibly undergoing interaction with the SNR blast wave. Assuming a 770 pc distance SNR distance, the size of the X-ray emitting region, from Table 6.2, is $\sim$ 7 pc. McKee and Cowie (1975), in investigating the interaction of an adiabatic shock wave with a spherical cloud (to explain quantitatively the optical/X-ray velocity problem) noted that, although the size of the Loop filaments were consistent with representing a thin cooling layer behind a shock penetrating a (Spitzer (1968)) standard cloud of $\sim$ 7 pc, their shape was not. Filaments associated with large, spherical clouds would be curved inward, since the cloud shock would lag behind the blast wave. In order for the cloud shock to keep up with the blast wave, the clouds must have at least one small dimension.

Sgro (1975) considered models of soft X-ray emission from shock wave/cloud collisions. The X-ray temperature in NGC 6990 has an apparent value $T_e \sim 2 \times 10^6$ K (6.2.3) and hence the plane parallel shock velocity $v^2 = T/11.3$ where the post incident shock temperature $T \sim 1.6 \times 10^6$ K, $T \cong 0.8\ T_e$ from Rappaport et al. (1974). From (2.5) the preshock medium density $n_i \sim 0.25\ cm^{-3}$ and the (HI) cloud density near

Fig. 6.6 Overlay of X-ray contour plot (MEM) onto POSS print.

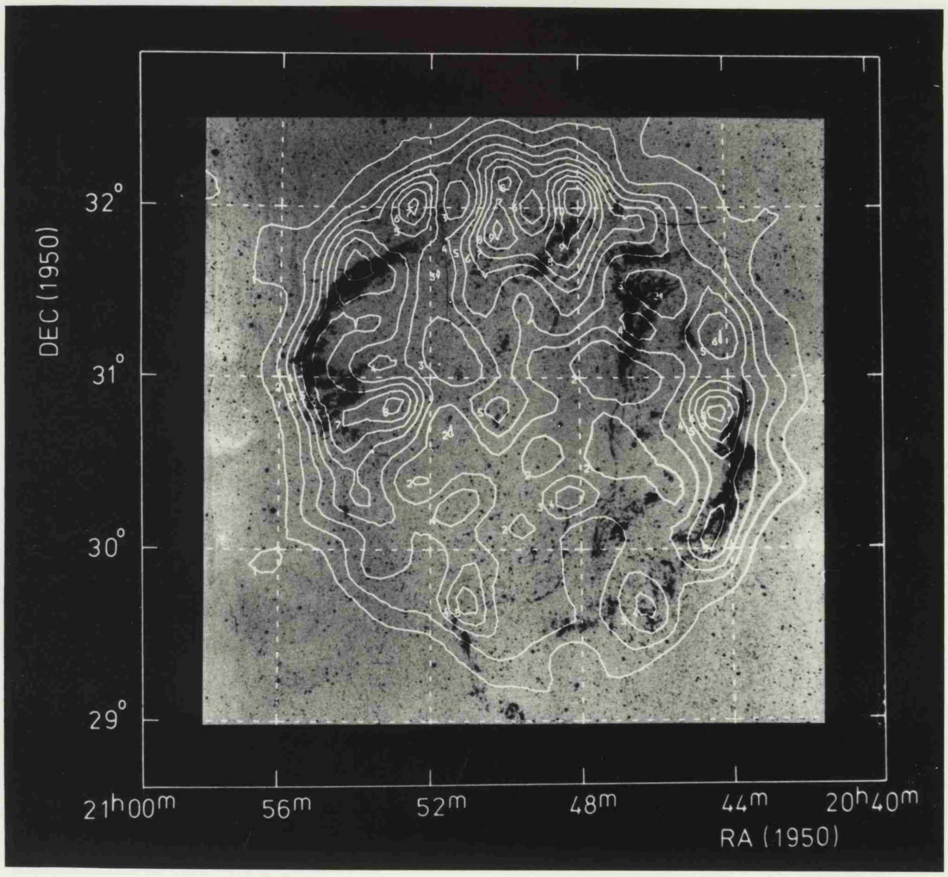
DEC (1950)
32°
31°
30°
29°
21h00m
56m
52m
48m
44m
20h40m
RA (1950)

Fig. 6.7 Overlay of X-ray contour plot (top hat filter).

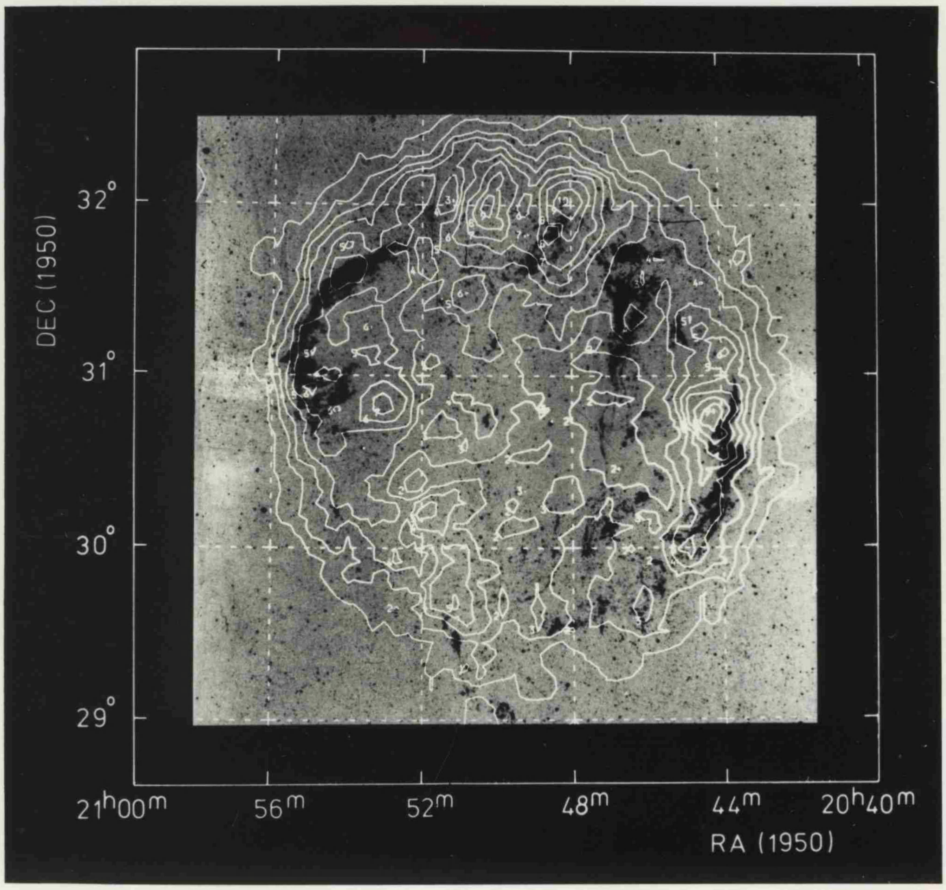
DEC (1950)
32°
31°
30°
29°
21h00m
56m
52m
48m
44m
20h40m
RA (1950)

NGC 6990, $n_c \sim 5-10\ cm^{-3}$ (2.3.3). Then, from Sgro (1975), for $n_c/n_i \sim 40, \beta \sim 5$ where β is the ratio of post transmitted shock pressure through the cloud and the post incident shock temperature. Then, for soft X-ray emission from a 'hot' cloud,

$$n_c' = \frac{5.8 \times 10^{-4} \beta^{5/7} v^{10/7} n_i^{5/7}}{d^{2/7}} > n_c$$

where d is the effective cloud dimension perpendicular to the shock. Rearranging and evaluating, an upper limit for d is found, $d < 6 \times 10^{-3}\ pc$. Thus, possibly the X-ray emission from a region near NGC 6990 may be derived from heated clouds in the form of sheets with dimensions comparable to observed filament dimensions of $\simeq$ 4 pc x 4 x 10^{-3} pc (2.2.2). Such a 'hot' cloud may be observed as a source of soft X-rays (and possibly coronal lines) for an estimated time (Sgro 1975)) $\tau_H = 7 \times 10^4 T_6^2/n_c = 1.8 \times 10^4\ yr$, comparable with the SNR age. (Table 2.4) That the fact the clouds appear distributed over the X-ray shell, may be explained, to a first approximation, by the standard cloud model (Chapter 1). For a cloud density of 5 x 10^4 Kpc^{-3} and Loop volume $\sim$ 10^{60} cm^3, standard radius 7 pc, the probability of one or more clouds being encountered by the Loop is $\simeq$ 1.

Little comment can be made with respect to the cloud evaporation and evaporation models (McKee et al. (1977, 78)) for SNR evolution in a cloudy medium. In particular, the close correlation between the [Fe XIV] , [Fe X] and soft X-rays may be explainable by these models (2.4.3). However, from the X-ray images, no finer correlation than 10' with the soft X-ray emission and the regions observed in [Fe XIV], [Fe X] (2.4.3) may be made. Also, no values of X-ray emission measure, directly comparable from the models, may be reasonably estimated. No evidence has been found (from HI studies (2.3.3)) to support the (smooth) cloud acceleration mechanism as applied to the Loop, by McKee et al. (1978), to explain the high $H\alpha$ velocities. It is suggested that [Fe XIV], (< 1') observations be made near NGC 6990, in a similar way as reported by Clarke et al. (1979), to establish the validity of the cloud evaporation model, together with high resolution X-ray imaging (scale < 1' ≡ 0.2 pc).

It should be noted here however, that the models of McKee et al. (1977, 1978) assume SNR evolution in a medium of $\sim$ 0.003 cm^{-3}, and that the evaporation effects become important for SNR radii $\gtrsim$ 50 pc. From the review of Cygnus Loop SNR observations, the evaporation model may not be applicable.

The current X-ray images of the Loop compared with the optical morphology, may perhaps be best described adequately on the basis of the standard cloud model of the local interstellar medium, and by the blast wave/cloud models of Sgro (1975) and McKee and Cowie (1975).

Finally, from the demonstration above, that the NGC 6990 cloud may be described as a sheet of material seen edge on may indicate that the observed filament proper motions (2.2.3) represent the velocity of fronts rather than cloud material, and thus the distance determination of the Loop, 770 pc, would be an underestimate.

6.3.3 X-ray/radio comparison.

Fig. 6.8 shows the overlay of the X-ray image of Fig. 5. 19 onto reduced isophotes of the radio map of Keen et al. (1973) and (2.3.2).

To within the X-ray image 10' resolution, there is close correlation of X-ray maxima with radio maxima in the regions NGC 6992 - 95, 6990, as expected from the shell compression models based on HI studies (2.3.3), with the separation (2.4.3) clearly visible in NGC 6992 - 95. There is weak correlation between X-ray features and radio emission in the northern regions and no correlation in the southern regions, where the interstellar medium density is perhaps very much more homogenous. The X-ray emission originates almost entirely within the radio contours.

There is no significant flux from the discrete radio sources CL6 and CL7 (2.3.2) or from the variable source CL4 (with an upper limit flux of $\simeq$ 10^{-10} $erg/cm^2/s$).

In summary, the X-ray image emission features near NGC 6992 - 95, 6990 correlate (to within 10' response) with

Fig. 6.8 Overlay of X-ray map (MEM) onto radio map.

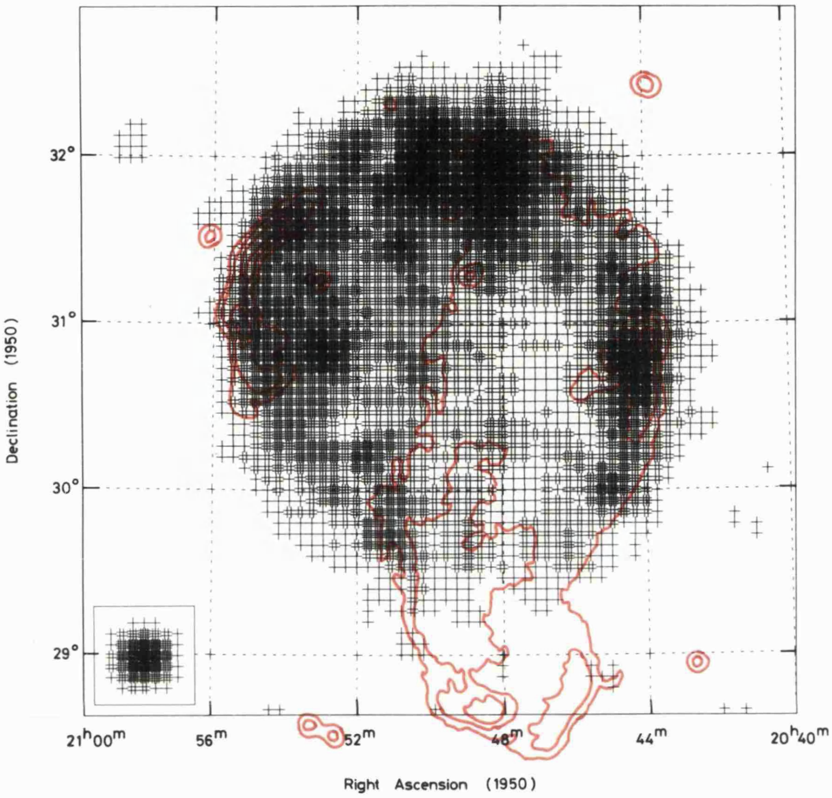
32°
31°
30°
29°
Declination (1950)
21h00m
56m
52m
48m
44m
20h40m
Right Ascension (1950)

radio knots of emission, described by the local magnetic field compression model involving dense clouds, with densities of $\simeq$ 5 cm^{-3} (2.3.3), of the order of the values of the standard cloud densities. The $1'$ resolution radio map tends to indicate that the (shocked) clouds tend to form thin sheets, or that they originally had dimensions much less than the current SNR shock radius.

6.4 Summary and conclusions.

The soft X-ray (0.15 - 1.12 keV) images ($10'$ resolutions) of the Cygnus Loop SNR, Fig. 5. 14 - 19, have been discussed.

Using the MEM analysis (6.2.2.1) in regions delineated as in Fig. 6.1 ($32' \times 32'$), applying a simple thermal bremsstrahlung model revealed significant differences in apparent electron temperature, 3 - 8 x 10^6 K for a columnar density, 6 x 10^{20} cm^{-2}. This range of temperature is in agreement with the estimated range of temperatures reported by Gronenschild (1978) and Inoye et al. (1979). However, it is argued that there is insufficient evidence for gross columnar density changes across the Loop (6.2.3). A smooth variation of temperatures was found to exist across the Cygnus Loop image, with the temperature increasing NW to SE, possibly indicating a local interstellar medium density gradient perpendicular to the galactic plane. Anomalous, discrete X-ray emission, 0.8 - 1.0 keV, possibly Ne $\overline{IX}$, Fe $\overline{XVII}$ - $\overline{XVIII}$ flux at 1 - 2 x 10^6 K, may be associated with the W limb, near NGC 6990, possibly the site of SNR blast wave - cloud interaction.

General features (6.3.1) of the X-ray images, Fig. 5. 14 - 19 generally contained the gross features of recent X-ray maps, Fig. 2. 4 - 2.5, but more feature definition, through the imaging advantages of increased sensitivity and uniformity of exposure. The images revealed an incomplete, assymmetrical, thick shell of X-ray emission with several discrete, small scale X-ray regions, possibly sites of blast wave - cloud interactions (Table 6.2). No X-ray central source of the SNR was detected. Regions of low X-ray intensity, particularly in the SW, were generally associated with the higher X-ray temperatures.

X-ray/optical comparisons (6.3.2) revealed that particularly in the region NGC 6992 - 95, 6990, the X-ray and optical structure was highly (10$'$) correlated. An application of the shock wave/cloud interaction models of Sgro (1975) to the X-ray paramters, near NGC 6990, demonstrated that, on the scale $\sim$ 10$'$, X-ray emitting clouds most likely form sheets of material, of sizes comparable to the optical filaments. Mckee and Cowie (1975) quantitatively explained the differences in X-ray/optical shock velocities. The optical emission and properties of a shocked cloud has been discussed by Cox (1972) and Sgro (1975). In order to quatitatively explain the close association of the X-ray/optical emission, particularly in the region NGC 6992 - 95, 6990, Fig. 6. 6 - 7, a multiple phase interstellar medium must be invoked, consisting of an intercloud medium, a (Sgro) cold dense cloud core, surrounded by a warmer envelope (which may then become the Sgro hot cloud). SNR evolution in an extremely inhomogenous cloudy, medium, where the dynamics are dominated by interactions between the remnant and interstellar clouds, has been studied in detail by McKee and Ostriker (1977) in presenting their theory of the interstellar medium. They presented an analysis of SNR evolution in a multi - component medium, including evaporation of cloud material. McKee and Ostriker deduced the existence of interstellar clouds consisting of two components : cold ($\sim$ 80 K), high density ($\sim$ 40 cm^{-3}), cores of radii $\sim$ 0.1 - 10 pc and separated by $\sim$ 90 pc, embedded in a warm ($\sim$ 8000 K) ionised, low density ($\sim$ 0.2 cm^{-3}) component 2 - 10 pc in radius, with intercloud distances of 10 pc. X-ray emission would be produced only in the low density region, and the optical/radio emission would originate from the high density regions.

However, with the limiting 10$'$ resolution ($\sim$ 7 pc), no comment may be made on the close X-ray/optical correlation. X-ray imaging with 0.1 pc ($\simeq$ 10$''$) is clearly needed.

X-ray/radio comparisons (6.3.3) again revealed, particularly in regions NGC 6992 - 95, 6990, the close correlation. However, as stated above, both X-ray and radio (including HI) surveys with $\simeq$ 10$''$ resolution are required in these regions, to investigate fully the shock wave - cloud interactions, and to search for HI cool cloud cores.

In conclusion, the results derived from the Cygnus X-ray images, and from comparisons with recent X-ray maps, optical structure and radio survey and HI observation may be presented as follows :

(1) The images contain the same gross features as the recent X-ray maps, but due to the higher sensitivity, several discrete features are clearly associated with the X-ray shell, coincident (to $\simeq 10'$) with bright optical and radio features, possibly sites of SNR blast wave/cloud collisions.

(2) The gross structure of the images may be adequately described by the Sedov blast wave model, but the small scale ($\lesssim 10'$) structure requires a quantitative description of shock wave/cloud interactions. Down to the present image resolutions, X-ray emission from the discrete features associated with the X-ray shell (e.g. NGC 6990) appear to be described by Sgro hot clouds, forming sheets of the order of sizes of the optical filaments. The apparent close correlation of optical/radio (from cold clouds) and X-ray emission features would seem to require the existence of a multi - phase medium, of the nature described by McKee and Ostriker (1977).

(3) The broad band images with $\simeq$ 10:1 dynamic energy range enabled estimates of X-ray spectral parameters in $32' \times 32'$ regions of the images. Subsequent X-ray spectral analysis yielded apparent temperatures $3 - 8 \times 10^6$K, with a smooth temperature gradient. Both the temperature and X-ray intensity distributions are consistent with local medium density changes and for the existence of a density gradient perpendicular to the galactic plane.

(4) The anomalous, discrete X-ray emission (0.8 - 1.0 keV), possibly Ne IX , Fe XVII - XVIII , associated with the W limb, near NGC 6990, may indicate an overabundance of Ne or Fe by an order of magnitude.

Results from the above analysis and discussion have been published or submitted for publication (Rappaport et al. 1979, Kayat et al. 1979).

Future observations of the Cygnus Loop SNR must be made at radio, X-ray and optical wavelengths, at high angular resolution ($\lesssim 10''$), possibly near the more intense regions in the X-ray images, to further elucidate the SNR evolution in the interstellar medium. Detailed study of the SNR blast wave/cloud interaction are important to validating recent models. In particular :

(1) High resolution X-ray imaging ($10''$) must be made, in the regions of discrete emission in the X-ray images, to be able to make detailed optical/radio (knot) comparisons.

(2) High resolution X-ray spectral observations, in the lower temperature regions (e.g. NGC 6990) would give accurate data on plasma temperatures, densities and state of ionization equilibrium.

(3) High resolution [Fe XIV], ([O III], [N I]) would complement X-ray spectral observations and possibly give greater insight into the detailed X-ray/optical correlation, and compare with cloud emission models.

(4) High resolution HI observations of the discrete X-ray features may yield evidence for cool, dense clouds, within the X-ray emitting envelopes of clouds.

(5) Finally, since the optical filament proper motions and radial velocities, currently available, may yield an underestimate for the SNR distance, if the filaments represent shock fronts. Since SNR parameter estimates depend on the distance d , critically ($E_0 \propto d^{5/2}$ on the Sedov model) important for the understanding of SNR dynamics, simultaneous measurements of proper motions and radial velocities on individual filaments are required.

References.

Ables, J., 1974. Astron. Ap. Suppl., 15, 383.

Charles, P., Culhane, J. and Zarnecki, J., 1975. Ap. J., 196, L19.

Cox, D., 1972. Ap. J., 178, 159.

Cruddace, R., Bowyer, S., Lampton, M., Mack. J. and Margon, B., 1972. Ap. J., 174, 529.

Culhane, J., 1969. MNRAS, 144, 375.

Culhane, J. and Acton, L., 1970. MNRAS, 151, 141.

Geiss, S., 1978. Thesis, Cambridge.

Gorenstein, P., Gursky, H. and Garmire, G., 1968. Ap. J., 153, 885.

Greene, J., 1959. Ap. J., 130, 693.

Gronenschild, E., 1978. Mem. Soc. astr. ital., 49, 553.

Gronenschild, E., 1979. Utrecht preprint.

Inoye, H., Koyama, K., Matsuoka, M., Ohashi, T., Tanaka, Y. and Tsunemi, H. ISAS preprint.

Kayat, M., Rolf, D., Smith, G. and Willingale, R., 1979. Submitted to MNRAS.

Keen, N., Wilson, W., Haslam, C., Graham, D. and Thomasson, P., 1973. Astron. Ap., 28, 197.

Lampton, M., Margon, B. and Bowyer, S., 1976. Ap. J., 208, 177.

McKee, C. and Cowie, L., 1975. Ap. J., 195, 715.

McKee, C. and Ostriker, J., 1977. Ap. J., 218, 148.

McKee, C., Cowie, L. and Ostriker, J., 1978. Ap. J., 219, L23.

Rappaport, S., Doxsey, R., Solinger, A. and Borken, R., 1974. Ap. J., 194, 329.

Rappaport, S., Petre, R., Kayat, M., Evans, K., Smith, G. and Levine, A., 1979. Ap. J., 227, 285.

Ryter, C., Cesarsky, C. and Audouze, J., 1975. Ap. J., 198, 103.

Spitzer, L., 1968. Diffuse Matter in Space, Wiley NY.

Willingale, R., Private communication, Leicester.

"Imaging X-ray Astronomy: The Cygnus Loop SNR"

A Ph.D. thesis submitted to the University of Leicester by

Michael A Kayat

August 1980

ABSTRACT

Supernovae and supernova remnants (SNR) are probably important energy sources in the interstellar medium (ISM) and an understanding of the intermediate and advanced stages of SNR evolution are particularly essential.

This thesis describes, first a brief review of the current understanding of the ISM and later stages of SNR evolution, then a detailed review of observations of the Cygnus Loop SNR, a relatively old SNR. Details are given of the design and instrumentation of a rocket - borne experiment, which subsequently was utilized to obtain the first X-ray image of a SNR, the Cygnus Loop. The results of X-ray image and spectral analysis are presented, and discussed with respect to previous optical, radio and X-ray observations, and to current SNR blast wave and ISM models.